Statistical Mechanics of Sediment Transport

A DISSERTATION
SUBMITTED TO THE FACULTY OF THE GRADUATE SCHOOL
OF THE UNIVERSITY OF MINNESOTA
BY

Arvind Singh

IN PARTIAL FULFILLMENT OF THE REQUIREMENTS
FOR THE DEGREE OF
Doctor of Philosophy

Efi Foufoula-Georgiou, Adviser

December, 2011

Acknowledgements

I would like to express my sincere gratitude to my adviser, Efi Foufoula-Georgiou, for helping me and supporting me during these years. Without her inspiration and constant support, I would never have been able to finish my doctoral research.

I would also like to express my sincere gratitude to the members of my committee, Heinz Stefan, Christopher Paola, and Fernando Porté-Agel for their invaluable suggestions and comments. Special thanks to Prof. Vaughan Voller who agreed to be a member of my thesis committee at the last moment.

I am indebted to Peter Wilcock, Stefano Lanzoni, Bill Dietrich, Tryphon Georgiou, Doug Jerolmack and Kurt Fienberg, for the stimulating ideas and fruitful collaborations.

This thesis could not have been conducted without the unflagging and generous support (both material and intellectual) from the staff at the St. Anthony Falls Laboratory. I thank Craig Hill, Sara Johnson, Jeff Marr, Chris Ellis and many others for creative technical and logistic assistance in running experiments over the past few years.

This research has been supported by the National Center for Earth-surface Dynamics (NCED), Doctoral Dissertation Fellowship (DDF), and computational resources were provided by the Minnesota Supercomputing Institute (MSI).

Finally, I would like to thank my family and friends for their continuous support during my doctoral years.

Dedication

To my family and friends

Abstract

Accurate prediction of the evolution of rivers and landforms under varying climatic and human-induced conditions requires quantification of the total sediment transported by a river. Based on a series of controlled laboratory experiments conducted at the St. Anthony Falls laboratory, University of Minnesota, we demonstrated that (a) bedload sediment transport at very small time scales can be an order of magnitude larger or smaller than the long-time average; (b) bed morphodynamics can be inferred from the spectral properties of turbulent velocity fluctuations above the bed; and (c) the nature of scaling and the degree of complexity and non-linearity in bed elevation fluctuations and sediment transport rates depend on the bed shear stress. These results are discussed in the context of understanding and exploring the dependence of sediment transport scaling on near-bed turbulence, bed topography, and particle-size distribution, and deriving stochastic transport models which give rise to the observed scaling. They also form the foundation of relating microscale dynamics of particle movement to the macroscale statistics of sediment transport via minimum complexity stochastic models.

Contents

List of Tables

List of Figures

Chapter 1

Introduction

The ability to accurately predict the evolution of rivers and landforms under varying climatic and human-induced conditions requires the accurate quantification of the total sediment transported by a river. Bedload transport (resulting from the motion of particles rolling, sliding or traveling along the stream bed) represents a considerable fraction of this total sediment flux (up to 60 %), especially in gravel-bed rivers. Despite the large body of work on bedload transport, our understanding still remains poor to this day and the predictive capacity required for protecting eroding river banks against floods and for developing sustainable measures for protecting and restoring aquatic ecosystems interacting with river beds remains below satisfactory levels. A major hindrance to advancing accurate prediction of bedload transport is the fact that the movement of gravel particles exhibits a complex random structure which cannot be adequately captured by the bulk deterministic theories available to date (e.g., [4] and references therein). New measurement technologies which can track individual particles and record their velocities, distances traveled, and rest periods, as well as track the evolution of river beds and near-bed turbulence, have opened-up new opportunities for break-through research on this problem. The research discussed here promises to advance the predictive modeling of bedload sediment transport via a combination of laboratory experiments and new physical- mathematical formalisms based on statistical theories of turbulence and nonlinear dynamical systems [5, 6]. An important innovation of this research is the development of methodologies for relating microscopic properties of individual gravel particles (not always feasible to monitor in real systems) to macroscopic properties of

bedload transport for prediction purposes using the approach of statistical mechanics which is a branch of physics that applies probability theory and provides a framework for relating the microscopic properties of individual particles to the bulk properties of materials.

The main objective of this research is to contribute to a better understanding of the interaction between sediment transport, bed morphodynamics and near-bed turbulence over a continuum of flow discharge conditions and grain size distributions and use this understanding to accurately predict the evolution of river beds under changing climatic conditions and land-use. This research involved a combination of experimental observations and advanced mathematical techniques with the specific objectives to: 1. Characterize the statistical structure of sediment transport rates at different time and space scales and its relation to particle-scale dynamics and propose a theoretical framework that offers the ability to compare sediment transport rates at different time and space scales. 2. Detect nonlinearity and complexity in gravel bed dynamics and its implication for setting the upper limit to prediction in numerical models of sediment transport. 3. Transfer theoretical results to practice by proposing surrogate bedload measurement techniques (for example by using auxiliary information from velocity fluctuations, grain size distribution, and bed elevations) which are easier to implement in real rivers for prediction of bedload sediment transport.

As part of this research, experiments were conducted in the Main Channel facility located at St. Anthony Falls Laboratory, University of Minnesota. These experiments were the follow-up of an interdisciplinary experimental program conducted in the spring of 2006 known as "StreamLab06". The Main channel is 55 m long, 2.74 m wide and has a maximum depth of 1.8 m with a maximum discharge capacity of 8000 l/s. The Main channel is a partially sediment recirculating channel, while the water flows through the channel without recirculation. Intake of the water in the channel is directly from the Mississippi river. The data used in this research are mainly the sediment transport series, velocity fluctuations, temporal bed elevation collected at the downstream end, and the longitudinal transects of bed profile, measured during flow-on and flow-off conditions along the centerline of the channel, and grain size distributions sampled during the flow (bedload sampling), and after the flow (surface and subsurface sampling). Measurements were taken over a range of discharges corresponding to different bed shear

stresses.

- In Chapter 2, we present a complete theory to explain the scale-dependence in sediment transport rates which allows renormalization from one scale to another [7, 5]. For example, one would expect that doubling the time period over which the weight of bedload material is collected in a river, would simply double the collected material weight (this would imply that the mean sediment transport rate is independent of the time period over which it is computed). Yet, as counter-intuitive as it might seem, it has been documented in real rivers and in laboratory experiments that this is not the case, and instead the mean sediment transport rate considerably depends on the time-interval over which it is computed. This has been noted previously in field experiments by Bunte and Abt [2], who observed that in moderate to high flows 2 min sampling led to an average transport rate 2 to 5 times lower than that found with 10 min sampling. This is because, sediment transport rates exhibit very high fluctuations (up to 20 or more times the mean transport rate, resulting from "bursts" of sediment production due to particle-to-particle interactions and near-bed turbulence) and these fluctuations are sampled at different frequencies depending on the time interval over which the mean transport rate is computed. After some long time interval, the mean sediment transport rate becomes constant but for shorter time intervals (relevant for many biological activities or comparable to the intervals over which bedload traps are used in practice to estimate bedload transport) the time-scale dependence is a major issue.

- In Chapter 3, we propose for the first time the use of complexity theory to study the sensitivity of sediment transport/bed elevations predictions to initial and boundary conditions (using theory of non-linear dynamics and phase-space reconstruction). The results have suggested the potential of developing methods to assess the upper limits to prediction from numerical models in real systems and also quantifying the uncertainty of predictions [6].

- In Chapter 4, an important new recent result of this research, that is, the discovery of a "spectral gap" in turbulence velocity fluctuations collected above a river bed with evolving bedforms is presented. Verified by simultaneous velocity and bed

elevation observations [8], it was concluded that the spectrum of turbulence carries information about the evolving multi-scale nature of bed topography (specifically, detection of length scales of the smallest and largest bedforms) and can thus form a useful tool for non-invasive and economical/robust field monitoring methodology in real rivers.

- In Chapter 5, we present a space-time characterization of gravel and sand bed elevation series for different flow conditions. Using a wavelet decomposition we quantify the presence of a rich multiscale statistical structure and estimate the scale-dependent celerity of migrating bedforms showing the faster movement of smaller bedforms relative to the larger ones. The nonlinear dynamics of gravel and sand bedforms is also examined and the predictability time, i.e., the interval over which one can typically forecast the system, is estimated. Finally, we demonstrate that the multiscale dynamics, and degree of nonlinearity and complexity in bedform evolution have a dependence on discharge as well as on bed sediment composition.

- In Chapter 6, using simultaneous sampled high resolution measurements of velocity fluctuations, bed elevations and sediment flux at the downstream end of the channel we quantify the joint statistics and the feedback between the co-evolution of sediment transport, bedforms and the near-bed turbulence. These results complement our previous findings [8] in which the signature of bedform evolution on the near-bed velocity fluctuations was confirmed via the presence of a spectral gap and two distinct power-law scaling regimes in the spectral density of velocity fluctuations. We report a strong asymmetry in the probability distribution of bed elevation fluctuations and instantaneous Reynolds stresses. We interpret this asymmetry, in view of the established intermittency (multi-fractality), as the result of scale coupling. In short, small-scale structures do not lose the information of the large-scale structures of flow and transport, rendering thus the scale-to-scale energy transfer locally anisotropic. We also propose a relationship to quantify sediment transport using instantaneous Reynolds stress.

- In Chapter 7, we show how multiscale-complex structures in bed topography affect the tracer migration in order to understand and quantify how particle dynamics

(microscale) relates to macroscale dynamics i.e., of bedforms, trapping potential, waiting times etc., and how these dynamics can be best accounted for in tracer dispersal and sediment transport models.

- Chapter 8 presents concluding remarks and perspectives on future research.

Chapter 2

Experimental evidence for statistical scaling and intermittency in sediment transport rates

Understanding bed load transport fluctuations in rivers is crucial for development of a transport theory, and for choosing a sampling interval for "mean" transport rates. Field-scale studies lack sufficient resolution to statistically characterize these fluctuations, while laboratory experiments are limited in scale and hence cannot be directly compared to field cases. Here we use a natural-scale laboratory channel to examine bed load transport fluctuations in a heterogeneous gravel substrate under normal flow conditions. The novelty of our approach is the application of a geometrical/statistical formalism (called the multifractal formalism), which allows characterization of the "roughness" of the series (depicting the average strength of local abrupt fluctuations in the signal) and the "intermittency" (depicting the temporal heterogeneity of fluctuations of different strength). We document a rougher and more intermittent behavior in bedload sediment transport series at low discharge conditions, transitioning to a smoother and less intermittent behavior at high discharge conditions. We derive an expression for the

dependence of the probability distribution of bedload sediment transport rates on sampling interval. Our findings are consistent with field observations demonstrating that mean bedload sediment transport rate decreases with sampling time at low transport conditions and increases with sampling time at high transport conditions. Simultaneous measurement of bed elevation suggests that the statistics of sediment transport fluctuations are related to the statistics of bed topography.

2.1 Introduction

Measurements of bed load transport rates are fundamental to estimating material transport in a river, yet even defining a representative time period over which to sample is difficult due to the inherent variability and stochastic character of sediment transport. This variability is present over a wide range of scales, from the movement of individual grains [9, 10, 11, 12, 13, 14] up to the propagation of dunes and bars [15, 16, 17, 18], even under steady flow conditions. Computed statistics of instantaneous bed load transport rates (flux) have shown that probability distributions are often skewed toward larger values [e.g., [16]], implying a high likelihood of extreme fluctuations, the prediction of which is essential for protecting hydraulic structures and assessing the stability of riverine habitat [19]. It has also been observed that the mean sediment flux depends on the time interval (sampling time) over which the mean is computed, and previous work has suggested that this time dependence is the result of large, infrequent transport events [see [2], and references therein].

An analogous time-dependence that has been more thoroughly studied is that of the sedimentary record, where apparent deposition rate (measured from two dated surfaces) diminishes rapidly with measurement duration in virtually all depositional environments [20, 21]. Models show that this scale dependence is a direct result of the statistics of transport fluctuations [e.g., [22]]. In the case of geologic rates the data have been assumed to obey simple scaling over a wide range of time scales, i.e. the statistical moments can be fitted as power-law functions of scale, with the exponents linear in moment order. This power-law relationship provides a value for the Hurst exponent, H, which may be used to compare rates at one scale to rates at a different scale via a simple statistical transformation (see also discussion that follows). However, many

geophysical processes exhibit multiscaling (or multifractal behavior), which implies that a range of exponents (and not a single exponent) is required to describe the changes in the probability density function (pdf) with scale. Examples include rainfall intensities (e.g., [23, 24]], cloud structures [e.g., [25, 26]], river flows [e.g., [27]], river network branching topologies [e.g., [28, 29, 30]], braided river systems [e.g., [31]], and valley morphology [e.g., [32]]. This rich multiscale statistical structure includes extreme but rare fluctuations ("bursts") that occur inhomogeneously over time, giving rise to the so-called "intermittency" and leading to a nontrivial scaling of the statistical moments. A prime example of this is the velocity fluctuations in fully developed isotropic turbulence [e.g., [33, 34, 35]].

To the best of our knowledge, bedload sediment transport series have not been analyzed before from the perspective of quantifying how the statistical moments of the series change with scale. In an early study Gomez et al. [16] acknowledged that the probability distribution of sediment transport rates depends on sampling time (scale) and extended the Einstein and Hamamori distributions to a scale-dependent form, without however attempting any scale-renormalization. Knowledge of the variability inherent in bed load transport rates at all scales is essential for quantifying material flux, for designing appropriate measurement programs, and for comparison among different data sets and model predictions at different temporal and spatial scales. Also, quantifying the statistical structure of these fluctuations across scales may yield insight into the fundamental physics of sediment transport and provide a set of diagnostics against which to rigorously test competing theories and bed load transport models [see also [4, 14]].

One would expect that the statistics of bed load sediment transport would relate in some way to the statistics of the fluctuations in bed elevation. Although river bed elevations have been analyzed much more than sediment fluxes and have been found to exhibit fluctuations across a wide range of scales, in both sandy [e.g., [36, 36, 18]] and gravelly [37, 38, 39] systems, the link between bed topography and sediment flux remains largely unexplored due to the difficulty in simultaneous data acquisition. Establishing a relationship between the statistics of bed elevations and sediment transport rates is important for effective modeling of river bed morphodynamics and also for understanding the physics of sediment transport. More practically, since bed elevation data are far easier to collect than sediment flux measurements, an understanding of

how the statistics of the one variable relate to those of the other, at least over a range of temporal scales, could greatly facilitate estimating sediment transport rate in the field.

To address these issues we present here an analysis of data from a unique experimental laboratory setup capable of mimicking transport conditions in the field (see section 2.3). High resolution, long duration time series of sediment transport rates and bed elevation were simultaneously collected in a suite of experiments with a heterogeneous gravel bed. We use the multifractal formalism, originally developed for fluid turbulence [33, 34, 40], to quantify the "roughness" (the average strength of local burstiness in the signal) and the "intermittency" (the temporal variability or heterogeneity of bursts of different strengths) and relate those geometrical quantities to the statistics of sediment flux and bed topography over a range of time scales. (Note that throughout the paper the term "roughness", as defined mathematically via the strength of local singularities, refers to the signal roughness being that sediment transport rates or bed elevation fluctuations and it is not to be confused with other uses of the term roughness such as bed roughness or hydraulic roughness.) We substantiate the findings of Bunte and Abt [2] that mean sediment transport rate diminishes with increasing sampling time at low bed stress (slightly above critical) but does the opposite for high transport conditions, and we relate this reversal in trend to the influence of large-scale bed forms. Our analysis also allows characterization of the sampling time dependence of all of the statistical moments, allowing thus the prediction of extremes at small scales from the statistics at larger scales.

2.2 Experimental setup

The experiments reported here were conducted in the Main Channel facility at the St. Anthony Falls Laboratory, University of Minnesota, as part of the StreamLab06 project undertaken by the National Center of Earth-Surface Dynamics [41]. StreamLab06 was an 11 month multi-disciplinary laboratory channel study focused on various aspects of ecogeomorphology in gravel bed streams. Five separate projects were conducted as part of StreamLab06 and an extensive data set was collected including hydraulic conditions (discharge, water slope, bed slope, depth average velocity, and flow field), morphological conditions (bed topography, bar locations and shapes, photo images of

the bed), sediment transport characterization (continuous sediment flux, recirculation grain size information), water chemistry (temperature, dissolved oxygen, nutrient concentrations) and biological conditions (heterotrophic respiration, biomass accumulation, nutrient processing rates). For the work presented here, we focus on bed topography and sediment flux data collected in the first of the five StreamLab06 projects, which focused on ground-truth testing of various conventional and surrogate bedload monitoring technologies.

The Main Channel is 2.74-m wide and has a maximum depth of 1.8 m. It is a partial-recirculating channel with the ability to recirculate gravel while the water flows through the channel without recirculation. Water for the channel was drawn directly from the Mississippi River, with a maximum discharge capacity of 8000 l/s. Water discharge was controlled by a sluice gate situated at the head-end of the facility while flow depth was regulated by a sharp-crested weir located at the downstream end of the channel. The channel has a 55-m long test section and in the experiments reported here a poorly sorted gravel bed extended over the last 20 meters of this test section. Short, 0.4m high bulkhead walls were located upstream and downstream of the test section and served to contain the gravel bed material. The gravel used in these experiments had a broad particle size distribution characterized by d50 =11.3 mm, d16 = 4.3 mm and d84 = 23.1 mm (see also [7]). The thickness of the gravel bed at the start of run was approximately 0.45 m.

The Main Channel was equipped with a sediment flux monitoring system that provided the ability to collect high resolution, long duration data sets of sediment transport dynamics using field-scale gravel particle sizes and transport rates. The sediment flux and recirculation systems were co-located in the channel at the downstream end of the 20-m test section. The flux monitoring system was composed of five adjacent, identical aluminum weighing pans (positioned 0.54 meters apart) that spanned the width of the channel and independently measured the submerged weight of the gravel intercepted by the bedload trap (see Fig. 2.1). Each pan could accommodate up to 76-mm-diameter particles and hanged from an aluminum frame that extended from its sides to a load cell connected to the ceiling above the Main Channel (see Fig. 2.2). The system used load cells manufactured by Interface Advanced Force Measurement (SM-250) that had a capacity of 113 kg and were accurate to gram-force. As a safety margin to avoid

exceeding the capacity of the weighing pan system, the pan rotation that voided each bin's contents was triggered at a user-specified net weight, which in our case was set to 20 kilogram-force (kg-f).

Removable stainless steel cover plates with 45-cm by 15-cm slots served to funnel the intercepted bedload downward into the pans. The pans (also referred as drums) were constructed of aluminum and had three radial baffles welded to a common 3.8-cm diameter hub and to two 81.3-cm diameter end plates. They were oriented horizontally and transverse to the channel under the sediment trap. The three radial baffles formed two adjacent 120-degree "V"-shaped bins, each of which had a capacity of 62 liters. The submerged weight of sediment in a bin at maximum capacity was 62 kg-f. Each pan operated independently using a tipping-bucket arrangement with "tips" consisting of alternating clockwise and counterclockwise 120-degree rotations. When the sediment mass in a pan reached a specified threshold, an air cylinder either extended or retracted, causing the pan to rotate 120 degrees. This action resulted in dumping the contents of one bin and repositioning the adjacent empty bin under the funnel to continue collecting bedload. In this manner, all bedload was continuously captured and weighed in the five independently operating pans.

Bed load material that was transported out of the test section fell by gravity into the pans and incrementally added to the weight of the pan which was recorded every 1.1 sec. Material dumped out of the pans was collected in a large hopper located underneath the pans, which also served as the material source for the recirculation system. The rate of gravel removal out of this hopper, and delivery to the upstream end of the channel via a large pump, was manually set by adjusting the rotation speed of a large helix, which served to push gravel laterally out of the hopper and into the recirculation line. In this way, the collection hopper and helix served to buffer small fluctuations in sediment flux out of the test section, providing a more steady "feed-type" delivery of sediment to the upstream end. Because the physical size of the collection hopper was finite, the auger speed (and hence upstream input sediment feed rate to the test section) was manually adjusted periodically to maintain storage in the hopper. In other words, an auger rate set too high could potentially remove material faster than the test section would deliver resulting in emptying of the hopper. Conversely, an auger rate set too low would result in overfilling of the hopper. We used periodic visual observations of the

fill level in the collection hopper to inform our manual adjustments of the auger speed. Slight adjustments to auger speed were necessary every 30-60 min and very rarely did the system collection hopper empty or overfill meaning that the feed rate out of the collection hopper was in balance with the long-term flux of bedload out of the test section.

The experimental setup also included five stationary 2.5-cm diameter, submersible sonar transducers deployed 0.95-m below the water surface and 0.95-m upstream of each pan. The sonar transducers, mounted to the end of rigid 1.5-cm steel tubes and directed perpendicular to the bed, were used to collect continuous temporal bed elevation information upstream of the each pan. Sonar data was sampled at every 10sec with a vertical precision of 1 mm. The acquisition times for the bed elevation and sediment accumulation data were based on precisely synchronized clocks allowing the two data sets to be analyzed together. Water temperature was also measured using YSI thermistor capable of measuring up to +/-0.1 ^{o}C. Water temperature for the two runs studied in this research averaged 3.0 ^{o}C.

Measurements of bed elevation and sediment transport were taken over a range of discharges corresponding to different bed shear stresses. Bed shear stress is often characterized in terms of the dimensionless Shields stress, τ_b^*. For steady, uniform flow it may be approximated as $\tau_b^* = h_R S/Rd_{50}$, where h_R and S are the hydraulic radius and channel slope, respectively, and $R = 1.65$ is the relative submerged density of silica. In the analysis presented here, we report on two different discharges: a low discharge case, with a discharge of 4300 l/s, corresponding to a dimensionless bed stress of about twice the critical value (Shields stress, $\tau_b^* = 0.085$ using median diameter) and a high discharge, 5500 l/s, corresponding to a bed stress about five times the critical value (Shields stress, $\tau_b^* = 0.196$); see Table 2.1 for relevant hydraulic parameters. (Note that the critical Shields stress (also known as Shields number) was estimated to be 0.047 [42].

For both bed stress conditions, the channel was allowed to run prior to data collection such that a dynamic equilibrium was achieved in transport and slope adjustment of the water surface and bed. Determination of the dynamic equilibrium state was evaluated by checking the stability of the 60 min average total sediment flux at the downstream end of the test section. Using the pan accumulation data, the acquisition software computed

a 60 min mean of sediment flux in all five pans. Dynamic equilibrium was reached when variation in this value became negligible. In other words, when the average of the previous 60 min of instantaneous flux values computed from the pan data stabilized, we determined the channel to be in dynamic equilibrium and proceeded with formal data collection and sampling.

The bedload sediment accumulation series and the corresponding bed elevation series were then recorded over a span of approximately 20 hrs for each experiment. Fig. 2.3 (a) and (b) display the time series of sediment accumulation over 2 min and 10 min intervals respectively for pan 4, and Fig. 2.3(c) the corresponding bed elevation series (recorded by the sonar transducer immediately upstream of pan 4) for the low discharge conditions over a period of 10hrs. Fig. 2.4 shows the same series for the high discharge conditions. Considering the bed elevation series, it can be observed that the low bed stress run (Fig. 2.3c) produced a channel bed with only limited topographic variation, i.e. without obvious large scale structures in the bed (the standard deviation in the bed is 10.1 mm, compared to a d50 grain size of 11.3mm). However, the higher stress run (Fig. 2.4c) generated substantial bed variability at large scale in the form of dunes, with intermediate to particle-scale fluctuations superimposed on these larger-scale features. In this study we focus on comparing these two runs using the multiscale analysis techniques to be described in section 2.3.

2.2.1 Sources of error in the data

One source of error in the accumulated sediment series was the tipping events of the pans. To account for this, the raw sediment accumulation data were pre-processed prior to the analysis presented here. The pre-processing involved removal of pan dumping events from the data and translating the data set into a continuous accumulation of sediment time series for each pan over the duration of the experiment. A single tipping event required the removal of no more than eight data points (8.8 sec) from the record. To get the final time series of accumulated sediment transport, the time series prior to the tipping event was left unchanged, the tipping event was removed from the series, and all subsequent points were shifted backwards in time to create a continuous time series as though the tipping event never occurred. Overall, the data affected by the pan tipping constituted less than 0.15% of the total data record and is, thus, negligible.

There were other sources of error however. Sediment accumulation data in the pans should increase monotonically, when corrected for tipping of the scales as discussed above. At the resolution of our measurements (approximately 1 sec), however, sediment accumulation showed negative excursions which would imply negative bed load flux, which is not physically possible given the experimental setup (see Fig. 2.4 in [7]). These errors have been attributed to (1) the fluctuating water surface over the pan, (2) the natural oscillation of the pans after being hit by the falling gravel, and (3) to the vibration caused by the large gravel recirculation pump which was placed near to the pans. This error makes the raw sediment data at small time scales (from 1 sec up to approximately 1-2 min accumulations) unusable. As a check, we computed distributions of sediment flux values averaged over different time scales and found that data averaged over less than two minutes showed negative values, supporting the contention that scales smaller than two minutes are error prone. Also, although there were five pans, Pans 1 and 5 (Fig. 2.4) were not used in order to avoid data potentially impacted by wall effects.

Bed elevation data were substantially less error prone, due to the acoustic (rather than mechanical) nature of the measurements. Our multiscale analysis showed a small noise regime which was only a small factor larger than the sampling interval of 10 sec.

2.3 Roughness, Intermittency and Statistical Scaling

2.3.1 Characterizing Signal Roughness and Intermittency

Previous authors (e.g.[16, 4]) have observed and documented high fluctuations in bed load sediment transport rates or particle counts at short time-scales, and have described these series as "intermittent". In these and other studies it has also been noted that as flow rate increased, the sediment transport was seen to be "smoother" or more continuous, whereas at low flow rates it was "rougher" or more "bursty". These terms have been used in a qualitative way to describe the presence (or absence) of sudden bursts of sediment or high fluctuations at short time-scales that arise from the stochastic nature of the transport and the collective behavior of particle dynamics.

In this paper the "roughness" and "intermittency" of the sediment transport series are mathematically defined, allowing a more precise quantification of the nature of the

fluctuations in bed load sediment at small time scales. A mathematical characterization of the strength of local fluctuations in a function $X(t)$ is given by the Hölder or singularity exponent $h(t_0)$, defined at any point t_0 to be the largest exponent such that:

$$|X(t) - X(t_0)| \leq C|t - t_0|^{h(t_0)}, ast \to t_0 \tag{2.1}$$

where C is a constant. This definition holds for $0 \leq H \leq 1$, but it can be generalized to $h > 1$, as will be discussed in section 2.3.3 (see also [40]). The Hölder exponent gives a local measure of the smoothness or degree of differentiability of the function $X(t)$: a value of $h(t_0) \geq 1$ indicates that the function is smooth at t_0, in the sense that it is at least once-differentiable at the point t_0, whereas a function with $h(t_0) = 0$ is so rough that it is discontinuous at that point. Between these extremes, a value of $0 \leq h(t_0) \leq 1$ means that the function is continuous but not differentiable at t_0, with a higher h value (closer to 1) implying that the function is "smoother" or more regular, and a lower h value (closer to zero) implying that the function is "rougher" or more irregular.

Having established a measure of local (point-wise) roughness in a signal, it is natural to ask what kind of $h(t_0)$ values are present in an observed time-series, and how they are distributed. If we denote the set of all points in the function $X(t_0)$ with a particular value of Hölder exponent h as:

$$\Omega(h) = \{t_0 : h(t_0) = h\} \tag{2.2}$$

then, in general, for a multifractal function these sets of points are interwoven fractal sets whose distribution can be characterized by the so-called singularity spectrum $D(h)$, defined as

$$D(h) = Dim_H(\Omega(h)) \tag{2.3}$$

where Dim_H is the Hausdorff dimension of the fractal set (e.g. [43]). In other words, the singularity spectrum $D(h)$ describes the relative frequency of occurrence of local abrupt fluctuations (singularities) with strength h. In a one-dimensional function like a time series, the value of h corresponding to the peak of the singularity spectrum indicates the most frequently occurring singularity or fluctuation strength. (Note that if $D(h)$ is symmetric, which is a good approximation for most signals, then this value

characterizes the "average roughness" of the signal as it coincides with the arithmetic mean of the local singularities h .) The range of h over which $D(h) \geq 0$, or the spread of the singularity spectrum, reflects the temporal heterogeneity of the local singularities, i.e., it measures the degree of clustering in the abrupt local fluctuations of various strengths. Simply put, a signal with a wide $D(h)$ will have sparse regions where the strength of the local fluctuations is much greater than (or much less than) the mean fluctuation strength, and hence will display infrequent but exceptionally large "bursts" at small scales embedded within bursts of lesser strength, i.e. the signal will be very "intermittent". On the other hand, a $D(h)$ spectrum which is just a spike, i.e., $D(h)$ at $h = H$ and zero elsewhere, indicates a signal which exhibits one strength of singularity only, H also called the Hurst exponent, which is homogeneously distributed throughout the signal (in this case the signal has zero intermittency). It is noted that H, which is a local measure of variability, provides different information than the standard deviation of a signal, which is a global measure of variability; in other words two signals with the same standard deviation can have considerably different values of (e.g., see [44]).

2.3.2 Multiscale analysis

While the spectrum of singularities $D(h)$ can be used to describe the "roughness" and "intermittency" of a signal, it can be difficult to estimate it directly from the data. An interesting mathematical result (the so-called multifractal formalism, [33, 40]) establishes that $D(h)$ relates to how the probability density function (pdf), or equivalently the statistical moments, of the signal fluctuations changes with scale. Let the fluctuation $S(t_0, a)$, at any time t_0 and scale a, be defined as

$$S(t_0, a) = X(t_0 + a) - X(t_0) \tag{2.4}$$

and the statistical moments of the absolute values of these fluctuations by

$$M(q, a) =< |S(t_0, a|^q > \tag{2.5}$$

where $\tau(q)$ denotes expectation over time. For a process that exhibits statistical scale invariance, the statistical moments of the fluctuations behave as a power-law function of scale:

$$M(q, a) \sim a^{\tau(q)} \tag{2.6}$$

where $\tau(q)$ is the so-called spectrum of scaling exponents and is a function of the moment order q. Thus if the series exhibits scale invariance, the function $\tau(q)$ completely describes the manner in which the statistical moments of the pdf of fluctuations varies with scale.

It is the scaling function $\tau(q)$ that can be used to retrieve the spectrum of singularities $D(h)$. The precise transform between these two representations is given by the Legendre transform [33, 40]:

$$D(h) = min_q[qh - \tau(q) + 1] \tag{2.7}$$

In this way the spectrum of singularities describing the average roughness and intermittency of the signal can be estimated through the scaling properties of the statistical moments of the signal fluctuations.

2.3.3 Generalized Fluctuations and the Wavelet Transform

Although the fluctuations $S(t_0, a)$ of a time series can be computed by directly taking the first order increments, as in equation (2.4), calculating the statistical moments in this way (which gives rise to the so-called structure function approach) has some limitations. Firstly, these fluctuations can be corrupted by small-scale noise (since observations are used directly without local smoothing); in addition, they do not remove higher order non-stationarities (it is easy to show that the first order increments remove only constant-level trends); and finally, they cannot estimate singularity strengths $h > 1$. To overcome these limitations, the continuous wavelet transform can be used to define generalized fluctuations in the time series (e.g., see [45, 46, 47, 30]). In this framework we redefine the (generalized) fluctuations $S(t_0, a)$ to be

$$S(t_0, a) = \int_{-\infty}^{\infty} \psi_{a,t_0}(t) X(t) dt \tag{2.8}$$

where $\psi_{a,t_0}(t)$ is a "differencing function", as for example, the first derivative of a Gaussian function. In particular $\psi_{a,t_0}(t)$ is a wavelet resulting from shifting and scaling a mother-wavelet $\psi(t)$, such that,

$$\psi_0(t) = \frac{1}{a}\psi(\frac{t - t_0}{a}) \tag{2.9}$$

where t_0 is the location and a is the scale parameter. For the continuous wavelet transform to be invertible, the mother wavelet must satisfy the invertibility condition $\int_{-\infty}^{\infty} t\psi(t)dt = 0$ i.e., it must have a zero mean (which makes it a kind of local differencing function e.g., see Mallat, [48], or Kumar and Foufoula-Georgiou, [49]). A commonly used mother wavelet is the family of Gaussian wavelets defined as the N-order derivatives of a Gaussian function $g_0(t)$, i.e., $g_N(t) = d^N/dt^N)g_0(t)$, modulus a proper multiplicative factor to ensure correct normalization. Defining the fluctuations $S(t_0, a)$ using the first order derivative of the Gaussian function can be seen as computing first order increments of the series after the series has been locally smoothed with a Gaussian kernel or, equivalently, as computing first-order increments and then performing a smoothing (weighted averaging). (This can be easily deduced from the convolution theorem; see also [30].) Similarly, defining multiresolution coefficients using $g_N(t)$ can be considered as smoothing the series with a moving Gaussian window, followed by N-th order differencing (the standard deviation of the Gaussian function determines the "scale" at which the smoothing and thus differencing is done; see [30]). The smoothing operation removes the noise and the higher order differencing removes nonstationarities from the signal, rendering the wavelet-based generalized fluctuations appropriate for characterization of statistical scaling (e.g., see [40]).

One property that should be considered when choosing an appropriate mother wavelet for defining the mutiresolution coefficients is the number of vanishing moments. Note that the mother wavelet is said to have N vanishing moments if $\int_{-\infty}^{\infty} t^k\psi_0(t)dt = 0$ for $0 \leq k < N$. The Gaussian wavelet $g_N(t)$, defined above as the N-th derivative of the Gaussian, can be easily shown to have N vanishing moments. Defining multiresolution coefficients with a mother wavelet which has N vanishing moments can be shown to remove from the series an additive polynomial trend of degree less than N (e.g., see [49]). Therefore, the wavelet-based multiscale analysis proposed here renders the fluctuation series stationary if one chooses a wavelet with more vanishing moments than the degree of nonstationarity in the data. In practice, the degree of nonstationarity of the data series is not known in advance, so one applies the wavelet transform with increasing values of N until the results of the analysis do not vary with N: this will imply that the order has been chosen large enough to remove any nonstationarities. The correct selection of multiresolution coefficients is important for a meaningful multifractal analysis as has

been recently demonstrated in Lashermes and Foufoula-Georgiou ([30]). For example, using standard fluctuations (first order differences) to analyze a non-stationary signal will result in a spurious estimate of $H = 1$ misleading one to assume that the signal is smooth and differentiable.

In this study, the fluctuations, $S(t_0, a)$, of the bed load sediment and bed elevation series at various scales were computed using the wavelet transform (equation (2.8)) with the wavelet g_3, since this was the lowest order wavelet able to remove all nonstationarities from the sediment transport series (a lower order wavelet g_3 proved sufficient for the bed-elevation series but the use of the higher order wavelet g_3 does not alter the results; this will be discussed more in section 2.4). The moments $M(q, a)$ were then estimated using equation (2.5), and the scaling exponents $\tau(q)$ computed from the log-log linear relationships (equation 2.6) over the scaling range. This in turn allowed the calculation of the singularity spectrum $D(h)$ via equation (2.7).

2.3.4 Scale dependence of the pdf of the fluctuations

The scaling exponents τq are not only of interest for calculating the singularity spectrum $D(h)$, but also for describing how the pdf of the fluctuations depends on scale. As was discussed earlier, the statistical moments $M(q, a)$ in equation (2.5) describe how the fluctuations of a process change with scale and, for a scale-invariant process, this change is captured in the curve. In the case of simple scaling, the scaling exponent function is linear in moment order, i.e. $\tau(q) = qH$ for some constant H (called the Hurst exponent), which can be shown to imply that the pdf of the fluctuations at scale a, $P_a(S) \equiv P(S(t, a))$, is related to the pdf at another scale a by

$$P'_a(S) = (\frac{a}{a'})^{-H} P_a((\frac{a}{a'})^{-H} S) \quad for \quad a' < a \tag{2.10}$$

[e.g., see [50] and [47]]. Note that the normalizing factor $(a/a')^{-H}$ is a deterministic kernel that depends on H and the ratio of scales (not each scale individually). As this type of statistical scaling behavior is controlled by a single parameter only, it is referred to as monoscaling. Note that equation (2.7) implies that in the monoscaling case $D(h) = \delta(h - H)$, i.e. the only Hölder exponent with dimension greater than zero is $h = H$, and the function is completely uniform in its roughness i.e., not intermittent, at small scales.

In the more general case of multiscaling, the scale invariance relation (equation 2.6) still holds, but $\tau(q)$ is not linear but a concave function of the moment-order q. In this case, the pdf of the fluctuations does not maintain its shape between two different scales, but changes continuously via convolution with a kernel that depends on the ratio of scales [35, 47]. The generalization of equation (2.10) for multifractals is obtained [51] by considering that H is not a constant but has a probability density function $\rho(h)$. In this case, the expression (2.10) becomes:

$$P'_a(S) = \int_{-\infty}^{\infty} \rho(h)(\frac{a}{a'})^{-h} P_a((\frac{a}{a'})^{-h} S)dh \quad for \quad a' < a \tag{2.11}$$

In general, the pdf of the fluctuations is expected to widen and have fatter tails as the scale decreases. In turbulence for example, the above transformation renormalizes the almost Gaussian pdf of turbulent velocity fluctuations at very large scales to a thick tailed pdf at small scales. It is noted that the probability density involved in the renormalization of the pdfs is related to the spectrum of singularities $D(h)$, $\rho(h)$, and reflects the presence of Hölder exponents of various strengths which are inhomogeneously distributed throughout the signal (see [34] and also [47] for a discussion of the equivalency of the geometrical and statistical interpretations). The pdf rescaling of (2.11) can be expressed in a convolution form as

$$P'_a(S) = \int_{-\infty}^{\infty} G_{aa'}(u) e^{-u} P_a(e^{-u} S)du \quad for \quad a' < a \tag{2.12}$$

where $u = hln(a/a')$ and $G_{aa'}(u) = \rho(u/ln(a/a'))/ln(a/a')$. This implies that the pdf at scale a' can be expressed as a weighted sum of dilated pdfs at larger scales $a > a'$. The kernel $G_{aa'}(u)$ is called the propagator and can be estimated from the data (see [51] for the theory and [47] for an application to high resolution temporal rainfall series). Once the propagator is known, a known pdf at any scale can be used to derive the pdf at any smaller scale via equation (2.12). To gain better insight into how the $\tau(q)$ (or $D(h)$) curve controls the pdf change over scales, let us consider the coefficient of variation, C_v, which is the ratio of the standard deviation to the mean, $C_v = \sigma/\mu$. For a monoscaling process, this ratio would be constant with scale, as both the mean and standard deviation are rescaled equally, as shown by equation (2.6). In a

multiscaling situation, however, the increasing width of the pdf leads to C_v increasing with decreasing scale. The precise behavior of C_v with scale can be seen by noting that $C_v^2 + 1 = M(2,a)/M(1,a)^2$, so that for a multiscaling process, equation (2.6) implies $(C_v^2 + 1) \sim a^{\tau(2)-\tau(1)}$. In other words, $\tau(1) - 2\tau(1)$ characterizes the (second order) relative stretching of pdfs across scales, and its magnitude is also a measure of deviation from monoscaling. Similar relationships can be worked out for higher-moment ratios. As we will see for the sediment transport series, C_v significantly depends on scale, attesting to the presence of multiscaling.

2.3.5 Parameterizing the scaling properties and singularity spectrum

While knowing the $\tau(q)$ (or $D(h)$) curve completely characterizes the scale dependence of the pdfs of fluctuations, for practical purposes it is often desirable to parameterize these curves concisely. Assuming an analytic form of the $\tau(q)$ curve, the simplest parameterization for multiscaling is to extend the linear model of used for monoscaling to a quadratic model, that is,

$$\tau(q) = c_1 q - \frac{c_2}{2} q^2 \tag{2.13}$$

In this parameterization, the constant $c_0 = \tau(0)$ is the scaling exponent of the zeroth-order moment, which will be equal to zero if the support of the field under analysis fills the space, as we see for both sediment flux and bed-elevation. This leaves two parameters to describe the (multi)scaling: the parameters c_1 and c_2 control the scaling of all the moments and the change in shape of the pdf with changing scale. The two parameters c_1 and c_2 in (2.13) can be estimated by fitting a quadratic function to the empirical $\tau(q)$ curve, or via a more robust methodology called the cumulant analysis (see Delour et al. [52] and Venugopal et al. [47] for an application to rainfall series). For such a quadratic $\tau(q)$, it can be shown from equation (2.7) [e.g. [47] that the spectrum of singularities is also quadratic, with

$$D(h) = 1 - \frac{1}{2c_2}(h - c_1)^2 \tag{2.14}$$

This shows that the most frequently occurring value of the Hölder exponent (peak of the $D(h)$ curve), and hence the mean roughness/smoothness of the function, is given by the parameter c_1 (note that $D(h) = 1$ and $D(h)$ in (2.14) is symmetric around c_1).

Alternatively, c_2 provides a measure of the spread of the $D(h)$ curve and hence prescribes the degree of intermittency. For this reason, c_2 is referred to as the "intermittency coefficient". The limiting case of $c_2 = 0$, that is the case of a monofractal, leads to a delta function $D(h) = \delta(h - c_1)$, and hence gives a single Hölder exponent $H = c_1$, (the same exponent H as in equation 2.10). This means there is no intermittency: the function will have the same degree of local roughness (irregularity) everywhere. For a multifractal ($c_2 > 0$) however, a range of local fluctuation strengths will be inhomogeneously distributed throughout the signal, with the minimum and maximum Hölder exponents given by $h_{min/max} = c_1 \mp \sqrt{2c_2}$ (where the $D(h)$ curve crosses below 0). So with increasing c_2 there is a wider range of local fluctuation strengths present in the signal, and hence a greater degree of intermittency.

2.4 Results

2.4.1 Sediment transport scaling

Bed load sediment transport fluctuations were analyzed using the multifractal formalism. Fluctuations were computed by applying a differencing filter on the accumulated sediment series $S_c(t)$, i.e., equation (2.8) with the generic function $X(t)$ replaced now by $S_c(t)$ and using as differencing filters wavelets of increasing order $g_N(t)$, where $N =$ 2, 3, and 4. It is noted that by using the third derivative of the Gaussian, $g_3(t)$, on the accumulated sediment series, gives fluctuations that represent second order increments of the bedload transport rates, that is, they capture the local rate of change in the sediment transport rates. This filtering guarantees removal of linear trends in the rate of sediment transport series, which, if present, can influence the results. Indeed such rate changes were found present during the 20 hour duration of our data collection (see Fig. 3 in [7]) and thus the $g_3(t)$ was adopted for our analysis. However, it is noted that the use of lower order wavelets does not significantly change the estimates of the parameters as can be seen from the detailed Table 2.2. Having defined the fluctuations, the statistical moments $M(q, a)$ were then computed (equation 2.5), and are shown as a function of scale in Fig. 2.5, for pan 3 (see Fig. 2.1). Similar results were obtained for the other pans, except for pans 1 and 5 which suffered from wall effects and showed no good scaling range. Three different regimes can be distinguished for both the low and

high discharge: a small-scale regime (scales below 1 min) which is judged to be noise-dominated (see section 2.2.1); a log-log linear scaling regime in the temporal range of approximately 1 to 10 min; and then a short transitional regime before a leveling-off of the moments is reached. Here we focus on the longer scaling regime between 1 min and 10 min marked by the dashed lines in Fig. 2.5. The scaling exponents of the various moment orders, $\tau(q)$, were estimated using linear regression within this scaling range, and are shown for both discharges in the lower half of Fig. 2.5. It can be seen that both curves deviate from linear behavior, and hence depart from simple scaling and instead demonstrate multiscaling. The parameters c_1 and c_2 found by fitting the quadratic model (equation 2.13) to these curves are presented in Table 2.3, along with a summary of the scaling range and parameters for the other pans for which uninterrupted data were available. It is noted that the quadratic fit is very good and the fitted curves are indistinguishable from the measured points.

This scaling of the moments reflects the scaling of the pdf of sediment fluctuations. Fig. 2.6 shows the pdfs of the sediment transport rates (defined as accumulations over an interval divided by the length of that interval) for 2 min and 10 min intervals for both high and low discharge. It can be seen that for both flow conditions, the very skewed and fat-tailed pdf at 2 min changes to a much more symmetrical pdf at 10 min, although in the case of the low flow there is still some skewness present even at the larger sampling time. It is recalled that the parameters c_1 and c_2 control this pdf change over scales through the rescaling kernel (equation 2.12). An easy way to observe the relative narrowing of the pdf with increasing scale is via the coefficient of variation C_v computed from the data, which is plotted in Fig. 2.7 as a function of scale. The decreasing values of C_v with increasing scale show that the width (spread) of the pdf changes with scale in a different manner compared to the mean (it reduces more quickly) - in agreement with earlier observations by Kuhnle and Southard (1988) - and hence reinforces the conclusion that sediment transport fluctuations exhibit multiscaling. A monoscaling function would have constant C_v as mean and standard deviation would rescale similarly - see equation (2.6).

Concentrating on the first order ($q = 1$) statistical moment, which is the mean sediment accumulation in an interval $\Delta(t)$ (scale a in the previous notation), we note that it scales as $\Delta(t)^{\tau(1)}$ where $\tau(1) = c_1 - c_2/2$ from equation (2.13). Using the

values of c_1 and c_2 (Table 2) for low flows, it implies that within the scaling range of 1 and 10 min the mean amount of accumulated sediment ($< S(t, \Delta t) >$) increases as approximately $\sqrt{\Delta t}$. If one doubles the sampling interval, for example, the amount of sediment accumulated does not double but increases only by a factor of about 1.41. When considering the mean sediment transport rate, ($< S(t, \Delta t)/\Delta t >$), the above results imply that it scales as $(\Delta t)^{-0.5}$ or that the bedload transport rate decreases with increasing sampling interval Δt. In other words, doubling the sampling interval results in a transport rate that is approximately 0.7 ($= 1/\sqrt{2}$) times smaller.

For high flow rates, the estimated value of $\tau(1)$ is approximately 1.1 (using the values of c_1 and c_2 from Table 2.3 in equation 2.13) implying that within the scaling range of 1 and 10 min, the mean amount of accumulated sediment increases as approximately $(\Delta)^{1.1}$. In this case, doubling the sampling interval increases accumulated sediment by a factor of about 2.1. Considering the mean sediment transport rate, one sees that in the high flow conditions the rate does not remain constant with sampling interval (within the range of sampling interval of 1 to 10 min) but rather slightly increases by a factor of approximately 1.1 ($= 2^{0.10}$). The above scaling applies only to the mean and is controlled by the value of $(c_1 - c_2)$. As discussed before, our analysis allows one to quantify how higher order statistical moments change with sampling interval in a similar way, for example the second moment about the origin changes as a power law on scale with an exponent $2(c_1 - c_2)$ etc. as dictated by equations (2.6) and (2.13).

Turning to the singularity spectrum $D(h)$ which characterizes more directly the abrupt fluctuations of the sediment transport series, we recall that it can be computed from the scaling exponents $\tau(q)$ via the Legendre transform (equation (2.7) or directly from equation (2.14) using the fitted parameters c_1 and c_2). Fig. 2.8a shows the $D(h)$ spectrum for the sediment transport in pan 3, calculated from the quadratic model fit using the parameters in Table 2.3. It can be seen that at the low discharge, the sediment transport series is both rougher on the average and more intermittent (lower c_1 and higher c_2, respectively). Conversely, the high discharge case results in a much smoother and less intermittent sediment transport series (higher c_1 and lower c_2, respectively). As it can be seen from Fig. 2.8a, for low flow rates h_{min} is approximately zero and h_{max} is slightly larger than 1. This implies that there are clustered regions in the sediment transport rate series where very high fluctuations are expected over very small intervals

(a value of h corresponds to a discontinuous signal) while there are also regions that are very smooth (a value of $h = 1$ corresponds to a signal with continuous first derivative). For high flow rates the values of h_{min} and h_{max} are approximately 0.8 and 1.5, implying that the sediment transport series is very smooth overall but there are limited clustered regions where some abrupt fluctuations at small scales are encountered (signal slightly non-differentiable as $h < 1$) while the majority of the series is very smooth. One would expect that these bursts in the sediment transport series are connected to high fluctuations in the bed elevation series which would allow to a lesser or larger degree a collective mobilization of gravel particles. In the next section a multifractal analysis to characterize the roughness and intermittency of bed elevation fluctuations is presented.

2.4.2 Bed elevation scaling

Spatial bed elevation fluctuations have been previously analyzed in terms of their scaling properties, and deviation from simple scaling has been reported [38]. Here the temporal fluctuations of bed-elevation were analyzed with the wavelet-based multiscale framework, and scaling of the moments was documented within the range of scales from approximately 1 to 10 min (see Fig. 2.9), which coincides with the scaling range observed in the sediment transport series and suggests a close link between the dynamics of the two series. Above the characteristic scale of 10 min, the moments leveled off and the statistical quantities became independent of time-scale. The scaling exponents $\tau(q)$ for these moments are shown in Fig. 2.9, for the high and low discharge experiments. As other authors have reported (e.g., see [38]), a deviation from simple scaling is observed for both discharge rates indicating the presence of temporal heterogeneity in the local roughness (what we have called "intermittency") in bed elevation fluctuations. The parameters c_1 and c_2 fitted to the $\tau(q)$ curves of the bed elevation fluctuation series are displayed in Table 2.4, and the corresponding singularity spectra $D(h)$ are presented in Fig. 2.8b. Similar to the sediment transport fluctuations, we observe that bed-elevation fluctuations are rougher on an average in the low discharge case than in the high discharge case (c_1= 0.57 vs. $c_1 = 0.68$), although to a lesser extent than in the sediment series. However, considering the degree of intermittency in the bed elevation fluctuations, we see that it is higher at the high transport case (a wider $D(h)$ spectrum and a larger c_2 value) with a coefficient of intermittency $c_2 = 0.13$, versus a narrower

c_2 and = 0.06 in the case of low transport. This is reverse from what is observed in the sediment transport fluctuations (see also Fig. 2.8a) and calls for an explanation based on further experimentation and mechanistic modeling.

2.5 Discussion

The simultaneous collection of bed load transport and bed elevation data in a field-scale channel is the major strength of the experimental setup used in this work. The large channel geometry, and high temporal resolution of the data, allowed robust statistical analysis over a wide range of temporal scales. Despite the more comprehensive data sets collected as part of the STREAMLAB-06 experiments our analysis here is concentrated on two data sets at two different flow rates, as these are the only data currently available for analysis. The mixed grain size distribution of the feed material, while beneficial for mimicking a natural gravel stream, makes it more difficult to discern the influences of spatial grain size sorting [9, 15, 17, 53] from those of bed topography and collective grain motion [16, 18, 14] on sediment transport fluctuations. Also, for this experiment we do not have any data regarding armoring of the stream bed over the duration of the experiments, or the grain size distributions of individual sediment pulses. With these limitations in mind, in this section we place our experimental results and analysis in the context of laboratory and field studies of sediment transport fluctuations in uniform and mixed-grain size channels.

The multiscaling analysis demonstrates how the statistical moments of bed load transport rate depend on the time scale of observation. To illustrate, we first examine the behavior of the mean transport rate (the first moment). Estimating mean sediment transport rate is essential for measuring the material flux through a river, and for model input and/or calibration. For the low discharge run ($\tau_b^* = 0.085$), mean transport rate decreased with sampling interval, while at higher discharge ($\tau_b^* = 0.196$), the trend reversed: mean transport rate slightly increased with sampling interval over a comparable time range. A similar trend was discovered by Bunte and Abt [2], who studied the effect of sampling interval on bed load transport rates measured using Helley-Smith samplers deployed in a mixed gravel-cobble stream of a size comparable to our experiments. They found that in moderate to high flows (50 % bankfull to almost bankfull conditions) 2

min sampling led to an average transport rate 2 to 5 times lower than that found with 10 min sampling. However, at lower flows (close to the incipient gravel motion) 2 min sampling overestimated the transport rates at 10 min sampling by a factor of almost 3. Although not directly comparable, the trends observed are qualitatively the same as our experiments (Fig. 2.10). Bunte and Abt [2] attribute the higher discharge trend to the effect of large but infrequent transport events associated with the crests of bed forms: small sampling intervals underestimate mean transport because they are likely to miss these events. They suggest that the reversal in trend for the low discharge observations is the result of sampling and computational difficulties, rather than a "real" effect. Our high-resolution experiments demonstrate that this trend reversal might in fact be real.

It is stressed that it is difficult to quantitatively compare the field results to our laboratory experiments, due to differences in transport and lack of the detailed field data. Bunte and Abt [2] do not report Shields stress, but they report that their low flow observations correspond to incipient sediment motion which is supported by our calculation of their critical Shields stress ($\tau^* = 0.047$) using their reported bankfull flow characteristics. Our low flow experiment had a Shields stress almost twice the critical value, making it comparable in terms of stress to their moderate flow observations. Thus it seems that in both the study of Bunte and Abt and our study, suggest a reversal in trend, from decreasing to increasing mean transport rate with sampling interval, as bed stress increases. The fact that the reversal appears to occur for different stress values in the field and the laboratory may be the result of the multiple intricacies of sediment transport and grain size sorting of heterogeneous mixtures in turbulent flows. Clearly, experiments systematically document how the statistics of transport rate change with bed stress over a wide range of values would be helpful in illuminating this point.

Several field and laboratory experiments have documented sediment transport fluctuations in mixed-grain size sediments. Iseya and Ikeda [9] found strong longitudinal grain size sorting in mixed gravel and sand experiments, which caused periodic fluctuations in transport rate due to changing local sediment supply. Such periodic pulses in gravel-sand mixtures have also been reported by Kuhnle and Southard [15] and Frey et al. [53]. These experiments cannot be directly compared to our results, however, because they had limited bed topography and/or antidunes, while our experimental channel allowed for the growth of large bed forms in subcritical flow. These studies

suggest that the creation and destruction of sediment patches of different grain sizes [see also [17] due to longitudinal grain size sorting within the channel likely contributed somewhat to the observed transport fluctuations in our experiments, but are not capable of explaining all of this variability.

Sediment transport rates became smoother and less intermittent with increasing bed stress in our experiments, in agreement with previous observations. Near the threshold of motion, grains are in partial transport because local bed stress fluctuates above and below the threshold value. These turbulent fluctuations, along with grain-to-grain interactions at the bed, result in intermittent and collective motion of grains, leading to nonrandom transport rate fluctuations with heavy tails [14]. In a mixed grain size bed, size selective transport often occurs which may enhance this effect [15]. The experiments of Ancey et al. [2008] demonstrate that such fluctuations can occur even in glass spheres of uniform size, with little or no bed topography. As bed stress is increased such that the local stress fluctuations are always above the critical value, all grains become entrained in the flow as the intermittent, collective motions of grains gives way to continuous transport [9, 15, 14, 54]. While this effect has been documented qualitatively by previous authors, our results quantify these changes in the statistics of sediment fluctuations with bed shear stress.

Bed elevation also became smoother with increasing transport, meaning that the magnitude of high frequency fluctuations at small scales was reduced overall. At low flow conditions, topographic fluctuations were of the order of the grain scale (Fig. 2.3), supporting the idea that grain-grain interactions (and perhaps longitudinal grain-size sorting) dominated transport fluctuations as described above. With increasing bed stress, and presumably full mobility of all grains in transport based on Shields stress calculations, the bed organized into large-scale bed forms (Fig. 2.4). Data indicate that higher frequency (smaller-scale) topography, likely representing clusters of grains, became less prevalent at higher flows where bed topography was dominated by dune forms. Interestingly, although the bed became smoother overall from low to high discharge, intermittency increased. In other words, high small-scale frequency fluctuations in bed topography became less prevalent overall, but also less uniformly distributed. This may be due to irregular clusters of grains superimposed on larger scale, more regular dune features. However, observations of grains on the bed were not made and so these ideas

remain speculative at this stage. Our experiments highlight the need to simultaneously document bed topography, bed load transport rates and individual particle motions (e.g., as those of [55, 56, 4]) in order to further our understanding of what contributes to transport fluctuations at the smallest to largest scales.

The scaling ranges of both transport rates and bed elevation series are similar with a leveling off, or saturation, at approximately the same time scales, indicating that fluctuations in transport are intimately related to bed topography. While the nature of these dependencies is still unclear, a practical result may be obtained. The scale-dependent nature of transport (within 1 and 10 min in this study) means that measured rates at different time intervals are not directly comparable. In our experiments, both transport and bed elevation exhibit no time dependence when measured over intervals greater than 10 to 15 min. In other words, if we measure for a period of time that is larger than the timescale associated with the migration of the largest topographic feature, we can obtain mean values for bed topography and transport rate that have no time dependence [7]. From a practical point of view, this is the mean transport rate one should try to obtain in the field. Measurements of bed topography from a river could be used to determine the upper scaling limit of fluctuations - which determines the timescale over which one should deploy a sampler to obtain a representative "mean" bed load transport value. As discussed by Fienberg et al. [7], this approach is possible in flumes and small streams where the timescale is of the order of tens of minutes. Since the size of bed forms scales with river depth, however, this approach quickly becomes impractical as river size increases - deployment of bed load samplers for long durations can result in overfilling and clogging [e.g., [2]], or integrating over changing flow conditions. In this case, determining the scale-dependent nature of transport rate becomes critical.

2.6 Conclusions

In this paper we introduced a formalism, typically used in turbulence studies, to quantify two properties in sediment transport and concurrent bed elevation series: the "average roughness" of the series (depicting the average strength of local abrupt fluctuations in

the signal) and the "intermittency" (depicting the temporal heterogeneity of fluctuations of different strength). In the bedload sediment transport rates, we documented the presence of a rougher and more intermittent behavior at low transport conditions (dimensionless bed shear stress of about twice the critical value) transiting to a smoother and less intermittent behavior at high transport conditions (dimensionless shear stress of about five times the critical value).

Apart from simply quantifying roughness and intermittency of the sediment transport rates, the results of our analysis provide a framework for quantifying how the probability distribution of sediment transport rates changes with sampling interval and thus have important practical implications. (It is interesting to note that the change of pdf with scale is parameterized in terms of the roughness and intermittency parameters which characterize the burstiness of the series.) Specifically, our analysis demonstrated that the statistics of bedload sediment transport rates depend strongly on scale (sampling interval) and this dependence varies with the discharge conditions. Our results agree with the field observations reported by Bunte and Abt [2005] for mean bedload rates and call for a more systematic study to precisely quantify this scale dependence in terms of grain size sorting and bed shear stress. It is noted that the theoretical framework we propose here offers the ability to go beyond the mean and compare the whole probability density function, including extreme values or quantiles, at different scales. This is important for example when the pdf of sediment transport rates has been estimated from data at one particular sampling interval and an extreme exceedance quantile (say, relevant to an ecological smaller-scale functional disturbance) needs to be estimated. Our methodology can bridge this gap in scales and also provide a framework with which comparison of sediment rates sampled with different instruments can be made.

A problem of continuous interest in the literature is the relation of microscale (particle-scale) dynamics to the macroscale behavior of sediment transport (e.g., [10, 56, 55, 12, 4, 14], among several others). Although not precisely quantified in this paper, it is worth noting that the multi-scale statistical behavior of sediment transport rates (as quantified here via the signal roughness and intermittency) seems consistent with known particle-scale dynamics. For example, at low flows, a rougher but more temporally homogeneous (less intermittent) bed elevation series was documented, indicative

of the dominance of high-frequency localized grain clusters; this bed micro-topography apparently gave rise to sediment transport rates that are almost of equal roughness but are more inhomogeneous in time (more intermittent); see Fig. 2.8. This might be due to the collective motion of grains responding to local bed stress fluctuating above and below the critical value. It appears that as bed stress increased, grain patches became less prevalent and more irregular (roughness in bed elevations decreased but intermittency increased) as the bed organized into large-scale dunes, and bedload transport became smoother and more homogeneous in time as entrainment of all grains commenced. This speaks for the collective or cooperative behavior of particle movement that has different dynamics at low and high flows and depends on the presence or absence of self-formed structures on the bed [e.g., [10, 14]].

We see our study as a first step in the direction of understanding the scale-dependency of sediment transport rates over the continuum of flow discharge conditions and grain size distributions and relating the statistics of bed elevations to the statistics of bedload sediment transport. More controlled experiments have to be performed and analyzed with different particle sizes (from a single particle size to a broad particle size distribution and for gravel and sand-beds) and a spectrum of discharge rates, to fully characterize the intermittency of bedload sediment transport rates and how it relates to that of the bed elevation fluctuations, and (eventually) to particle-size dynamics. Also, the documented statistical structure of sediment transport rates can be seen as providing an additional model diagnostic that mechanistic models should be able to reproduce, and as such, it is interesting to ask as to whether any known sediment transport model can reproduce the multiscaling characteristics reported in this study.

Q_w (l/s)	Depth (m)	V (m/s)	h_R (m)	S_w (%)	τ_b*	T_{mean} (^oC)
4300	1.3	1.20	0.67	0.23	0.085	3.5
5500	1.3	1.54	0.67	0.53	0.196	2.7

Variables: Q_w = Design water discharge for the run
Depth = average depth of flow in test section
v = velocity of flow
h_R = Hydraulic radius
S_w = water surface slope
τ_b* = Dimensionless Shields stress (computed using hydraulic radius)
T_{mean} = Mean water temperature

Table 2.1: Hydraulic conditions for the two studied discharges.

Q (l/s)	Shields stress	Pan	Scaling Range (min)	Wavelet	c_1	c_2
4300	0.085	2	1.2-10	g2	0.57	0.12
		2	1.2-10	g3	0.56	0.14
		2	1.2-10	g4	0.54	0.12
		3	1.2-10	g2	0.52	0.11
		3	1.2-10	g3	0.49	0.13
		3	1.2-10	g4	0.48	0.13
		4	1-8	g2	0.49	0.10
		4	1-8	g3	0.47	0.10
		4	1-8	g4	0.45	0.10
5500	0.196	2	1-10	g2	1.04	0.09
		2	1-10	g3	1.07	0.09
		2	1-10	g4	1.09	0.10
		3	1-10	g2	1.04	0.11
		3	1-10	g3	1.07	0.10
		3	1-10	g4	1.09	0.11
		4	1-10	g2	1.09	0.11
		4	1-10	g3	1.12	0.11
		4	1-10	g4	1.14	0.11

Table 2.2: Multifractal parameters estimated for low and high flows using different Gaussian wavelets (see text for definitions).

Q (l/s)	Pan	Scaling Range (min)	Shields stress	$\tau(2) - 2\tau(1)$	c_1	c_2
	2	1.2-10		-0.20	0.56	0.14
4300	3	1.2-10	0.085	-0.19	0.49	0.13
	4	1- 8		-0.15	0.47	0.10
	2	1-10		-0.13	1.07	0.09
5500	3	1-10	0.196	-0.16	1.07	0.10
	4	1-10		-0.15	1.12	0.11

Table 2.3: Summary of statistical scaling analysis results for the bedload sediment series (see text for definition of variables).

Q (l/s)	Probe	Scaling Range (min)	Shields stress	$\tau(2) - 2\tau(1)$	c_1	c_2
	4	1-10	0.085	-0.04	0.57	0.06
4300	5	1-10		-0.06	0.53	0.08
	2	0.5-8		-0.18	0.65	0.12
5500	3	0.5-8	0.196	-0.19	0.68	0.14
	4	0.5-8		-0.20	0.76	0.13

Table 2.4: Summary of statistical scaling analysis results for the bed elevation time series (see text for definition of variables).

Figure 2.1: Weighing pans located at the downstream end of the experimental Main Channel.

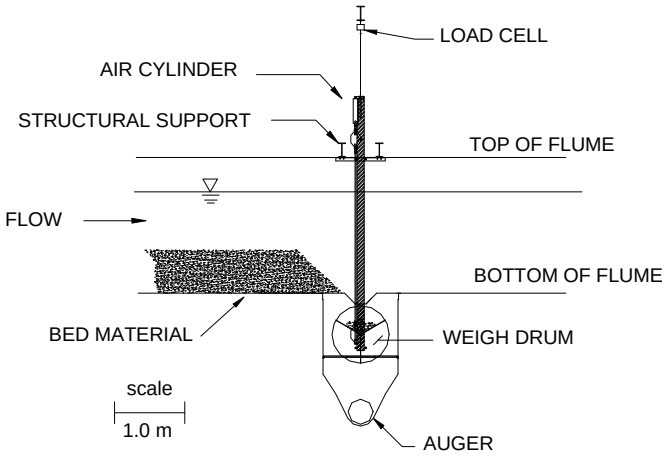

Figure 2.2: Side view schematic of a weigh pan and sediment recirculation system in the Main Channel.

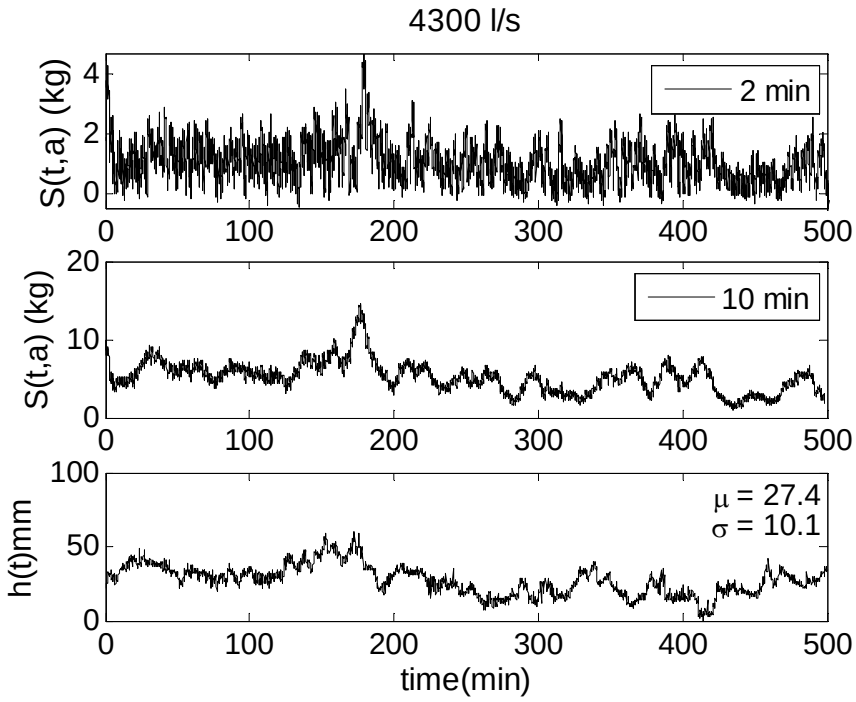

Figure 2.3: Low transport conditions (flow rate 4300 l/s): Bedload sediment transport series accumulated every 2 minutes (a), and 10 minutes (b), and the corresponding series of gravel bed elevations (c).

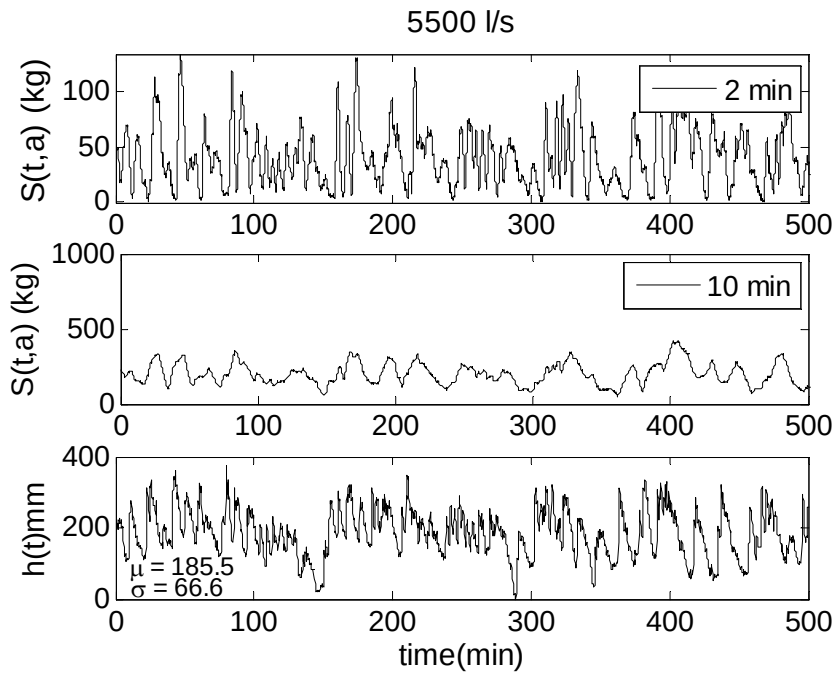

Figure 2.4: High transport conditions (flow rate 5500 l/s): Bedload sediment transport series accumulated every 2 minutes (a), and 10 minutes (b), and the corresponding series of gravel bed elevations (c).

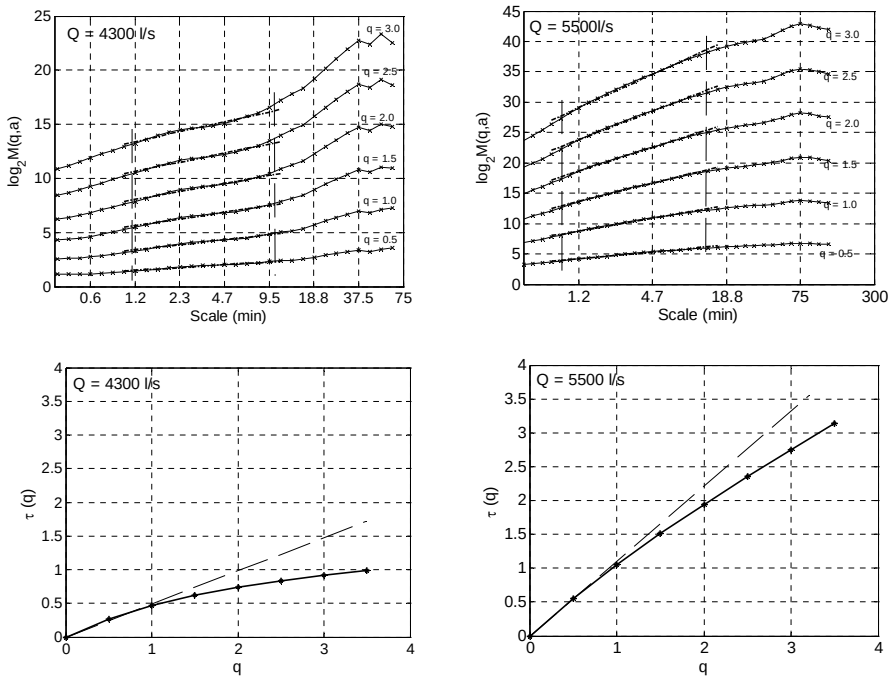

Figure 2.5: Statistical moments of the fluctuations of the sediment transport series as a function of scale for several moment orders q (upper plots) and the scaling exponents $\tau(q)$ estimated from the log-log linear regressions (bottom plots). The vertical lines in the upper plots denote the scaling region within which estimation of the scaling exponents was performed. Notice the deviation of $\tau(q)$ from the linear line establishing the presence of multi-fractality. The left panels are for low transport conditions and the right for high transport conditions.

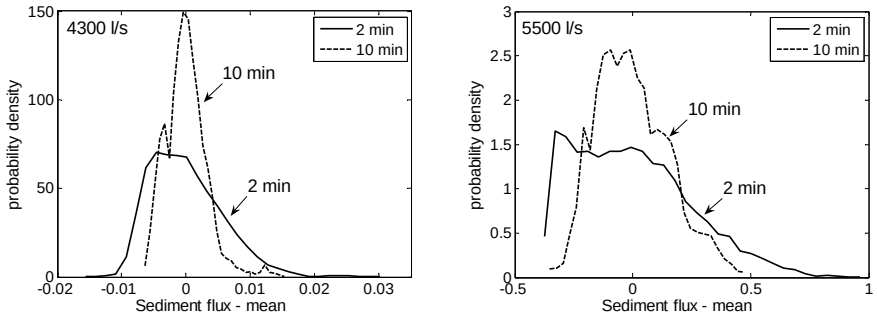

Figure 2.6: Probability distribution functions of the sediment transport rate (flux) for sampling intervals of 2 and 10 minutes for low (left) and high (right) discharge rates. The probability distributions have been shifted to zero mean for comparison.

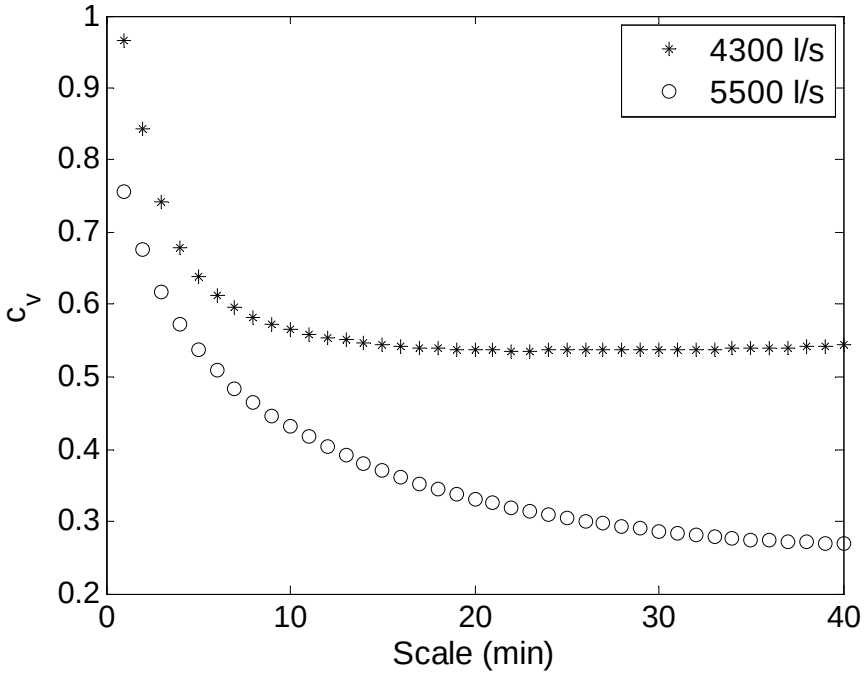

Figure 2.7: Coefficient of variation of the bedload sediment transport series.

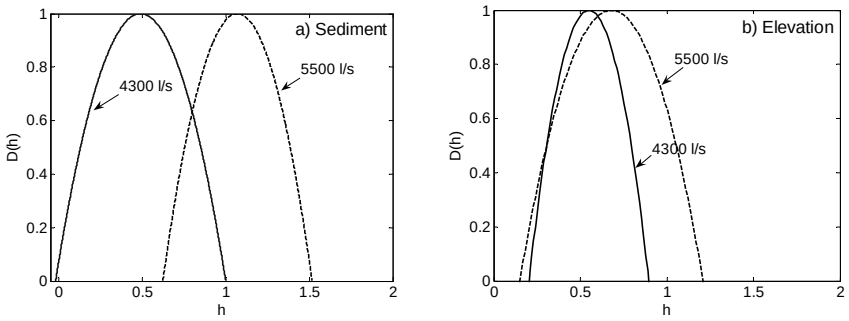

Figure 2.8: Fitted quadratic singularity spectra obtained for (a) bedload sediment transport series and (b) bed elevation fluctuation series respectively for the low and high discharge cases.

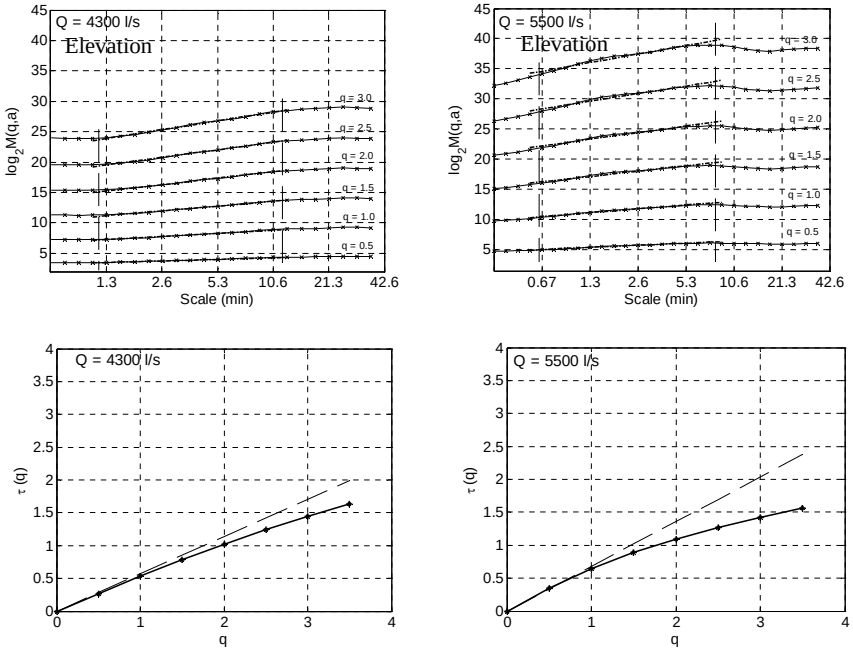

Figure 2.9: Statistical moments of the fluctuations of the bed elevation time series as a function of scale (upper plots) and the scaling exponents $\tau(q)$ estimated from the log-log linear regressions within the scaling regions (bottom plots). Notice the deviation of $\tau(q)$ from the linear line establishing the presence of multi-fractality. The left panels are for low transport conditions and the right for high transport conditions.

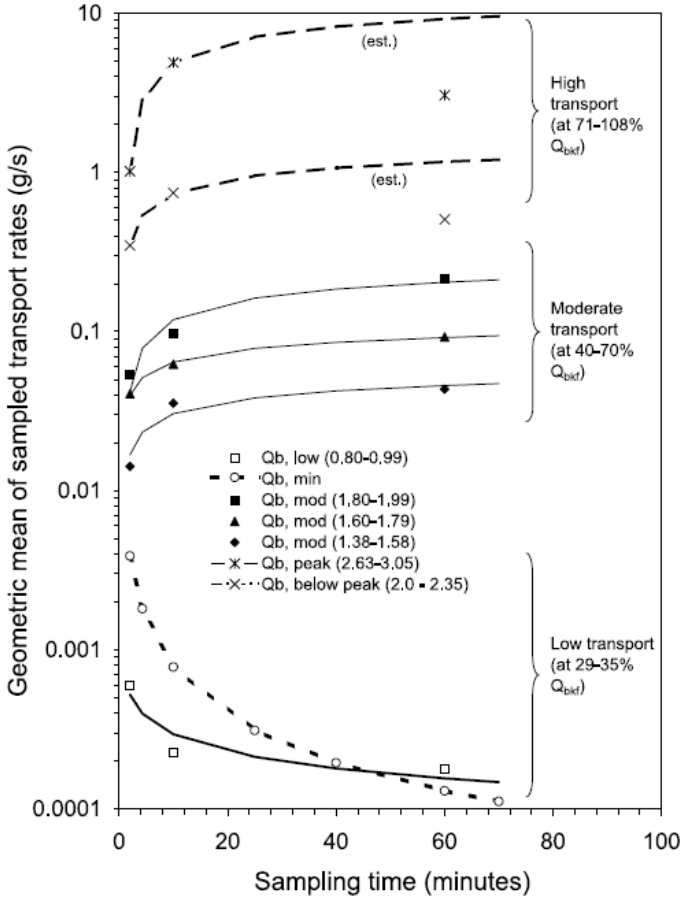

Figure 2.10: Geometric means at different sampling times from: (a) field experiments [reproduced from Bunte and Abt, [2]], and (b) theoretical curves from this study.

Chapter 3

Nonlinearity and Complexity in Gravel Bed Dynamics

The dynamics of river bed evolution are known to be notoriously complex affected by near bed turbulence, the collective motion of clusters of particles of different sizes, and the formation of bedforms and other large-scale features. In this paper, we present the results of a study aiming to quantify the inherent nonlinearity and complexity in gravel bed dynamics. The series analyzed are bed elevation fluctuations collected via submersible sonar transducers at 0.1 Hz frequency in two different settings of low and high discharge in a controlled laboratory experiment. We employed surrogate series analysis and the transportation distance metric in the phase-space to test for nonlinearity and the Finite Size Lyapunov Exponent (FSLE) methodology to test for complexity. Our analysis documents linearity and underlying dynamics similar to that of deterministic diffusion for bed elevations at low discharge conditions. These dynamics transit to a pronounced nonlinearity and more complexity for high discharge, akin to that of a multiplicative cascading process used to characterize fully developed turbulence. Knowing the degree of nonlinearity and complexity in the temporal dynamics of bed elevation fluctuations can provide insight into model formulation and also into the feedbacks between near-bed turbulence, sediment transport and bedform development.

3.1 Introduction

The evolution of alluvial river beds is the result of a number of often strongly nonlinear processes which give rise to the extraordinary large variety of patterns observed in nature. In gravel bed rivers, where the dominant form of sediment transport is bedload, both field observations [10] and laboratory experiments ([57, 58]) suggest that most of the transport occurs by the collective motion of clusters of particles mobilized by turbulent sweep events and outward interactions, while a relatively smaller contribution is associated with bursts (see also review of Best 1993). Clearly, the bed evolution is likely to be strongly affected by the intermittent process whereby coherent turbulent structures are randomly generated, grow and decay in the near wall region.

Coherent structure dynamics, in turn, depend on the range of scales characterizing a given bed topography, and the flow variability at a given point contains both locally derived flow structures and structures inherited from upstream ([59]). The bed evolution is further complicated by the formation of either free bedforms (e.g., [16]), arising as a result of the instability of a cohesionless bed subject to a turbulent flow, or bedforms forced by geometrical constraints (e.g., channel curvature) ([60]). Finally, the heterogeneous character of the sediment leads to patterns associated with a spatial and temporal rearrangement of the grain size distribution of the sediments ([61]) which are strongly related to the different mobility of particles having different diameter ([62, 63]).

It then clearly appears that river bed evolution, even in the simplest case of a flat bed configuration, is an extremely complex phenomenon whose understanding needs the use of refined theoretical, experimental and data analysis techniques.

Several contributions have been so far devoted to the study of the spatial properties of water-worked gravel bed surfaces measured both in the laboratory and in the field (e.g., see [38], and references therein). In addition to conventional statistical parameters (i.e., standard deviation, skewness and kurtosis) of the bed elevation spatial distribution, second-order and higher-order structure functions have been proved particularly helpful for exploring the statistical properties and potential multiscaling behavior of bed elevations fields ([39]). In a recent study, the multiscale statistical structure of the temporal evolution of bed elevation fluctuations at several locations on the evolving gravel bed under steady-state conditions has also been analyzed and the presence of a

multiscaling behavior has been reported ([5]).

In the present contribution, a different type of analysis of temporal elevation series is performed aiming at quantifying the nonlinearity and complexity in gravel bed dynamics. It is noted that these dynamics are internally generated by the system itself rather than by an external stochastic forcing, since the discharge is kept constant and the system is under steady state conditions. To the best of our knowledge, the only other study that attempted a similar analysis is that of Gomez and Phillips ([64]) who analyzed sediment transport rates (interestingly collected from a controlled laboratory experiment conducted in the same flume almost 20 years ago; see [65]). The overall goal of that study was to identify deterministic sources of uncertainty, or unexplained variation, in the time series of bedload transport rates by computing how much of the observed variability (quantified in terms of Kolmogorov entropy) was not explained by bedform migration effects. The assumption was made that the variability (entropy) due to bed migration would be fully captured by a Hamamori probability distribution. It is noted that the Hamamori distribution is derived from sediment movement over a purely geometrical self-similar bed morphology ([66]) and does not account for the natural variability in bedform shapes and sizes. It is also restricted to sediment transport rates that are at most four times the mean rate - not the case in most observed series including the series analyzed in Gomez and Phillips ([64]).

The purpose of the present study is to revisit the problem of quantifying the deterministic complexity in gravel bed dynamics with an assumption-free methodology and using more powerful techniques recently developed in the study of nonlinear systems (e.g., [67]). The adopted methodologies have been proven to give a deep insight in other complex geophysical processes such as fluid turbulence ([68, 69]), atmospheric boundary layer dynamics ([70]) and dispersive mixing in porous media ([71]), among others.

The paper is organized as follows. In section 2 we briefly describe the bed elevation data collected in two laboratory experiments under low and high discharge conditions. Section 3 introduces the mathematical methodology used first to identify the presence or absence of inherent nonlinearity in time series and second the Finite Size Lyapunov Exponent (FSLE) methodology to quantify the complexity and predictability of processes exhibiting many scales of motion. In section 4, results of the analysis of the temporal sequences of bed elevation data series are presented. Finally, section 5 presents concluding

remarks and suggestions for future research.

3.2 Experimental data

The data examined in the present contribution were collected during a series of experiments conducted in the Main Channel facility at the St. Anthony Falls Laboratory, University of Minnesota. The channel is 2.74-m wide and has a maximum depth of 1.8 m. It is a partial-recirculating flume in that it has the ability to recirculate the sediment while the water flows through the flume without recirculation. Water for the channel was drawn directly from the Mississippi River, with a maximum discharge capacity of 8000 l/s. The channel has a 55-m long test section and, in the experiments reported here, a poorly sorted gravel bed extended over the last 20 meters of this test section. The gravel used in these experiments had a broad particle size distribution characterized by d_{50} =11.3 mm, d_{16} = 4.27 mm and d_{84} = 23.07 mm. More details on this experimental setting can be found in [5].

Measurements of bed elevation and sediment transport were taken at a range of discharges corresponding to different bed shear stresses. Here we focus our attention on the series of bed elevations collected under two different discharges: a low discharge case, with a discharge of 4300 l/s, corresponding to a dimensionless bed stress of about twice the critical value (Shields stress = 0.085 using median diameter) and a high discharge, 5500 l/s, corresponding to a Shields stress about five times the critical value (Shields stress = 0.196). For both bed stress conditions, the flume was allowed to run long enough prior to data collection such that a dynamic equilibrium was achieved in transport and slope adjustment of the water surface and bed. Determination of the dynamic equilibrium state was made by checking that the 60 min average sediment flux was stabilized to an almost constant value during the flume run. The bed elevation was then recorded over a span of approximately 20 hrs for each experiment, by using submersible sonar transducers, with a frequency of 0.1 Hz and a vertical precision of $\sim$ 1mm. Figure 3.1 displays the time series of bed elevations measured at a location aligned with the main channel axis for both the low (Figure 3.1a) and the high (Figure 3.1c) discharge conditions over a period of 10 hrs during which the bed-elevation and sediment flux series were stationary. The low bed stress run (Figure 3.1a) produced

a nearly plane channel bed, with only limited topographic variations, i.e. without obvious large scale structures in the bed elevation (the standard deviation in the bed is 10.06 mm, compared to the initial d50 grain size of 11.3mm). On the contrary, the higher stress run (Figure 3.1c) generated substantial bed variability at large scale in the form of dunes, with intermediate to particle-scale fluctuations superimposed on these larger-scale features. In this study we focus on comparing these two runs in terms of the complexity of the underlying forming processes imprinted in the time series of bed elevation fluctuations. The analysis methodologies we employed are briefly described below.

3.3 Analysis methodologies

3.3.1 Test for linearity

Nonlinearity is a necessary condition for deterministic chaos and thus methodologies for testing whether a time series has been generated by a linear or inherently nonlinear process have gained considerable attention in the literature. By inherent nonlinear process it is meant a process whose nonlinearity is not external, i.e., the result of a static nonlinear transformation applied on an otherwise linear underlying process, but it is weaved into its dynamics such as for example in a series arising as a result of a multiplicative cascade generator, a popular phenomenological model for turbulence (e.g., [34]). Detection of nonlinearity is not a trivial task and several methods are available, as for example based on "reversibility", information-theoretic approaches, singular value decomposition, and the use of "surrogates" (e.g., see a review in Basu and Foufoula-Georgiou, [72] and references therein). Here we adopt a surrogate-based methodology. Surrogate series maintain the pdf and correlation structure (and thus spectrum) of the original series but destroy any inherent nonlinearity since the process of generating the surrogates randomizes the phases in the Fourier space.

The method we used for surrogate series generation is the Iterative Amplitude Adjusted Fourier Transform (IAAFT) method of Schreiber and Schmitz ([73]). This method is an improvement of the earlier Amplitude Adjusted Fourier Transform (AAFT) method of [74], and iteratively adjusts both the pdf and linear correlation structure to minimize their deviation from the original series. The reader is referred to the original

publications for details to supplement the brief exposition presented below.

The surrogate series $\{S_n\}$ is assumed to be generated by a process of the form

$$s_n = S(y_n), y_n = \sum_{i=1}^{M} a_i y_{n-1} + \sum_{i=1}^{N} b_i \eta_{n-1}, \tag{3.1}$$

where S could be any invertible nonlinear function, $\{y_n\}$ is the underlying linear process, $\{a_n\}$ and $\{b_n\}$ are constants, and $\{\eta_n\}$ is Gaussian white noise. The steps involved in generation of surrogate series are as follows:

1. Randomly shuffle the data points of the original series $\{x_n^0\}$ to destroy any correlation or nonlinear relationship, while keeping the pdf unchanged. The reshuffled series is the starting point for the iteration $\{s_n^{(0)}\}$.

2. Construct the discrete Fourier transform of the current series $\{s_n^{(i)}\}$, and adjust the amplitudes to recreate the power spectrum of the original data. Keep the phases unchanged. Perform inverse Fourier transform.

3. The pdf will no longer be correct. Transform the data to the correct pdf by rank ordering and replacing each value with the value in the original series $\{x_n^0\}$ with the same rank. This will result in updated series $\{s_n^{(i+1)}\}$.

4. Repeat steps 2 and 3 until discrepancy in the power spectrum is below a threshold, or the sequence stops changing (reaches a fixed point). In this manner a surrogate data series can be generated with an identical pdf and optimally similar power spectrum to the original series.

Figures 3.1b,d show two realizations of the surrogate series corresponding to the bed elevation series for low and high flow discharge. It is noted that in both cases it is difficult to distinguish visually any difference between the original series and their surrogates (compare Fig 3.1a to 3.1b and Fig 3.1c to 3.1d). (It is reminded that the original and surrogate series share the same pdf and correlation structure or spectrum, but the surrogate series contain only linear correlation). However, as it will be demonstrated later, our methodologies depict important differences in the case of high discharge, emphasizing the presence of inherent nonlinearity in the bed forming process.

Once an ensemble of surrogate series is generated, a probabilistic metric of the "distance" between each one of those series to the original series $\{x_n^0\}$ and between multiple realizations of the surrogate series $\{s_n\} = \{x_n^i\}, i = 1, ..., N_s$ is formed. If the

original series were linear, these two distance metrics would overlap as one would not be able to discriminate the original series from members of the ensemble of surrogates; however, if they do not overlap, nonlinearity in the original series can be inferred with confidence.

Following Basu and Foufoula-Georgiou ([72]), we use the transportation distance functions $d_{oi} = d(\{x_n^0\}, \{x_n^i\})$ and $d_{ij} = d(\{x_n^i\}, \{x_n^j\})$, $i \neq j$ to measure, respectively, the difference in the long term behavior between the original data set and the i-th surrogate data set and the mutual distances between surrogates. The idea is to transform two given scalar time series (x, y) in vector time series (X, Y) by phase-space reconstruction using an embedding dimension (e) and an integer delay (τ), thus obtaining an e-dimensional embedding space $\Re^r$ which captures the dynamics of the x and y systems' attractors ([75]). The details of determining embedding dimension and delay can be found in ([76, 77]). In practice, a box in the reconstructed phase space, $\Re^r$, containing both the X and Y vector time series is divided into a finite number $B_k, k = 1, ..., b$ of sub boxes, each characterized by the discretized probability measures p_k and q_k defined as

$$p_k = \sum_{i=1}^{b} \mu_{kl}, q_k = \sum_{i=1}^{b} \mu_{kl}, l = 1, ..., b \tag{3.2}$$

where $\mu_{kl} \geq 0$ defines the amount of "material" (information) shipped from box B_k to box B_l. These constraints ensure that the initial and final distributions are preserved and allow us to determine the set $M(p, q)$ [with $p = (p_1, ..., p_b)$ and $q = (q_1, ..., q_b)$] of all transportation plans. The transportation function is then obtained by minimizing (e.g., through the network simplex algorithm) the transportation cost

$$d(p, q) = inf_{\mu \epsilon M}(p, q) \sum_{k,l=1}^{b} \mu_{kl} \delta_{kl} \tag{3.3}$$

where δ_{kl} is the taxi cab metric ([75]) normalized to the embedding dimension between the centres of B_k and B_l. If the pdf of the transportation distances d_{oi} between the original series and the surrogates is distinct from the pdf of the mutual distances d_{ij} between the surrogates, nonlinearity is inferred. Details of the methodology and examples of its application to known linear and nonlinear series, e.g., autoregressive

series, Lorenz series, stochastic Van der Pol oscillator series, and the Santa Fe Institute competition series, can be found in Basu and Foufoula-Georgiou ([72]).

3.3.2 Quantification of complexity

It is well known that many natural systems, although deterministic, are characterized by a limited degree of predictability owing to the presence of deterministic chaos which makes small errors in the initial conditions to grow exponentially fast with time (e.g., [78]). In the traditional sense, predictability is assessed via computation of the maximum Lyapunov exponent which dictates that the predictability time is

$$T_p \sim \frac{1}{\lambda_{max}} ln \frac{\Delta}{\delta}. \tag{3.4}$$

where λ_{max} is the leading (or maximum) Lyapunov exponent, measuring the average exponential rate of separation of nearby trajectories, δ is the size of the initial (strictly infinitesimal) perturbation, and Δ is the (still small) accepted error tolerance. The above formula holds only for infinitesimal perturbations, and, by construction, it cannot assess the predictability in systems with many scales of variability, such as turbulence which possesses a hierarchy of eddy turnover times. In those multiscale systems the predictability time T_p is determined by the nonlinear mechanism responsible for the error growth and it is not captured by λ_{max} which is governed by the linearized equations of motion, given the assumption of small perturbations. To address these issues, Aurell et al. ([79]) proposed a generalization of the maximum Lyapunov exponent method. Specifically, they introduced the quantity $T_p(\delta, \Delta)$ which is the time it takes for a finite perturbation to grow from an initial size δ (in general not infinitesimal) to a tolerance level Δ. The so-called Finite Size Lyapunov Exponent (FSLE) $\lambda(\delta, \Delta)$ is then the average of some function of this predictability time, such that if both δ and Δ are infinitesimally small one would recover the usual Lyapunov exponent:

$$\lambda(\delta, \Delta) = \left\langle \frac{1}{T_p} \right\rangle ln \left(\frac{\Delta}{\delta} \right). \tag{3.5}$$

Various methodologies are available for computing finite-size Lyapunov exponent (see [67]). In the present contribution we have adopted the method of Boffetta et al. ([80]).

3.4 Results and Discussion

3.4.1 Nonlinearity

The results of nonlinearity tests carried out on the two time series of bed elevations are reported in Figure 3.2. For low discharge conditions (Figure 3.2a), the probability density function of the transportation distance between the original series and the surrogates overlaps the one obtained by considering multiple realizations of the surrogates. On the other hand, Figure 3.2b shows that for the high discharge case the probability density functions of the transportation distance between each surrogate series and the original time series and between multiple realizations of surrogates are completely different suggesting that strong nonlinearities are inherent in the processes which shaped the bed morphodynamics. These nonlinearities are likely to be connected to the irregular and unsteady large-scale bedforms, mainly dunes, observed in this high flow experiment, promoting the formation of patterns of sorting and leading to a strong reworking of the sediment bed ([81, 82]).

To shed light into the above findings, we proceed with the following analysis guided by some recent findings in Singh et al. [5]. We synthetically generated two series with known underlying dynamics: a fractional Brownian motion (fBm) series and a multiplicative cascade series. The fBm series (with the Hurst exponent $H = 0.5$) is known to have linear underlying dynamics, arising from the integration of white noise. A multiplicative cascade series, on the other hand, arises from a nonlinear (multiplicative) mechanism of energy transfer from larger to smaller scales and thus possesses clearly nonlinear underlying dynamics. These latter dynamics cannot be rendered linear by any external transformation but rather are intrinsically embedded in all scales of variability of the process. In this work, we generated multiplicative cascade series using the random wavelet cascade (RWC) model (e.g., [50]) parameterized by two coefficients: c_1 and c_2. These two parameters dictate how the energy breaks down from larger to smaller scales, i.e., they characterize the probability distribution of the multiplicative weights of the cascade generator. Here we set $c_1 = 0.7$ and $c_2 = 0.1$ on the basis of the results recently obtained by Singh et al. [5]. This study employed a wavelet-based multifractal formalism and reported that the spectrum of scaling exponents of the same bed elevation fluctuation series analyzed here is well described by a quadratic model with c_1 and c_2

ranging in the intervals 0.53 - 0.76 and 0.06 - 0.14, respectively.

For visual comparison, Fig. 3.3 shows the fluctuations (computed as first order differences) of the original bed elevation series at low discharge (Fig 3.3a), the generated fBm series with $H = 0.5$ and the same standard deviation as the original series (Fig. 3.3b), the original bed elevation series at high discharge (Fig. 3.3c) and the generated RWC series (Fig. 3.3d) with $c_1 = 0.7$ and $c_2 = 0.1$. It is noted that there is much more "clustering" in the bed elevation series at high discharge than at low discharge which mathematically is depicted by the larger parameter c_2 (0.1 at high discharge versus 0 at low discharge). More details of this multifractal analysis and interpretation of the parameters c_1 and c_2 can be found in Singh et al. ([5]).

The nonlinearity test described in Sect. 3 was applied to these two generated series. As was expected, the results of the test shown in Fig. 3.4 correctly depict the inherent linearity of the fractional Brownian motion series and the strong nonlinearity of the random wavelet cascade series. Comparison of Figs. 3.4 and 3.2 gives more confidence to conclude the presence of linear underlying dynamics in gravel bed formation at low discharge conditions which progressively evolve to strongly nonlinear dynamics at high flow conditions (i.e., when the bed shear stress is well above the critical value for incipient motion of sediments). The complexity analysis to follow will shed more light to those conclusions.

3.4.2 Complexity and predictability

As discussed before, bed elevation fluctuations are known to exhibit multiple scales of variability (e.g., see [38, 5]) and thus the Finite Size Lyapunov Exponent (FSLE) approach is a more appropriate methodology for quantifying complexity, than is the standard maximum Lyapunov exponent analysis.

The delay time and embedding dimension adopted in the analysis of the bed elevation series for low and high discharge were chosen to be ($d = 10$ and $e = 3$) following the mutual information and false nearest neighbor approaches, respectively (see [83]), and these algorithms were implemented using the TISEAN package ([77]). Figure 3.5a displays the Lyapunov exponent for the two series as a function of the initial perturbation size $\delta = 1$ mm while Figure 3.5b shows the predictability time T_p (in seconds) for the same two series as a function of the prescribed tolerance level Δ ($\Delta = r\delta$, where

r is the so-called threshold factor and is assumed to be as $\sqrt{2}$ in this work. (For more details about the threshold factor see [67].)

The following observations are worthwhile. First, from Figure 3.5b it is observed that the high-discharge bed elevation series is less predictable (more complex) than the series at low-discharge. This is not surprising given the previous results which inferred a pronounced inherent nonlinearity in the high-discharge bed elevation series and simpler linear dynamics for the case of low discharge. It is also interesting to observe that for an initial error of δ (measurement precision) the predictability time associated to a tolerance level of the order of the coarser sediment grain size ($\propto d_{84} = 23.07$) is of the order of 2×10^2 and 4×10^3 seconds for high and low flow condition here examined, an information which can be used to assess the performance of mechanistic models of sediment transport. Second, from Figure 3.5a it is interesting to observe that for larger δ, the FSLE has a slope of -2.0, i.e., $\lambda(\delta) \propto \delta^{-2}$, a behavior consistent with that of deterministic diffusion (e.g., Aurell et al. 1997). To verify this assertion, we generated a series of equal length to the bed elevation series, using the 1-D Lagrangian map

$$x_{n+1} = x_n + asin(2\pi x_n) \tag{3.6}$$

which is a well-known model for deterministic diffusion, and performed the FSLE on this series. Figure 3.6 shows the theoretically expected behavior of the size-dependent Lyapunov exponent for this series, that is, $\lambda(\delta) \propto const$ for small values of δ, while $\lambda(\delta) \propto \delta^{-2}$ for larger values of δ. The similarity of this behavior to that of Figure 3.5a for the low-discharge bed elevation series is worth noting and calls for further exploration.

It is encouraging that for the low-discharge series the linearity inference (Figure 3.2a), the similarity to a fBm with $H = 0.5$ (compare Figs. 3.3a,b and Fig 3.4a to Fig 3.2a), and the inference that the complexity of this series is similar to that of deterministic diffusion (compare Figs. 3.5a, 3.6), are all consistent with each other. It is also encouraging that for the high-discharge elevation series, the presence of strong nonlinearity (Figure 3.2b), similar to that of a multiplicative cascade series (Figure 3.4b) and the higher complexity (lower predictability) of this series (Figure 3.5b), are consistent to each other and also consistent with the multifractal analysis results of this series in Singh et al. (2008). An interesting result is that the predictability time seems

to follow a power law relationship with the tolerance level of prediction in both low and high discharge conditions, that is

$$T_p = \Delta^{\beta} \tag{3.7}$$

where β is approximately 2 for low discharge and 1.25 for high discharge (directly quantifying the lesser degree of predictability of bed elevation series at high discharge). This relationship can be of practical significance (sets the upper limit of prediction) and should also be reproducible by mechanistic models of sediment entrainment and transport.

3.5 Concluding Remarks

The goal of this paper was to gain insight into the complexity of the processes governing the temporal evolution of gravel bed elevation by objectively analyzing series from a controlled experimental setting. Specifically, we analyzed bed elevation series under low and high discharge conditions (i.e., with a bed shear stress slightly higher or significantly higher that the critical value for incipient sediment motion) to quantify the presence of inherent nonlinearity and the degree of complexity (the higher the complexity the lesser the degree of predictability of the series). We used the phase-space transportation distance metric to quantify the presence of nonlinearity in the series and the Finite Size Lyapunov Exponent methodology to quantify complexity.

Overall, our results indicate that under higher discharge conditions, the presence of bedforms and substantial bed variability at all scales (from grain size to well-formed dunes) leads to bed elevation series whose nonlinearity and complexity is demonstrably more pronounced compared to the bed elevation series under low discharge. For low discharge conditions, in the substantial absence of bedforms, the bed elevation series was found statistically indistinguishable from a series with linear underlying dynamics and also exhibiting a behavior similar to that of deterministic diffusion. Conversely, for high discharge conditions, the temporal evolution of bed elevation was clearly nonlinear and, in fact, it showed a behavior similar to that of a multiplicative cascade process, which is extensively used to model turbulent velocity fluctuations. Given that bedforms are shaped by the near-bed turbulence which is expected to posses nonlinear and multi-scale

structure for both low and high discharge, the above results are not obvious. Instead, they highlight the complex interconnections between turbulent flow, sediment transport and bedforms and the need to analyze each series separately and in conjunction under different flow regimes to understand the effects of coupling and two-way interactions.

We consider this study as a first step towards a more comprehensive study aimed to: (a) understand the complex multiscale dynamics of bed elevation and the resulting sediment transport series; (b) make inferences about the inherent predictability, or expected upper limit to prediction, by any mechanistic model of sediment transport; and (c) parameterize this complexity in terms of macroscopic flow and sediment properties (e.g., mean bed shear stress, grain size distribution) to provide useful information for physical model development.

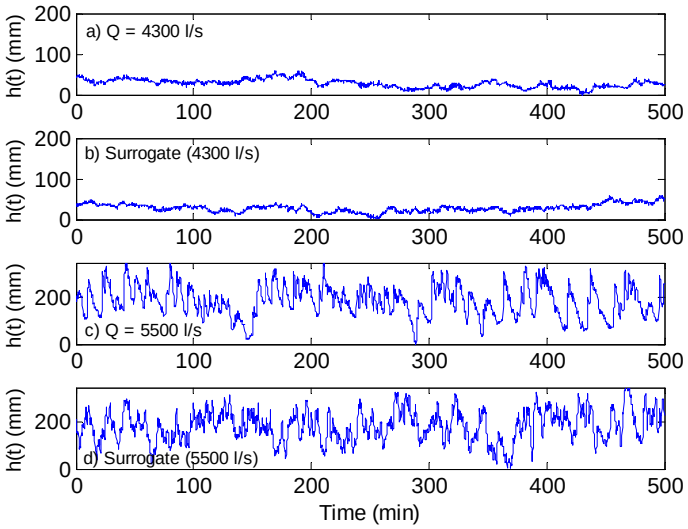

Figure 3.1: Bed elevation time series for a) low discharge (4300 l/s; bed elevation mean is 27.38 mm and standard deviation is 10.06 mm) and c) high discharge (5500 l/s; bed elevation mean is 185.51 mm and standard deviation is 66.61 mm). Surrogate series for b) low and d) high discharge. Notice that although it is difficult to distinguish any difference between the original and the surrogate series, the surrogate series in high discharge has linear underlying dynamics while the original series is shown to be highly nonlinear (see Fig. 3.2).

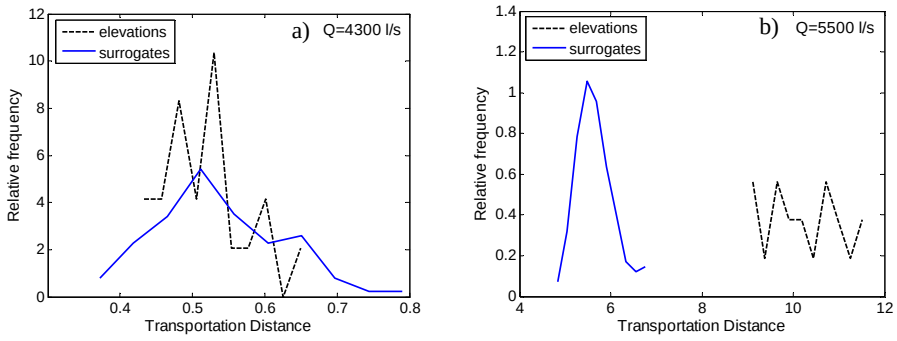

Figure 3.2: Probability density function (pdf) of the transportation distances between the original series and the surrogates (broken lines), and among the surrogates (solid lines) for a) low discharge, and b) high discharge runs. Notice the linear underlying dynamics in the case of low discharge (overlapping pdfs) and the nonlinear dynamics in the case of high discharge (distinct pdfs).

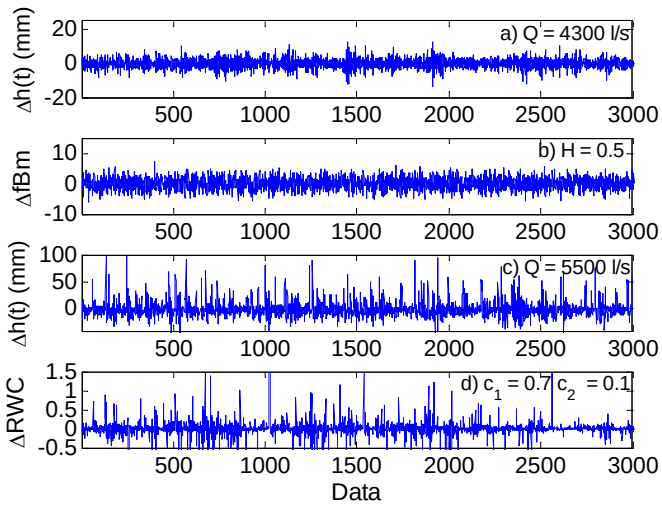

Figure 3.3: Fluctuations (first order differences) of a) measured bed elevation series for low discharge (4300 l/s), b) generated fBm series ($H = 0.5$), c) measured bed elevation series for high discharge (5500 l/s), and d) generated Random Wavelet Cascade (RWC) series with parameters $c_1 = 0.7$ and $c_2 = 0.1$.

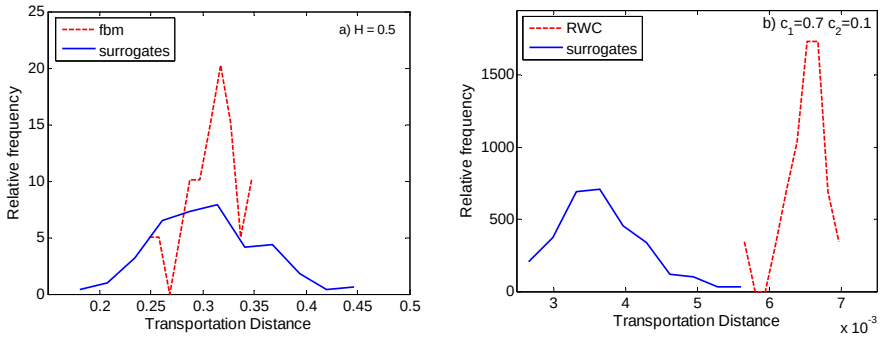

Figure 3.4: Probability density function (pdf) of the transportation distances between the synthetically generated fractional Brownian motion series (fBm) with $H = 0.5$ and the surrogates (broken lines) and among the surrogates (solid lines); b) same but for synthetically generated random wavelet cascade (RWC) series with $c_1 = 0.7$ and $c_2 = 0.1$. The comparison clearly depicts the expected linearity of the fBm series (overlapping pdfs) and the inherent nonlinearity of the RWC series (distinct pdfs). Notice the similarity with the results of Fig 3.2 which display the same analysis for the original bed elevation series at low and high discharge conditions, respectively.

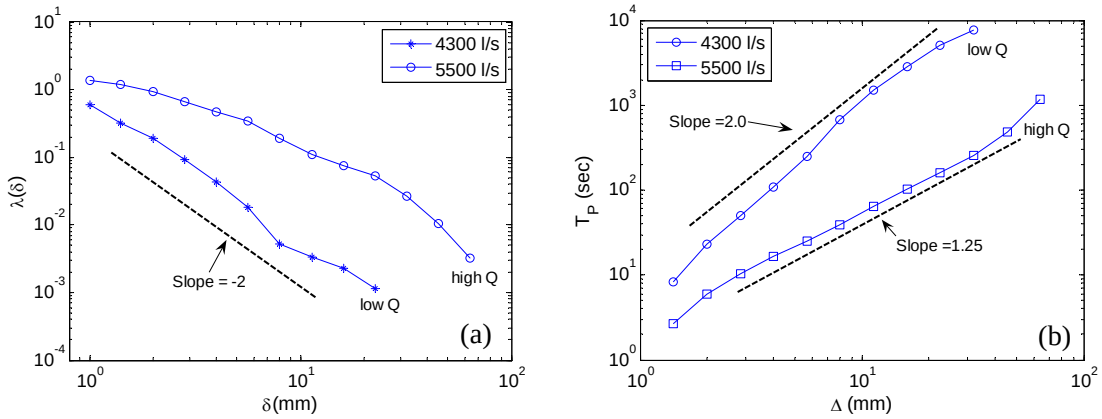

Figure 3.5: (a) Finite size Lyapunov exponent (FSLE) $\lambda(\delta)$ as a function of perturbation δ for bed elevation at low discharge (circle) and high discharge (square). The line of slope -2 (deterministic diffusive behavior) is also shown; (b) Predictability time T_p, based on FSLE, as a function of prediction error tolerance Δ for bed elevation at low discharge (circle) and high discharge (square). The initial perturbation was specified to be $\delta = 1mm$.

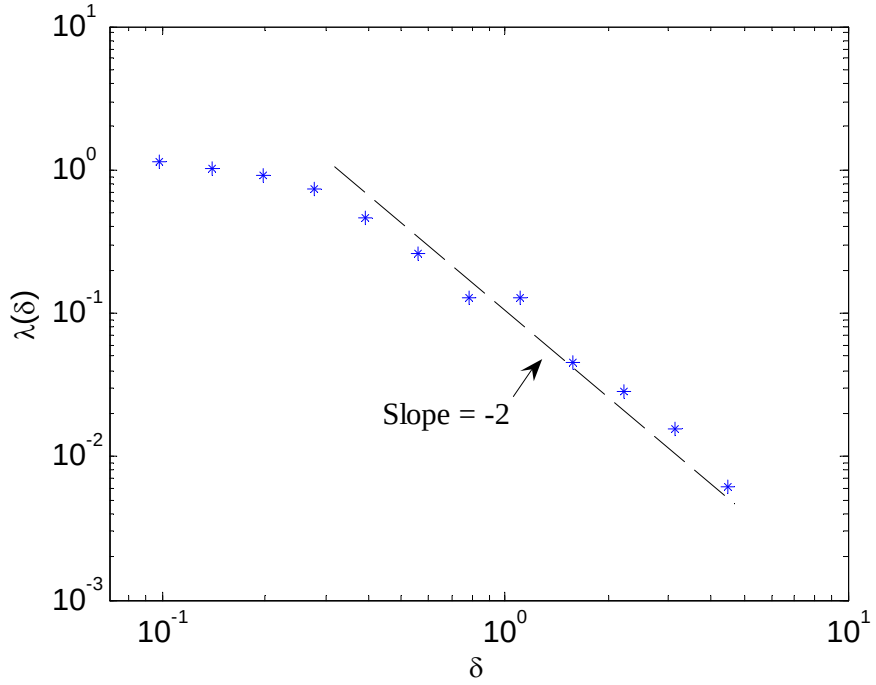

Figure 3.6: FSLE for deterministic diffusion generated by the 1-D Lagrangian map $x_{n+1} = x_n + asin(2\pi x_n)$, with a = 0.8, corresponding to a diffusion coefficient D = 0.18.

Chapter 4

On the influence of gravel bed dynamics on velocity power spectra

A series of flume experiments were conducted to study the effect of bedform dynamics on the flow over a gravel bed comprised of a wide distribution of grain sizes. Instantaneous high-frequency streamwise flow velocities were sampled using ADV at a frequency of 200 Hz, while the simultaneous bed elevations were sampled using sonar transducers at a frequency of 0.2 Hz for a duration of 20 hours. Spectral analysis of the measured velocity fluctuations reveals the existence of two distinct power-law scaling regimes. At high frequencies, an inertial subrange of turbulence with $\sim -5/3$ Kolmogorov scaling is observed. At low frequencies, another scaling regime with spectral slope of about -1.1 is found. We interpret this range as the signature of the evolving multi-scale bed topography on the near-bed velocity fluctuations. The two scaling ranges are separated by a spectral gap, i.e., a range of intermediate scales with no additional energy contribution. The high-frequency limit of the spectral gap corresponds to the integral scale of turbulence. The low-frequency end of the gap corresponds to the scale of the smallest bedforms identified by the velocity sensor, which depends on the position of the sensor. Our results also show that the temporal scales of the largest bedforms can be potentially identified from spectral analysis of low resolution velocity measurements collected near

the channel bed.

4.1 Introduction

Measurement of turbulent flow structures in a gravel-bedded environment has received considerable attention in the past few decades; yet, there is still debate about the origin and development of these flow structures and, in turn, their influence on the bed surface itself [84, 85, 86, 87, 88, 89]. It has been suggested that the initiation of gravel movement is strongly influenced by large transient coherent flow structures with time scales of about 1-10 seconds which are superimposed on the more random small-scale turbulence [10, 57, 90, 91, 92]. Over a rough boundary, such as in a gravel-bedded channel, friction created by individual gravel particles or clusters of particles (i.e., microtopography as well as bedforms) retards the flow velocity, but the effect diminishes with increasing height above the bed [88, 93]. This surface roughness creates near-bed turbulence which is responsible for entrainment of particles predominately linked to sweeps, bursts and larger coherent structures [86, 94, 95, 92, 96, 89]. These large-scale coherent flow structures are a key component of turbulent boundary layers and scale with the flow depth, h [97]. In a mobile gravel bed the size of these macro-turbulent flow structures is found to scale with h in the vertical direction and 2 to 12 times h in the horizontal direction [98, 97]. The downstream motion of these flow structures may cause quasiperiodic fluctuations of the local flow velocity components and could lead to the development of troughs and ridges on the mobile bed, inducing bed particle destabilization (sediment transport). [99, 100] investigated the turbulent flow structure over smooth and rough immobile beds and detected the existence of upwelling and downwelling circular fluid motion over the entire flow depth. They found that both the lateral and the longitudinal integral scale of fluid motion was about $2h$. [101] hypothesized that the macro-turbulent structures are closely linked to the bursting phenomena in boundary layers and do not originate in their full size ($\sim h$). According to [101] turbulent eddies are generated near the bed surface as a result of bursts with sizes much smaller than h, then grow until their size becomes approximately equal to h; they are then destroyed, prompting the generation of new smaller eddies, and so on. The complete cycle of the eddies' formation, evolution, and destruction occurs over a

distance of $\sim 6h$.

In spite of the important role that these macro-turbulent structures could play in the dynamics of rivers, there is no model that relates the interaction of turbulent flow structures to bed topography and sediment transport. This is partly due to the unavailability of long reliable records of turbulent data sampled at high-resolution and partly due to the presence of complex bed topography varying spatially and temporally in a gravel-bedded channel [102, 103]. In particular, little is known about how the relatively slow evolution of moving multi-scale topography can affect the scaling properties (e.g., spectral density) of the velocity field at different positions in the flow. For instance, [104] associated the presence of large-scale/low-frequency fluctuations of velocity, obtained from long velocity records, to migrating bedforms in gravel bed rivers. In a previous study [105] documented the passage of bedforms at periods ranging from 2 to 5 min that corresponds with velocity fluctuations. In a recent study [106] suggested that the currently used three-range spectral model (production range, inertial subrange and dissipation range) for gravel bed rivers should be further refined by adding an additional range, leading to a model that consists of four ranges of scales with different spectral behavior and should be tested with field and experimental observations. However, to resolve the potential differences in velocity spectra, for example, between fixed and weakly mobile gravel beds, much longer velocity records would be required [107].

Unlike the situation in river flows, a considerable amount of work has been performed in atmospheric boundary layer flows towards characterizing and isolating the signature of relatively slow (synoptic scale, mesoscale) variability from that of the turbulence (for examples, see [108, 109, 110]). In a classical work [108] showed a marked spectral gap between mesoscale (synoptic) and microscale (turbulent) flow variability in the analysis of large-range spectrum of horizontal wind velocity. Since then, several investigators have confirmed the existence of a spectral gap in the spectra of horizontal wind velocity over land. [111] also showed a tendency for a gap in the spectra of wind velocity measured at different heights between the surface layer and free atmosphere.

In this paper we use simultaneous high resolution long time series of bed elevations and velocity fluctuations along with longitudinal transects of bed profile measured over a gravel-bedded experimental channel to quantify the multi-scale variability of both flow structures and bed structures. Our results show the signature of bed structures

on the near-bed velocity fluctuations and point to the potential of using relatively low frequency measurements of velocity in the field to detect time scale of bed topography in real rivers.

4.2 Experimental setup and data analyzed

Experiments were conducted in the Main Channel facility at St. Anthony Falls Laboratory, University of Minnesota. These experiments were the follow-up of previous experiments conducted in spring of 2006 known as StreamLab06 [41]. StreamLab06 was an 11 month multidisciplinary laboratory channel study focused on various aspects of ecogeomorphology in gravel bed streams. Five separate projects were conducted as part of StreamLab06, while all the studies shared the same sediment and general experimental configuration. The extensive data set collected in these experiments includes hydraulic conditions (discharge, water slope, bed slope, depth average velocity, and flow field), morphological conditions (bed topography, bar locations and shapes, photo images of the bed), sediment transport characterization (continuous sediment flux, recirculation grain size information), water chemistry (temperature, dissolved oxygen, nutrient concentrations) and biological conditions (heterotrophic respiration, biomass accumulation, nutrient processing rates). For the experiments presented here (which we call Streamlab08), we focus on flow field and spatio-temporal bed topography for the discharges of 2000 l/s and 2800 l/s.

The Main Channel is a 55 m long, 2.74 m wide channel with a maximum depth of 1.8 m and maximum discharge capacity of 8000 l/s (Figure 4.1). It is a partially sediment recirculating channel while the water flows through the channel without recirculation. The sediment recirculation system is capable of entraining and recirculating particles up to 76 mm in size. The recirculation system's intake is in the bed trap below the weigh-pan system, where a horizontal auger, driven by a variable-speed motor, spans the full width of the channel. The rotating auger conveys sediments accumulated from weigh-pan dumps toward an outlet recessed in the right side of the flume and into the recirculation-pump (dredging-pump) intake. The recirculation auger speed was adjusted manually every 30 mins to maintain a constant elevation of sediment in the auger hopper and to continuously transport sediment through the recirculation pipe.

This procedure avoided sending large pulses of sediment through the pipe each time a weigh-pan dumped. Intake of the water in the channel was directly from the Mississippi River.

The bed of the channel was composed of a mixture of gravel (median particle size diameter, d_{50} = 11.3 mm) and sand (median particle size diameter, d_{50} = 1 mm). It is fluvial in nature. A total of 15% sand was added to the gravel. The final grain size distribution obtained after mixing the sediments had a d_{50} = 7.7 mm, d_{16} = 2.2 mm and d_{84} = 21.2 mm. The mean specific density of sediment of all size fractions was $\sim$ 2.65. The thickness of the bed at the start of the run was approximately 0.45 m. Figure 4.2 shows the patches of bed surface obtained at the end of the run for a discharge of 2000 l/s (Figure 4.2, left) and for 2800 l/s (Figure 4.2, right).

Prior to data collection a constant water discharge, Q, was fed into the channel to achieve quasi-dynamic equilibrium in transport and slope adjustment for both water surface and bed. Sediment transport rates were measured simultaneously during the entire course of the run. Determination of the dynamic equilibrium state was evaluated by checking the stability of the 60 min average total sediment flux at the downstream end of the test section. Using the pan accumulation data, the acquisition software computed a 60 min mean of sediment flux in all five pans. Dynamic equilibrium was reached when variation in this value became negligible. In other words, when the average of the previous 60 min of instantaneous flux values computed from the pan data stabilized, we determined the channel to be in dynamic equilibrium and proceeded with formal data collection and sampling. After attaining equilibrium, experiments ran for approximately 20 hrs. (More details about the experimental setup can be found in [5, 6]).

The data presented here are the velocity fluctuations (in the flow direction), simultaneous temporal bed elevation collected at the downstream end, and the longitudinal transects of bed profile, measured along the centerline of the channel. The continuous velocity fluctuations were measured using Acoustic Doppler Velocitimeter (ADV) at an approximate distance of 15 cm above the mean bed level. Relative heights, the ratio between D_p (distance of velocity probe from mean bed level) and D (average depth of flow), were computed to be 0.23 and 0.29 for the discharge of 2000 l/s and 2800 l/s respectively (see Table 4.1). $NortekVectrino^{+}$ ADV was used for this study. The ADV was mounted 20 cm upstream of the centrally located bed sonar (sonar 3, see Figure

4.3) and could measure 3D water velocity with a sampling frequency of 200 Hz, and a precision of +/- 1 mm/s.

For the bed elevation measurements, submersible sonar transducers of 2.5 cm diameter were deployed 0.3 m (on an average) below the water surface. These sonar transducers were mounted to the end of rigid 1.5-cm steel tubes and directed perpendicular to the bed. The transducers collected continuous temporal bed elevation information upstream of each weigh-pan. The sampling interval of bed elevation measurements was 5 sec with a vertical precision of 1 mm. Figure 4.1 and Figure 4.3 (schematic) show the setup of ADV and the sonar placed at the downstream end of the channel. Measurements were taken over a range of discharges corresponding to different bed shear stresses. Bed shear stress is often characterized in terms of the dimensionless Shields stress, τ_b^*. For steady, uniform flow it may be approximated as

$$\tau_b^* = \frac{h_R S}{R d_{50}}, \tag{4.1}$$

where h_R and S are the hydraulic radius and channel slope, respectively, and $R = 1.65$ is the relative submerged density of silica. Here we report the data collected at discharges of 2000 l/s and 2800 l/s corresponding to Shields stress of 0.058 and 0.099 respectively (for details about the hydraulic conditions see Table 4.1). (Note that for computing Reynolds number and Froude number, kinematic viscosity of water (ν), and acceleration due to gravity (g), were taken as $1 \times 10^{-6} m^2/s$, and 9.81 m/s^2 respectively). Critical Shields stress (τ_c^*) was assumed to be 0.03 as suggested by [112] and references therein. Figures 4a and 4c show the time series of velocity fluctuations (top) and the corresponding bed elevations (bottom) for discharges of 2000 l/s and 2800 l/s, respectively, collected for the duration of 20 hrs.

For the longitudinal bed profiles a three-axis positionable data acquisition (DAQ) carriage was used. This DAQ was designed, fabricated, and installed at St. Anthony Falls Laboratory. The DAQ carriage was capable of traversing the entire 55 x 2.74 meter test section and could position probes to within 1 mm in all three axes. Streamwise travel speeds of DAQ could be set up to 2 m/s. The DAQ carriage was controlled by a backbone computer that also served as the master time clock for all data collection in the study.

Because the data were collected in the fall, there were some leaves floating in the

channel which might have resulted in spikes in the velocity and bed elevation data. Even though the amount of spurious spikes in the data (0.81 percent for 2000 l/s and 0.79 percent for 2800 l/s) was found to be very small, these were removed as part of the data treatment for erroneous measurements using the methodology described in [113]. [113] used modified version of the Universal Phase-Space-Thresholding technique proposed by [114] for detecting the spikes and subsequently replacing them by the last valid data points with Sample-and-Hold technique [115].

4.3 Spectral analysis results

Power spectral density (hereafter PSD) is a commonly used tool to measure the distribution of energy (variance) in the signal across frequencies (or scales). In other words, it shows at which scales the contribution to the signal variance are strong and at which scales contribution to the signal variance are weak. For a signal $X(t)$, the power spectral density is given by

$$\Phi(\omega) = \frac{1}{2\pi} \int_{-\infty}^{\infty} R(\tau) e^{-i\omega\tau} d\tau \tag{4.2}$$

where $R(\tau)$ is the autocorrelation function defined as

$$R(\tau) = \frac{E[(X(t) - \mu)(X(t+\tau) - \mu)]}{\sigma^2}, \tag{4.3}$$

τ is the time lag, μ and σ are the mean and standard deviation of the signal respectively, and ω is the frequency. A simple way to estimate PSD is by taking the fast Fourier transform (FFT) of the signal [116, 88,]. In our case, the signal $X(t)$ is the flow velocity or the bed elevation in the streamwise direction. Special emphasis is placed here on identifying spectral scaling regimes, i.e., ranges of scales over which log-log linearity is observed in the power spectral density. (Note that the units for the velocity spectrum is $quantity^2/frequency$, i.e., m^2/s).

The power spectrum of the velocity fluctuations (measured at 200 Hz) at a discharge of 2000 l/s is shown in Figure 4.5a. Two clear scaling ranges can be observed, separated by a spectral gap. For relatively small scales (high frequencies) in the range of 0.1 sec to 0.5 sec, the slope of the PSD (power spectral density) is $\sim -5/3$, which corresponds to the inertial subrange of turbulence. A second scaling range is observed for scales between 2 min and 55 min, for which the slope of PSD is ~ -1.05. The range of

observed spectral gap is from 10 sec to 2 min (see Table 4.2). The scales from high frequency end of the spectral gap which also coincides with the integral scale of the turbulence (see the following section for discussion about ~ -1 spectral slope) to the low frequency end of the inertial subrange shows a spectral slope ~ -1. Figure 4.5b shows the PSD of the bed elevation (measured at sampling intervals of 5 sec). A clear scaling is also found in the elevation field, with a PSD slope of ~ -1.94 for the scales of 15 sec to 42 min (Table 4.2). Figures 4.6a and 4.6b show the power spectral density of the velocity fluctuations (measured at 200 Hz) and the bed elevations (measured at 0.2 Hz), respectively, for the discharge of 2800 l/s. The second scaling range (low frequency regime) in the PSD of velocity fluctuations at the discharge of 2800 l/s is shifted towards higher frequencies and is from 35 sec to 28 min with a spectral slope ~ -1.15 (Figure 4.6a). Temporal bed elevations for the same discharge show a scaling range of 15 sec to 28 min with a spectral slope of -2.1 (Figure 4.6b). Figures 4.7a and 4.8a show the spatial bed transects for the discharge of 2000 l/s and 2800 l/s respectively, measured along the centerline of the channel. The spectral slopes of spatial bed elevations are similar to those of temporal bed elevations as can be seen by comparison of Figures 4.5b, 4.7b, and Figures 4.6b, 4.8b.

4.4 Interpretation of the results and discussion

Power spectral densities of streamwise velocity have been studied extensively in the case of wall-bounded turbulent flows over flat homogeneous surfaces (e.g., [117, 118, 119]). In those flows, three scaling subranges have been identified. At low frequencies, a scaling subrange often referred to as the production subrange is found at scales larger than approximately $2\pi z$ (where z is the distance to the surface) and smaller than the integral scale of the turbulence (on the order of the depth of the flow in a channel). This range is characterized by a -1 spectral slope [120, 118]. At intermediate frequencies, an inertial subrange with a $-5/3$ spectral slope [121] is observed. It is associated with eddy scales smaller than approximately $2\pi z$. The third scaling subrange is the viscous subrange observed at smaller scales than the surface roughness size where spectra decays much faster than in the inertial subrange [122, 107].

In the case of flow over bedforms, it is expected that the turbulence will lead to

similar scaling regimes as those found in the velocity spectra calculated over flat surfaces. More specifically, one would expect to find both an inertial subrange and a production subrange, even though the transition scale between these two ranges and the slope of the production subrange are likely to be affected by the presence of the topography, which may cause eddy shedding effects [123, 87, 59].

In the hypothetical case of stationary bedforms, turbulence is the only source of velocity fluctuations and, consequently, no additional energy is introduced at scales larger than the integral scale of the turbulence (on the order of the flow depth in the channel). However, in the case of a moving bed, the evolution of the bedforms introduces additional variability in the velocity field at the range of temporal scales associated with that evolution. We set forth the hypothesis that this effect explains the existence of the second scaling range (between 2 min and 55 min for the case of 2000 l/s, and 0.5 min to 28 min for the case of 2800 l/s) in the power spectrum of velocity, as shown in Figures 4.5a and 4.6a. Notice that the largest scale in that range ($\sim$ 55 min for 2000 l/s and 28 min for 2800 l/s) corresponds to the integral scale of the measured bed elevation field presented in Figures 4.5b and 4.6b. This largest scale is the characteristic time scale at which the largest bedforms move. Also notice that the second scaling range in the velocity spectra (scaling range due to bedform migration) shifts towards the higher frequencies, right in PSD, (compare Figure 4.5a to Figure 4.6a) with an increase in discharge, suggesting that the bedforms at higher flow (2800 l/s) are moving faster than the bedforms in the lower flow (2000 l/s). The clear signature of the large-scale bedforms on the multi-scale variability of the velocity time series as captured in its PSD suggests the potential of using relatively low frequency velocity measurements near the bed to detect the characteristic time scales associated with the evolution of bed topography. The spectral analysis of our velocity measurements also shows that this scaling range is separated from the turbulence range by a spectral gap, i.e., a range of scales with virtually no additional contribution to the velocity variance.

We hypothesize that the presence of a spectral gap is due to the lack of physical processes which could support the velocity fluctuations in this frequency range. A similar spectral gap was reported in the seminal work of [108], who analyzed velocity time series collected in the atmospheric boundary layer.(Note that in that study the spectral density is plotted as $\omega S(\omega)$, while in our work it is $S(\omega)$). In that flow, the gap

separates the energy contributions associated with turbulence at the high frequencies from those corresponding to relatively slower frequency mesoscale and diurnal-cycle variability. The presence of this gap has important practical implications since it allows to separate the contribution of the turbulence from that of mesoscale motions to the total kinetic energy and fluxes. Similarly, the presence of the spectral gap in channel flows with moving bedforms should be considered when using velocity time series to study turbulent transport in these flows.

The high frequency end of the spectral gap coincides with the integral scale of the turbulence, i.e., the scale of the largest turbulent eddies present in the flow. (Note that integral sale of turbulence is computed via visual inspection from the figure of velocity spectra.) In Figures 4.5a and 4.6a, that integral scale is found at a frequency of approximately 0.1 Hz for both flow discharges under consideration. The low frequency end of the spectral gap is associated with the characteristic time scale of the smallest bedform structures that can be identified by the velocity sensor. From Figures 4.5a and 4.6a, that limit corresponds to frequencies of approximately 0.01 Hz and 0.02 Hz, for the 2000 l/s and 2800 l/s cases, respectively. This contrasts with the approximately 0.1 Hz associated with the relatively fast evolution of the smallest bedform structures, as shown in the spectral density of bed elevation (Figures 4.5b and 4.6b).

It is important to note that the size of the smallest features detected by the velocity sensor and, as a result, the width of the spectral gap, should depend on the distance from the sensor to the bed. This is consistent with results from a previous study of the multiscale wavelet correlation between surface shear stress and velocity in a flat turbulent boundary layer [124,]. That study showed that turbulent eddies of vertical size smaller than the distance to the surface z (and horizontal size smaller than $2\pi z$) that affect the surface shear stress do not produce a signature on the velocity measured at height z. With that in mind, here we speculate that the larger the distance between the velocity sensor and the surface, the larger the spectral gap. In general, the width of the spectral gap Δ_{gap} could be expressed as:

$$\triangle_{gap} = f(k, \tau_b^*), \tag{4.4}$$

where, $k = \frac{D_p}{\sigma_b}$, D_p is the distance from the probe to the mean bed level, and σ_b is the standard deviation of the temporal bed elevation (note that in our case, for both

discharges, the ratio k is constant and close to 5). In the limiting case of a deep flow (flow depth much larger than bedform variability), if the velocity sensor is placed far enough from the bed surface, above the blending height (level above which the effect of the bed surface heterogeneity cannot be detected), the spectral gap would not exist. Future research will investigate this issue through comparison of spectra from measurements collected at different distances from the bed surface and, consequently, different k ratios.

Bed elevation fields and their evolution are found to share important similarities with other natural surfaces such as landscapes. Landscapes present multiscale self-similar properties through a wide range of scales (see [125, 126, 127, 128] and references therein). In fact, [128] documented that landscapes also share important similarities with turbulence since both systems exhibit scale invariance (self-similarity) over a wide range of scales and their behavior can be described using comparable dynamic equations. This similarity can be seen, for example, in the behavior of power spectra of the landscapes which exhibit a log-log scaling range with a slope of approximately -2. Here also, we observe a slope of ~ -2 in power spectra of bed elevations for both the discharges of 2000 l/s and 2800 l/s (Figure 4.5b and 4.6b). Furthermore, [5] have shown the multi-scale behavior of bed elevations (bed topography) for different flow conditions in a gravel-bedded environment. In that study, they quantified the slope of the second order structure function $2H$ (which is related to slope of the PSD with a relation $\beta = 2H + 1$, where β is the slope of PSD, and H is the Hurst exponent), and found that it is similar to the slope obtained here in the PSD of bed elevation fluctuations (Figure 4.5b and Figure 4.6b). In the case of bedforms in gravel-bedded channels little is known about the scaling properties of bed surfaces [129, 130, 38,]. For instance [129] characterized gravel bed roughness using second order structure functions. They found that the bed elevation distribution in laboratory flumes (unworked beds) and in natural gravel-bed streams (water-worked beds) was close to Gaussian although the latter was skewed positively. They also observed that the scaling exponent (Hurst exponent) $H = 0.79$ for natural beds was significantly higher than that of unworked beds, $H = 0.5$. A similar analysis was performed in [39].

Spectral densities of the time series (Figures 4.5b and 4.6b) and of spatial transects (Figures 4.7b and 4.8b) of bed elevations are not independent of each other. Both have

a clear scaling range with slope of approximately -2, expanding over a similar range of scales (about two decades). The spatial spectra of bed elevation saturate at the same scale for both flow conditions (see Figures 4.7b and 4.8b, and Table 4.2). That scale is about 10 m and it can be interpreted as the integral scale, i.e., the characteristic scale of the largest bed forms. The temporal scales associated with these bed forms are approximately 55 min and 28 min for the 2000 l/s and 2800 l/s flows, respectively (Figures 4.5 and 4.6). Considering these integral spatial and temporal scales, it is possible to determine a characteristic travel speed of the largest bedforms. This advection velocity is approximately 14 m/hour and 22 m/hour for the 2000 l/s and 2800 l/s discharges, respectively.

Comparison of spectral densities of flow velocity and bed elevation measurements shows that relatively low-resolution velocity measurements collected near the channel bed can be used to estimate the travel time of the largest bedforms. This application can potentially be used in the field; though it would require a long time series of river flow velocities [131, 107,].

Two major priorities for further research are suggested by this work. First, a better understanding is needed of what controls the slope of low frequency velocity fluctuations in the PSD, and how it is related to the slope of PSD of temporal bed elevations and flow conditions. Second, the quantification of the dependence of length scale of the spectral gap on the Shields stress, depth-wise position of velocity measurements, and grain size distribution of the bed material should be undertaken. In order to meet these objectives, future work will be focused on the behavior of spectral density of velocity measured at different positions along the depth of the flow as a function of varying Shields stress and grain size distribution.

4.5 Conclusions

This paper investigates the behavior of power spectral density of flow velocity and bed elevation time series measured in a large-scale experimental channel under two flow conditions. The power spectral density of the velocity shows two distinct power-law scaling regimes. At high frequencies, an inertial subrange with $\sim -5/3$ Kolmogorov scaling is observed. It is associated with turbulent eddy motions of sizes smaller than

the distance from the velocity sensor to the gravel bed. For slightly larger eddy scales, up to the integral scale of the flow, the effect of the bed leads to a reduction in the slope of the velocity spectrum. At lower frequencies, another scaling range with spectral slope of approximately -1.1 is found. This range is associated with the relatively slow evolution of the multiscale bed topography. At intermediate scales, a clear spectral gap, i.e., a range of scales with no additional energy contribution, separates the turbulence and bed evolution spectral ranges. The high frequency limit of the spectral gap corresponds to the integral scale of the turbulence. The low-frequency end of the gap corresponds to the scale of the smallest bedforms identified by the velocity sensor, and it is expected to depend on measurement location and bed variability. Our results also show that the temporal scales of the largest bedforms can be potentially identified from spectral analysis of low resolution velocity measurements collected near the channel bed.

Q_w (l/s)	D(m)	v (m/sec)	S_w	h_R (m)	Shields stress (τ^*_b)	R_e	F_r	T_{mean} (^oC)	D_p (cm)	σ_b (mm)	k
2000	0.55	1.18	0.0019	0.39	0.058	646640	0.51	23.5	12.59	23.95	5.3
2800	0.64	1.55	0.0029	0.44	0.099	992000	0.62	16.23	19.17	38.65	5.0

where,

Q_w = water discharge for the run
D = average depth of flow in test section
v = average flow velocity
h_R = hydraulic radius
S_w = water surface slope
τ^*_b = dimensionless Shields stress (computed using hydraulic radius)
R_e = Reynolds number (kinematic viscosity of water, $\nu = 1X10^{-6}$ m^2/sec)
F_r = Froude number
T_{mean} = mean water temperature.
D_p = distance of the velocity probe from mean bed level
σ_b = standard deviation of temporal bed elevation series
k = ratio between D_p and σ_b

Table 4.1: Hydraulic conditions and characteristics of temporal series of bed elevation

Q_w (l/s)	Velocity v(t)			Temporal-bed elevation h(t)		Spatial-bed elevation h(x)	
	dynamic slope	scaling regime	spectral gap	spectral slope	scaling regime	spectral slope	scaling regime
2000	-1.05	2 min - 55 min	10 sec - 2 min	-1.94	15 sec - 42 min	-1.87	10 cm – 10 m
2800	-1.15	35 sec - 28 min	6 sec – 35 sec	-2.1	15 sec - 28 min	-2.06	15 cm - 10 m

Table 4.2: Characteristics of power spectrum for velocity, temporal bed elevations and spatial bed elevations

Figure 4.1: Experimental channel facility at St. Anthony Falls Laboratory, University of Minnesota showing the locations of ADV and the sonar at the downstream end of the channel. A total of seven submersible sonars were deployed. In this study the data collected from the ADV and the sonar (located 15 cm downstream of ADV) along the centerline of the channel (see also schematic in Figure 4.3) are used. The direction of the flow is from bottom to the top of the figure.

Figure 4.2: Photograph of bed surface at the end of the flow for the discharges of 2000 l/s (left), and 2800 l/s (right). The direction of flow in both cases is from the top to the bottom of the figures.

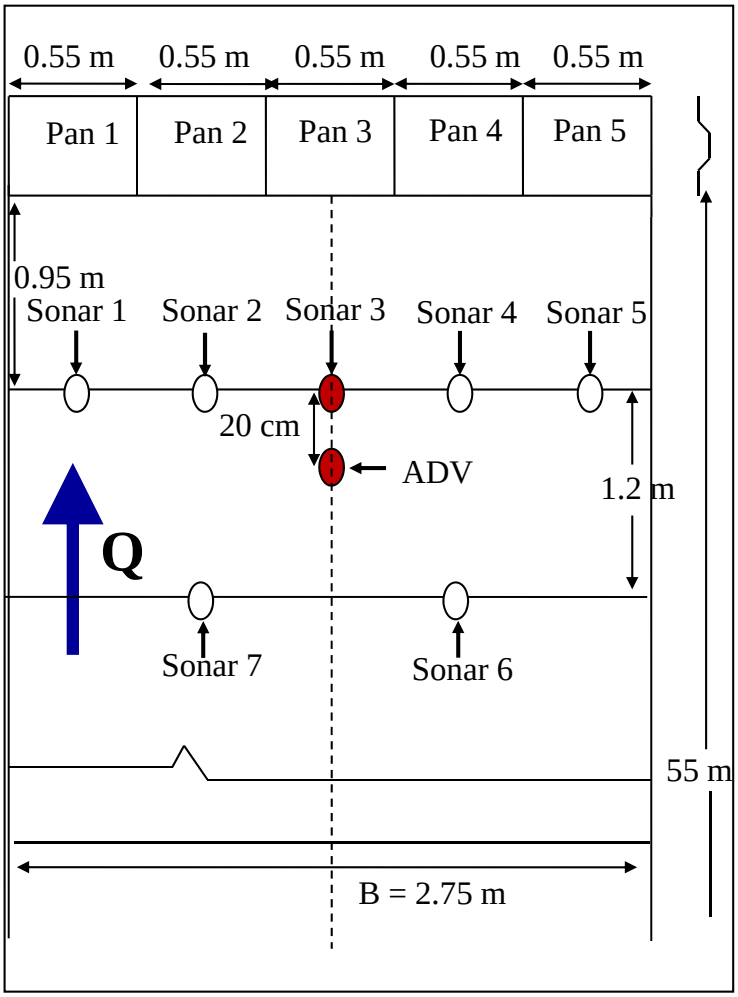

Figure 4.3: Schematic of experimental setup showing the locations of sonars (used for measuring temporal bed elevation) and the ADV (used for measuring velocity fluctuations) at the downstream end of the channel. Note that the solid dots represent the measurement locations of temporal bed elevations (h(t)) and velocity (v(t)) used in this study. The dash line represents the centerline of the channel.

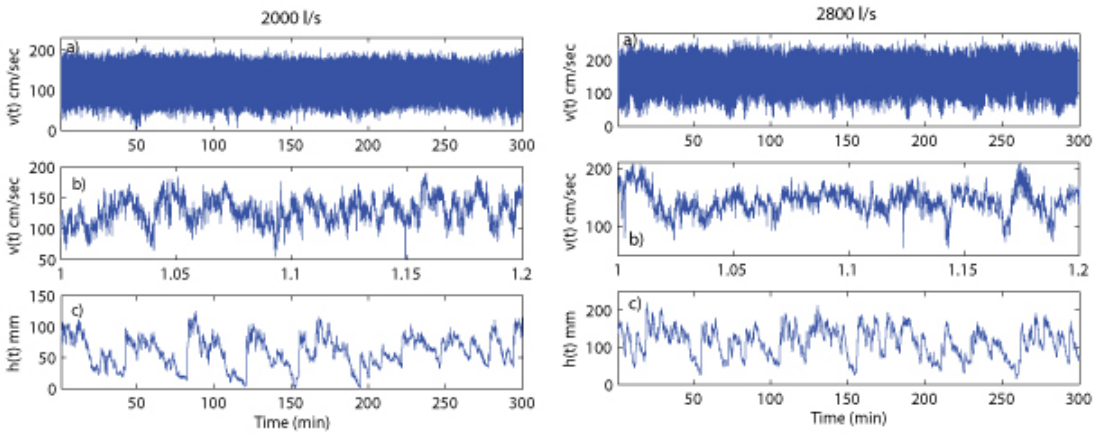

Figure 4.4: Time series of velocity (top) and bed elevation (bottom) measured at the downstream end of the channel for flow discharges of 2000 l/s (left) and 2800 l/s (right) over a duration 300 mins. The middle panels show a blown-up image of the velocity series shown in the top panels for a duration 0.2 mins. The flow velocity was measured at a frequency of 200 Hz (sampling interval, $\Delta t = 0.005$ sec) and the bed elevations were sampled at a frequency 0.2 Hz (sampling interval, $\Delta t = 5$ sec). In the case of bed elevation (bottom panel), it can be seen that short fluctuations are superimposed on larger ones. This suggests that small bedforms (small dunes, ripples or bedload sheets) are propagated over larger dunes.

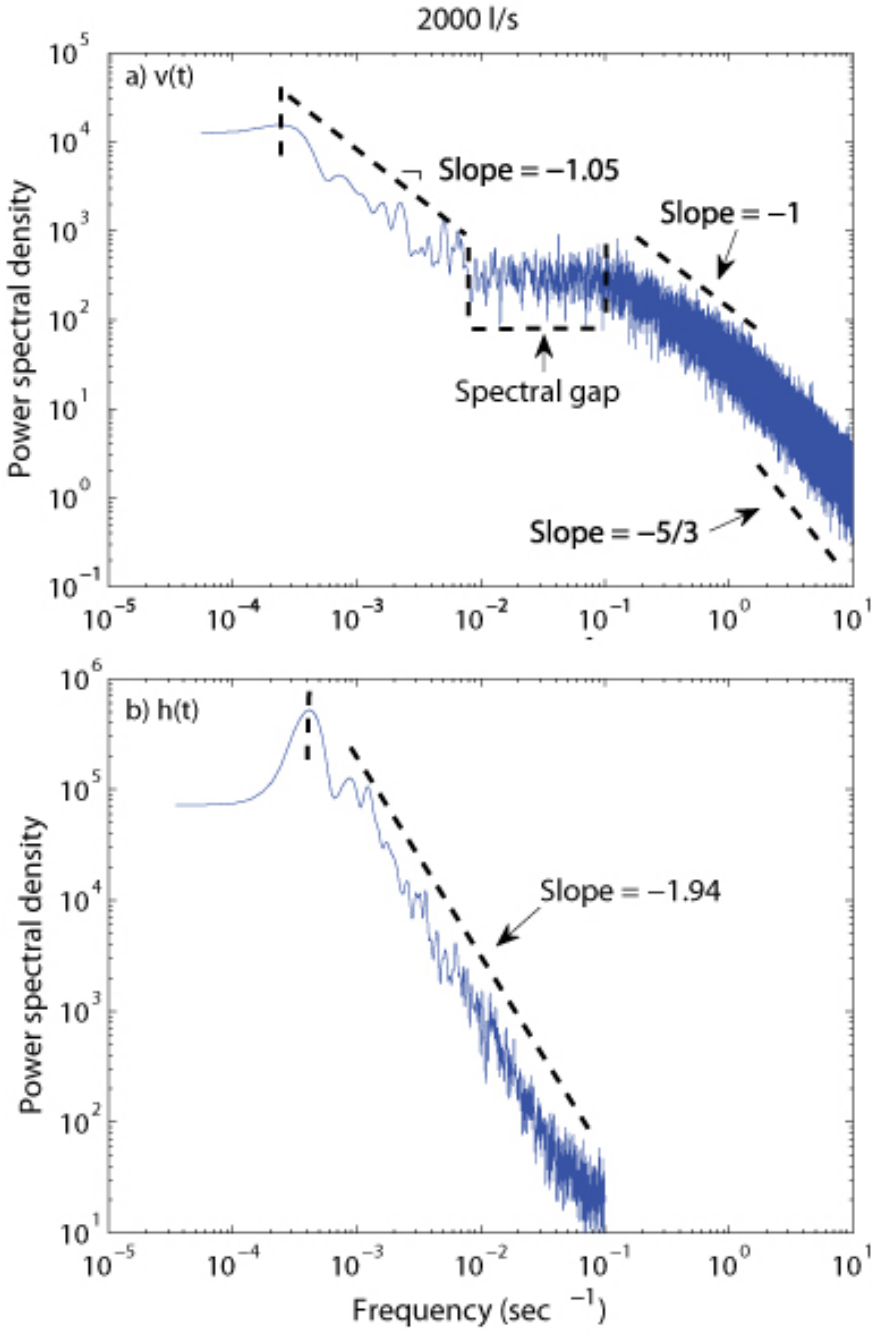

Figure 4.5: Power spectral density of a) velocity fluctuations and, b) corresponding bed elevations for a discharge of 2000 l/s. In the velocity spectrum, scaling at small scales is due to turbulence while at larger scales it is modulated by bed topography.

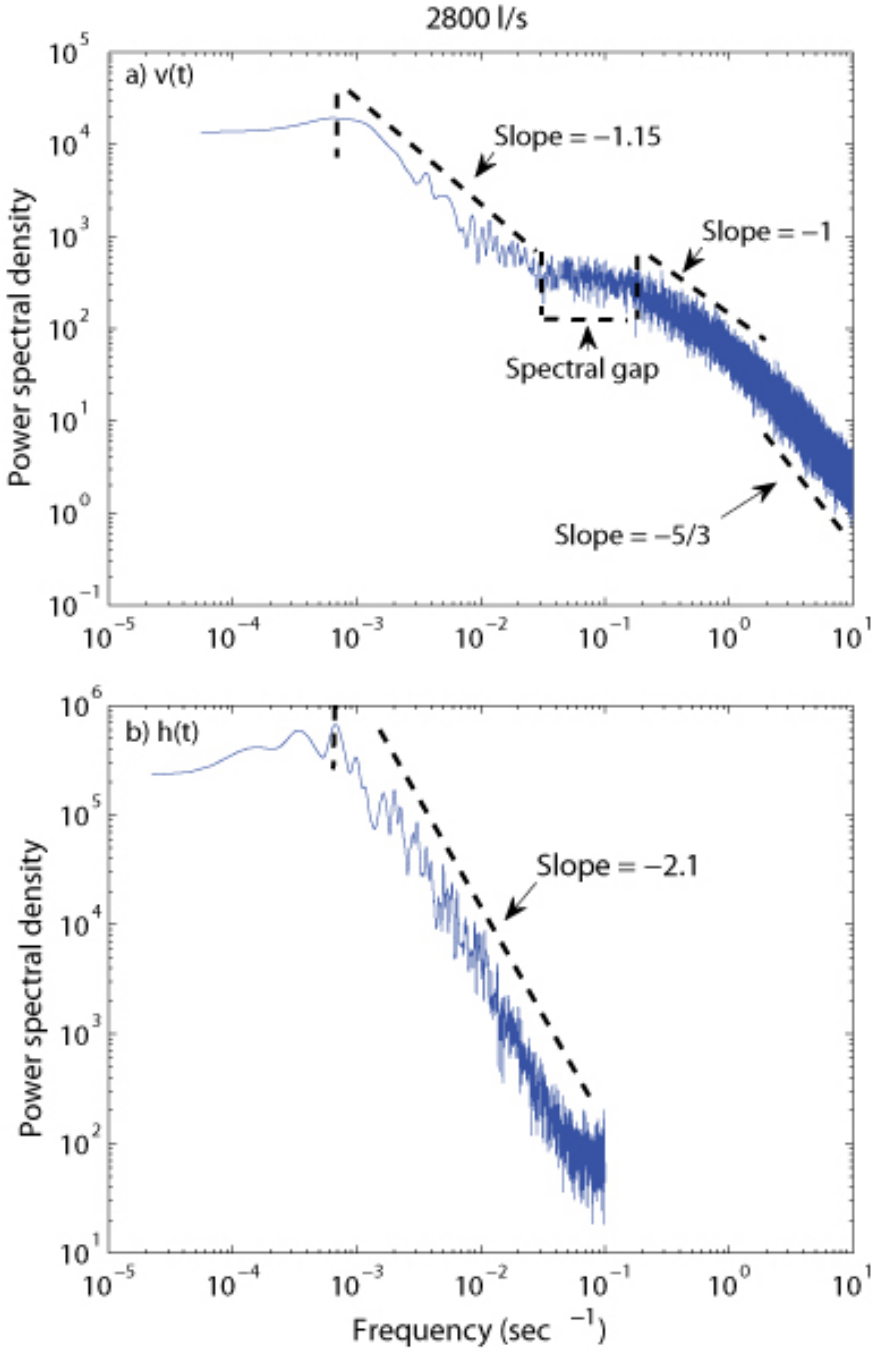

Figure 4.6: Power spectral density of a) velocity fluctuations and, b) corresponding bed elevation for a discharge of 2800 l/s. In the velocity spectrum, scaling at small scales is due to turbulence while at larger scales it is modulated by bed topography.

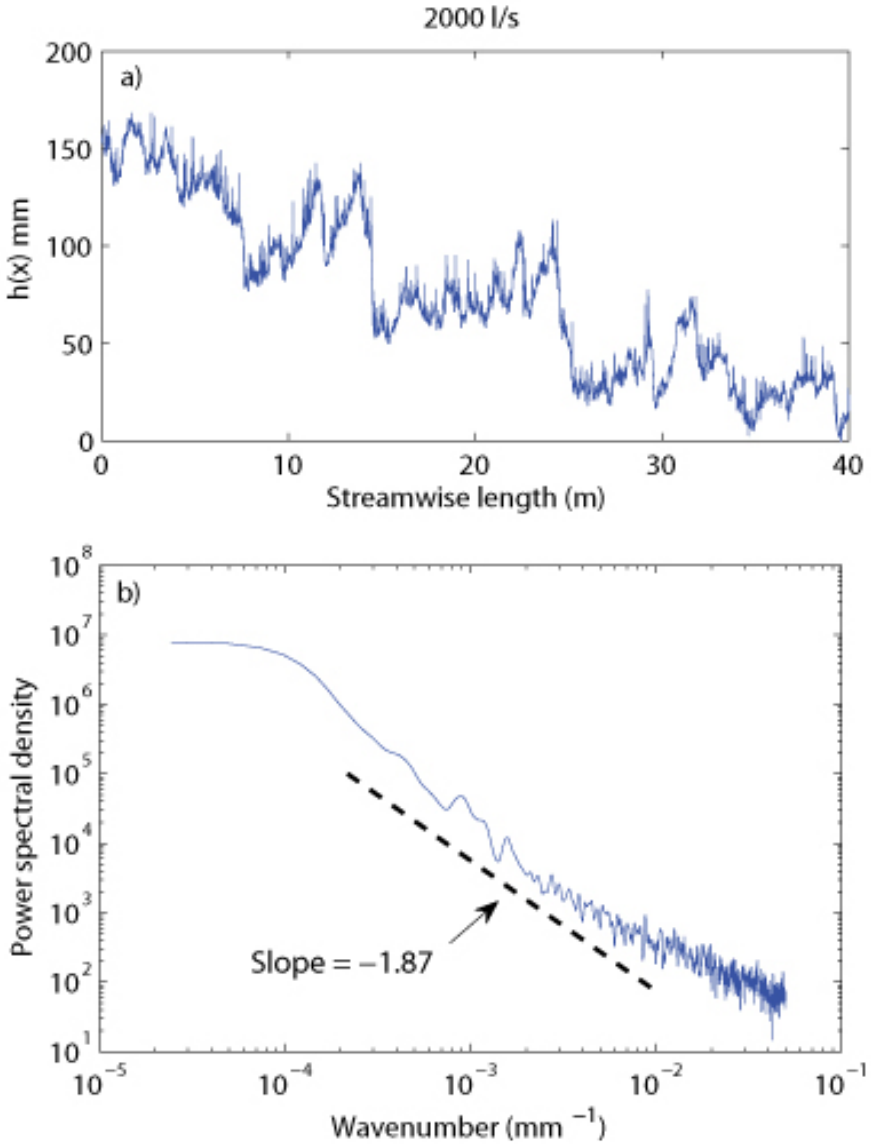

Figure 4.7: a) Longitudinal transect of bed profile elevations at a resolution of 10mm and, b)its power spectral density for a discharge of 2000 l/s. Note that similar spectral slopes are observed in both temporal bed elevation and spatial bed elevation series (compare with Fig. 4.5b).

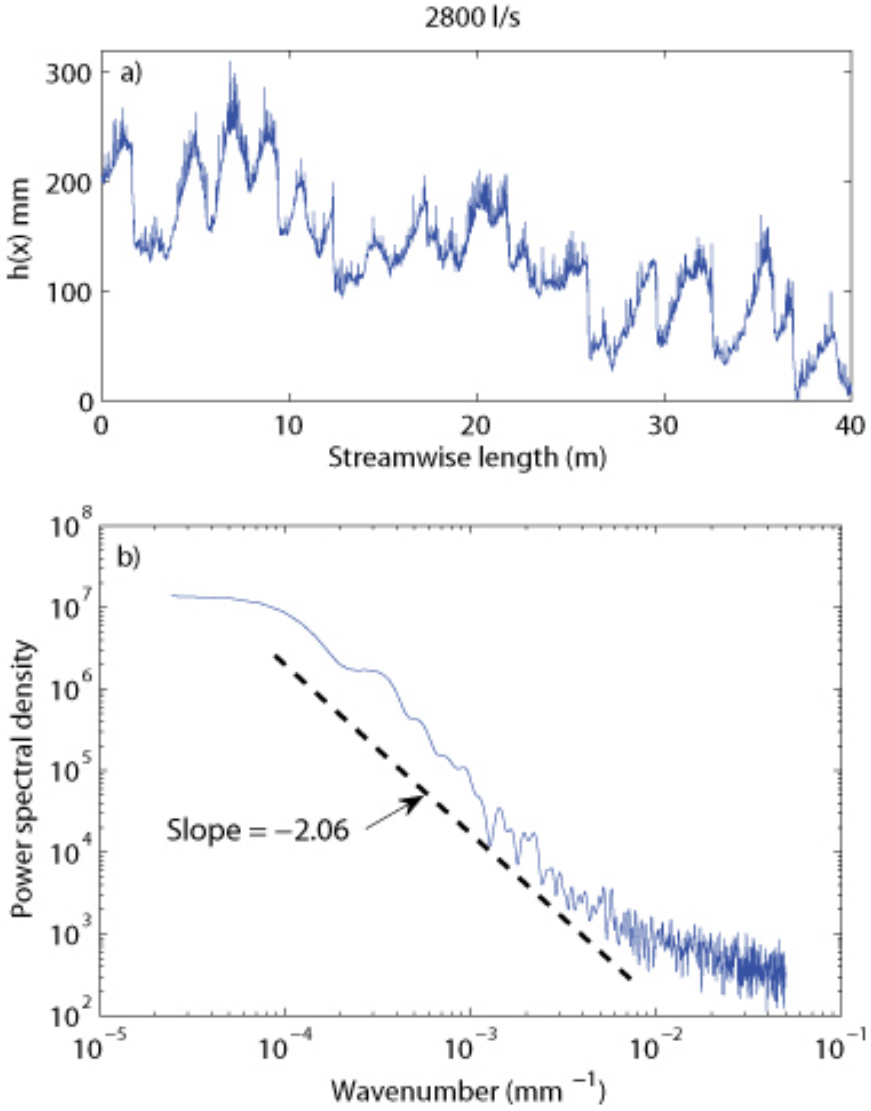

Figure 4.8: a) Longitudinal transect of bed elevations sampled at a resolution of 10mm and, b)its power spectral density for a discharge of 2800 l/s. Note that similar spectral slopes are observed in both temporal bed elevation and spatial bed elevation series (compare with Fig. 4.6b).

Chapter 5

Multi-scale statistical characterization of migrating bedforms in gravel and sand bed rivers

Migrating bedforms strongly influence hydraulics, transport, and habitat in river environments. Their dynamics are exceedingly complex, making it difficult to predict their geometry and their interaction with sediment transport. Acoustic instrumentation now permits high-resolution observations of bed elevation, as well as flow velocity. We present a space-time characterization of bed elevation series in laboratory experiments of sand and gravel transport in a large 55 m long, 2.75 m wide flume. We use a simple filtering and thresholding methodology to estimate bedform heights and report that their PDF, for both gravel and sand, is close to Gaussian with a slightly thicker positive tail. Using a wavelet decomposition we quantify the presence of a rich multiscale statistical structure and estimate the scale-dependent celerity of migrating bedforms showing the faster movement of smaller bedforms relative to the larger ones. The nonlinear dynamics of gravel and sand bedforms is also examined and the predictability time, i.e., the interval over which one can typically forecast the system, is estimated. Our results demonstrate that the multiscale dynamics, and degree of nonlinearity and complexity in bedform

evolution have a dependence on discharge as well as on bed sediment composition.

5.1 Introduction

Sediment waves often occur in alluvial rivers as the result of the complex interactions and feedbacks between the turbulent flow field, sediment transport and the cohesionless bed. Depending on the bed shear stress and sediment grain size, the river bed can in general be either plane, or covered by ripples, dunes, bars, or anti-dunes. Among these bedforms, dunes and bars are the most common and their formation and evolution have important consequences not only for river management [132], but also for the interpretation of sedimentary structure [133]. Bedform structure and dynamics is also recognized to exert considerable effects on biota and ecosystem river dynamics (e.g., [19]).

Dunes usually form in the lower flow regime (i.e., subcritical flow) and, under steady flow conditions, tend to reach a dynamic equilibrium state, whereby the average dune height, length and celerity remain approximately constant [134]. Nevertheless, observational evidence indicates that continuous splitting and merging of dunes at different spatial scales characterizes this equilibrium [132, 135, 136]. Smaller, faster migrating dunes are often observed to superimpose on larger, slower moving dunes. In some cases coalescence occurs, whereby two different dunes merge resulting in a new larger bedform [137]. Both superposition and coalescence affect the structure of the turbulent flow field, total flow resistance, and sediment transport [138, 139, 140, 141, 142]. Observations also show that in rivers, dune fields are often three-dimensional [143], implying a flow pattern significantly different and much more complex than that established over two-dimensional dunes [144, 145, 146]. Dunes can form in both sand and gravel rivers, although they are more prevalent in sand-bed systems.

Bars are observed in both sand and gravel bed rivers. They essentially consist of migrating alternating regions of scour and deposition with horizontal scales of the order of a few channel widths and vertical scales of the order of flow depth. These bars are formed as a result of a three-dimensional instability which gives rise to a stable periodic pattern [147, 148]. Both linear and weakly nonlinear theories have been developed to explain the development of these free bars in the straight channels for the case of both

bedload dominated and suspended load dominated sediment transport [149, 150, 151].

To predict the occurrence of bedforms and to characterize their geometrical properties, several approaches have been pursued to date. Empirical relationships were firstly developed on the basis of flume experiments, relating the steady state bedform features (i.e., height, length and migration speed) to physical parameters such as flow intensity, flow depth, sediment size (see, among others, [152, 153, 154]). Since the seminal work of [155], several studies making use of stability analysis techniques were carried out to determine the critical conditions for bedform formation in the space of the relevant physical parameters [156, 149, 150, 134, 157, 158, 151, 159]. More recently, increasingly refined numerical models have been developed to investigate the features of the turbulent flow field over fixed bedforms [145, 160, 161] as well as the morphodynamic evolution of these bedforms, starting from a plane bed configuration and evolving towards an equilibrium state with bedforms of different scales continuously merging and splitting [162, 163, 164, 18, 165]. These latter morphodynamic models, although simplified, yield realistic and promising results, simulating successfully, important qualitative physical features of bedform evolution, including coalescence and asymmetric geometry.

A parallel body of work has been devoted to understanding the statistical structure of bedforms at different scales. In sand bed rivers, spectral analysis of spatial and temporal bed elevation series (e.g. [166, 167, 168, 152, 169, 36, 170]) has established the presence of a broad scaling regime (log-log linear spectrum) and a scale-dependent celerity of migrating sand dunes (e.g., [171, 172, 134, 36, 173, 140, 18]). In gravel bed rivers, the statistical properties of bed elevation fluctuations have only recently been analyzed and mostly on plane beds [129, 130, 38, 39]. To the best of our knowledge, the multiscale statistical structure of migrating gravel bedforms has not been investigated before, apart from the recent work of [37] and [5, 8].

To address these goals, we focus on the multi-scale statistical characterization of bed elevation series collected at multiple locations in large-scale steady state laboratory experiments in which gravel and sand are transported by range of water discharges. We propose a filtering methodology for extracting bedforms and quantify the statistics of bedform heights in terms of their mean, variance and probability of exceedance. We compare bed elevation series at adjoining locations to document lateral variability in bedform geometry. We compare wavelet and Fourier spectra for the purpose of

estimating the scaling range and spectral slope of bed elevation series and to characterize its multifractal nature. We use cross-correlation analysis via wavelet to estimate the scale-dependent celerity of bedforms. Finally, we propose a non-linear analysis of the bed elevation series to quantify the degree of their complexity. Complexity is inversely related to predictability: a more complex series is less predictable and the results of this analysis are used to infer the upper limits of predictability and its relation to the three-dimensional elevation structure of the bedforms.

The paper is structured as follows. In section 5.2 a brief review of the experimental setup is given. Physical characteristics of bedforms are presented in section 5.3. Section 5.4 presents the results of the Fourier and wavelet spectra and the scale-dependent wavelet cross-correlation analysis which leads to the estimation of the scale-dependent celerity. In section 5.5 higher order structure functions (capturing the whole PDF) of the bed elevation increments are computed and their scaling parameterized. Section 5.6 presents a non-linear analysis of bed elevation series to quantify the complexity of bedform evolution beyond linear statistics using a phase-space representation. Finally, concluding remarks and some thoughts on the application of the described methodologies are presented in section 5.7.

5.2 Experimental set-up and data collected

5.2.1 Experimental set-up

The experiments reported here were conducted in the Main Channel facility of the St. Anthony Falls laboratory, University of Minnesota. The flume was 55 m long, 2.75 m wide and had a maximum depth of 1.8 m. The flume used water feed from the Mississippi River and was operated with sediment recirculation. The sediment recirculation system allowed continuous monitoring of the sediment transport rates. The flux monitoring system was located at the downstream end of the 55 m flume and was composed of five adjacent, identical aluminum weighpans (positioned 0.55 m apart) that spanned the width of the channel and independently measured the submerged weight of the sediment intercepted by the bedload trap. The sediment recirculation system was capable of entraining and recirculating particles up to 76 mm in size. Water discharge was measured using a sharp crested weir located 18 m downstream of the

sediment trap. Water level was continuously recorded using an acoustic sensor. The water depth within the channel was regulated by sharp crested weir, which acted as a tail gate. The maximum discharge capacity of the channel was 8000 l/s.

In the case of gravel bed experiments, the entire channel bed was covered with a 45 cm thick layer of sediment composed of a mixture of 85 percent gravel (median particle size diameter, d_{50} = 11.3 mm) and 15 percent sand (median particle size diameter, d_{50} = 1 mm). The final grain size distribution obtained in the gravel bed experiment after mixing the sediment had a d_{50} = 7.7 mm, d_{16} = 2.2 mm and d_{84} = 21.2 mm. In the case of sand bed experiments, the first 35 m of the flume consisted of a fixed concrete bed, while the remaining downstream 20 m reach of the channel was filled with a 45 cm thick layer of uniform sand with median grain size diameter d_{50} = 1 mm, d_{16} = 0.75 mm and d_{84} = 1.42 mm. In both series of experiments, the mean specific density of sediment was $\sim$ 2.65.

Prior to the data collection a constant water discharge, Q, was fed into the channel to achieve quasi-dynamic equilibrium in transport and slope adjustment for both water surface and sediment bed. The assessment of this dynamic equilibrium state was evaluated by checking the stability of the 60 min average total sediment flux at the downstream end of the channel. Using the pan accumulation data, the acquisition software computed a 60 min mean of sediment flux in all five pans. Dynamic equilibrium was assumed to be reached when variation in this value became negligible. In other words, when the average of the previous 60 min of instantaneous flux values computed from the pan data stabilized, we determined the channel to be in dynamic equilibrium and proceeded with formal data collection and sampling. Moreover, the tail gate at the end of the flume was suitably adjusted in order to ensure that the water surface and the channel bed were nearly parallel, thus minimizing nonuniform flow. After attaining equilibrium, experiments were ran for a period of approximately 15 hrs for sand bed tests and 20 hrs for gravel bed tests, during which time data were collected. More details about the experimental setup can be found in [5].

5.2.2 Data collected

The data considered here are the temporal series of bed elevations collected at several locations of the channel as well as sediment transport rates measured at the downstream

end of the channel (see Figure 5.1). The bed elevation was measured through seven stationary submersible sonar transducers of 2.5 cm diameter, mounted at the end of rigid steel tubes, of diameter 1.5 cm. The transducers were placed approximately 0.3 m above the mean bed elevation, and were directed perpendicular to the bed. The spatial locations of the sonar probes are depicted in Figure 5.1 for both the gravel (Figure 5.1a) and sand (Figure 5.1b) bed experiments. In all experiments, the first five sonars (G1 to G5 in gravel and S1 to S5 in sand) were located 0.95 m upstream of each of the five pans used to collect and weigh the transported sediment. For the gravel bed experiments, sonars G6 and G7 were located 1.21 m upstream of sonars G2 and G4, respectively (see, Figure 5.1a). In the sand bed experiments, sonars S6 and S7 were set along the centerline of the channel, at distances of 7 m and 12 m upstream of S3, respectively. Sonars sampled bed elevation every 5 sec for the gravel bed experiments and 10 sec for the sand bed experiments, with a vertical precision of $\sim$ 1 mm. The acquisition time was synchronized with that of the sediment accumulation data. In order to avoid data potentially impacted by wall effects, sonars G1, G5 and S1, S5 were not considered in the analysis, but their first order statistics (mean and standard deviation) are presented in Table 5.1. The data collected by sonar S7 in the sand bed experiments were also disregarded, owing to the upstream effects induced by the fixed concrete bed, located about 7 m (i.e., $\sim$2.5 times the channel width) upstream of S7.

Sediment transport rates were sampled through the bedload traps located at the downstream end of the channel. The weight of the sediment falling within the pans was automatically recorded every 1.1 sec. In all the experiments, the sediment was dominantly transported as bedload. More details about the data collection can be found in [5].

The experiments documented here covered a range of bedform-producing discharges. Specifically, we will consider the data collected for the discharges of 2000 l/s and 2800 l/s for gravel and 2500 l/s and 3200 l/s for the sand bed experiments. The relevant hydraulic conditions characterizing these experiments are given in Table 5.1.

5.3 Physical characteristics of bedforms

5.3.1 Three-dimensional nature of bedforms

Figure 5.2 shows the pictures of the experiments depicting the bedforms formed in the gravel bed (left) and in the sand bed (right) for the discharges of 2800 l/s and 2500 l/s, respectively. The observed gravel bedforms were transitioning from two-dimensional to three-dimensional at the discharge of 2000 l/s and were fully three-dimensional at the discharge of 2800 l/s, whereas the sand bedforms were primarily three-dimensional for both the discharges. This three-dimensionality can be appreciated from the time series of bed elevations reported in the left panels of Figure 5.3 (for gravel) and Figure 5.4 (sand), which show the simultaneously sampled bed elevations at probes G2, G3 and G4 (gravel bed) and probes S2, S3 and S4 (sand bed). Close inspection reveals a lateral variation in bedform structure. This variation can be shown by computing the difference in simultaneously sampled signals located in-line across the width of the channel. Such a plot is shown in Figure 5.5, in which the time series difference of simultaneously sampled bed elevations at the locations of probes G2, G3, and G4 and S2, S3, and S4 across the width of the channel are shown for the gravel bed experiments (top panel) and the sand bed experiments (bottom panel) for the discharges of 2000 l/s (Figure 5.5a), 2800 l/s (Figure 5.5b), 2500 l/s (Figure 5.5c) and 3200 l/s (Figure 5.5d). In the case of two-dimensional bedforms the time series of bed elevation differences should be laterally consistent. However, this is not the case in any of the bed configurations.

The gravel bed experiments, exhibiting an aspect ratio (ratio of flume width to flow depth) of 4.3 for the discharge of 2000 l/s and 5 for the discharge of 2800 l/s, were characterized by the formation of dunes and by the presence of diagonal fronts indicating the possible presence of incipient bars [147, 148] as well as sorting waves with distinct coarse fronts of one or two coarse grain height (Figure 5.2a). For the lower discharge (2000 l/s), the bed shows three dimensional, relatively small bedforms, as documented by the elevation differences of Figure 5.5a. For the higher discharge (2800 l/s), the bedform height and degree of three-dimensionality increases (Figure 5.5b). The mean bedform heights are about 5 cm and 8 cm, respectively (see Table 5.1 and discussion in section 5.3.2). These values are similar to those obtained from high resolution longitudinal profiles (not shown here) surveyed at the end of the two gravel

bed experiments. The longitudinal profiles indicate that the bedform wavelength is $\sim$ 4 m for both discharges.

In the case of the sand bed experiments, ripples were observed to coexist with dunes which were of the order of 3-5 m in length and 1-2 m in width (Figure 5.2b). In particular, Figure 5.2b suggests that in the sand bed experiments there were approximately 1-2 bedforms of characteristic size per cross-section of the channel. From Table 5.1 it can be seen that the mean bedform height increases with increasing discharge. The mean bedform height was $\sim$ 11 cm at the discharge of 2500 l/s and $\sim$ 14 cm for 3200 l/s. The issue of the number of bedform units across the channel width is strictly related to the effects exerted by the flume walls on the bedform geometry. [174] demonstrated experimentally that the aspect ratio plays an important role in bedform development. Bedform height, length and spectral width were observed to decrease as the channel width became comparable with that of the bedforms. In particular, by decreasing the width to depth ratio from 8.4 to 2.4, all the other quantities being almost unchanged, [174] found that the decrease in bedform height turned out to be of the order of 10-20 %. Moreover, channel narrowing was observed to inhibit short bedform wavelengths and imparting a strong two-dimensional character to bed features. In principle, the reproduction of the actual geometry of natural dunes then requires very large, unpractical experimental installations and, hence, field investigations, as those carried out by [36], are needed. Nevertheless, laboratory flumes provide controlled experimental conditions which usually help data analysis and interpretation. The aspect ratio attained in the present sand bed experiments is 2.2 and 2.27 for the discharges of 2500 l/s and 3200 l/s, respectively, and is similar to the smallest one investigated by [174]. The observed sand dunes then should be smaller and shorter than those attained in a larger channel. However, we note that the overall bed configuration shown in our Figure 5.2b is much more similar to that obtained by [174] for the intermediate aspect ratio (4.8), i.e., it does not exhibit a clear two-dimensional structure as that observed in [174]'s narrower channel. This suggest that, despite the low aspect ratios here investigated, the flume width is likely large enough to include at least the width of a typical bedform unit, thus implying a reduced width dependence. In particular, the observed dunes wavelength turns out to be slightly lower than those estimated according to [153] and [175] predictors, yielding a dune length of the order of 6.2-7.3 the flow depth, and therefore about

2.8-3.3 the channel width in the present sand bed experiments.

5.3.2 Extraction of bedform heights

A fundamental difficulty in studies concerning bedform dynamics is to decide on an objective method for characterizing the geometry of the various bedform units [174, 81, 175]. Figure 5.6a shows the bed elevation observed for the gravel bed experiment at the location of probe G2 for the discharge of 2000 l/s, while Figure 5.6f shows the bed elevation observed at the location of Probe S3 at a discharge of 3200 l/s for the case of the sand bed experiment (see the sketch in Figure 5.1 for probe locations). To obtain a reliable measure of bedform heights, the high frequency fluctuations associated with the presence of very small bedforms, were filtered out from the bed elevation signal $h(t)$ using the Fourier transform (Figure 5.6b,g). The local maxima and the local minima in the filtered signal were then determined (Figure 5.6c,h) and the differences between consecutive local minima and local maxima were computed. Finally, to obtain an estimate of the average bedform height, the bedform heights above a certain threshold were extracted. The threshold was assumed to be 25 percent of the maximum bedform height at that particular discharge and location [81]. Figures 5.6d,e (gravel) and 5.6i,j (sand) show the distribution of bedform heights before and after this extraction. The summary of the statistics of bedform heights for both the gravel and sand bed experiments, collected at different probe locations, are shown in Table 5.1. Figure 5.7 shows the cumulative frequency histograms of the standardized bedform heights $((h_b - \overline{< h_b >})/\overline{std(h_b)})$ for the gravel and the sand bed experiments. Interestingly, it is observed that the distribution of bedform heights does not change in shape for gravel and sand and that the tails are slightly thicker than those of the Gaussian distribution (shown for comparison in Figure 5.7).

The mean values of bedform heights reported in Table 5.1, indicate that the differences between the bedform height estimated from probes located along the same longitudinal coordinate (probes G2,G6 and G4,G7 for the gravel bed experiments and probes S3,S6 for the sand bed experiments) are at maximum of the order of 1-2 cm, except in the case of probes 1 and 5 for both gravel and sand bed experiments. Specifically, probes G1 and G5 at 2000 l/s for the gravel bed experiment and S1 and S5 at 3200 l/s for the sand bed experiment show an appreciable deviation from the mean

bedform height estimated at other probe locations, likely associated with wall effects. The spatial distribution of bedform heights provided by all the other probes suggests a substantially steady behavior of bedforms.

5.4 Scale-dependent bedform migration

5.4.1 Wavelet spectra and cross-correlation analysis

For signals that exhibit multiple scales of variability and frequency content that change with time, a localized (e.g. via wavelets) vs. global (Fourier) analysis is often insightful.

The wavelet transform of a function $h(t)$ is defined as the integral transform with a series of functions $\psi_{a,b}(t)$, i.e.,

$$W_{h(t)}(a,b) = \int_{-\infty}^{+\infty} h(t)\psi_{a,b}(t)dt \tag{5.1}$$

where the functions $\psi_{a,b}$, called wavelets, are obtained from the "mother" wavelet $\psi(t)$ by translation and scaling, i.e.,

$$\psi_{a,b}(t) = \frac{1}{\sqrt{a}}\psi(\frac{t-b}{a}); a > 0; b \in R. \tag{5.2}$$

Here a is the scaling parameter and b is the location parameter. The factor $\frac{1}{\sqrt{a}}$ is a normalizing constant chosen to ensure that the $\mathcal{L}^2$ norm is preserved (e.g. [48]; see also [49]).

For the wavelet transform to be invertible, the mother wavelet must have finite support and satisfy the admissibility condition $\int_{-\infty}^{+\infty} \psi(t)dt = 0$, i.e., it must have area under the curve zero (which makes it a kind of local differencing filter; e.g., see [48] and [49]). Wavelets with higher order vanishing moments i.e., $\int_{-\infty}^{+\infty} t^k\psi(t)dt = 0, (k = 0, 1, 2.., N-1)$, where N is the order of vanishing moment, are possible, resulting in higher order differencing filters which can remove polynomial trends from a signal. For example it can be shown (e.g., [49]) that a wavelet with N vanishing moments removes a polynomial trend of order (N-1). That is, if N=1 the wavelet acts as a first order differencing filter and removes a constant value trend; if N=2, the wavelet acts as a

second order differencing filter removing a linear trend, and so on. A commonly used mother wavelet is the family of Gaussian-based wavelets defined as the N-th order derivatives of a Gaussian function $g_0(t)$, i.e., $g_N(t) = (d^N/dt^N)g_0(t), (N = 1, 2, ..)$, where N is the order of derivative. It is noted that $g_N(t)$ has N vanishing moments and that for $N = 2$ the wavelet is the well known Mexican hat wavelet removing a piecewise linear trend from the signal. In this study, the fluctuations of bed elevations at various scales were computed (equation 5.1) using the Mexican hat wavelet $g_2(t)$

$$g_2(t) = \frac{2}{\sqrt{3}}\pi^{-1/4}(1 - t^2)e^{-t^2/2}. \tag{5.3}$$

It is important to note that the wavelet transform provides a localized decomposition of the signal as opposed to the Fourier transform which is a global filtering operation. As such, the relative contribution of the signal energy contained at a specific scale a and location b is given by the two-dimensional wavelet energy density function

$$E(a, b) = |W_{h(t)}(a, b)|^2. \tag{5.4}$$

A plot of $E(a, b)$ is known as the scalogram. Integrating over all locations b, one obtains the wavelet power spectrum

$$WS_{h(t)}(a) = \int_{-\infty}^{+\infty} |W_{h(t)}(a, b))|^2 db. \tag{5.5}$$

One can convert the scale dependent wavelet energy spectrum into a frequency dependent wavelet energy spectrum $WS_{h(t)}(f)$ in order to compare it with the Fourier spectrum of the signal. To do this, we assign to the scale a a characteristic frequency which is typically the bandpass center of the wavelet's power spectrum. For the Mexican hat wavelet, the band pass frequency at scale a is $f_c = 0.251/a$ (see Figure 5.8 and also [3]). Due to the frequency distribution within each wavelet, the wavelet spectrum is smeared compared with the Fourier spectrum. At the same time, the wavelet filter interrogates the signal locally and as such it correlates its shape with specific local features of the signal making it a more accurate metric for the energy distribution over scales (frequencies) [176, 177]. A comparison of the Fourier and wavelet spectra for the bed elevation series will be demonstrated in the next section.

Cross-correlation analysis enables the statistical determination of the degree of waveform similarity between two stationary time series. The cross-correlation coefficient provides a quantitative measure of the linear dependence between two signals as they are progressively shifted in time with respect to each other. A standard two point cross-correlation between two signals, $h_1(t)$ and $h_2(t)$, is defined as

$$C_{h_1,h_2}(\Delta t) = \frac{E[(h_1(t) - \overline{h_1(t)})(h_2(t+\Delta t) - \overline{h_2(t)})]}{\sigma_{h_1(t)}\sigma_{h_2(t)}} \tag{5.6}$$

where t is the time, Δt is the time lag, $\overline{h_1(t)}$ and $\overline{h_2(t)}$ denote the mean value, and $\sigma_{h1(t)}$ and $\sigma_{h2(t)}$ denote the standard deviation of $h_1(t)$ and $h_2(t)$, respectively.

For two bed elevation time series observed at distance L apart, the standard cross-correlation analysis can be used to estimate the average bedform celerity using the time lag that results in the maximum correlation between the two series (assuming that peak correlation captures, in a statistical sense, the passage of the same bedform). The bedform celerity (velocity) can then be estimated as $v_c(a, \Delta t) = L/\Delta t_{max}$, where a is the scale (wavelength of bedform), L is the distance between the two probes, and Δt_{max} is the Δt such that $C_{h_1,h_2}(\Delta t_{max}) = max[C_{h_1,h_2}(\Delta t), \forall \Delta t]$.

Since bed elevation series are known to contain energy (variability) at multiple scales, cross-correlation analysis at multiple scales is expected to offer valuable insight. The most efficient way to perform such an analysis is via wavelets.

The wavelet cross-covariance between two signals $h_1(t)$ and $h_2(t)$ can be computed as:

$$WCC_{h_1,h_2}(a, \Delta t) = \int_{-\infty}^{+\infty} W_{h_1}(a, b) W_{h_2}(a, b + \Delta t) db \tag{5.7}$$

where $W_{h_1}(a, b)$ and $W_{h_2}(a, b + \Delta t)$ are the wavelet coefficients of $h_1(t)$ and $h_2(t)$ respectively at scale a and two adjacent locations b and $b + \Delta t$, respectively. The wavelet cross-correlation can be obtained by appropriate normalization by the variance of the signals. This wavelet cross correlation can then be used to estimate the bedform celerity as a function of scale as demonstrated in the next section.

5.4.2 Scale-dependent gravel bed topography

Wavelet spectra: Various studies (e.g. [129, 130, 38, 39, 5, 8] have reported the scaling properties of gravel bed topography using spectral analysis or structure function analysis i.e., analysis of the statistical moments of bed elevation increments at different scales. The scaling exponent $2H$ of the second order structure function (variance of increments) relates to the spectral slope β via the relationship $\beta = 2H + 1$, where H is the so-called Hurst exponent. [129] found that the scaling exponent $H = 0.79$ for natural beds was significantly higher than for unworked beds, $H = 0.5$. Spectral slopes in gravel bed topography series have been reported to be of the order of $\beta = 1.9 - 2.2$ (e.g., [8]).

As discussed in section 5.4.1, the wavelet transform of a signal provides a local interrogation of the frequency content of the signal at different scales. At each scale a, by integrating over all locations the squared magnitude of the local wavelet coefficients (equation 5.5), one depicts the energy of the signal over a range of frequencies centered around a bandpass frequency which depends on the scale a and the chosen wavelet (e.g. $f_c = 0.251/a$ for the Mexican hat wavelet used in this study). Thus the wavelet spectrum is smoother than the Fourier spectrum and for signals with frequency content which evolves over time it provides a better measure of the variance attributed to localized events of a given frequency compared to the Fourier spectrum which assumes that features of that frequency are uniformly distributed throughout the signal.

Figure 5.9 shows a comparison of the Fourier and wavelet spectra for bed elevations recorded at probe G2 at the discharge of 2000 l/s for the gravel bed and probe S3 at the discharge of 3200 l/s for the sand bed experiment. The smoother nature of the wavelet spectrum is clearly observed allowing for a more robust estimation of the spectral slope and also a more robust identification of spectral regime transitions, as for example seen in the sand bed spectrum for very high frequencies (see Figure 5.9d).

Figure 5.10 shows the wavelet spectra of gravel bed elevations measured at the location of probes G2, G3, G4 and G7 for discharges of 2000 l/s (left panel) and 2800 l/s (right panel). A clear scaling range (log-log linearity) is observed within the scales of 0.5 min to 28 min for the discharge of 2000 l/s (Figure 5.10, left panel) and 0.4 to 16 min for the discharge of 2800 l/s (Figure 5.10, right panel). In addition, the slopes of the wavelet spectrum in the scaling range, equal to ~ -1.9 and ~ -2.1 for 2000 l/s and 2800 l/s, respectively, are similar to those estimated in previous studies from

the analysis of the Fourier spectrum of bed elevation fluctuations [8]. A summary of spectral slopes and scaling ranges is given in Table 5.2.

Scale-dependent celerity: First, we consider bedform celerity determined using standard two point cross-correlation analysis. Table 5.3 shows the statistics obtained by standard two point cross-correlation analysis for the probes G2-G6 and G4-G7 for the discharges of 2000 l/s and 2800 l/s. The estimated average bedform celerities are $\sim$ 14.8 m/hr for 2000 l/s, and $\sim$ 25.6 m/hr for 2800 l/s. These values are similar to those predicted by the formula proposed by [1] for a regular sequence of triangular bedforms, migrating without deforming:

$$q_s = \frac{(1-p)V_c h_b}{2} + q_0 \tag{5.8}$$

where, V_c is the bedform celerity, q_s is the sediment transport rate per unit width, p is the porosity (here assumed to be 0.3), h_b is the bedform height and q_0 is a suitable integration constant, set to zero for a dune covered bed [1, 178, 142]. In particular, the average celerity V_c predicted by equation 5.8 on the basis of the sediment discharges measured at the central weighing pan and using the mean bedform height of 5 cm and 8.5 cm, is $\sim$ 15 m/hr for 2000 l/s, and $\sim$ 28 m/hr for 2800 l/s, respectively.

As discussed above, various researchers have documented, both numerically and experimentally, that the celerity of bedforms is roughly inversely related to bedform height, and merging of bedforms occurs due to varying migration speeds [134, 173, 18, 137, 165,]. [18] proposed a nonlinear stochastic surface evolution model to simulate bedform growth, showing that the steady state solution to the model consists of a train of bedforms. [165] used a numerical model to show that the bedform celerity decreases with increase in size of bedform geometry. These results have also been observed in laboratory and field studies (see [137], and references therein).

Cross-correlation analysis at multiple scales, carried out through wavelets, can provide greater insight into the dependence of bedform celerity on their size. The correlation between two multiscale processes (characterized by the presence of energy over a range of scale as shown in Figure 5.10) can be decomposed into correlations at multiple scales. In other words, two multiscale processes can be represented as a combination of functions at different scales. Figure 5.11 shows the decomposition of bed elevation time series at scales of 2 min and 10 min for probe G4 (top set of figures) and probe G7 (bottom set

of figures) for discharges 2000 l/s (left) and 2800 l/s (right). This decomposition of the original signals via wavelets forms the basis for the computation of the scale-dependent cross-correlation coefficients. Note that these scales (2 min and 10 min) are arbitrarily picked from within the scaling range of the power spectral density (see Figure 5.10 and Table 5.2). Also note that these filtered signals were computed using the Mexican hat wavelet and are equivalent to computing generalized second order increments.

Figure 5.12 (top panel) shows the magnitude of the maximum correlation coefficient between probes G2-G6 and probes G4-G7 as a function of scale for the discharges of 2000 l/s and 2800 l/s, respectively. The lag corresponding to the maximum correlation at each scale was computed and used for the estimation of the scale-dependent celerity. Figure 5.12 (bottom panel) shows the estimated bedform celerity (probes G2-G6 and G4-G7) as a function of scale for discharges of 2000 l/s and 2800 l/s, respectively. The plot suggests that the bedform celerity progressively decreases as the scale increases, i.e., larger size bedforms travel slower.

A few additional observations can be made from the plots of Figure 5.12. First, for very small scales (say less than 5 min) the cross-correlation coefficients are very small (order of 0.1 to 0.5) implying either decorrelation of these small features or that linear analysis does not really capture their evolution. Such small bedforms tend to be transient and are most likely to disappear or reorganize, thus preventing any correlation between the time signals measured by the two probes. For larger scales, the correlation coefficient becomes progressively larger varying in the range of 0.5 -0.95. Figures 5.12c and 5.12d show that the average velocity of small scale features is generally larger than that of larger bedforms (as expected) and that the velocity of bedforms corresponding to a time scale of order of 10 min and larger is in close agreement to that obtained via a standard cross-correlation analysis (see Table 5.3). This last result is also expected as the standard cross-correlation analysis is dominated by the larger features present in the signal, ignoring thus smaller scales.

5.4.3 Scale-dependent sand bed topography

Wavelet spectra: Spectral properties of sand bed elevation series have been studied in the past both theoretically and experimentally [166, 167, 168, 152, 169, 36, 170]. In particular, it has been found theoretically, and confirmed experimentally, that the

wavenumber spectral slope of the sand waves (computed from the spectrum of spatial bed profiles) is close to –3, in the region of large wavenumbers. On the other hand, two scaling regions with slopes –3 and –2 are have been reported for the frequency spectrum (computed from time series of bed elevations), even though contrasting results exist on the range of slopes and scaling regimes where these slopes should be attained (see [36] for discussion).

Figure 5.13 shows the wavelet spectra of sand bed elevations measured at the location of probes S2, S3, S4 and S6 for discharges of 2500 l/s (left panel) and 3200 l/s (right panel). In all probes, a clear scaling range (log-log linearity) is observed within the scales of approximately 2 min to 35 min, except 1 to 21 min for probe S6, at the discharge of 2500 l/s, and 2 to 24 min for probe S4 at the discharge of 3200 l/s (see Table 5.2 for details). The slope of the wavelet spectrum in the scaling range varies between -2.3 and -3 (see Figure 5.13). Although this range is larger than that observed in the gravel bed series, it is still within the range of slopes observed in other experimental and field studies (see for example [36] and references therein).

Comparison of the gravel and sand bed spectra provides some interesting insights. First, in the gravel bed spectra the scaling regime extends all the way to the smallest scales (highest frequency) present in the signal (Figure 5.10). However, in the sand bed spectra there is a clear transition from one scaling regime to another or simply a break in scaling at some intermediate frequency of approximately 2 min corresponding to a wavelength of $\sim$ 12 cm for the discharge of 2500 l/s with an estimated speed of 3.5 m/hr and $\sim$ 14 cm for the discharge of 3200 l/s with an estimated speed of 4 m/hr (see Figure 5.13 and Table 5.4 for celerity of bedforms). In other words, a cascade-type of energy transfer across scales (log-log linear spectrum) does not hold down to the smallest scale in sand bed elevations as it does in the gravel bed. [36] reported such a transition in scaling regime in which the higher frequency scaling regime showed –2 spectral slope whereas the lower frequency scaling regime showed a –3 spectral slope.

A second observation from Figure 5.13 is that for the sand bed elevations, the wavelet spectrum does not always saturate (level off) at low frequencies (large scales) as for example in probes S2 and S4 for the low discharge (2500 l/s). This is indicative of the presence of very large scales perceived as non-stationarities in the limited length of the signal. These large scale features are readily apparent in the series of probes S2 and

S4 at the discharge of 2500 l/s in Figure 5.4. Nevertheless, there is a clear scaling regime in all spectra from which reliable estimates of spectral slopes have been obtained and shown in Table 5.2. The transitional and three-dimensional nature of sand bedforms might be partially responsible for the wider range of spectral slopes observed in sand bedforms compared to that of the gravel bedforms.

Scale-dependent celerity: Table 5.3 shows the statistics obtained by standard two point cross-correlation analysis between probes S3-S6 for the discharges of 2500 l/s and 3200 l/s. The corresponding average bedform celerities are $\sim$ 20 m/hr and $\sim$13.5 m/hr, respectively. These values are much larger than those estimated through equation 5.8 on the basis of mean bedform height and mean sediment transport rate and also by considering the number of bedform units present in the time sequence. For example, assuming that 12 bedforms (see Figure 5.6j) are sampled in about 540 min with an average wavelength of about 4 m, implies a bedform period of about 45 min (3/4 hr). The corresponding celerity is approximately 5 m/hr, quite close to the mean value of 4.2 m/hr predicted by the equation 5.8. This inability of cross-correlation to estimate correctly bedform celerity is related to the relatively large distance (7 m) between probes S3-S6 (see Figure 5.19 in the appendix). Clearly, cross-correlation analysis cannot capture the evolution of bedforms much smaller than this distance. Moreover, the distance between probes is also too large to give reliable information on the migration of even the largest dunes, which were observed to undergo significative deformations as they move downstream. These deformations are responsible for the low correlation coefficients (of the order of 0.4-0.5 for the largest scales) compared to the corresponding 0.9 correlation coefficient observed in the gravel bed experiments (see Figure 5.12). Unfortunately cost and logistics precluded us from repeating these sand experiments, an issue that we plan to address in future.

5.5 Scale-dependent statistics of bed elevation increments

5.5.1 Higher order structure function analysis

In order to investigate the multi-scale structure of the bed elevation series $h(t)$ over a range of scales, a higher order statistical analysis can be performed on the bed elevation

series. For that purpose, one can use the wavelet coefficients at different scales as computed earlier via the Mexican hat wavelet, or simply use the bed elevation increments, $\Delta h(t, a)$ defined as:

$$\Delta h(t, a) = h(t + a) - h(t) \tag{5.9}$$

where t is the time and a is the scale. Notice that while $h(t)$ can only be positive (since $h(t)$ is computed with reference to the lowest bed elevation i.e., the global minimum), the increments $\Delta h(t, a)$ can be both positive and negative, and in fact they have a zero mean. Using first order increments defined as above is equivalent to using the simplest wavelet (Haar wavelet) and it is warranted to remove piecewise constant trends from the series. We note that we have performed the analysis using different wavelets with no appreciable difference in the results, so we resort here to reporting the results of the first order increments analysis as also done in [38].

The estimates of the q^{th} order statistical moments of the absolute values of the increments at scale a, also called the partition functions or structure functions $M(q, a)$, are defined as:

$$M(q, a) = \frac{1}{N} \sum_{t=1}^{N} |\Delta h(t, a)|^q \tag{5.10}$$

where N is the number of data points of the series at scale a. The statistical moments $M(q, a)$ for all q completely describe the shape of the probability density function (PDF) of the increments at scale a. Statistical scaling, or scale invariance, requires that $M(q, a)$ is a power-law function of the scale, that is:

$$M(q, a) \sim a^{\tau(q)} \tag{5.11}$$

where $\tau(q)$ is the so-called scaling exponent function. For most processes the non-linear relationship describing $\tau(q)$ with q can be parameterized as a polynomial, and the simplest form is a quadratic approximation:

$$\tau(q) = c_1 q - \frac{c_2}{2} q^2 \tag{5.12}$$

The multi-scale analysis in this framework provides a compact way, using two parameters c_1 and c_2, of parameterizing the change of the PDF over a range of scales. The

parameter c_1 is a measure of the average "roughness" of the series (akin to the Hurst exponent H) and c_2 is the so-called intermittency parameter. A value of c_2 different than zero implies that the tails of the distribution stretch differently than the body as one changes scale. Following the geometrical interpretation of the statistical scaling (e.g., [34], see also [47]), the parameter c_2 relates to the local roughness or degree of differentiability of the signal, as measured by the local Hölder exponent h. A value of $c_2 \neq 0$ implies a temporarily or spatially inhomogeneous arrangement of spikes and thus the presence of a distribution $D(h)$ of local Hölder exponents h as opposed to a single value of H for a simple scaling process. In other words, the signal contains pockets of high fluctuations arranged over its domain in such a way that they manifest statistically in complicated ways.

5.5.2 Scale-dependent PDF of bed elevation increments

Most studies to date have concentrated on characterizing the PDF of bed elevation "fluctuations around the mean". Mean-removed elevations are meaningful in plain beds for which the mean bed elevation can be approximately defined, and have been reported to be approximately Gaussian (e.g., [179]). However, in the presence of bedforms, bed elevation increments rather than "fluctuations around the mean", are more meaningful for statistical analysis as differencing removes non-stationarities (due to bedforms) rendering the increment series stationary and amenable to statistical analysis. (Note that, following the turbulence terminology the increments as defined in equation 7.4 were called "fluctuations" in [5]. Here we will use the terms "increments" and "fluctuations" interchangeably and in contrast to the "fluctuations around the mean".) To the best of our knowledge, the PDFs of gravel and sand bed elevation increments have not been explicitly reported before although their statistical moments have been characterized via structure function analysis (e.g. [36, 129, 130, 38, 39, 5]).

Figure 5.14 shows the semilog PDFs of the bed elevation increments for the gravel bed (Figure 5.14, top panel) and sand bed (Figure 5.14, bottom panel) elevations. These PDFs were computed from the bed elevation recorded by probe G3 for discharges of 2000 l/s (Figure 5.14a) and 2800 l/s (Figure 5.14b) and by probe S3 for discharges of 2500 l/s (Figure 5.14c), and 3200 l/s (Figure 5.14d). Similar PDFs have been obtained from the bed elevation sampled at other probe locations and for brevity are not shown

here. The PDFs were computed at the scales of 0.5 min, 2 min, and 5 min for the gravel bed experiments and 1 min, 5 min, and 10 min for the sand bed experiments. These scales were arbitrarily chosen from within the scaling range obtained from the structure function analysis of bed elevations (see Table 5.2 and discussion in the next few paragraphs). The PDFs at all scales have heavier tails than a Gaussian PDF (solid line in Figure 5.14). However, on close inspection one can see that the PDFs of bed elevation increments tend to become thinner tailed at larger scales as can be seen more clearly from Figure 5.15, showing the log-log plots of the probability of exceedance of the positive bed elevation increments ($\Delta h(t) > 0$) measured through probe G3 (top panel) and probe S3 (bottom panel) for a discharge of 2000 l/s (Figure 5.15a) and 2800 l/s (Figure 5.15b) for the gravel and 2500 l/s (Figure 5.15c) and 3200 l/s (Figure 5.15d) for the sand bed experiments. This behavior is similar to that experienced by turbulent velocity fluctuations: at smaller scales (close to Kolmogorov scale) the PDFs of the velocity fluctuations are stretched exponential, whereas they tend to become Gaussian at larger scales (close to the integral scale)[34, 180]. The change in PDF shape over different scales implies the presence of multi-fractality in the signal and is typically interpreted in the context of a multiplicative process distributing energy across scales [180].

Structure function analysis, as described in sections 5.5.1, was performed on the bed elevation time series shown in Figures 5.3 and 5.4. Figures 5.16 and 5.17 (top panels) show the scaling of the moments of the bed elevation increments $\Delta h(t, a)$ as a function of scale a for gravel bed experiments (probe G3, discharges of 2000 l/s and 2800 l/s), and sand bed experiments experiments (probe S3, discharges of 2500 l/s and 3200 l/s). Note that these plotted moments are offset vertically (along the y axis) for better visualization. For the gravel bed experiment, the structure functions follow power-law scaling over a range of 0.5 to 10 min for the discharge of 2000 l/s and 0.4 to 7 min for the discharge of 2800 l/s. For the sand bed experiment, the structure functions follow a power-law relation with scale a, over a range of scales from 1 to 32 min and 1 to 28 min for the discharge of 2500 l/s and 3200 l/s, respectively (see Figure 5.17). A summary of scaling ranges for the other probe locations at different discharges for both gravel and sand bed experiments can be seen in Table 5.2.

Figures 5.16 and 5.17 (bottom panels) show the computed $\tau(q)$ curves from the

slopes of the moments shown in Figures 5.16 and 5.17 (top panels) within the scaling range, respectively. We see that the $\tau(q)$ curves have a nonlinear dependence on q, indicating the presence of multi-fractality for both gravel and sand bed experiments for all the discharges. The parameters of multifractality (for all locations and discharges considered in the previous analysis) were calculated by approximating the $\tau(q)$ as a quadratic function in q and are shown in Table 5.2. Note that for brevity we have plotted the structure functions and the $\tau(q)$ curve for probes G3 and S3 only for both the discharges and bed configuration; however the multifractality parameters c_1 and c_2 of the other probes (probes G2, G3, G4, G6 and G7 for gravel bed experiments and probe S2, S3, S4 and S6 for sand bed experiments for all the discharges considered in this study) are reported in Table 5.2 along with their scaling range.

Several observations can be made from the multifactal properties of the bed elevations shown in Table 5.2 for gravel and sand bed experiments. In general, the intermittency parameter, c_2, is larger in the case of gravel bed elevation than sand bed elevation, suggesting a more inhomogenous arrangement of the various strength singularities or abrupt bed elevation fluctuations over time in the gravel bed compared to the sand bed. This is consistent with the presence of sorting waves and grain clusters present at scales between the grains and the dunes. On the other hand, the roughness parameter c_1 is smaller in the case of gravel bed experiments than sand bed experiments, suggesting that sand bed elevation fluctuations are smoother than gravel bed elevation fluctuations. Also, in comparing the scaling range of structure functions, the scaling range is much smaller in the case of gravel bed (of the order of 1-10 min, on an average) than the scaling range in the sand bed (of the order of 1-30 min, on an average) experiments.

5.6 Nonlinearity and Complexity in bedform dynamics

Many natural systems, although deterministic, exhibit a limited degree of predictability due to complex nonlinear dynamics which amplifies small perturbations and leads to chaotic behavior (e.g., [78]). Simply put, two points infinitesimally close to each other grow apart as the system evolves and the rate of exponential growth of their trajectories can be used as a measure of the nonlinear complexity or lack of predictability in the system. Let us consider the bed elevations $h(t)$ as a dynamical system with an evolution

law given by the differential equation

$$\frac{dh}{dt} = F(h) \tag{5.13}$$

or in the case of discrete time by

$$h(t+1) = G(h(t)) \tag{5.14}$$

Note that the state of the system $h(t)$ can be replaced by a vector $\mathbf{h}(t)$, i.e, be augmented to include elevations at previous times, such that $\mathbf{h}(t)$ uniquely specifies the state of the system. (Here we will denote the state of the system simply as $h(t)$). Non-linear dynamical system analysis studies the separation between two trajectories $h(t)$ and $h'(t)$ starting from two close initial conditions $h(0)$ and $h'(0) = h(0) + \delta h(0)$, respectively. As long as the difference between the trajectories, $\delta h(t) = h'(t) - h(t)$ remains small (strictly speaking infinitesimal), a standard indicator of the behavior of such a dynamical system with respect to the asymptotic evolution of an infinitesimal perturbation is the maximum Lyapunov exponent λ_{max}, i.e.,

$$|\delta h(t)| \sim |\delta h(0)| e^{\lambda_{max} t}. \tag{5.15}$$

That is, if $\lambda_{max} > 0$ one has a rapid (exponential) amplification of an error on the initial condition. In such a case, the system is chaotic and unpredictable at long times. Indeed, if we put $\delta = |\delta h(0)|$ for an initial error and want to predict the state of the system with a certain tolerance Δ, the prediction is possible only up to a predictability time given by

$$T_p \sim \frac{1}{\lambda_{max}} ln \frac{\Delta}{\delta}. \tag{5.16}$$

This equation shows that T_p is basically determined by the maximum Lyapunov exponent since its dependence on δ and Δ is very weak. It is emphasized that the above formula holds only for infinitesimal perturbations, and, by construction, it cannot assess the predictability in systems with many scales of variability, such as turbulence or bed elevation fluctuations, which possess a hierarchy of scales. In those multiscale systems the predictability time T_p is determined by the nonlinear mechanism responsible for the error growth of finite size perturbations. As such, it is not captured by λ_{max} which

pertains to the linearized equations of motion, under the assumption of infinitesimally small perturbations. To address these issues, [79] proposed a generalization of the maximum Lyapunov exponent method. Specifically, they introduced the quantity $T_p(\delta, \Delta)$ which is the time it takes for a finite perturbation to grow from an initial size δ (in general not infinitesimal) to a tolerance level Δ. The so-called Finite Size Lyapunov Exponent (FSLE) $\lambda(\delta)$ is then the average of some function of this error growing time n_r (time for a perturbation of initial size δ to grow to a size $\delta(n_r)$):

$$\lambda(\delta) = \langle \frac{1}{n_r} \rangle ln[\frac{\delta(n_r)}{\delta}] \tag{5.17}$$

In this case the average predictability time can be written as:

$$T_p(\delta, \Delta) = \int_{\delta}^{\Delta} \frac{dln\delta'}{\lambda(\delta')} \tag{5.18}$$

Various methodologies are available for computing finite-size Lyapunov exponents (see [67]). In the present contribution we have adopted the method of [80, 69] (see also [70] and [6]). There are two parameters that need to be determined for the computation of the FSLE. These are the delay time (d) and the embedding dimension (e). The delay time ensures the removal of linear auto correlation in the series by considering values that are further than the decorrelation distance. The embedding dimension is the dimension of the space where the times series is projected for assessing the evolution of the trajectories of nearby "points" in that projection space (called the phase space) as time evolves. The delay time d and embedding dimension e adopted in this analysis of the bed elevation series for both discharges and materials (gravel and sand) were chosen to be $d = 10$ and $e = 3$ following the mutual information and false nearest neighbor approaches, respectively (see [83, 6]). The estimation of d and e and the computation of the FSLE were performed using the TISEAN package [77], a set of algorithms available online for analyzing nonlinear time series which includes data representation, prediction, noise reduction, dimension and Lyapunov exponent estimation, and nonlinearity testing [77].

Figure 5.18 shows the predictability time T_p (in sec) computed using the FSLE methodology as a function of the tolerance level Δ in mm for the discharges of 2000 l/s and 2800 l/s at the location of G3 for gravel bed (Figure 5.18a) and for the discharge

2500 l/s and 3200 l/s at the location of S3 for sand bed (Figure 5.18b) experiments. The initial error δ was specified to be $\sim d_{50}$, i.e., 8 mm for the gravel bed and 1 mm for the sand bed. As expected, the predictability time, i.e., the time interval over which one can typically forecast the system, is longer for the slower moving bedforms (smaller discharge rates) than for the faster moving bedforms (higher discharge rates); note that the curves for lower discharge are above the corresponding high discharge curves.

Moreover, this predictability time increases approximately as a power-law with the tolerance level Δ, that is,

$$T_p \sim \Delta^{\gamma} \tag{5.19}$$

where $\gamma \sim 1.9$ to 2.1 for gravel and $\gamma \sim 1.25$ to 1.5 for sand. This indicates that, for example, doubling the tolerance level Δ increases the rate of predictability by a factor of approximately 2^2 in gravel bed versus $2^{1.4}$ in sand bed, suggesting that the gravel bed elevation dynamics are, in general, more predictable compared to the sand bed dynamics. This result from non-linear dynamics analysis point of view is consistent with the results obtained from the linear analysis performed earlier which indicated a more three-dimensional structure and higher deformation rates of the sand bedforms compared to the gravel bedforms. Also, slower increase of the predictability time for a given rate of tolerance level Δ increase (smaller slope γ) for the case of higher discharges (for both gravel and sand bed configuration), possibly quantifies the fact that higher discharge introduces more complex bed features enhancing nonlinearity and complexity on the bed topography.

Overall, this data-based non-linear analysis suggests that the information provided by the predictability time estimated through FSLE can be used to objectively quantify the complex behavior of a migrating bed and, therefore, to develop metrics for assessing the performance of mechanistic models of sediment transport and estimate upper limits of prediction time by any model.

5.7 Concluding Remarks

Migrating bedforms strongly influence hydraulics, transport, and habitat in river environments. Their dynamics are exceedingly complex, making it difficult to predict their

geometry and their interaction with sediment transport. Bed elevations can now be easily measured with acoustic probes, as can turbulent velocity fluctuations in the flow. This technology introduces the opportunity to perform advanced statistical analysis of the flow, transport, and bed configuration. In a previous publication ([8]), we demonstrated how the time scales of moving bedforms can be estimated from the spectra of the turbulent velocity fluctuations, based on the presence of a spectral gap between an energy production regime and the inertial subrange regime. Here, we focus on multiscale measures for characterizing the complex nature of bedform migration. Our goal is to provide objective techniques for comparing bedforms, such that inferences can be made beyond average quantities (e.g., mean bedform height, length and celerity), hypotheses can be tested, and guidance for further model development can be provided.

Our analysis is based on a multiscale statistical study of bedform evolution in a laboratory flume. Different water discharges were used to transport sediment and create bedforms in sand and gravel in a 55 m long and 2.75 m wide channel at the St. Anthony Falls Laboratory of University of Minnesota. The primary data used in the analysis are time series of bed elevations recorded with acoustic probes at different locations within the channel as well as a continuous record of sediment transport at the downstream end of the flume.

A simple filtering and thresholding methodology is introduced to estimate bedform height. Interestingly, the probability distribution of bedform height has a similar shape for both gravel or sand substrates. The distribution is close to Gaussian, but with a slightly thicker tail at large values, indicating that, in both gravel and sand, rare bedforms of heights larger than those expected by a Gaussian distribution were observed.

Both gravel and sand bed elevation series exhibit a multiscale structure, i.e., the presence of features of multiples scales, which manifests itself in a power-law spectrum within a range of scales. The spectral signature of bed elevation of evolving bedforms is of theoretical and practical interest and has been explored before in the literature via modeling experimental and field observations. Wavelet analysis of the bed elevation series produces much smoother spectra than Fourier analysis, which allows for a more robust identification of spectral slope and spectral regime transitions. Our results show a range of spectral slopes from -1.9 to -2.1 for the gravel bed and -2.3 to -3 for the sand bed experiments.

The spectra characterize only second order statistics of bed elevations increments. We present evidence that the PDFs of bed elevation increments (elevation at one time less the elevation at a previous time) have heavier tails than a Gaussian distribution and that the shape of the PDF depends on scale. This suggests a multifractal signal in analogy with turbulent velocity fluctuations, for which velocity fluctuations are stretched at the Kolmogorov scale and approach Gaussian at the integral scale.

The higher order statistical moments analysis demonstrates the presence of multifractal scaling parameterized here with two parameters: the roughness and the intermittency parameter. The roughness parameter is larger for the sand bed case, indicating dependence on bedform, rather than grain scales. The intermittency parameter is larger for the gravel bed case, suggesting a more inhomogeneous arrangement of bed elevation fluctuations, which may arise from sorting and clustering microforms intermediate in size between the grain and bedform scales.

We use a wavelet-based scale-dependent correlation analysis to estimate the average velocity (celerity) of bedforms of various sizes and demonstrate that smaller bedforms move faster relatively to the larger bedforms. This leads to bedform deformation, superposition and coalescence and produces the multiscale structure of the bed elevation series. We are able to clearly demonstrate this in the gravel case. In the sand experiments, the elevation probes were located too far apart (order 2-3 bedforms wavelengths) to accurately estimate the scale-dependent celerity in the sand bedforms.

The complex evolution of bedforms is clearly a nonlinear process and linear stability analysis has limitations in assessing the complexity and inherent lack of predictability in these series. We use a nonlinear dynamical approach (Finite Size Lyapunov exponent) to depict the rate of growth of finite size perturbations and estimate the predictability horizon given a specified tolerance level of uncertainty. The results demonstrate that gravel bedforms are more predictable than sand bedforms and that the predictability decreases as the rate of discharge increases.

Experiment	Q_w (l/s)	D(m)	v (m/sec)	S_w	R_H (m)	shear velocity (u^*_b) (m/sec)	Probes	$<h_b>$ (cm)	std(h_b) (cm)	$\overline{<h_b>}$ (cm)	$\overline{std(h_b)}$ (cm)
Gravel	2000	0.55	1.18	0.0019	0.39	0.102	(G1)	2.79	1.18	4.77	1.83
							G2	5.06	1.74		
							G3	5.45	2.14		
							G4	4.45	1.73		
							(G5)	2.78	1.14		
							G6	4.17	1.49		
							G7	4.73	2.03		
	2800	0.64	1.55	0.0029	0.44	0.135	(G1)	8.25	3.49	8.23	2.79
							G2	8.24	2.69		
							G3	8.34	2.97		
							G4	9.23	2.95		
							(G5)	7.45	2.67		
							G6	7.02	2.61		
							G7	8.32	2.76		
Sand	2500	1.25	0.73	0.0021	0.65	0.161	(S1)	10.12	4.39	11.43	5.17
							S2	10.23	3.83		
							S3	9.93	4.07		
							S4	14.54	7.09		
							(S5)	15.73	6.81		
							S6	11.02	5.68		
							(S7)	10.26	3.50		
	3200	1.21	0.96	0.0028	0.64	0.182	(S1)	15.95	7.01	13.84	5.00
							S2	12.31	5.23		
							S3	13.86	5.33		
							S4	14.24	4.11		
							(S5)	18.95	5.43		
							S6	14.95	5.31		
							(S7)	8.31	3.96		

where,
Q_w = water discharge (l/s)
D = average depth of flow in test section (m)
v = velocity of flow (m/sec)
R_H = hydraulic radius (m)
S_w = water surface slope
u^*_b = shear velocity (computed using sqrt(gHS_w), where g is the acceleration due to gravity and is 9.81 m/sec^2) (m/sec)
$< h_b >$ = mean bedform height (cm)

std(h_b) = standard deviation of bedform heights (cm)

$\overline{< h_b >}$ = average of bedform height over probes G2, G3, G4, G6 and G7 for gravel bed experiments and probes S2, S3, S4, and S6 for sand bed experiments (cm)

$\overline{std(h_b)}$ = average of standard deviations of bedform heights over probes G2, G3, G4, G6 and G7 for gravel bed experiments and probes S2, S3, S4, and S6 for sand bed experiments (cm)

* Note: Probes in the brackets have not been used in the analysis.

Table 5.1: Hydraulic conditions and statistics of bedforms

Experiment	Discharge (l/s)	Probes	Spectral slope	Spectral scaling range (min)	Multi-fractal parameters		Structure function scaling range (min)
					c_1	c_2	
Gravel	2000	G2	1.92	0.5-28	0.52	0.12	0.5-11
		G3	1.91	0.5-28	0.53	0.12	0.5-10
		G4	1.87	0.5-27	0.48	0.12	0.5-11
		G6	1.85	0.5-28	0.50	0.12	0.5-10
		G7	1.92	0.5-27	0.49	0.10	0.5-11
	2800	G2	2.09	0.4-16	0.57	0.13	0.4-7
		G3	2.12	0.4-16	0.55	0.13	0.4-7
		G4	2.12	0.4-16	0.59	0.12	0.4-8
		G6	2.06	0.4-16	0.57	0.13	0.4-8
		G7	2.04	0.4-16	0.56	0.13	0.4-8
Sand	2500	S2	2.55	2-40	0.66	0.03	1-25
		S3	2.45	2-35	0.63	0.10	1-32
		S4	2.93	2-41	0.68	0.04	1-30
		S6	2.97	1-21	0.66	0.07	1-19
	3200	S2	2.32	2-40	0.58	0.06	1-31
		S3	2.47	1-33	0.59	0.05	1-28
		S4	2.78	2-24	0.66	0.06	1-19
		S6	3.0	2-38	0.69	0.07	1-32

Table 5.2: Multiscale properties of bed elevation

Experiment	Discharge (l/s)	Probes	Distance between probes (m)	Max correlation	Lag (sec)	Bedform Velocity (m/hr)
Gravel	2000	G2 – G6	1.21	0.97	280	15.55
		G4 – G7	1.21	0.97	310	14.05
	2800	G2 – G2	1.21	0.97	170	25.62
		G4 – G7	1.21	0.96	170	25.62
Sand	2500	S3 – S6	7	0.32	1270	19.78
	3200	S3 – S6	7	0.25	1860	13.51

Table 5.3: Standard cross-correlation statistics

Experiment	Discharge (l/s)	Pan	q_s (m^2/hr)	V_c (m/hr)
Gravel	2000	2	0.29	16.83
		3	0.25	14.44
		4	0.27	15.64
	2800	2	1.06	37.85
		3	0.85	28.73
		4	0.99	29.91
Sand	2500	2	0.17	3.99
		3	0.15	3.74
		4	0.13	3.24
	3200	2	0.22	4.55
		3	0.20	4.13
		4	0.19	3.92

q_s = sediment flux per unit width (m^2/hr)
V_c = Bedform velocity (m/hr) obtained using Simons et al. (1965) relationship.
Note that for computing bed form velocity mean bed form height was used in the relationship (see eqn. 5.8).

Table 5.4: Bedform migration celerity obtained using [1]'s relation (Eqn. 5.8)

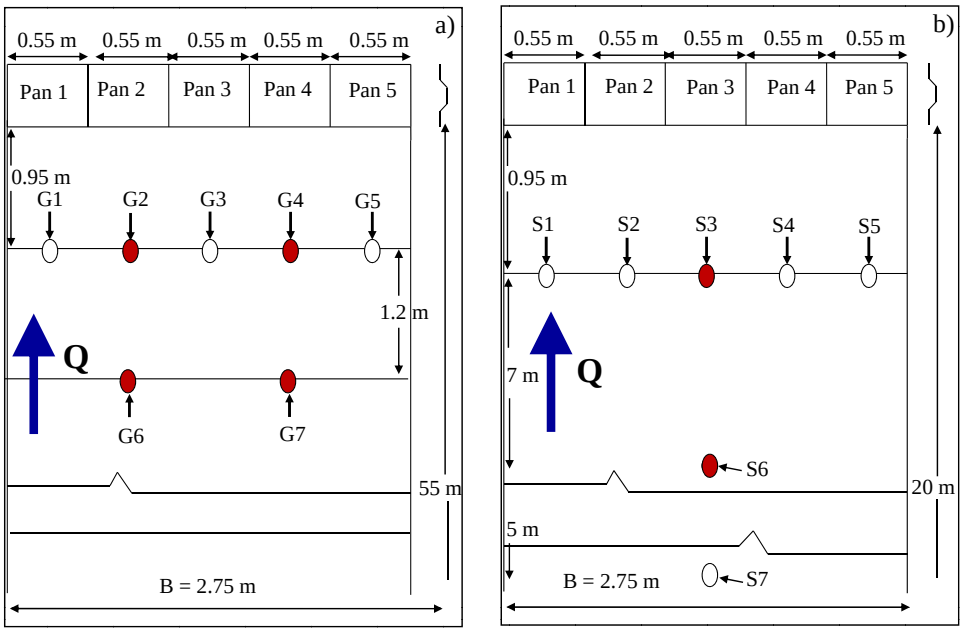

Figure 5.1: Schematic diagram of location of probes in the experimental channel of the St. Anthony Falls Laboratory at the University of Minnesota for the gravel bed experiments (left) and the sand bed experiments (right). Solid dots represent the pair of probes (upstream to downstream) used in the cross-correlation analysis.

Figure 5.2: Bedforms formed in the Main channel facility at the St. Anthony Falls Laboratory for the gravel bed experiment at a discharge of 2800 l/s (left) and sand bed experiments at a discharge of 2500 l/s (right). The flow direction in the left figure is from the top to the bottom and in the right figure is from bottom to the top of the figure.

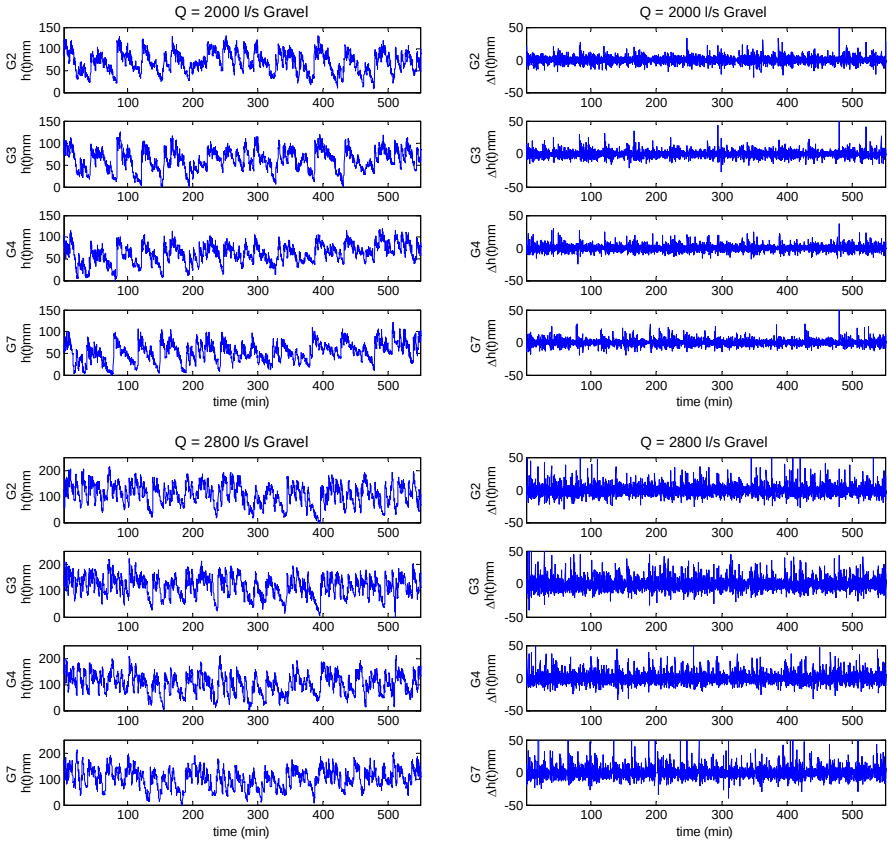

Figure 5.3: Time series of bed elevation, $h(t)$, (left panel) and bed elevation increments, $h(t+1) - h(t)$, (right panel) for gravel bed experiments for discharge of 2000 l/s (top) and 2800 l/s (bottom) at four different locations for each discharge (see Figure 5.2, left).

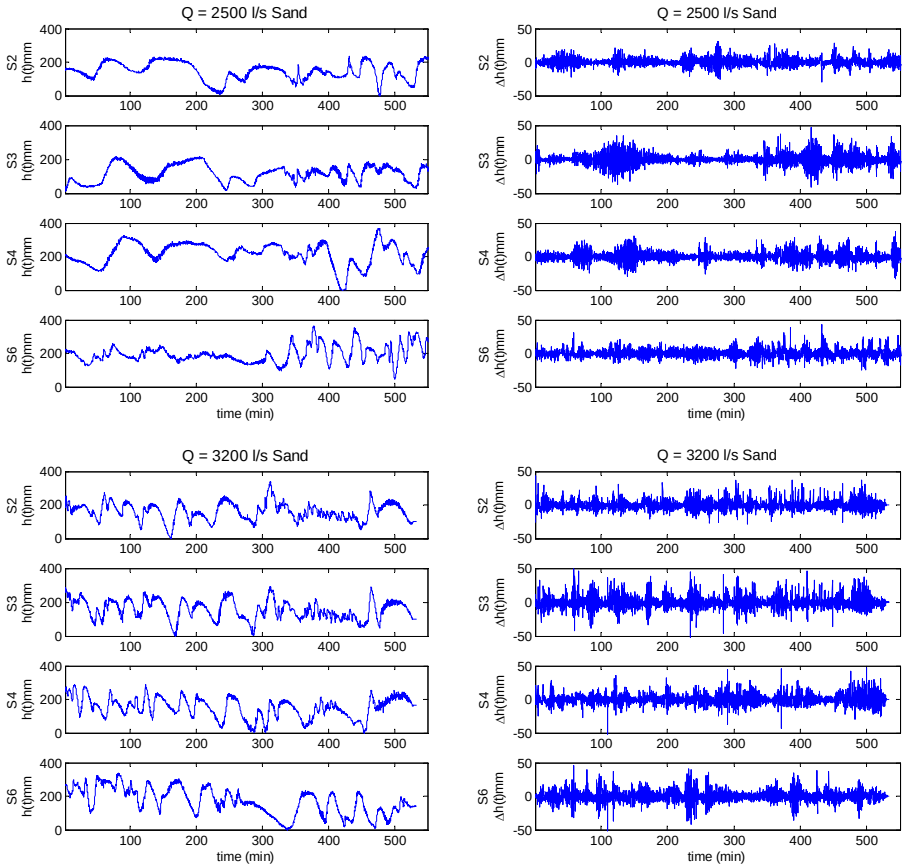

Figure 5.4: Time series of bed elevation, $h(t)$, (left panel) and bed elevation increments, $h(t+1)-h(t)$, (right panel) for sand bed experiments for discharge of 2500 l/s (top) and 3200 l/s (bottom) at four different locations for each discharge (see Figure 5.2, right).

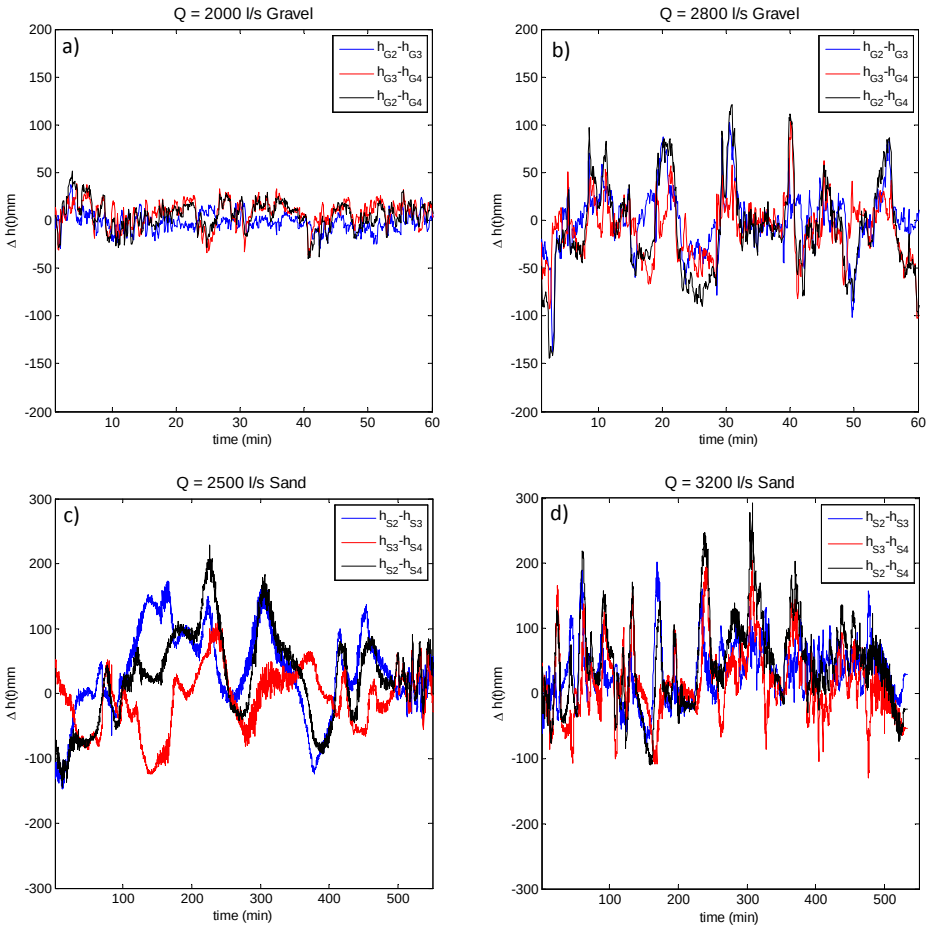

Figure 5.5: Time series of differences of simultaneously sampled bed elevation at the locations of probes G2, G3 and G4 across the width of the channel for the gravel bed experiments (top panel) and probes S2, S3 and S4 for the sand bed experiments (bottom panel) for the discharge of 2000 l/s (a), 2800 l/s (b), 2500 l/s (c) and 3200 l/s (d). Note that in the case of two dimensional bedforms the bed elevation differences of different probes, located in-line across the width of the channel, as a function of time would be constant.

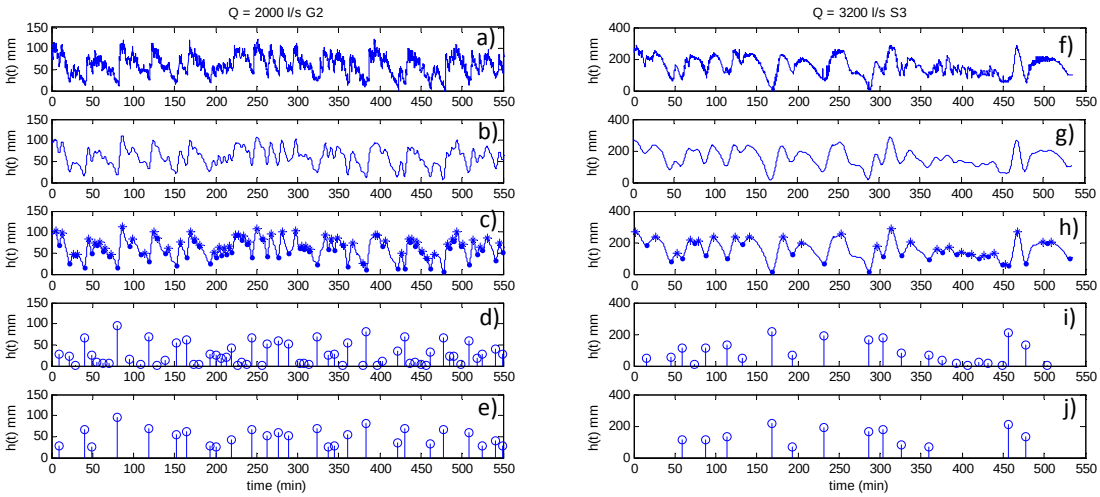

Figure 5.6: Time series of bed elevation (a), filtered bed elevation using fourier transform (b), bed elevation showing the location of local maxima and local minima (c), extracted bedform heights (d) and extracted bedform heights above a certain threshold (e) for the gravel bed experiment (left panel) and the sand bed experiment (right panel) at the discharge of 2000 l/s and 3200 l/s, respectively. Note that the sampling time for the bed elevation in the gravel bed experiments was 5 sec while for sand bed experiments was 10 sec.

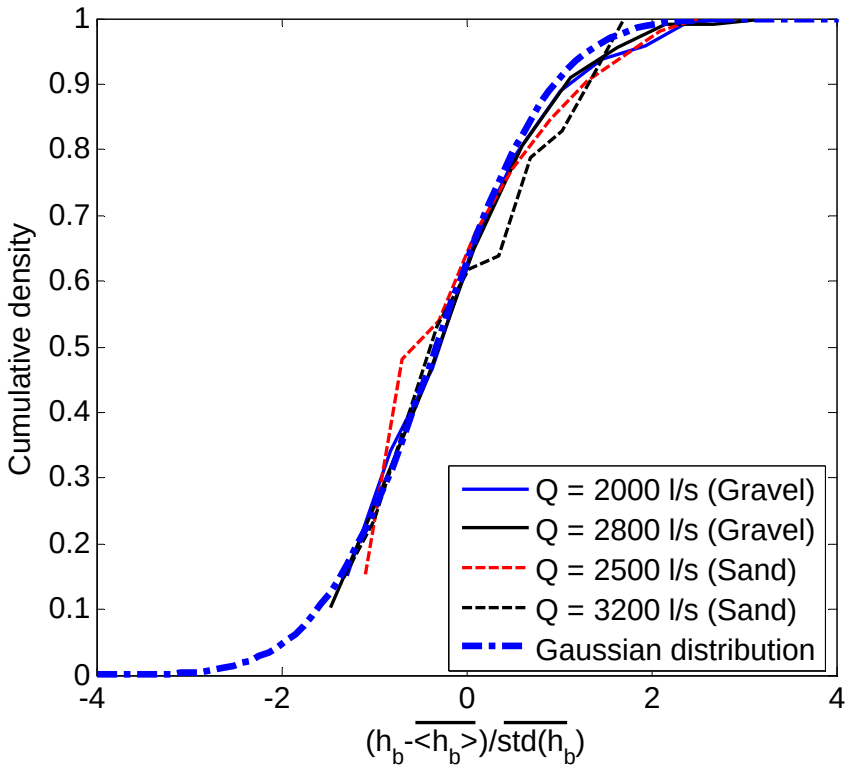

Figure 5.7: Cumulative density function of bedform heights obtained from the time series of bed elevation (see section 5.3.2 for bedform extraction). Note that the distribution of bedform heights for each discharge was obtained from the ensemble of bedform heights extracted from all the probes at that particular discharge excluding the probes in the parenthesis ( ) in Table 5.1.

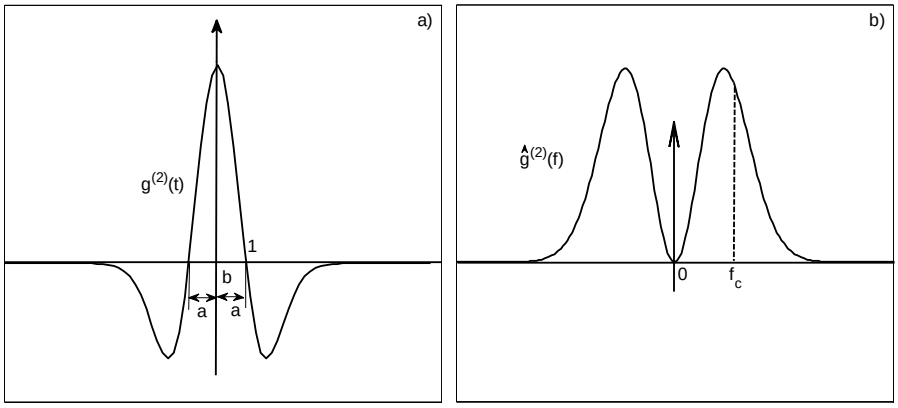

Figure 5.8: Mexican hat wavelet (a) and its Fourier transform (b); a denotes scale, b location and f_c is the bandpass frequency attached to scale a. For the Mexican hat wavelet $fc = \sqrt{(}5/2)/2\pi a = 0.251/a$ (e.g. see [3]).

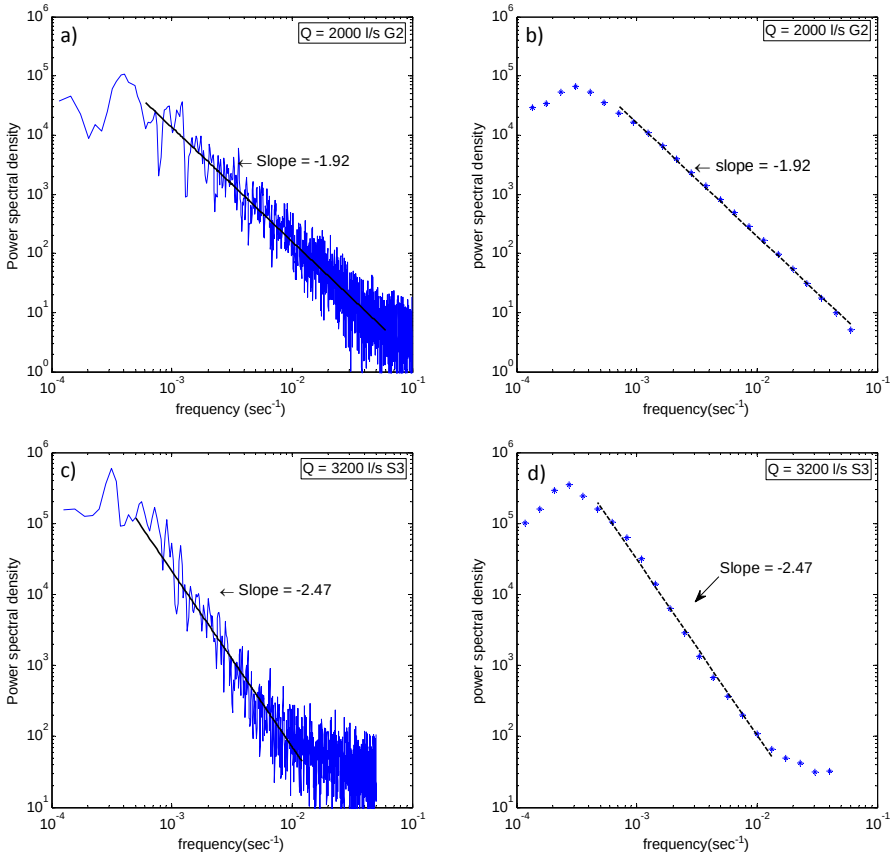

Figure 5.9: Comparison between the Fourier power spectrum (left column) and the wavelet power spectrum (right column) of bed elevation time series recorded by probe G2 in gravel bed (Q = 2000 l/s, upper panel) and probe S3 in sand bed (Q = 3200 l/s, lower panel) experiments.

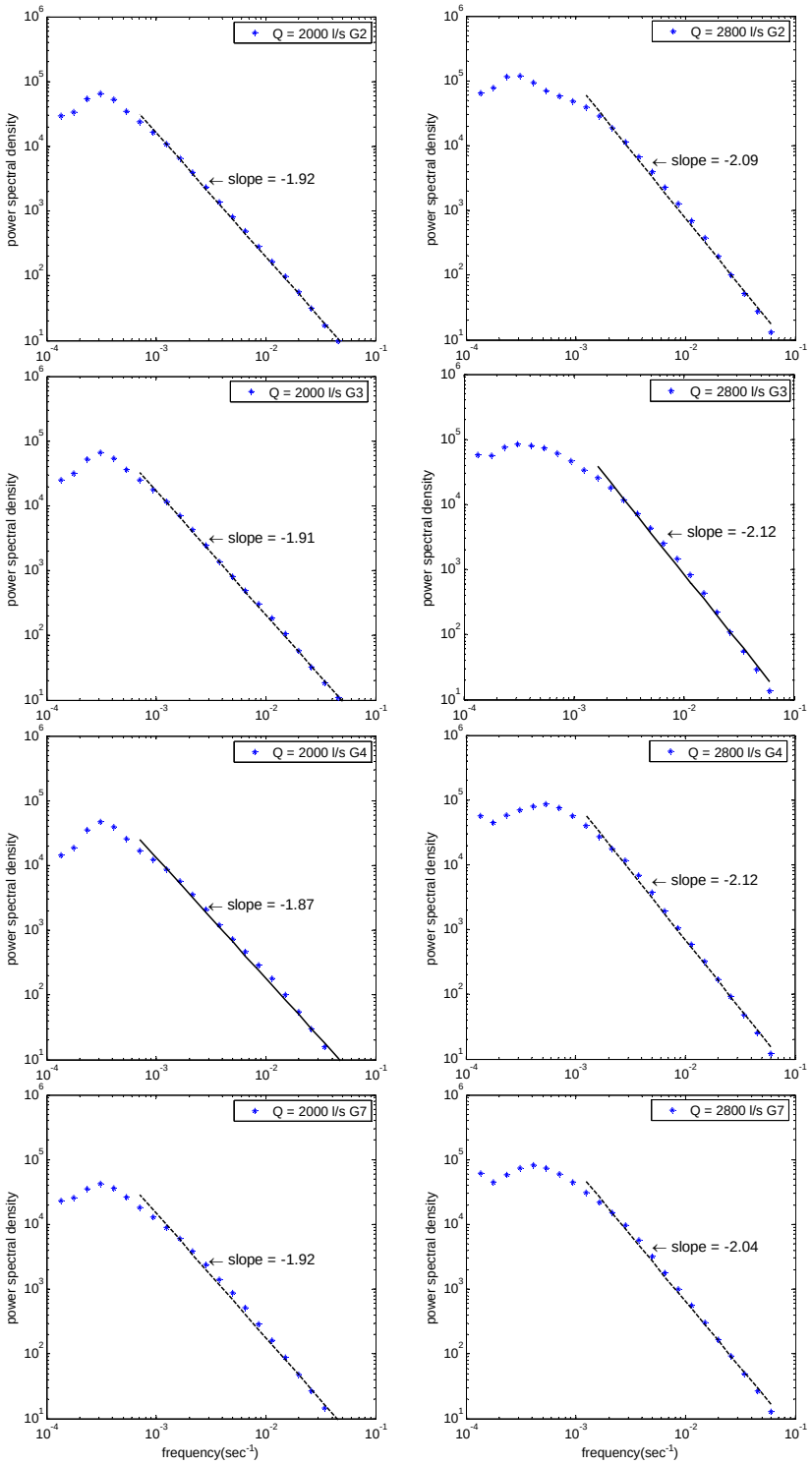

Figure 5.10: Wavelet spectrum of the gravel bed elevations for a discharge of 2000 l/s (left panel) and 2800 l/s (right panel) for probes G2, G3, G4 and G7 (top to bottom) respectively.

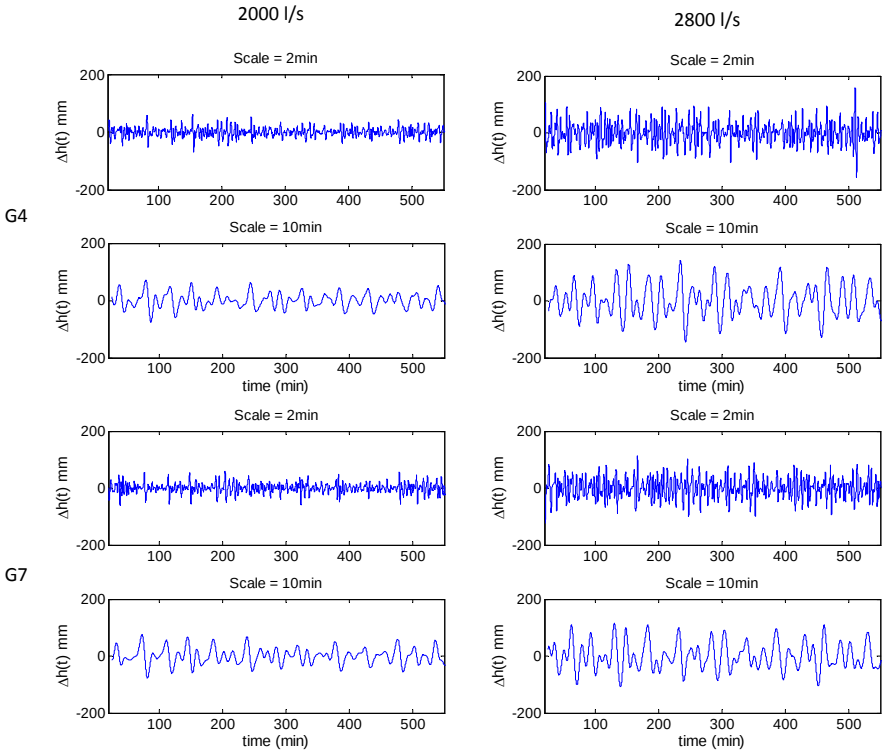

Figure 5.11: Wavelet coefficients of the gravel bed elevation series at scales of 2 min and 10 min for the discharges of 2000 l/s (left panel) and 2800 l/s (right panel). Top panel is for probe G4 and bottom panel is for probe G7, respectively.

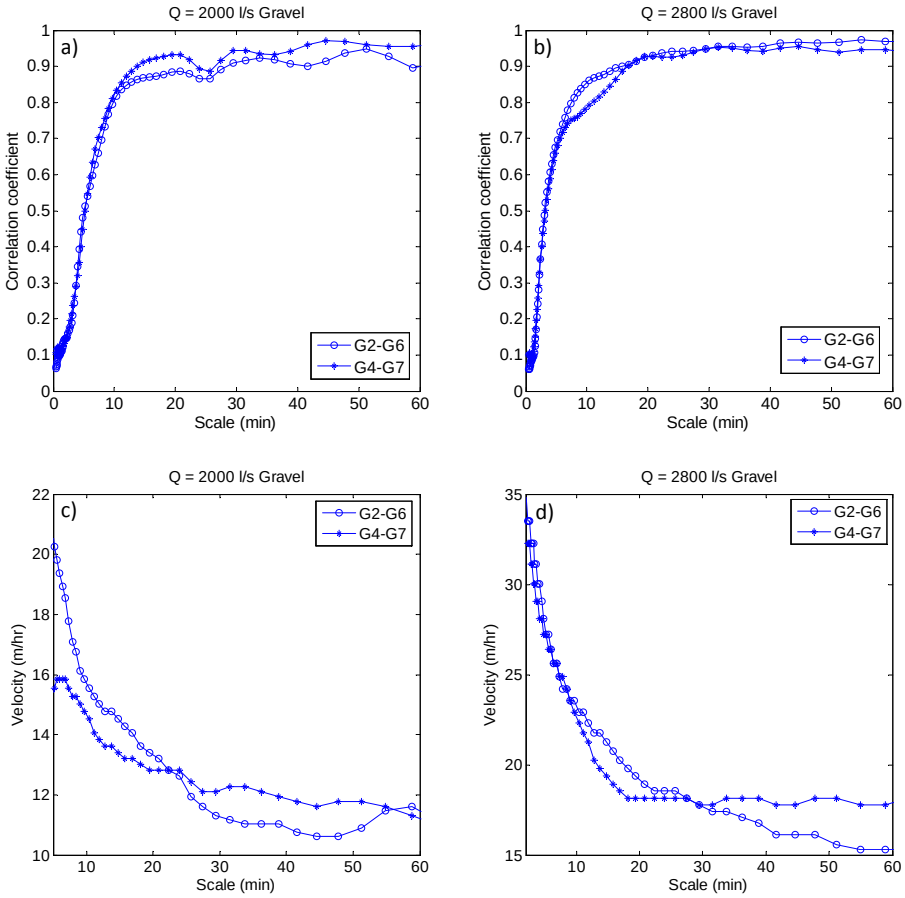

Figure 5.12: Plot of maximum cross-correlation obtained between probes G2-G6 and G4-G7, for the discharge of 2000 l/s (a), and 2800 l/s (b), as a function of scale using wavelet analysis. Celerity of bedforms as a function of scale for the discharge of 2000 l/s (c), and 2800 l/s (d). Note that the lag used in computing celerity at given scale corresponds to the maximum cross-correlation coefficient obtained between probes G2-G6 and G4-G7 at that scale.

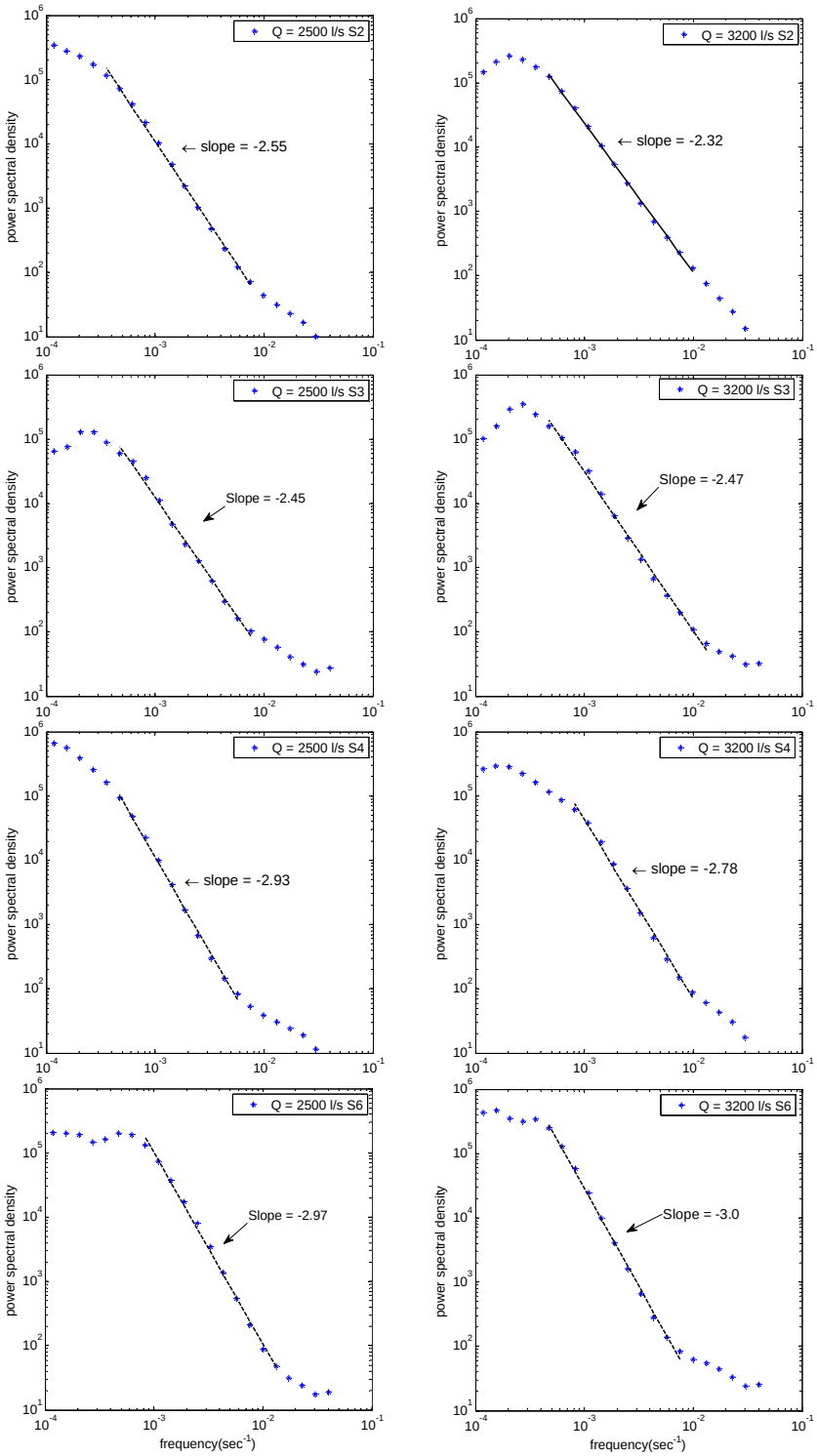

Figure 5.13: Wavelet spectrum of the sand bed elevations for a discharge of 2500 l/s (left panel) and 3200 l/s (right panel) for probes S2, S3, S4 and S6 (top to bottom) respectively.

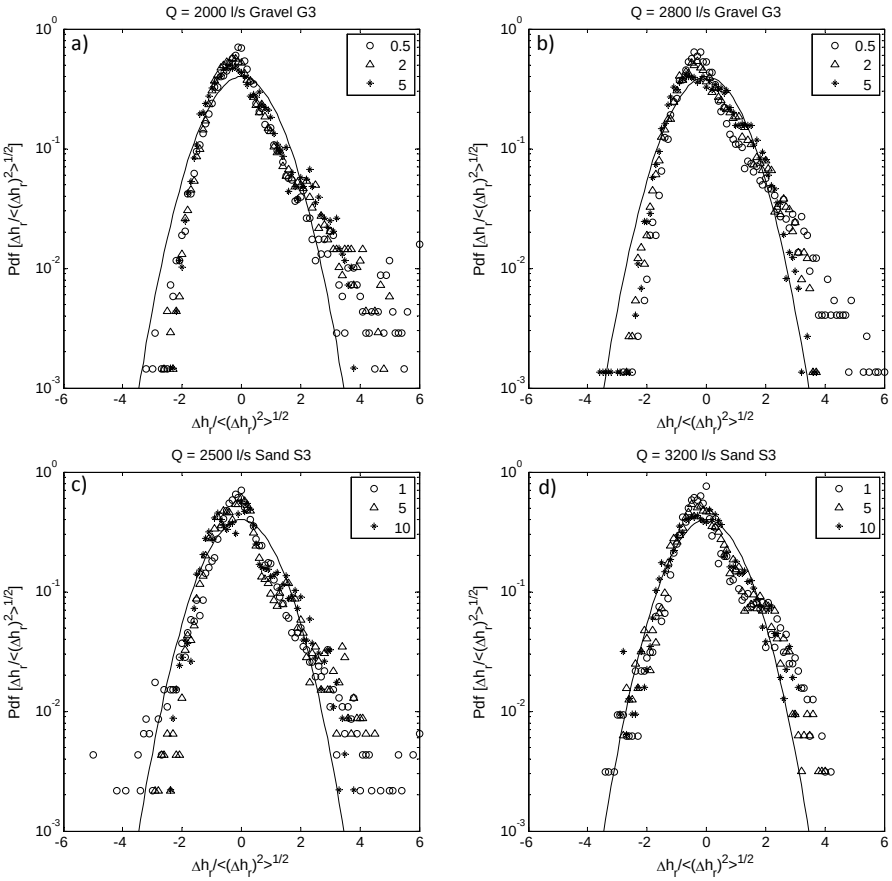

Figure 5.14: Semi-log PDFs of the normalized increments of the bed elevation measured at the location of probe G3 for the gravel bed experiments (top panel) and probe S3 for the sand bed experiments (bottom panel) for a discharge of 2000 l/s (a), 2800 l/s (b), 2500 l/s (c) and 3200 l/s (d). For the gravel bed experiments (top panel) circles correspond to r = 0.5 min, triangles to r = 2 min, and stars to a time r = 5 min, while for the sand bed experiments (bottom panel) circles correspond to r = 1 min, triangles to r = 5 min, and stars to a time r = 10 min. The solid curve designates the Gaussian distribution.

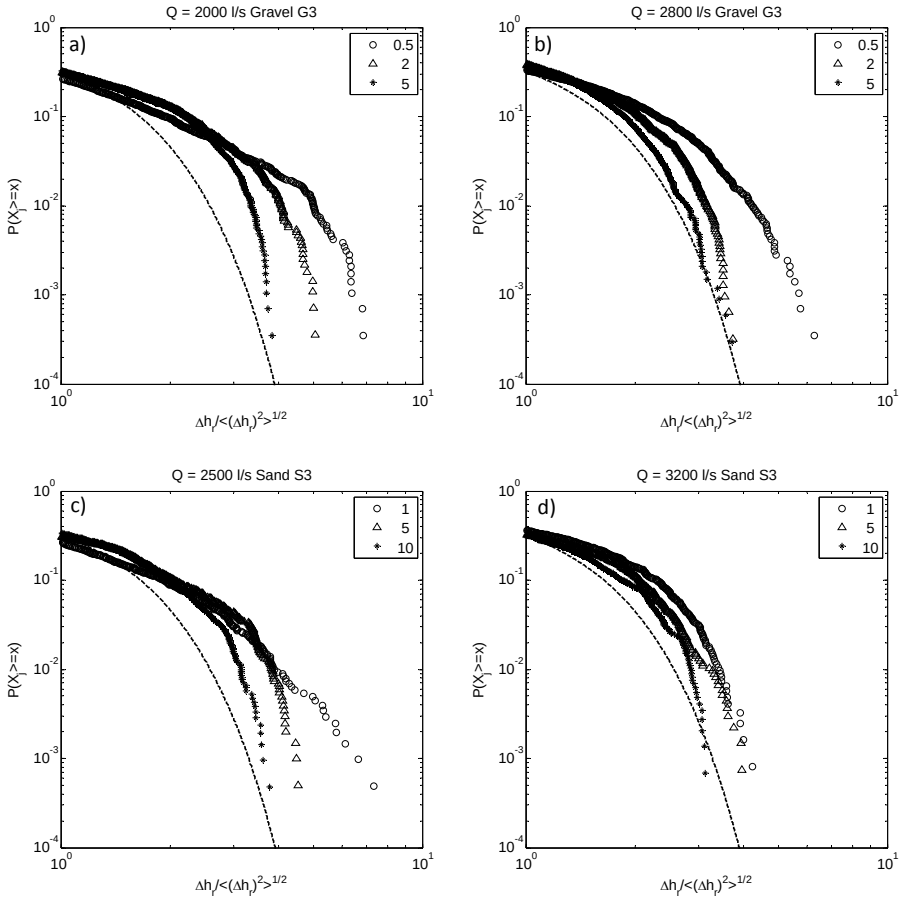

Figure 5.15: Log-log exceedance probabilities of the normalized positive increments of the bed elevation measured at the location of probe G3 for the gravel bed experiments (top panel) and probe S3 for the sand bed experiments (bottom panel) for a discharge of 2000 l/s (a), 2800 l/s (b), 2500 l/s (c) and 3200 l/s (d). For the gravel bed experiments (top panel) circles correspond to r = 0.5 min, triangles to r = 2 min, and stars to a time r = 5 min, while for the sand bed experiments (bottom panel) circles correspond to r = 1 min, triangles to r = 5 min, and stars to a time r = 10 min. The dash line curve designates the Gaussian distribution.

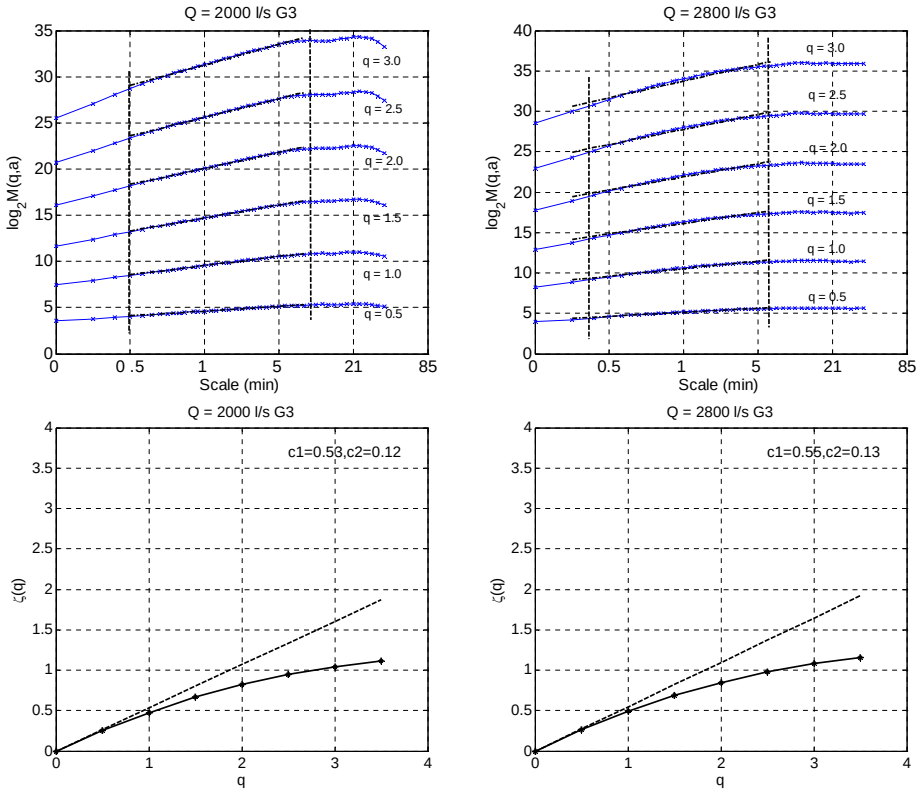

Figure 5.16: (top panel) Statistical moments of the increments of the gravel bed elevation time series as a function of scale and, (bottom panel) the scaling exponents $\tau(q)$ estimated from the log-log linear regressions within the scaling regions for discharges of 2000 l/s (left panel) and 2800 l/s (right panel). Notice the deviation of $\tau(q)$ from the linear line establishing the presence of multifractality.

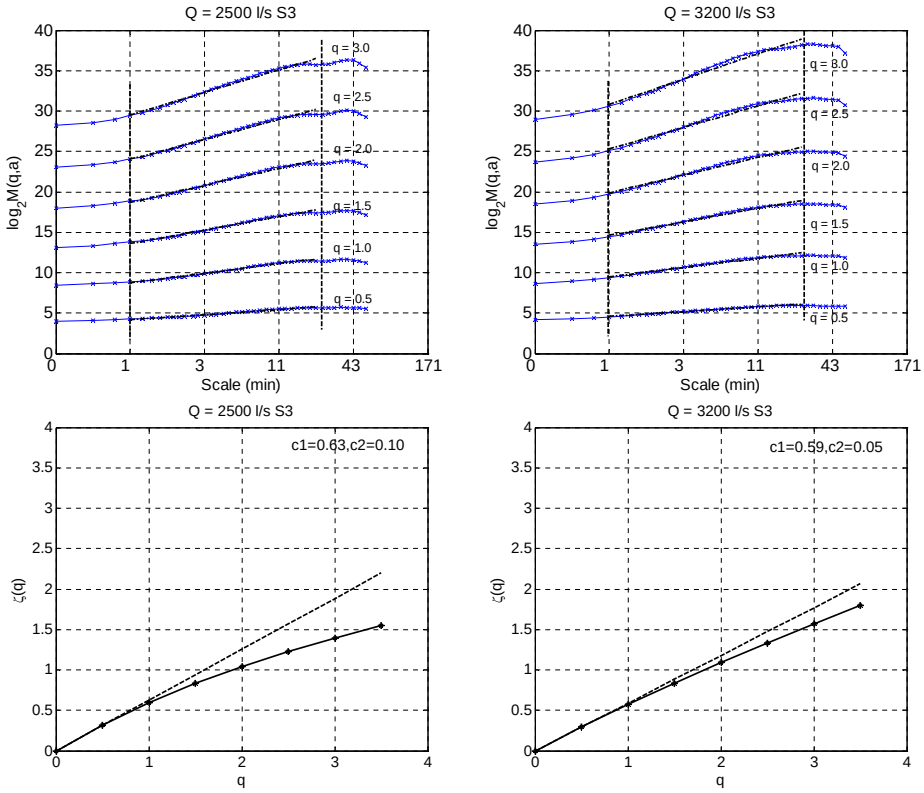

Figure 5.17: (top panel) Statistical moments of the increments of the sand bed elevation time series as a function of scale and, (bottom panel) the scaling exponents $\tau(q)$ estimated from the log-log linear regressions within the scaling regions for discharges of 2500 l/s (left panel) and 3200 l/s (right panel). Notice the deviation of $\tau(q)$ from the linear line establishing the presence of multifractality.

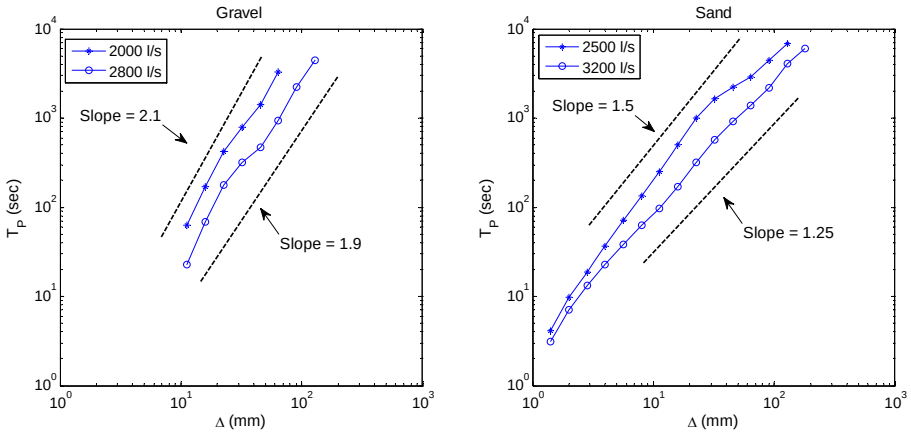

Figure 5.18: Predictability time T_p, based on FSLE, as a function of prediction error tolerance Δ for bed elevation sampled at the location of probe G3 for the discharge of 2000 l/s and 2800 l/s for gravel bed (left panel) and at the location of probe S3 for the discharge of 2500 l/s and 3200 l/s for gravel bed experiments (right panel). The initial perturbation was specified to be d_{50}, i.e., 8 mm for the gravel bed and 1 mm for the sand bed.

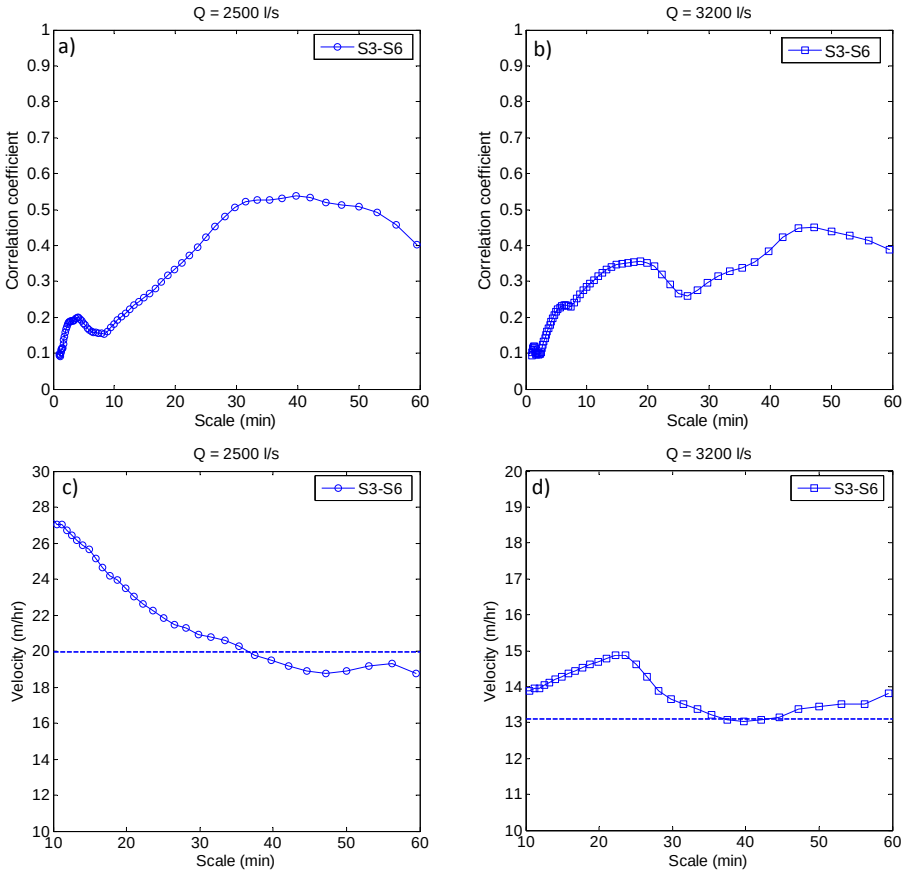

Figure 5.19: (**Appendix)** Plot of maximum cross-correlation obtained between probes S3-S6, for the discharge of 2500 l/s (a), and 3200 l/s (b), as a function of scale using wavelet analysis. Celerity of bedforms as a function of scale for the discharge of 2500 l/s (c), and 3200 l/s (d). The dotted line represent the celerity obtained from standard cross-correlation (see Table 5.3). Note that the lag used in computing celerity at given scale corresponds to the maximum cross-correlation coefficient obtained between probes S3-S6 at that scale.

Chapter 6

Coupled dynamics of the co-evolution of bed topography, flow turbulence and sediment transport in an experimental flume

A series of flume experiments were conducted in a large experimental channel at the St. Anthony Falls Laboratory to understand the coupled dynamics of flow and bedforms above the sediment-water interface. Simultaneous high resolution measurements of velocity fluctuations, bed elevations and sediment flux were sampled at the downstream end of the channel for a range of discharges. Probability density functions (pdfs) of the bed elevation fluctuations and the instantaneous Reynolds stress reveal heavy-tail statistics and a strong feedback between the co-evolution of bedforms and the near-bed turbulence. These results complement our previous findings [8] in which the signature of bedform evolution on the near-bed velocity fluctuations was confirmed via the presence of a spectral gap and two distinct power-law scaling regimes in the spectral density of velocity fluctuations. We report herein a strong asymmetry in the probability distribution of bed elevation fluctuations and instantaneous Reynolds stresses. We interpret this

asymmetry, in view of the established intermittency (multi-fractality), as the result of scale coupling. In short, small-scale structures do not lose the information of the large-scale structures of flow and transport, rendering thus the scale-to-scale energy transfer locally anisotropic. We also propose a relationship to quantify sediment transport using instantaneous Reynolds stress.

6.1 Introduction

One of the most striking features of turbulence is the stochastic nature of its eddies and their self-similar behavior over a range of scales [51, 180]. The energy cascades from large scale flow structures (large eddies) to the small scale flow structures by an inertial and inviscid mechanism. As documented earlier by many researchers, these turbulent eddies play an important role in river morphodynamics, as well as sediment and nutrient transport [107, 98]. They interact with the fluvial bed over a wide range of scales, from the scale of the grain, to the scale of the bedforms [106, 8]. Depending on the size and position of these eddies, they can exert shear on the boundary (bed surface, banks, etc.), which, in turn, mobilizes the material present on it (the higher the boundary shear stress, the more is the sediment transport). Due to variation in sediment transport (caused by variation in shear stress), bedforms are created and modified. Once the bedforms are created, their presence induces flow acceleration/deceleration, which, as a feedback, modulates the sediment transport. Hence, a strong feedback between flow turbulence, bed topography and sediment transport is generated.

The evolution of bedforms is not completely determined by the flow but it also depends on the substrate composition, i.e., the bed material grain size distribution. For example, if we consider a gravel bed channel, a uniform grain size distribution over the bed is more likely to produce bedforms of less variable nature (i.e., the bed will have a more narrow range of scales of variability (bedforms) as compared to the range of scales of variability a bed will have with a wider grain size distribution). On the other hand, two fluvial beds with similar grain size distribution, subjected to a low and high discharge respectively, will produce larger bedforms (more variable bed topography) at higher discharge as compared to lower discharge. As a result of a wider range of scales of bedforms produced by the combination of grain size and flow conditions, turbulence

field will be different, perhaps more variable in the presence of many scales and sizes of bedforms. In a recent work [8] have shown that with increasing discharge, the slope of power spectral density of temporal bed elevation increases. Moreover, in that particular study they have shown that the migrating bed topography imprints a distinct signature on the near-bed velocity fluctuations. This has also been conceptually shown in [106].

The effect of bed topography on flow structures and sediment transport has been quantified by several studies both in sand-bed (e.g., [181, 94, 140, 18]) and gravel-bed channels (e.g., [98, 129, 38, 92]. However, most of these studies were conducted either on a flat bed or on a immobile bed. To the best of our knowledge there are very few studies which quantify interaction of bed topography with flow turbulence over a migrating bed in gravel-bed environment [98, 97, 8].

The purpose of this study is to quantify the variability in bed topography when subjected to a constant flow field and how this bed topography co-evolves with the turbulent field over a range of scales and for a range of discharges to imprint its variability in the bedload transport rates. The paper is structured as follows. In the following section a brief review of the experimental setup is given. Section 6.3 is devoted to the results obtained from the experimental data followed by discussions as section 6.4. Finally concluding remarks are given in section 6.5.

6.2 Experimental Setup and data collected

Experiments were conducted in the Main Channel facility at the St. Anthony Falls Laboratory, University of Minnesota, as part of Streamblab08, a follow-up of the interdisciplinary project StreamLab06 [41, 8]. The channel is 55 m long, 2.74 m wide and has a maximum depth of 1.8 m with a maximum discharge capacity 8000 l/s. It is a partially sediment recirculating channel while the water flows through the channel without recirculation. Intake of the water in the channel was directly from the Mississippi river.

The channel bed was composed of a mixture of gravel (median particle size diameter, $d_{50} = 11.3$ mm) and sand (median particle size diameter, $d_{50} = 1$ mm), with an overall grain size distribution with $d_{50} = 7.7$ mm, $d_{16} = 2.2$ mm and $d_{84} = 21.2$ mm. The mean specific density of sediment of all size fractions was ~ 2.65. The thickness of the bed

at the start of the run was approximately 0.45 m. Continuous data collection occurred for about twenty hours after the channel had reached quasi-dynamic equilibrium. The assessment of this dynamic equilibrium state was evaluated by checking the stability of the 60 min average total sediment flux at the downstream end of the channel. Using the pan accumulation data, the acquisition software computed a 60 min mean of sediment flux in all five pans. Dynamic equilibrium was assumed to be reached when variation in this value became negligible. In other words, when the average of the previous 60 min of instantaneous flux values computed from the pan data stabilized, we determined the channel to be in dynamic equilibrium and proceeded with formal data collection and sampling. More details about the experimental setup can be found in [5, 8].

The data collected included velocity and bed elevation fluctuations at several locations as well as sediment flux at the downstream end of the channel (see Figure 6.1). The velocity fluctuations were measured using Acoustic Doppler Velocitimeter (ADV) at an approximate distance of 10 cm above the mean bed level. Table 6.1 shows the other relevant flow parameters and the distance of ADV from the mean bed elevation (D_p) for other discharges. Although the distance, D_p, changes with increasing discharge, the ratio k (where $k = D_p/\sigma_b$, σ = std. dev. of bed elevation) remains constant ~ 5. Bed elevation fluctuations were sampled using submersible sonar transducers of 2.5 cm diameter which were deployed 0.3 m (on an average) below the water surface. The sampling interval of bed elevation measurements was 5 sec with a vertical precision of 1 mm. For sampling sediment transport rates, bedload traps located at the downstream end of the test section, consisting of 5 weighing pans of equal size that spanned the width of the channel, were used. Any bedload sediment transported to the end of the test-section of the channel would fall into the weigh pans, which automatically recorded the mass they contained every 1.1 sec. Upon filling with a maximum of 40 kg, the weigh pans would tip to release the sediment and reset the weigh pan. The released sediment was re-circulated and released back into the channel at the upstream end of the 55 m test section, to maintain a closed system. Figures 1a (photo) and 1b(schematic) show the setup of the ADV, the Sonars and sediment monitoring weigh pan system placed at the downstream end of the channel. Measurements were taken over a range of discharges corresponding to different bed shear stresses. For steady, uniform flow bed shear stress is often characterized in terms of dimensionless Shields stress, τ_b^*, and can

be approximated as

$$\tau_b^* = \frac{h_R S}{R d_{50}}, \tag{6.1}$$

where h_R and S are the hydraulic radius and channel slope, respectively, and $R = 1.65$ is the relative submerged density of silica. Here we report the data collected at discharges of 1500 l/s, 2000 l/s and 2800 l/s. As the data was collected in the fall season, there were some leaves floating in the channel which might have resulted in spikes in the velocity and bed elevation data. Even though the amount of spurious spikes in the data was found to be very small, these were removed as part of the data treatment for erroneous measurements.

6.3 Results

6.3.1 Flow conditions and physical characteristics of bed topography

Bedforms were formed on the gravel-bed surface of the Main channel. They were mainly dunes and bedload sheets. Both the mean and the standard deviation of the bed elevation increased with increasing discharge. Table 6.1 shows the statistics of the flow conditions and the bed elevations for the discharges of 1500 l/s, 2000 l/s and 2800 l/s.

Figure 6.2 shows the data collected for a discharge of 2000 l/s. The bed elevations sampled using sonar 3 are shown in Figure 6.2a, simultaneously sampled 5 min accumulated sediment transport series in Figure 6.2c, velocity fluctuations around the mean in the flow direction as Figure 6.2e, velocity fluctuations around the mean in vertical direction as Figure 6.2g, and the instantaneous Reynolds stress computed as a product of velocity fluctuations in longitudinal and vertical directions ($-\rho u'w'$, where ρ is the density of the water assumed to 1000 kg/m^3) is shown in Figure 6.2i. Note that we will use the terminology 'fluctuations' and 'increments' of a signal $X(t)$ interchangeably, which are the increments of the signal denoted as $\Delta X(t)$ (defined later) and 'fluctuations around the mean' which is mean removed signal denoted as $X'(t)$. Figure 6.2b, 6.2d, 6.2f, 6.2h and 6.2j show the derivatives of the bed elevations(Figure 6.2a), sediment flux (Figure 6.2c), velocity fluctuations in horizontal direction (Figure 6.2e), velocity fluctuations in vertical direction (Figure 6.2g), and instantaneous Reynolds stress (Figure 6.2i) respectively. Also note that the flow direction in the case of bed topography (Figure 6.2a) is from right to left of the figure.

6.3.2 Marginal statistics (pdfs) of $\Delta h(t)$, $\tau(t)$ and $\Delta S(t)$

Figure 6.3a shows the pdfs of the bed elevation fluctuations (increments: $\Delta h(t) = h(t+\Delta t) - h(t)$) at the highest resolution of $\Delta t = 5$ sec for the discharges of 1500 l/s, 2000 l/s and 2800 l/s. These bed elevations were sampled at the location of sonar 3 positioned at the downstream end of the channel (see Figure 6.1b). As can be seen in the figure, the width of the pdf increases with increasing discharge. At the same time it is observed that as the discharge increases, the pdf becomes more skewed to the right indicating chance of finding high positive bed elevation fluctuations, $h(t+\Delta t)-h(t) > 0$ in the bed. These large positive temporal fluctuations are associated with large changes (abrupt decreases) in the direction of flow (see Figure 6.4) corresponding to the lee side of the bedforms at all scales. Note that the positive values in the increments of the bed elevation fluctuations correspond to deposition and negative values to erosion.

To the best of our knowledge, the asymmetry of the pdf of the bed elevation fluctuations has not been reported before in the literature except [39], although in their study the bed elevation fluctuations were mean removed bed elevations. They documented the similar trend that is the change in the shape of pdf and the asymmetry, however, the experiments mentioned in that particular study were performed under armored bed conditions. They related the grain size distribution to the standard deviation in the bed elevation and the asymmetry to the armoring effect. Moreover, they mentioned that with rising armoring discharge the range of bed elevations increases and the number of observations around the mean decreases.

The asymmetry can be documented by the coefficient of skewness (S), the asymmetry index (A_S) and the flatness index (F) defined as

$$S = \frac{\langle (\Delta h)^3 \rangle}{\langle (\Delta h)^2 \rangle^{3/2}} \tag{6.2}$$

$$A_S = \frac{\langle (\Delta h)^3 \rangle}{\langle |(\Delta h)^3| \rangle} \tag{6.3}$$

$$F = \frac{\langle (\Delta h)^4 \rangle}{\langle (\Delta h)^2 \rangle^2} \tag{6.4}$$

These metrics are shown in Figure 6.5 for different discharges. For example, in the case of bed elevation fluctuations skewness and asymmetry increases with increasing

discharge. Although [180] argued that the asymmetry factor A_S is a better measure of the asymmetry of the pdf than the skewness, however, we found that both skewness and asymmetry in our experiments behave quite similarly. In contrast to the skewness/asymmetry in the bed elevation, the skewness/asymmetry in the instantaneous Reynolds stress and the sediment transport rates does not vary significantly with increasing discharge (see Figure 6.2a, 6.2b), however, the magnitude of skewness/asymmetry in case of instantaneous Reynolds stress is quite significant (of the order if 2.5/0.8), while for sediment transport rates is close to zero. In comparison to the skewness/asymmetry, flatness index of bed elevations decreases with increasing discharge (Figure 6.2c). This is in agreement with the findings of [39] where they showed that the pdf of bed elevations at lower discharge show more peakedness (flatness index) and it decreases with increasing discharge. Note that for a Gaussian distribution, skewness, asymmetry and flatness are 0, 0, and 3 respectively.

An effective way to depict the asymmetry of a pdf ($f(x)$) is by displaying odd moment functions of f(x) as $x^3 f(x)$ or $x^5 f(x)$. Such plots are shown in Fig 6.3 (right panel). Figure 3b shows the pdf of the third moment of the bed elevation fluctuations.

Figure 6.3c shows the pdfs of the normalized instantaneous Reynolds stresses computed as a product of longitudinal velocity fluctuations around the mean and vertical velocity fluctuations around the mean for the discharges of 1500 l/s, 2000 l/s and 2800 l/s. These normalized instantaneous Reynolds stresses can be mathematically expressed as:

$$\tau^* = \frac{-\rho_w u' w'}{(\rho_s - \rho_w) g d_{50}}, \tag{6.5}$$

where ρ_w is the density of water (assumed as 1000 kg/m^3), ρ_s is the density of the dry sediment (assumed as 2650 kg/m^3) and g is the acceleration due to gravity (assumed as 9.81 m/sec^2). Figure 3d shows the pdf of the third moment of the normalized instantaneous Reynolds stress. Note that all these above mentioned pdfs are computed at the highest resolution, i.e., resolution of the measurements (200 Hz in case of velocity fluctuations).

Sediment transport rates were sampled at a resolution of 1.1 sec. These rates at the resolution of our measurements (1.1 sec) showed negative excursion, which would imply negative sediment flux, which is not physically possible given the experimental setup. Details about removing the noise (negative values) and the sources of errors can

be seen in [5]). To overcome this, a moving average window of 5 min was used, although the negative values can be removed by a window of 2 min size. Figures 6.3e and 6.3f show the pdfs of the derivatives of 5 min accumulated sediment transport series and the corresponding third moment for the discharges of 1600 l/s, 2000 l/s and 2800 l/s, respectively. Although the pdfs of sediment transport rates for all the discharges look symmetric, the tails of the pdfs become heavier with increasing discharge.

6.3.3 Parameterizing heavy-tail statistics of bed elevation increments and instantaneous Reynolds stress

Along with the asymmetry, documented in the previous section, it is noted that the pdfs of the bed elevation fluctuations exhibit concave-up decay in their tails (both in right and left tails) indicating a heavy-tail behavior and a considerable departure from the Gaussian pdf (Fig 6.6a, top panel). In contrast to a thin-tailed distribution, where the chance of occurrence of an extreme event is close to zero, in heavy-tailed pdfs an extreme event has small, but significant chance of occurrence. These heavy-tailed pdfs have a power-law decay, which is slower decay than exponential (e.g., exponential pdf) and super-exponential-decays (e.g., Gaussian pdf). To further investigate the heavy-tail behavior of the pdfs of bed elevation fluctuations, the probability of exceedance for both positive and the negative part of the pdfs (Fig 3a) were computed separately and shown in Figure 6.6 (top panel). It can be seen from these figures (Figure 6.6, top panel) that the tail of the pdf decay log-log linearly suggesting heavy-tail behavior both in positive and negative part of the bed elevation pdfs which can be well characterized by power-law distributions, at least approximately, for larger values of x.

A common distribution with a power-law decay is a Pareto distribution whose probability density function can be expressed as:

$$f(x) = \alpha \frac{\gamma^{\alpha}}{x^{\alpha+1}} \tag{6.6}$$

where α is the tail index, γ is the minimum possible value of the random variable also known as lower bound and the density is defined for $x \geq \gamma$. The probability of exceedance of a Pareto distribution is given by:

$$f(x) = (\frac{\gamma}{x})^{\alpha} \tag{6.7}$$

.

In many natural systems, for example, in the case of bed elevations here where the positive tails of the pdfs truncates at the maximum bed elevation fluctuation, it is natural to consider an upper bound that truncates the tail. In particular, Pareto distribution fits reasonably well the central part but fail in the tails which experimentally decay faster than predicted by a Pareto distribution. To avoid this problem, a three parameter truncated Pareto distribution has been proposed. The density of the truncated Pareto is given by:

$$f(x) = \frac{\alpha\gamma^{\alpha}x^{-\alpha-1}}{1-(\gamma/\nu)^{\alpha}} \tag{6.8}$$

and its probability of exceedance can be expressed as:

$$P(X > x) = \frac{\gamma^{\alpha}(x^{-\alpha}-\nu^{-\alpha})}{1-(\gamma/\nu)^{\alpha}} \tag{6.9}$$

where ν is the truncation parameter also called upper bound on the random variable, α is the tail index and γ is the lower bound on the random variable X.

Figure 6.6 (middle panel) shows the fitted Pareto and truncated Pareto distributions to the pdf of the bed elevation fluctuations for the both left and right tails. Table 6.2 shows the parameters obtained from the fitted distribution for positive part and Table 6.3 shows the parameters of the fitted distribution for the negative part.

To estimate the parameters of the fitted Pareto and truncated Pareto distributions a method of maximum likelihood estimation (MLE) proposed by [182, 183] was used in this study. This estimation involves the conditional MLE based on the (r+1) largest-order statistics representing only the portion of the tail where the truncated Pareto approximation holds. Consider a random sample X = X_1,X_2,...,X_n and let $X_{(1)} \geq X_{(2)} \geq .... \geq X_{(n)}$ denote its statistics, where $X_{(r)}$ is the r^{th} largest observation. The conditional MLE for the parameters of the truncated Pareto distribution based on the (r+1) largest-order statistics is given by $\hat{\nu} = X_{(1)}$, $\hat{\gamma} = r^{\frac{1}{\hat{\alpha}}}(X_{(r+1)})[n-(n-r)(X_{(r+1)}/X_{(1)})^{\hat{\alpha}}]^{-1/\hat{\alpha}}$, and $\hat{\alpha}$ is obtained by solving the equation

$$\frac{r}{\hat{\alpha}} + \frac{r(X_{(r+1)}/X_{(1)})^{\hat{\alpha}} ln(X_{(r+1)}/X_{(1)})}{1-(X_{(r+1)}/X_{(1)})^{\hat{\alpha}}} = \sum_{i=1}^{r}[lnX_{(i)} - lnX_{(r+1)}] \tag{6.10}$$

For a dataset that graphically exhibits a power-law tail, [182] proposed an asymptotic level-q test ($0 < q < 1$) which rejects the null hypothesis $H_0 : \nu = \infty$ (Pareto distribution) if and only if $X_{(1)} < [(nC)/(-lnq)]^{1/\hat{\alpha}}$, where $C = \gamma^{\alpha}$. The corresponding p value is given by $p = exp(-nCX_{(1)}^{-\alpha})$. In practice, they proposed the use of Hill's estimator,

$$\hat{\alpha_H} = [r^{-1} \sum_{i=1}^{r} [lnX_{(i)} - lnX_{(r+1)}]^{-1}, and \tag{6.11}$$

$$\hat{C} = \frac{r}{n}(X_{(r+1)})^{\hat{\alpha_H}} \tag{6.12}$$

for the estimation of parameter C and α. Note that a small value of $p < 0.1$ (suggested by [183]) in this case indicates that the Pareto distribution is not a good fit to the data. For more details about the description of the proofs and the method for the parameter estimation see [182].

Figure 6.6 (middle panel) shows the fitted Pareto and truncated Pareto distribution for both positive increments (middle left) and negative increments (middle right) as a function of discharge. The estimated p-values for positive increments for the discharges of 1500 l/s, 2000 l/s and 2800 l/s are 0.0066, 0.0024 and 0.0005 respectively, while for negative increments are 0.0092, 0.004 and 0.0011 respectively. Based on the estimated p-values ($p < 0.1$) we rejected the Pareto distribution for the bed elevation at the discharges of 1500 l/s, 2000 l/s and 2800 l/s. However, Figure 6.6 (middle panel) shows that the truncated Pareto distribution provided an acceptable fit to the data. The upper bounds on the pdfs of positive increments for the discharges of 1600 l/s, 2000 l/s and 2800 l/s were found to be 29.7 mm, 43.5 mm and 73.4 mm, respectively, which also correspond to the maximum bed elevation fluctuation (increment) for the aforementioned discharges respectively. Table 6.2 and Table 6.3 show the other relevant estimated parameters of fitted Pareto and truncated Pareto distribution for the discharges of 1500 l/s, 2000 l/s and 2800 l/s for both positive and negative increments. Note that the tails of the pdfs of bed elevation fluctuations for the probability of exceedance $P(X > x_{95\%})$ decay in a similar manner irrespective of discharge with a slope ~ -3.6 for positive increments and ~ -5 for negative increments (Figure 6.6 (bottom panel)).

Comparing the tail parameter (α) of the pdfs of the positive and the negative increments of the bed elevation (see Table 6.2 and Table 6.3), it can be seen that the

tail in positive increments is much heavier than in the negative increments for all the discharges considered in this study. This can be seen as another measure of quantifying the asymmetry in the pdfs of the bed elevation fluctuations. Moreover, this difference indicates that the dynamics of negative increments (erosion, stoss side of bedform) vs positive increments (deposition, mostly occurring in lee side of bedform) behave differently. Also note that the tails in pdfs of negative increments decay much faster (close to exponential decay) than tails in pdfs of positive increments.

In comparison to the positive tails of the bed elevation, the pdfs of the positive tails of instantaneous Reynolds stress decay faster (see Figure 6.7 and Table 6.4). Notice that the tails of the pdfs of instantaneous Reynolds stress become heavier as the discharge increases.

6.3.4 Physical interpretation of presence of asymmetry in instantaneous Reynolds stress distribution

In the previous section we characterize the asymmetry in the pdf's of the bed elevation and how it grows as a function of discharge. In this section we focus on the signature of asymmetry of bed elevation fluctuations on to the instantaneous Reynolds stress. Figure 6.8 shows the joint probability distribution of longitudinal velocity fluctuations (u') with transverse velocity fluctuations (w') obtained by removing their respective mean velocity component for the discharges of 1500 l/s (top left), 2000 l/s (top right) and 2800 l/s (bottom left). The asymmetric growth of the quadrants captured by the best fitted ellipse (using least square error) as a function of discharge is shown in the bottom right plot. Notice that, although the mass is more concentrated in quadrant 4, the scatter of joint distribution of velocity fluctuations in quadrant 2 becomes more prominent as the discharge increases leading to anisotropic growth of ellipse as a function of discharge (see Table 6.5). Also note that in case of plain or fixed bed, the shape of the ellipse will change symmetrically as a function of discharge.

Figure 6.9 shows the conditional pdfs of longitudinal velocity fluctuations (left panel) and transverse velocity fluctuations (right panel) as a function of discharge for each quadrant. Although the evolution of the pdf in each quadrant follow similar trend, it can be seen that with increasing discharge and hence evolving topography, the chance of finding a higher value of u' and w' is much higher in quadrant 2.

6.3.5 Interaction of instantaneous Reynolds stress and bedload transport

Figure 6.10 a, b and c show the power spectral density (PSD hereafter) of the bed elevation for the discharge of 1500 l/s, 2000 l/s and 2800 l/s. It can be seen from the PSD of the bed elevation that the variability in the bed elevation saturates at the scales of around 30 to 40 mins for the discharges of 1500 l/s, 2000 l/s and 2800 l/s suggesting that the largest scale of variability or bedform is of the order of 40 mins. This largest scale of variability was used as a moving average window to smooth the sediment transport and shear stress time series fluctuation smaller than 40 min. Figure 6.11 shows the observed sediment transport as a function of instantaneous Reynolds stress averaged over the largest bedform scale (40 mins). Note that the variability, shown as error bar, for both sediment transport and averaged instantaneous Reynolds stress increases with increasing discharge. A model is fitted to the data and compared with modified Muyer-Peter-Muller [184] empirical relation (Figure 6.11). The fitted model can be expressed as:

$$\widetilde{q_s} = 34.69\widetilde{\tau_{u'w'}}^{2.68} \tag{6.13}$$

It is evident from the figure (Figure 6.11) that the MPM relation under-estimate the sediment transport in the presence of bedforms. We suggest that a closer term including the variability in the transport rate should be added to get the representative transport condition under migrating bed forms. Although a formal derivation is beyond the scope of this paper and also number of discharges considered in this study are too less to interpret, we have attempted to propose the following relation:

$$< q_s >= K < \tau >^{3/2} + \frac{1}{2} \times \frac{3}{2} var(\tau) < \tau >^{-1/2} \tag{6.14}$$

where q_s is the sediment discharge per unit width, K is a constant of proportionality, τ is the dimensionless shear stress and $<>$ and var denote the mean and the variance of shear stress, respectively.

6.3.6 Multiscale statistics of bed topography

Structure function analysis was used to quantify the manner in which the statistics of the local fluctuations, or variability, in a bed elevation series change with scale. In particular, in order to examine the multi-scale structure of a time series $x(t)$ over a range of scales, a statistical analysis is performed on the differences (or increments) of the series at different scales a, denoted by $\delta x(t,a)$, and formally defined as:

$$\delta x(t,a) = x(t+a) - x(t) \tag{6.15}$$

with $\delta x(t,a)$ as the increment at time t and scale a. Note that while $x(t)$ is always positive, the fluctuation series $\delta x(t,a)$ can be both positive and negative; in fact, its mean value is zero. The estimates of the q^{th} order statistical moments of the absolute values of the increments at scale a, also called the partition functions or structure functions, $M(q,a)$, are defined as:

$$M(q,a) = \frac{1}{N}\sum_{t=1}^{N} |\delta x(t,a)|^q \tag{6.16}$$

where N is the number of data points of the series at scale a. The statistical moments $M(q,a)$ for all q completely describe the shape of the probability density functions (pdfs) of the increments as the scale a changes. If a series shows statistical scaling (is scale-invariant), $M(q,a)$ is a power law function of the scale a, that is:

$$M(q,a) \sim a^{\tau(q)} \tag{6.17}$$

where $\tau(q)$ is called the scaling exponent function. For a scale-invariant series, it can been shown that the function $\tau(q)$ completely determines how the pdf of the variable changes with scale [e.g.,[51, 47, 5]]. The most basic form of scaling, known as simple scaling or mono-scaling, occurs when the scaling exponents are a linear function of the moment order i.e., when $\tau(q) = Hq$. In this case, the single parameter H describes how the whole pdf changes over scale. If $\tau(q)$ is nonlinear, more than one parameter is required to describe how the behavior of the pdf changes over scale [e.g.,[51, 47]] and the series is called a multi-fractal. For most processes the non-linear relationship of $\tau(q)$ with q can be parameterized as a polynomial. The simplest form is a quadratic

approximation:

$$\tau(q) = c_1 q - \frac{c_2}{2} q^2 \tag{6.18}$$

Multi-scale analysis in this framework provides a simple way, using only two parameters c_1 and c_2, of parameterizing the change of the pdf over a range of scales. The parameter c_1 is a measure of the average "roughness" of the series; c_2, the intermittency parameter, gives a measure of the variability of the local fluctuations in the series. c_2 is related to the variance of the local Hölder exponent which measures the local degree of non-differentiability of the series [47, 5,].

Figure 6.12a shows the structure functions plotted as a function of scale of bed elevations monitored at sonar 3 for a discharge of 2000 l/s. The scaling range (the range of scales where structure functions show log-log linearity) in case of bed topography is of the order of 1-10 min, however, the largest scale of the bedform is of the order of 40 min. We observe that the $\tau(q)$ has a nonlinear dependence on q, which is an indication of the presence of multi-fractality (Figure 6.12b). Note that for brevity we have plotted the structure functions and $\tau(q)$ curve for the bed elevations sampled at probe 3 of 2000 l/s only. For the other discharges, the multifractal parameters are given in Table 6.6. From Table 6.6, it can be seen that the roughness coefficient c_1 along with the intermittency coefficient c_2 increases with increasing discharge.

This increase in intermittency (c_2) with increasing discharge suggests that the pdf of the bed elevation across the range of scale is changing faster, implying the bed is evolving/changing faster and is more inhomogeneous at higher discharge than at the lower discharge. Note that in case of mono-fractal the pdf of the fluctuations do not change with scales. (Also note that, one could relate the slope of the second moment of the structure functions to the slope of power spectrum with a relation $\beta = 2H + 1$, where β is the slope of power spectrum, and H is the Hurst exponent.)

6.4 Scale to scale interaction of bed elevation and instantaneous Reynolds stress

In the previous sections we computed the marginal statistics of the bed elevation, instantaneous Reynolds stress and the sediment transport at the resolution of our measurements. We discussed the physical reasoning for the presence of asymmetry in the

bed elevation fluctuations, instantaneous Reynolds stress and sediment transport distributions. In this section we show scale-to-scale interaction between bed elevation and instantaneous Reynolds stress distribution.

In principle, one could do similar scale-to-scale interaction analysis to show the interaction between instantaneous Reynolds stress and sediment transport but with the given experimental setup, our measurements of simultaneously sampled velocity fluctuations (resulting in instantaneous Reynolds stress) and sediment transport do not support this analysis. This is due to the spacing between the measurement location of velocities and the sediment transport which is $\sim$1.2 m in the flow direction in this case (see schematic of the experimental setup, figure 6.1 (right)) and will affect the interpretation of the results. Therefore, we focus on the scale-to-scale interaction of bed elevations and instantaneous Reynolds stresses.

Similar to the quantification of the contribution of energy at each scale to the overall energy as in the case of power spectral density or second order structure function (see Figure 6.12a), one can also evaluate the contribution of correlation between two multiscale processes (characterized by the presence of energy over a range of scale) to the overall correlation as a function of scale. In other words, two multiscale processes can be represented as a combination of functions at different scales.

For two signals or functions containing energy (variability) at multiple scales, cross-correlation analysis at multiple scales often offers valuable insight. The most efficient way to perform such an analysis is via wavelets, however, one could also use traditional increment analysis. The advantages for using wavelets over traditional increment analysis are the following. In general, increments and wavelet coefficients at a given scale share the same idea of analysis. In fact, wavelet coefficient computed using a wavelet similar to dirac delta function (for example Haar wavelet) at a given scale are same as traditional increments at that scale. However, such a wavelet is a poor wavelet because it is very irregular, and has low spectral localization and one vanishing moment. Using wavelets with higher vanishing moments and more regularity with better joint time/frequency localization results in wavelet coefficients with better statistical properties and better achievement of the data analysis at a given precise time scale. Moreover, wavelet transform with a suitable wavelet provides an efficient and robust framework for the detection-estimation of the scaling and scaling parameters.

The wavelet transform of a function $f(t)$ is defined as the integral transform of the function with a series of functions $\psi_{a,b}(t)$, i.e.,

$$W_{f(t)}(a,b) = \int_{-\infty}^{+\infty} f(t)\psi_{a,b}(t)dt \tag{6.19}$$

where the functions $\psi_{a,b}$ are obtained from the "mother" wavelet $\psi(t)$ by translation and scaling, i.e.,

$$\psi_{a,b}(t) = \frac{1}{\sqrt{a}}\psi(\frac{t-b}{a}); a > 0; b \in R. \tag{6.20}$$

Here a is the scaling parameter and b is the location parameter. The factor $\frac{1}{\sqrt{a}}$ is a normalizing constant chosen to ensure that the $\mathcal{L}^2$ norm is preserved.

For the wavelet transform to be invertible, the mother wavelet must have finite support and satisfy the invertibility condition $\int_{-\infty}^{+\infty} \psi(t)dt = 0$, i.e., it must have the area under the curve zero (which makes it a kind of local differencing function; e.g., see [48]; see also [49] for a review of applications in geomorphology). Wavelets with higher order vanishing moments i.e., $\int_{-\infty}^{+\infty} t^k\psi(t)dt = 0, (k = 1, 2.., N-1)$ are possible, resulting in higher order differencing filters which can remove polynomial non-stationarities from a signal. A commonly used mother wavelet is the family of Gaussian wavelets defined as the N-th order derivatives of a Gaussian function $g_0(t)$, i.e., $g_N(t) = (d^N/dt^N)g_0(t), (N = 1, 2, ..)$. It is noted that $g_N(t)$ has $(N-1)$ vanishing moments and that for $N = 2$ the wavelet is well know Mexican hat wavelet [49].

Once the wavelet transform is obtained, the wavelet cross-covariance between two signals $f_1(t)$ and $f_2(t)$ can be then computed as:

$$WCC_{f_1,f_2}(a,\Delta t) = \int_{-\infty}^{+\infty} W_{f_1}(a,b)W_{f_2}(a,b+\Delta t)db \tag{6.21}$$

where $W_{f_1}(a,b)$ and $W_{f_2}(a,b)$ are the wavelet coefficients of $f_1(t)$ and $f_2(t)$ respectively at scale a and location b. The wavelet cross-correlation can be obtained by appropriate normalization by the variance of the signals.

In this study, the fluctuations of bed elevations and instantaneous Reynolds stress at various scales were computed using the wavelet transform (equation(10)) with the wavelet $g_2(t)$. More details about the wavelet analysis can be found in [5, 185, 47].

Figures 6.13a and 6.13b show the timescale plot of wavelet coefficients for a range of scales for both bed elevation and corresponding instantaneous Reynolds stress for a discharge of 2000 l/s respectively. The branching of energy from larger to smaller scales, for both bed elevation and instantaneous Reynolds stress, is evident from these plots. To aid readers for better understanding of these timescale plots and visualizing the decomposition at different scales, transects at a scale of 6 min, for both the timescale plot of bed elevation (Figure 6.13a) and the instantaneous Reynolds stress (Figure 6.13b), are displayed in Figure 13c and 13d respectively. The maximum cross-correlation obtained between the scale-decomposed bed elevation and instantaneous Reynolds stress as a function of scale is shown in Figure 6.14. As expected, it is observed that with increasing scale the cross-correlation coefficient increases which shows larger scales are more highly correlated than smaller scales.

A few observations can be made from the plot of Figure 6.14. First, for very small scales (say less than 5 min) the cross-correlation coefficients are very small (order of 0.2) implying that the linear correlation does not capture the interaction of small scale features of turbulence and bedforms. This may be due to the distance of the velocity sensor (ADV) to the bed. Eddies modulated by the bed and smaller in size than the distance between the sensor and bed will not be detected by the sensor. A closer presence of velocity sensor to the bed might result in higher correlation coefficient. For larger scales, (scales greater than 20 min) correlation-coefficient becomes larger (~ 0.7) and statistically significant.

6.5 Discussion

Several mutifractal models for generating cascades (for example, Random multiplicative cascade models) have been proposed in the literature to model the multifractal nature of a signal or a function (e.g, rainfall, turbulence and other geophysical signals [49, 186]. In general, cascades are generated through a scale-invariant operator acting from largest scale L down to the smallest scale l of the system. These structures created at all scales $a\epsilon[l, L]$, for example, can be interpreted as typical eddies transferring energy to smaller scales through a shearing process. One of the limitations of these models is that they generally assume an instantaneous cascade i.e., the pdf at one scale (level) of cascade

only depends on the previous scale (level) (see [187] and references therein). Although these models can reproduce the similar multifractal parameters as obtained from the analysis of a natural signal, the asymmetric behavior of the pdf is not captured.

In the case of bed elevations analyzed in this study, the scaling range (log-log linear range) is approximately of the order of 1-10 min (for a discharge of 2000 l/s) depicting that the bedforms are organized or evolve in a self-similar way over that scaling range (Figure 6.12a). Considering all the three discharges studied here (Table 6.6), one can see that the degree of smoothness of bed elevation on an average, characterized by c_1 along with intermittency parameter c_2 increases with increasing discharge. This is consistent with the findings of [5] where it was shown that for the bed elevations at low discharge the intermittency coefficient is lower as compared to the bed elevations at high discharge. To this end, we have established the multifractal nature of bedforms. Note that these natural signals have a finite length of scaling range. This range can depend on the length and the resolution of the data collected. If the data set is long enough and sampled at a very high resolution one may capture the whole scaling range. Also note that in case of monofractals the shape of the pdf does not change over scales, while in multifractals the shape of pdf changes with scale.

In recent past, few studies have focused on intermittency together with scale-coupling in turbulent flows. For example, [188] have argued that small scales in turbulent flows are anisotropic and reflect the overall character of the flow, which is contrary to traditional notions. In other words, the information from the larger scales is transferred to the smaller scales (i.e, the scales at different levels are dependent) and that there is coupling between the larger scales and the smaller scales. Considering the bed elevations, the presence of multifractality and the asymmetry in the pdfs, indicate that the small scale features (bedforms) do not lose information of the large scale features (bedforms) and that there is a coupling between large scales and the small scales. We hypothesize that the water-worked plain bed topography has different statistics as compared to the plain bed obtained by removing the bedforms from a bedform dominated water-worked bed topography. We also suggest that, to model a flow or a process (e.g., bed topography) in a preferred direction, along with the multifractality (intermittency) asymmetry is another important quantity to account for, else the information of the flow direction will be unknown.

As mentioned earlier in section 6.3.2, the asymmetry in the case of temporal bed elevation (Figure 6.13a) is associated with large, abrupt changes (due to avalanche faces or sharp fronts) of bedforms. Figure 6.4b shows the fluctuations (increments) of the bed elevations shown in Figure 6.4a. From Figure 6.4b one can see that these large, abrupt changes in the bed elevation contribute to the heavy tail statistics of bed elevations. To gain further insight about the bed elevations, temporal bed elevations were transformed into spatial bed elevations using Taylor's hypothesis and are shown in Figure 6.4c. The simple relationship of Taylor's hypothesis (assuming the turbulence to be frozen) used can be expressed as:

$$X = UT, \tag{6.22}$$

where, X is the quantity in space, T is the quantity in time and, U is the average advection velocity. Here in this case the advection velocity is the celerity/velocity of the migrating bed forms. The average bed velocity obtained using cross-correlation between two sonars (sonar2-sonar6 and sonar4-sonar7, see figure 6.2b) is $\sim$ 15 m/hr. Note that in the real case bed forms keep on evolving (changes shape and size as in the case of turbulence eddies). It can also be seen from figure 6.4c that the wavelength of bedforms is of the order of 4m which is similar to the one obtained from high resolution longitudinal profiles (not shown here) surveyed at the end of the experiment.

It is interesting to note that the places on the bed profile where the bed topography is comparatively flat (Figures 6.2a,6.4a and 6.4c), the fluctuations in the bed elevations are close to zero (Figure 6.2b, 6.4b) and that they contribute to the density around the origin of the pdf. These locations are also the spots where the local bed shear stress is lower and has lower contribution to the overall sediment transport. This is also evident from the flatness index (Figure 6.4c, bed elevation) where for the lowest discharge (1600 l/s) the flatness index is higher as the bed is comparatively flat than bed at two other higher discharges.

One could relate the asymmetry seen in the pdf of the bed elevation fluctuations to the asymmetry in the pdf of instantaneous Reynolds stress. Over a bed topography, at the top of the crest higher shear stresses are observed while at the bottom of a crest lower magnitude of shear stresses are seen (due to recirculation and deceleration of the flow). Notice that the shape of the pdf of instantaneous Reynolds stress changes in a similar manner to that of bed elevation fluctuations as a function of discharge, implying that

bed structures can be inferred from the flow structures. This is also evident from the cross-correlation analysis (Figure 14) which shows scale-to-scale interaction of bedforms with instantaneous Reynolds stress that is with increasing scale the correlation obtained between bedforms and instantaneous Reynolds stress increases.

6.6 Concluding remarks

The experiments reported here were conducted in a large experimental channel at the St. Anthony Falls Laboratory to understand the coupled dynamics of flow and bedforms above the sediment-water interface. Simultaneous high resolution measurements of velocity fluctuations, bed elevations and sediment flux were sampled at the downstream end of the channel for a range of discharges.

The main results of this study can be stated as follows.

1. Probability density functions (pdfs) of the bed elevation fluctuations and the instantaneous Reynolds stress reveal heavy-tail statistics and a strong feedback between the co-evolution of bedforms and the near-bed turbulence. These results complement our previous findings [8] in which the signature of bedform evolution on the near-bed velocity fluctuations was confirmed via the presence of a spectral gap and two distinct power-law scaling regimes in the spectral density of velocity fluctuations.

2. A strong asymmetry in the probability distribution of bed elevation fluctuations and instantaneous Reynolds stresses is observed. We interpret this asymmetry, in view of the established intermittency (multi-fractality), as the result of scale coupling. In short, small-scale structures do not lose the information of the large-scale structures of flow and transport, rendering thus the scale-to-scale energy transfer locally anisotropic.

3. A simple relationship to quantify sediment transport using instantaneous Reynolds stress is proposed.

5. The higher order statistical moments analysis of bed elevations demonstrate the presence of multifractal scaling parameterized here with two parameters: the roughness and the intermittency parameter. Both roughness parameter and the intermittency parameter increases with increasing discharge.

4. The correlation obtained between bed elevation and instantaneous Reynolds stress at multiple scales increases with increasing scale.

5. Bed structures can be inferred from flow structures sampled close to the bed, although this potential application if used in the field would require a long time series of river flow velocities.

Q (l/s)	D(m)	v (m/sec)	S_w	h_R (m)	Shields stress (τ^*_b)	R_e	F_r	T_{mean} (^oC)	D_p (cm)	μ_b (mm)	σ_b (mm)	k
1500	0.43	1.04	0.0029	0.32	0 .05	454480	0.51	17.9	9.26	45.98	15	6.2
2000	0.55	1.18	0.0031	0.39	0.058	646640	0.51	23.5	12.59	59.21	23.95	5.3
2800	0.64	1.55	0.0044	0.44	0.099	992000	0.62	16.23	19.17	95.39	38.65	5.0

Q = water discharge for the run
D = average depth of flow in test section
v = average flow velocity
h_R = hydraulic radius
Sw = water surface slope
τ^*_b = dimensionless Shields stress (computed using hydraulic radius)
Re = Reynolds number (kinematic viscosity of water, $\nu = 1X10^{-6}$ m^2/sec)
Fr = Froude number
T_{mean} = mean water temperature.
D_p = distance of the velocity probe from mean bed level
μ_b = mean of temporal bed elevation series
σ_b = standard deviation of temporal bed elevation series
k = ratio between Dp and σb

Table 6.1: Hydraulic conditions and characteristics of temporal series of bed elevation

Parameters of truncated Pareto distribution				Pareto distribution	
Q (l/s)	alpha	Lower bound (gamma) (mm)	Upper bound (nu) (mm)	alpha	Lower bound (gamma) (mm)
1500	2.02	1.03	29.7	3.49	5
2000	2.08	1.54	43.5	3.24	5.3
2800	1.73	2.22	73.4	3.7	16.9

Table 6.2: Estimated parameters of truncated Pareto and Pareto distribution for positive increments of temporal bed elevations

Parameters of truncated Pareto distribution				Pareto	
Q (l/s)	alpha	Lower bound (gamma) (mm)	Upper bound (nu) (mm)	alpha	Lower bound (gamma)
1500	2.31	1.21	22.10	3.4	3.2
2000	2.65	2.09	26.9	4.91	7
2800	3.1	4.05	40	5.82	16.2

Table 6.3: Estimated parameters of truncated Pareto and Pareto distribution for negative increments of temporal bed elevations

Q (l/s)	alpha	Lower bound (gamma)
1500	5.79	0.84
2000	4.95	0.94
2800	4.25	1.09

Table 6.4: Estimated parameters of Pareto distribution for the positive tails of instantaneous Reynolds stress distribution

	Q = 1500 l/s			**Q = 2000 l/s**			**Q = 2800 l/s**		
	σ (u')	σ (w')	Corr.Coeff.	σ (u')	σ (w')	Corr.Coeff.	σ (u')	σ (w')	Corr.Coeff.
Q_{D1}	10.71	5.59	-0.11	11.77	5.97	-0.09	13.70	7.88	-0.06
Q_{D2}	12.98	6.46	-0.18	14.39	7.08	-0.21	18.64	9.58	-0.24
Q_{D3}	10.63	5.28	-0.08	11.77	5.93	-0.08	15.32	7.81	-0.03
Q_{D4}	12.68	6.03	-0.12	12.60	6.41	-0.09	15.49	7.97	-0.11

Table 6.5: Conditional statistics of u' and w' for different quadrants for the discharges of 1500 l/s, 2000 l/s and 2800 l/s

Q (l/s)	Probe	c_1	c_2	Scaling Range
1500	Probe 3	0.48	0.09	0.5-8 min
2000	Probe 3	0.53	0.12	0.5-10 min
2800	Probe 3	0.55	0.13	0.5-7 min

Table 6.6: Multifractal properties of bed elevation fluctuations

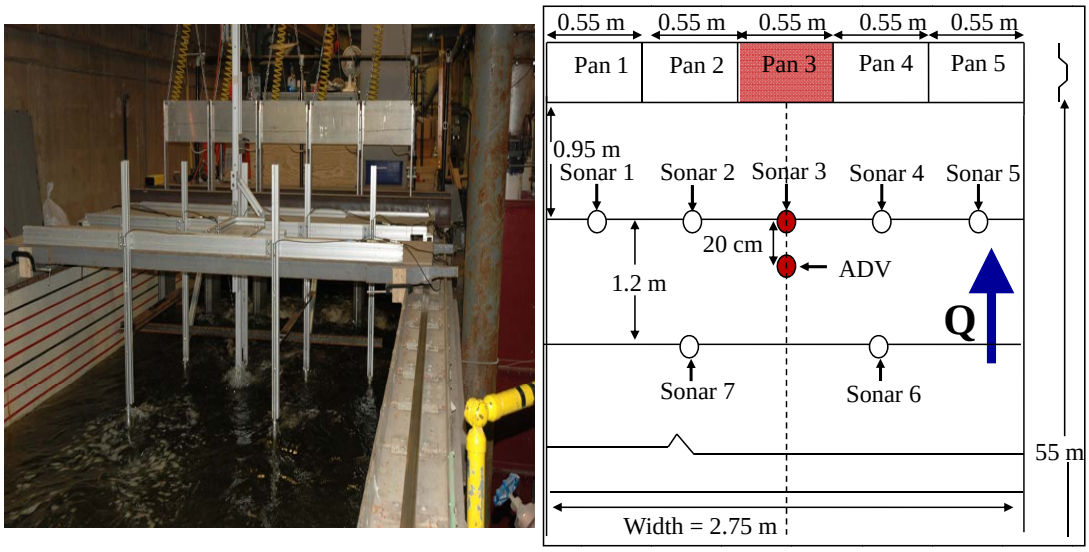

Figure 6.1: (Left) Experimental channel facility at the St. Anthony Falls Laboratory, University of Minnesota and, (right) schematic diagram showing the location of probes in the experimental channel. Sediment flux data were collected at five downstream pans, bed elevation fluctuations at seven sonar locations and the velocity fluctuations at one ADV location, for three different discharges. Note that the shaded parts (solid dots and box) along the centerline (dashed line) as we move from upstream to downstream represent the locations of velocity (v(t)), temporal bed elevation (h(t)) and sediment transport rates (S(t)), respectively, used in this study.

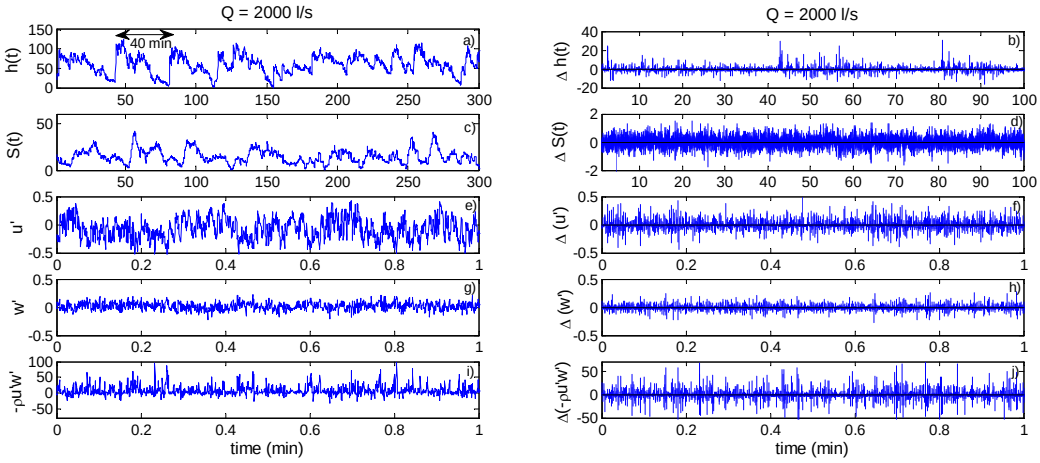

Figure 6.2: (Left Panel) Time series of the bed elevation (a), sediment transport (c), velocity fluctuations in the longitudinal direction (e), velocity fluctuations in vertical direction (g) and, instantaneous Reynolds stress (i). (Right panel) Derivatives (d/dt) of time series of the bed elevation (b), sediment transport (d), velocity fluctuation in the longitudinal direction (f), velocity fluctuation in vertical direction (h) and, instantaneous Reynolds stress (j). The flow direction in the case of bed elevation (Fig. 2a) is from the right to the left of the figure. Note that the S(t) series is obtained by using an averaging window of 5 min. Also note that all these measurements were obtained at a discharge of 2000 l/s.

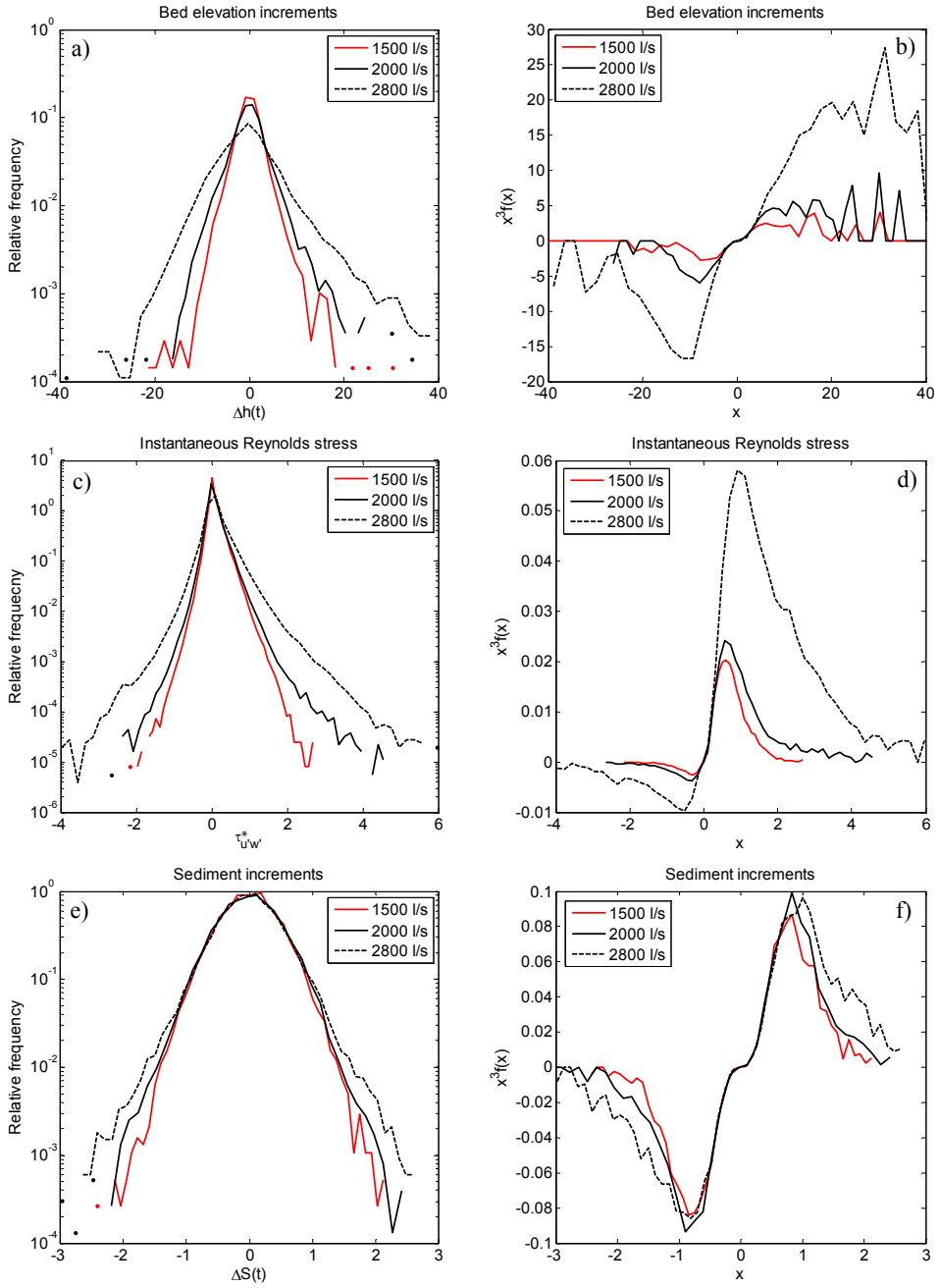

Figure 6.3: (Left panel) Semilog pdfs of bed elevation increments (top), instantaneous Reynolds stress (middle), sediment transport increments (bottom), and the right panel shows their third moment counterpart ($x^3 pdf(x)$), for the discharges of 1500 l/s, 2000 l/s and 2800 l/s.

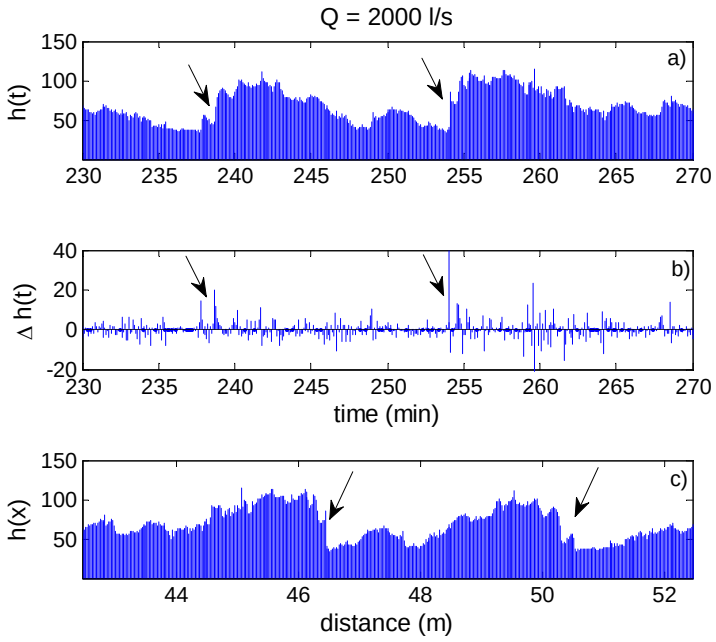

Figure 6.4: (Top) Zoomed-in time series of bed elevation (see figure 2a) and, it's increment (middle) for the discharge of 2000 l/s. (Bottom) shows the spatial transect of bed topography obtained by transforming temporal signal (top figure) using Taylor's hypothesis. Notice that the scales of bedforms are of the order of 4-5 m. The mean advected velocity of the bedforms used for transformation is $\sim$ 15 m/hr.

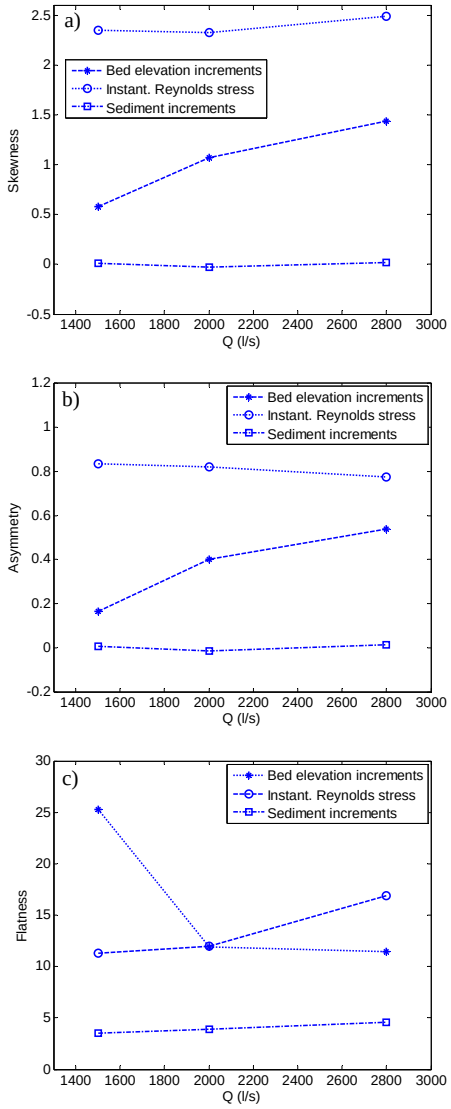

Figure 6.5: Skewness, Asymmetry and flatness as a function of discharge.

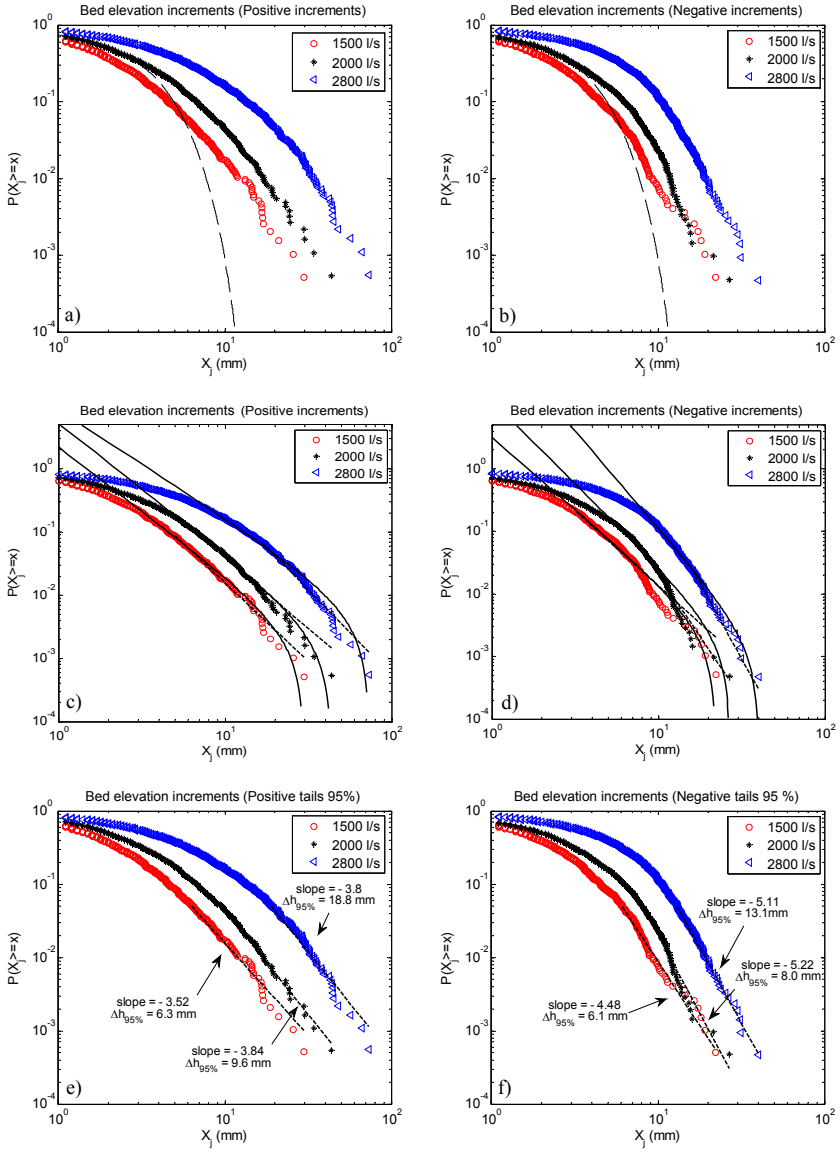

Figure 6.6: Log-log plot of the probability of exceedance of positive bed elevation increments (top left), and negative bed elevation increments (top right), fitted truncated Pareto (solid line) and Pareto distribution (dotted line) to positive increments (middle left) and negative increments (middle right). Bottom Panel shows the fitted Pareto distribution to the 95 percentile of the positive tails (bottom left) and negative tails (bottom right). The estimated parameters of these distributions are summarized in Table 6.2 and Table 6.3. Note that the dotted line in the top panel figures represent Gaussian distribution.

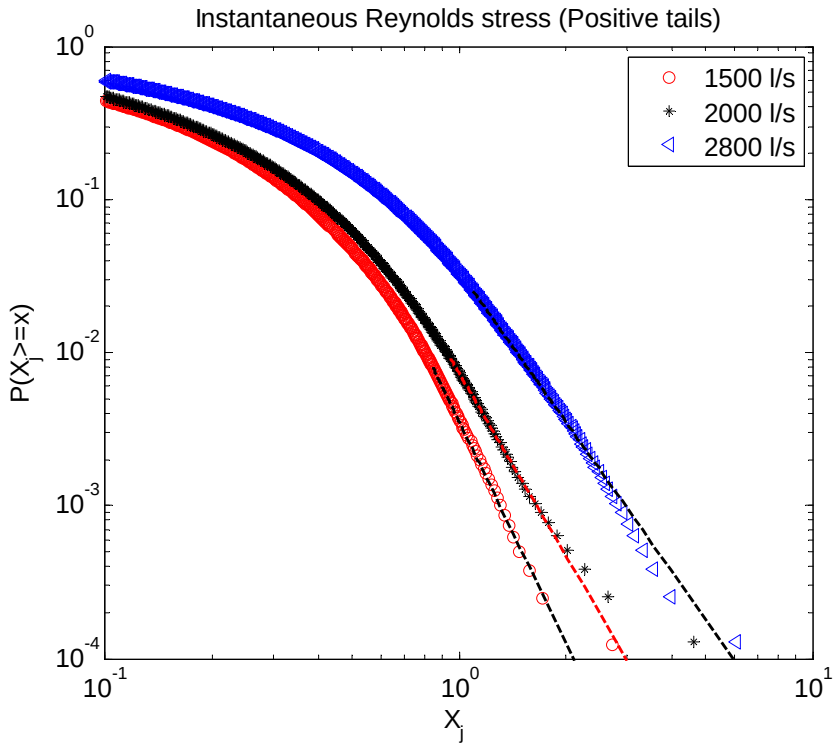

Figure 6.7: Log-log plot of probability of exceedance of the positive tails of instantaneous Reynolds stress distribution with fitted Pareto distribution. The estimated parameters of these distributions are summarized in Table 6.4.

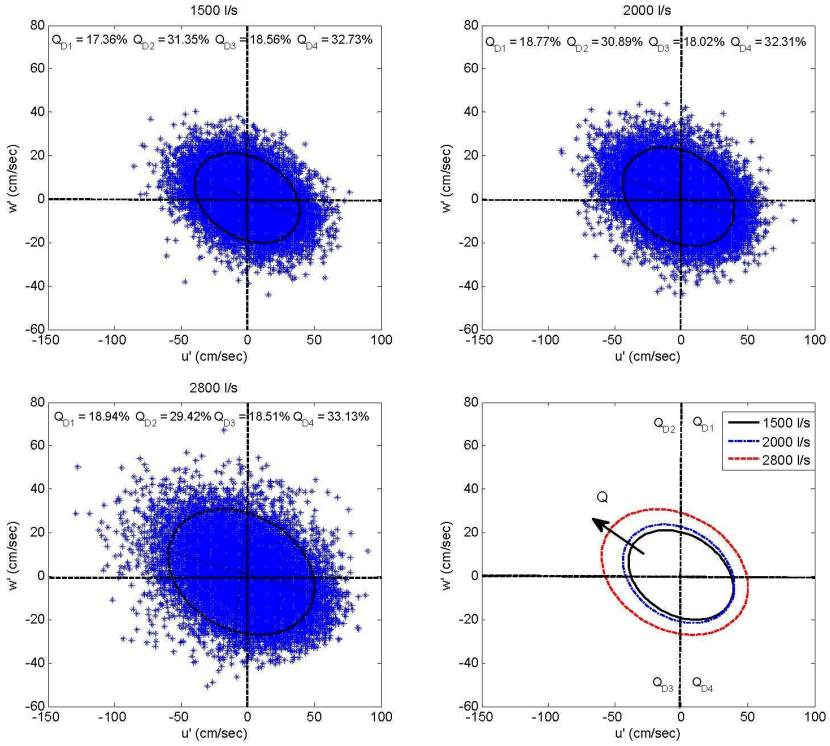

Figure 6.8: Joint probability distribution of longitudinal velocity fluctuations (u') with transverse velocity fluctuations (w') obtained by removing their respective mean velocity component for the discharges of 1500 l/s (top left), 2000 l/s (top right) and 2800 l/s (bottom left). The asymmetric growth of the quadrants captured by the best fitted ellipse as a function of discharge is shown in the bottom right plot. Notice that, although the mass is more concentrated in quadrant 4, the scatter of joint distribution of velocity fluctuations in quadrant 2 becomes more prominent as the discharge increases leading to anisotropic growth of ellipse as function of discharge.

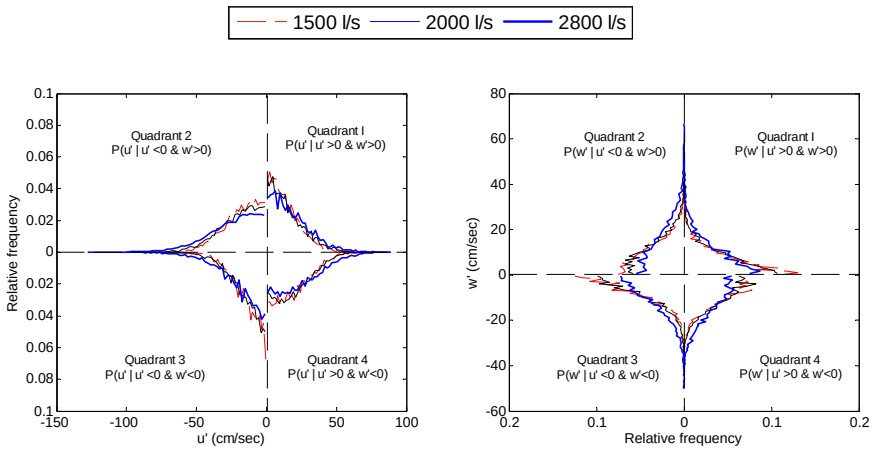

Figure 6.9: Conditional probability distribution of longitudinal velocity fluctuations (u') (left panel) and transverse velocity fluctuations (w') (right panel) for the discharges of 1500 l/s, 2000 l/s and 2800 l/s. Notice that, with increasing discharge the tails in pdfs of both longitudinal and transverse velocity fluctuation become heavier in quadrant 2 as compared to other quadrants.

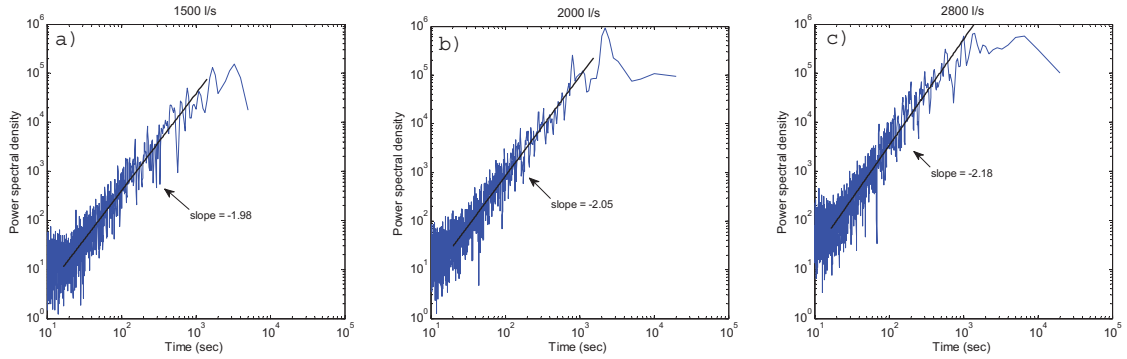

Figure 6.10: Power spectral density of temporal bed elevation for the discharge of 1500 l/s (left), 2000 l/s (middle) and 2800 l/s (right). Note that with increasing discharge the time-scale of occurrence of the largest bedform decreases.

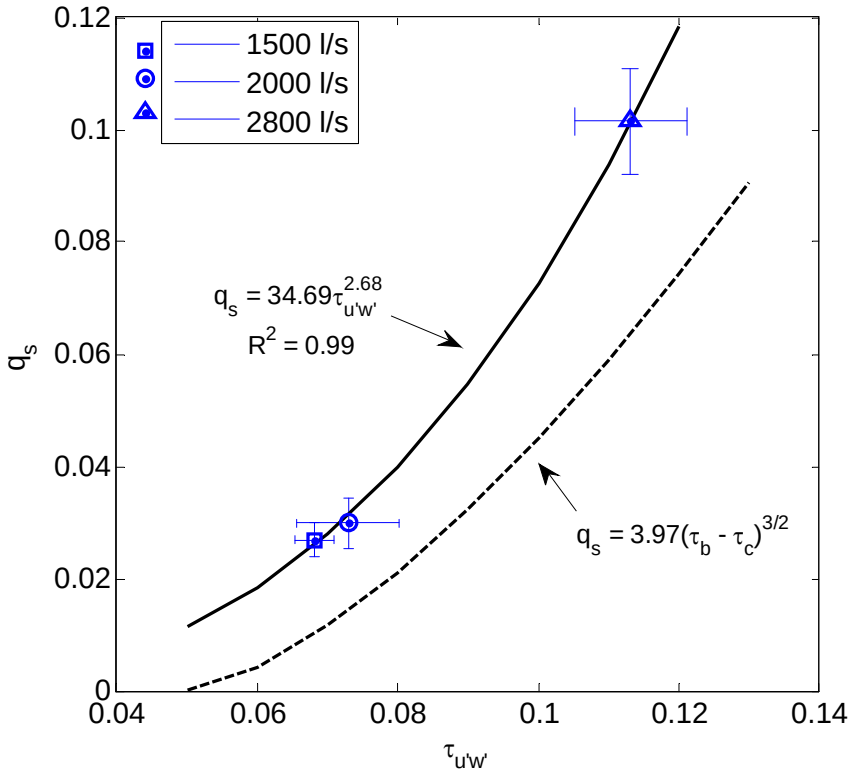

Figure 6.11: Sediment transport as a function of instantaneous Reynolds stress averaged over bedform length (40 mins). Solid line represents the power-law fit to the experimental data, while the dotted line represents the Muyer-Peter-Müller empirical relation. Note that in this figure both sediment transport rates and instantaneous Reynolds stress are dimensionless quantities.

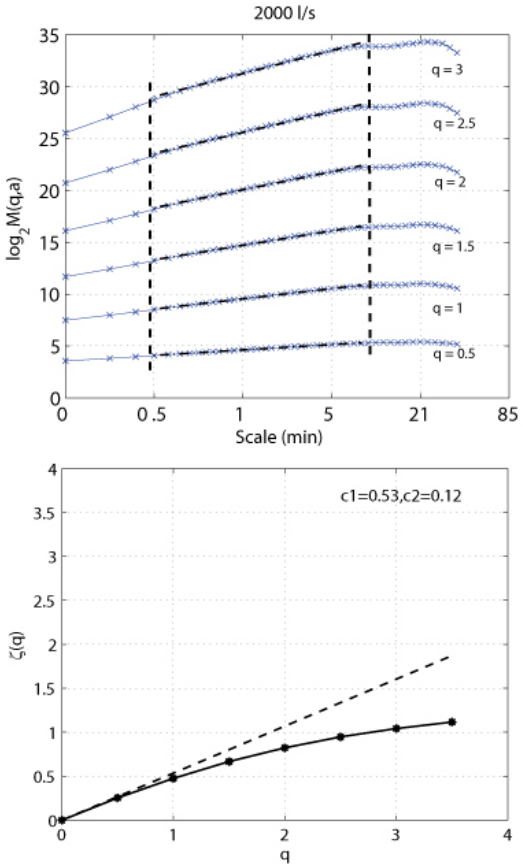

Figure 6.12: (Top) Statistical moments of the increments of the bed elevation time series as a function of scale and (bottom) the scaling exponents $\tau(q)$ estimated from the log-log linear regressions within the scaling regions. Notice the deviation of $\tau(q)$ from the linear line establishing the presence of multifractality.

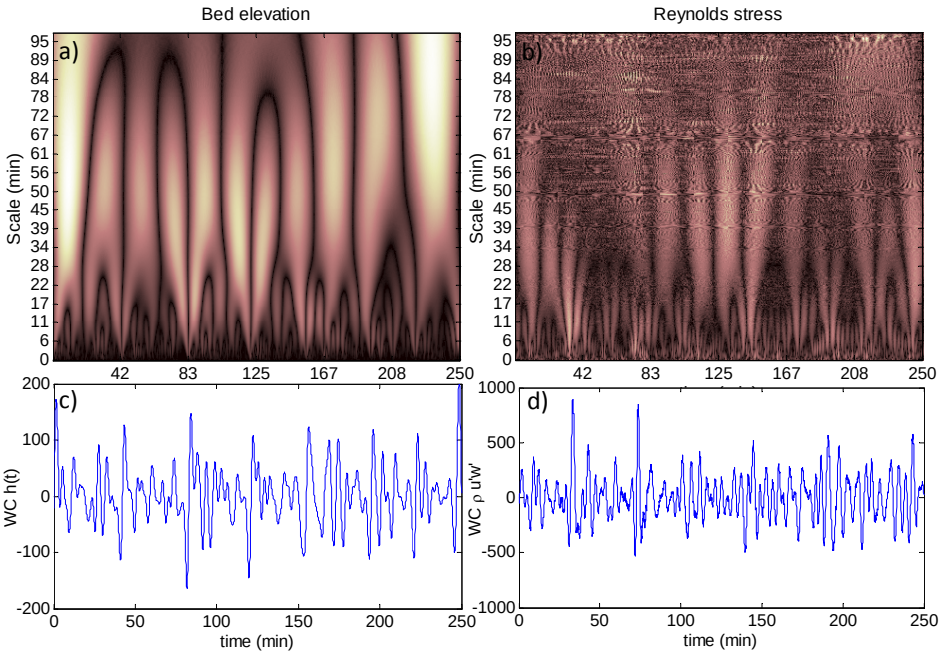

Figure 6.13: Timescale plots, obtained by wavelet analysis, of (a) bed elevation, (b) instantaneous Reynolds stress for a discharge of 2000 l/s. Bottom panel shows the transect obtained from the timescale plot (top) for the (c) bed elevation and (d) instantaneous Reynolds stress for a scale of 6 mins.

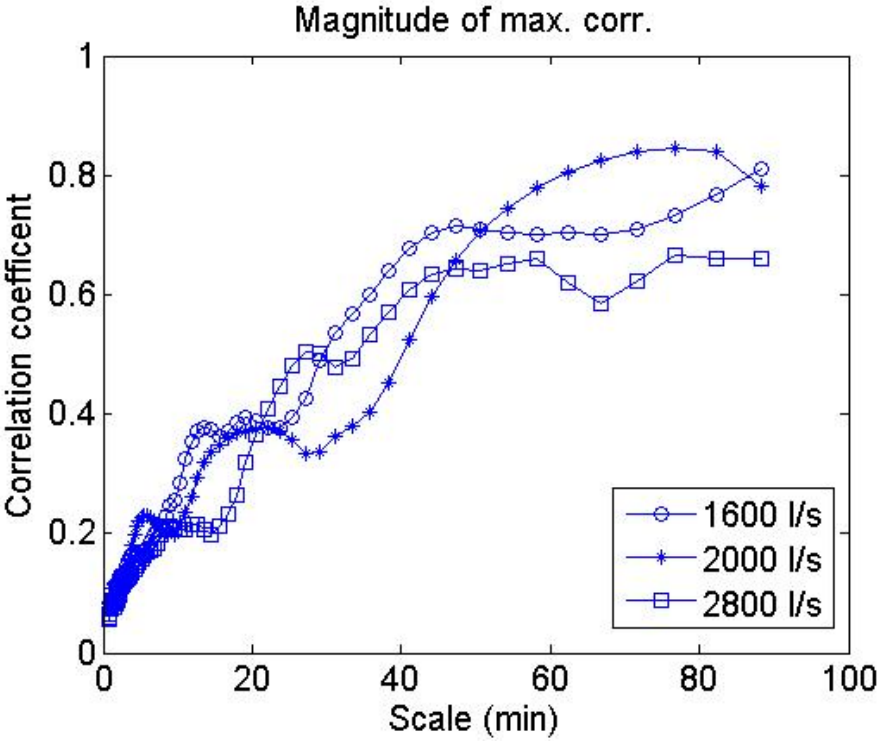

Figure 6.14: Plot of maximum cross-correlation obtained between temporal bed elevation and instantaneous Reynolds stress as a function of scale using wavelet analysis.

Chapter 7

On the influence of bed topography on tracer dynamics

A series of flume experiments were conducted at the St. Anthony Falls Laboratory to study the effect of migrating bed topography on tracer dynamics. Instantaneous, high-resolution bed elevations, velocity fluctuations and sediment transport rates along with travel distances of tracer particles representing the grain size distribution of bed material were measured, for a range of discharges. Spectral analysis of the bed elevations along with the statistics of tracer travel distances reveals a strong dependence of travel distances on spectral slope of the bed topography. We document that the statistics of tracer travel distances depend on the complexity of bed and that the larger particles move farther (once entrained) than smaller particles for the same duration of time. For the case of higher discharges where the bed topography is pronounced, it was demonstrated that the length of the bedforms dominates tracer travel distances. Results also show that the mean travel distance of smaller particles does not get much affected by the bed topography as the dynamics of smaller particles are mainly dominated by the particle hiding effect. The implications of these results for predictive modeling of sediment transport are discussed.

7.1 Introduction

Knowledge of tracer movement in gravel bed rivers is important for understanding transport of pollutants, nutrients, and sediments and for developing sediment transport models. Coarse material in these rivers primarily moves as bedload through rolling, sliding and saltation of particles. It has been observed that the movement of these particles is highly stochastic and depends on flow strength [189, 190, 191, 14, 192, 193]. Several stochastic theories of bedload transport have been proposed that reproduce the observed statistics of bedload transport and particle movement, e.g., [189, 190, 191, 194, 195, 179, 196, 197, 14, 193]. Although significant transport is generally associated with floods, bedload transport at low flow conditions is also of great interest e.g., [15, 2, 5, 198].

Though direct sampling of sediment transport is most common, tracer gravel particles offer some particular advantages and have found increased use in recent years (e.g. [194, 195, 199, 200]). For example, the stochastic behavior of a particle movement in a bedload dominated environment, which consists of a series of starts and stops can be well described by tracer particles [200]. Tracer particles also provide logistical and safety advantages, for example, they can be installed during low flow conditions in a river or a stream, thereby avoiding direct sampling of bedload during floods.

In recent years, the use of tracer particles to characterize motion of individual particles and bedload transport has increased significantly. Use of high frequency radiotracing techniques and magnetic tracers has made it possible to directly measure step lengths and rest periods in natural sedimentary systems, e.g., [201, 199, 194, 195, 202]. Nevertheless, rigorous quantitative studies of travel lengths and pathways of individual particles, duration of transport and rest periods, and the influence of particle characteristics on travel distances are relatively rare.

Several experimental studies have focussed on the tracer particle movement in the plain bed conditions (e.g., [189, 190, 191, 179, 203]. For example, [179] studied the movement of tracer particles in the plain bed conditions, where they showed that the statistics of tracer displacements can be related to channel-averaged hydraulic parameters, and thus linked to macroscopic aspects of bed load transport. Similar experiments were conducted by [203] where heavy tailed distributions in the travel distances of tracer

particle were proposed and explored. [197] reformulated the probabilistic Exner equation considering that the probability density function (PDF) of particle displacements has a heavy-tail, i.e., very large displacements are often possible albeit with small probability.

In contrast to the studies of tracer particles on plain bed, the studies of tracer particles in the presence of bedforms are rare, in fact, to the best of our knowledge, there is no such study which shows the direct influence of bed topography on tracer movement at varying discharges. The scope of the present study is to quantify the direct influence of bed topography on tracer movement at varying discharges and propose models for predictive modeling of bed evolution and sediment transport. Our results can be applied to a wide range of hydrologic regimes, from flash floods to snowmelt dominated systems.

The paper is structured as follows. In the following section a brief review of the experimental setup is given. Section 7.3 presents the physical characteristics of spatial bed topography. Section 7.4 characterizes the marginal statistics of tracer travel distances. Section 7.5 presents higher order structure function analysis of bed topography. Finally concluding remarks are given in section 7.6.

7.2 Experimental Setup and data analyzed

Experiments were conducted in the Main Channel facility at the St. Anthony Falls Laboratory, University of Minnesota. The Main Channel is 55 m long, 2.75 m wide and has a maximum depth of 1.8 m with a maximum discharge capacity 8000 l/s . It is a partially sediment recirculating channel while the water flows through the channel without recirculation. Intake of the water in the channel was directly from the Mississippi River. The bed of the channel was composed of a mixture of gravel and sand with a median particle size diameter, $d_{50} = 7.7$ mm, $d_{16} = 2.2$ mm and $d_{84} = 21.2$ mm. Figure 7.2a shows the photograph of the grains present on the bed surface whereas Figure 7.2b shows the grain size distribution of the bed material used in the experiments.

Prior to data collection a constant water discharge, Q, was fed into the channel to achieve quasi-dynamic equilibrium in transport and slope adjustment for both water and bed surface. Determination of the dynamic equilibrium state was evaluated by checking the stability of the 60 min average total sediment flux at the downstream end

of the test section. Using the pan accumulation data, the acquisition software computed a 60 min mean of sediment flux in all five pans. Dynamic equilibrium was reached when variation in this value became negligible. After attaining equilibrium, experiments ran for approximately 5 hrs. (More details about the experimental setup can be found in [5, 6, 8]).

The flow depth for all the experimental runs was in between 0.25 m and 0.5 m (see Table 7.1 for all other relevant hydraulic parameters). Three different sizes (9-16 mm, 16 mm and 22 mm) of paramagnetic particles (45 percent magnetite) having the same density as the bed material, each a different color, were used as tracers. These tracer particles were representative of bed grain size distribution (see Figure 7.2b).

In addition, 15 columns of blue painted tracer particles (non magnetic) were inserted at different cross-sections (Figure 7.1) in the channel prior to each run, but after the channel reached equilibrium. To insert the columns, a 6 inch diameter metal cylinder was inserted 10 cm into the bed. All sediment down to the bottom of the cylinder was excavated and sieved for grain size distribution. Sediment larger than the d_{50} of the bed material was replaced with three different sizes (8-11 mm, 11-16 mm and 16-22 mm) of blue painted rocks, matched by size and mass of the excavated material. The painted rocks and the native sediment smaller than the size of d_{50} from the excavated material were thoroughly mixed and returned to the cylinder to pre-sample elevation.

Once the tracer columns were installed, the channel was run at a constant depth and discharge for a duration of 5 hr. During the entire run, flow velocity, bed topography both in space and time, and sediment flux was measured at the end of the flume (see schematic of the channel in Figure 7.1). Flow velocities were measured using acoustic Doppler velocitimeter, bed elevations were sampled using submersible sonar transducers of 2.5 cm diameter for flow on condition whereas as laser scanner was used during flow off conditions. For the spatial bed elevation a three-axis positionable data acquisition (DAQ) carriage was used. This DAQ was designed, fabricated, and installed at St. Anthony Falls Laboratory. The DAQ carriage was capable of traversing the entire 55 x 2.74 meter test section and could position probes to within 1 mm in all three axes. Streamwise travel speeds of DAQ could be set up to 2 m/s. The DAQ carriage was controlled by a backbone computer that also served as the master time clock for all data collection in the study.

After this 5 hr. period, a number of marked paramagnetic tracer particles (200 large, 400 medium and 800 small) were released as a line source at the upstream end of the channel. The channel was allowed to run for another 5 minutes; then the channel was shut down and drained. Once the channel bed dried, the tracer particles that have not passed the full length of the channel were found in the channel bed via visual inspection and a handheld magnetometer. The location and the size of each tracer particle was noted. Most of the tracer particles lying on the bed surface were found visually and those trapped into the subsurface were excavated carefully by digging. As these tracers particles were collected, the planted tracer columns were also located and carefully excavated via an 8-inch diameter cylinder. The excavated material was sieved and the mass entrained from the column was recorded.

The data presented here are the spatial bed elevation (10 mm resolution) sampled at the end of the run using a range finding laser attached to the DAQ, the temporal bed elevation collected at the downstream end of the flume, and the travel distances of tracer particles exposed for approximately 5 min in the flow at the end of the run. Measurements were taken over a range of discharges corresponding to different bed shear stresses. Bed shear stress is often characterized in terms of the dimensionless Shields stress, τ_b. For steady, uniform flow it may be approximated as

$$\tau_b^* = \frac{h_R S}{R d_{50}}, \tag{7.1}$$

where h_R and S are the hydraulic radius and channel slope, respectively, and $R = 1.65$ is the relative submerged density of silica.

Here we report the data collected at the discharges of 600, 800, 950 and 1600 l/s corresponding to average bed shear stress of 0.085, 0.102, 0.105 and 0.105 respectively (for details about the hydraulic conditions see Table 1). Critical Shields stress (τ_c^*) was assumed to be 0.03 as suggested by [112] and references therein.

7.3 Physical characteristics of spatial bed topography

Quantification of bedform size: Figure 7.3 shows the transects of the bed elevations obtained at the end of the experimental run (flow off), in the centerline of the flume, as a function of discharge. It can be seen from these transects that with increasing discharge

the bedforms become higher in size. The average bedform heights extracted from the spatial bed transect estimated using the methodology described in [185] for the discharges of 600 l/s, 8000 l/s, 950 l/s and 1600 l/s were 2.5 cm, 3.34 cm, 4.64 cm and 5.26 cm, while the average bedforms lengths were 6.58 m, 4.93 m, 3.7 m and 3.58 m, respectively. Notice that with increasing discharge the bedforms height increases while their length decreases. These bedforms were mainly bedload sheets at the low discharge and transitioning to dunes as the discharge was increasing. Figure 7.4 shows the cumulative frequency histograms of the standardized bedform heights $((h_{bf} - \overline{< h_{bf} >})/\overline{std(h_{bf})})$ (top panel) and the standardized bedform lengths $((L_{bf} - \overline{< L_{bf} >})/\overline{std(L_{bf})})$ (bottom panel) for the discharges of 600 l/s, 800 l/s, 950 l/s and 1600 l/s. These distributions of bedform heights and bedform lengths for each discharge were obtained from the ensemble of bedforms heights and lengths extracted from the transects obtained at distances of 0.5 m across the width of the flume at that particular discharge, respectively. Interestingly, it is observed that the distribution of bedform heights and bedform lengths does not change its shape significantly as a function of discharge, however on a close inspection the tails look slightly thicker than those of the Gaussian distribution (shown for comparison in Figure 7.4a, b).

Figure 7.5 shows the ratio of mean bedform length $< L_{bf} >$ to mean bedform height $< h_{bf} >$ (aspect ratio) as a function of discharge. As can be seen from Figure 7.5 that with increasing discharge the aspect ratio of bedforms decreases, i.e., with increasing bedform height bedform length decreases.

Power spectral density: A commonly used tool to measure the distribution of energy (variance) in the signal across spatial or temporal scales and identifying transitions (scaling breaks) is the Power Spectral Density (hereafter PSD). A simple way to estimate PSD is by taking the fast Fourier transform (FFT) of the signal [116,]. For a discrete signal $X(t)$, the PSD is given by

$$\Phi(\omega) = \left| \frac{1}{\sqrt{2\pi}} \sum_{n=-\infty}^{\infty} X(t) e^{-i\omega t} \right|^2 = \frac{\hat{X}(\omega)\hat{X}^*(\omega)}{2\pi} \tag{7.2}$$

where $\hat{X}(\omega)$ is the discrete Fourier transform of $X(t)$, $\hat{X}^*(\omega)$ is its complex conjugate and ω is the wave number. In our case the signal $X(t)$ is the spatial transect of bed elevation. Special emphasis is placed here on identifying spectral scaling ranges, i.e.,

ranges of scales over which log-log linearity is observed in the power spectral density.

The PSDs of the spatial bed elevation (sampled at a resolution of 10 mm) for the discharges of 600 l/s, 800 l/s, 1000 l/s and 1600 l/s are shown in figure 7.6. In the case of low discharge (600 l/s), two clear scaling ranges can be observed with a distinct scaling break, one due to micro-topography and small bedforms and the other one due to bedload sheets. As the discharge increases the scaling break disappears suggesting that more organized bedform are evolving over the bed.

A few more observations can be made from the PSD of the spatial bed transects. The slope of the PSD of the spatial bed transect increases with increasing discharge as a power-law with wavelength ω, that is,

$$S(\omega) \sim \omega^{\beta} \tag{7.3}$$

where $S(\omega)$ is the PSD, ω is the wavelength and β is the scaling exponent which ranges from 1.3 to 2.4 for the discharges of 600 l/s, 800 l/s, 950 l/s and 1600 l/s. This indicates that for the low discharge smaller scale features contribute, relatively to the larger features, with a lot of energy to the PSD whereas at the higher discharges large scale features contribute to the energy (PSD). Note that the slopes are computed over the scaling range $\sim$ 15 cm to 2 m for all the discharges of 600 l/s, 800 l/s, 950 l/s and 1600 l/s.

7.4 Tracer travel distances

In order to understand and quantify the dynamics of individual particles over the evolving bed topography, 1400 paramagnetic tracer particles of three different sizes (small: 8 mm, medium: 16 mm, large: 22 mm) were introduced to the flow at the upstream end of the channel (see schematic in Figure 7.1) for a duration of $\sim$5 mins before the flow in channel was turned off. Figure 7.7 shows the mean travel distances for 8 mm, 16 mm and 22 mm size particles for the discharges of 600 l/s, 800 l/s, 950 l/s and 1600 l/s. It can be seen from Figure 7.7 that for the large size particle the mean travel distance decreases with increasing discharge. For example, the mean travel distance for the large particles at a discharge of 600 l/s is $\sim$ 24 m whereas for the discharge of 1600 l/s is $\sim$ 8 m. Similar results of decreasing mean travel distances with increasing discharge

are obtained for the medium size particle. However, the mean travel distances of the small size particle do not change significantly as a function of discharge. This is due to the fact that the smaller particles experiences shielding effect by larger particles which is often known as 'hiding effect' at all flows. In addition to the mean travel distances, the standard deviation of the travel distances also behaves in a similar manner, i.e., the standard deviation of the travel distances decreases with increasing discharge for both large and medium particles whereas does not get affected significantly by the bedform height for the small particles (see Figure 7.8).

It is interesting to note that the mean travel distances at the higher discharge is similar to the characteristic length scale of the largest bedform present on the bed topography (see Figures 7.7, 7.6) suggesting that the bedform acts as the first order control on the probabilistic structure of tracer travel distances conditional on the size of the tracer particle. Also note that in the case of planar bed with small bedfrom heights (low discharge), larger particles travel further as compared to the bed with higher bedforms, implying that larger bedforms (in height) have higher trapping potential.

In the case of higher discharge (taller bedforms) it has been observed that most tracer particles were found buried in the slip face of the bedforms. This observation is consistent with the observation of [204] where pebbles and cobles were found buried under the bed layers during the process of scours and fills.

Figure 7.9 shows the cumulative density functions (CDFs) of tracer travel distances for the discharges of 600 l/s (a), 800 l/s (b), 950 l/s (c), and 1600 l/s (d). From Figure 7.9 it can be seen that at lower discharge (600 l/s), the CDF of small size tracer particles behaves quite distinctly as opposed to the CDFs of medium and large particles. On the other hand, for higher discharge (1600 l/s) the pdfs of all three size tracer particles look similar. For example, at 600 l/s approximately 82% large particles, 62% medium particle and 2% small particles travels further than the characteristic length scale of the bedforms (∼8m), while at 1600 l/s discharge 24% large, 12% medium and 2% small particles travel further than the characteristic length scale of the bedform. This suggests that for the higher discharge the travel distance for larger particles is bedfrom dominated whereas in the case of smaller particles it is micro-topography dominated. Furthermore, these plots suggest that at higher discharges, bedform movement dominate sediment transport.

7.5 Higher-order multiscale statistics of bed topography

In section 3 we showed the power-law behavior of the PSD of the bed elevation suggesting that the energy is distributed over a broad range of scales. However, the spectrum characterizes only the second order statistics of bed elevations increments. In other words, the spectrum does not capture inhomogeneities coming from abrupt fluctuations present in the signal. In this section we present the higher order statistics and show the change in the shape of the pdfs of bed elevation increments as a function of scale as wells as discharge. For this purpose we use structure function analysis on the bed elevation increments, $\Delta h(x, a)$. Increments can be defined as:

$$\Delta h(x, a) = h(x + a) - h(x) \tag{7.4}$$

where x is the spatial location and a is the scale. Notice that while $h(x)$ can only be positive (since $h(x)$ is computed with reference to the lowest bed elevation i.e., the global minimum), the increments $\Delta h(x, a)$ can be both positive and negative, and in fact they have a zero mean.

The estimates of the q^{th} order statistical moments of the absolute values of the increments at scale a, also called the partition functions or structure functions $M(q, a)$, are defined as:

$$M(q, a) = \frac{1}{N} \sum_{x=1}^{N} |\Delta h(x, a)|^q \tag{7.5}$$

where N is the number of data points of the series at scale a. The statistical moments $M(q, a)$ for all q completely describe the shape of the probability density function (PDF) of the increments at scale a. Statistical scaling, or scale invariance, requires that $M(q, a)$ is a power law function of the scale, that is:

$$M(q, a) \sim a^{\tau(q)} \tag{7.6}$$

where $\tau(q)$ is the so-called scaling exponent function. The simplest form of scaling, known as simple scaling or mono-scaling, is when the scaling exponents are a linear function of the moment order i.e., when $\tau(q) = Hq$. If $\tau(q)$ is nonlinear, the process is called multiscaling and more than one parameter is required to describe the evolution of

the PDFs over scales [51, 47]. For most processes the non-linear relationship describing $\tau(q)$ with q can be parameterized as a polynomial, and the simplest form is a quadratic approximation:

$$\tau(q) = c_1 q - \frac{c_2}{2} q^2 \tag{7.7}$$

The multi-scale analysis in this framework provides a compact way, using two parameters c_1 and c_2, of parameterizing the change of the PDF over a range of scales. The parameter c_1 is a measure of the average "roughness" of the series (akin to the Hurst exponent H) and c_2 is the so-called intermittency parameter. A value of c_2 different than zero implies that the tails of the distribution stretch differently than the body as one changes scale. Following the geometrical interpretation of the statistical scaling (e.g., [34], see also [47]), the parameter c_2 relates to the local roughness or degree of differentiability of the signal, as measured by the local Hölder exponent h. A value of $c_2 \neq 0$ implies a temporarily or spatially inhomogeneous arrangement of spikes and thus the presence of a distribution of local Hölder exponents as opposed to a single value of H for a simple scaling process. In other words, the signal contains pockets of high fluctuations arranged over its domain in such a way that depending on the chosen wavelet they manifest statistically in complicated ways.

Figure 7.10 shows the schematic of the bedform depicting the stoss and the lee part of the bedform. It can be seen from Figure 7.10 that the positive increment ($\Delta h(t) = h(t + \Delta(t)) - h(t)$)) corresponds to erosion whereas negative increments corresponds to deposition. The flow direction is from left to right of the figure (Figure 7.10).

Figure 7.11 shows the scaling of the moments of bed elevation increments $\delta h(x, a)$ as a function of scale, as defined in the above section, for the discharges of 600 l/s, 800 l/s, 950 l/s and 1600 l/s. Note that for all discharges, the structure functions follow a power-law relation with scale, a, over a range of scales from 5 cm to 2 m.

Figures 7.12 shows the computed $\tau(q)$ curves from the slopes of the moments shown in Figure 7.11 within the scaling range, respectively. It can be seen that the $\tau(q)$ curves have a nonlinear dependence on q, indicating the presence of multi-fractality for all the discharges and the degree of nonlinearity increases with increasing discharge. The parameters of multifractality were calculated by approximating the $\tau(q)$ as a quadratic function in q and are shown in Table 3. Note that the slope of the second order structure

function $2H$ is related to slope of the PSD with a relation $\beta = 2H + 1$, where β is the slope of PSD, and H is the Hurst exponent.

A Few observations can be made from the multifactal properties of the bed elevations shown in Figure 7.12. In general, both the roughness parameter c_1 and the intermittency parameter, c_2, increase with increasing discharge. The increasing c_1 from 0.34 at the discharge of 600 l/s to 0.66 at the discharge of 1600 l/s suggests that the correlation in bed elevation fluctuations is changing from anti-correlation at low discharge to positive correlation at high discharge. In other words, the bed elevation fluctuations become smoother with increasing discharge. (Note that the Hurst exponent ($c_1 = H$ in mono fractals) $0 < H < 0.5, H = 0.5$ and $1 > H > 0.5$ represents anti-correlation, zero-correlation and positive correlation, respectively, in a signal). The increasing c_2 with increasing discharge suggests a more inhomogenous arrangement of the various strength singularities or abrupt bed elevation fluctuations over time in bed at higher discharges compared to the bed at lower discharges. Also note that the parameters c_1 and c_2 were computed from the similar scaling range 5 cm to 2 m for all the discharges of 600 l/s, 800 l/s, 950 l/s and 1600 l/s.

7.6 Summary and conclusion

This paper investigates the behavior of tracer particle movement in the presence of gravel bedforms formed in a large-scale experimental channel under different flow conditions. The main results of this study can be stated as follows:

1. Statistics of tracer travel distances reveal a strong dependence of travel distances on the multi-scale variability of bed elevation fluctuations.

2. In general, larger particles move farther (once entrained) than smaller particles for the same duration of time.

3. For the case of higher Q with pronounced bed topography, the characteristic length scale of the bedform acts as the first order control on the probabilistic structure of tracer travel distances conditional on the size of the tracer particle.

4. Micro-scale topography (scales $<$ bedform length, L_{bf}), which is a function of Q, exerts control on small particles.

5. Trapping potential increases with increasing bedform height.

6. With evolving bedforms as a function of discharge, bed topography becomes more inhomogeneous.

7. Need to incorporate macro-scale to micro-scale variability in bed topography to improve sediment transport modeling.

Q (l/s)	**Depth (m)**	**Avg BS**	**Avg WS**	**Hydraulic Radius (m)**	**T* (computed using WS)**	**T*/Tc**	**$<h_{bf}>$ (cm)**	**Std(h_{bf}) (cm)**	**Length of bedform (L_{bf}) (m)**
600	0.217	0.0051	0.0050	0.187	0.085	2.44	2.5	0.65	6.58
800	0.245	0.0053	0.0053	0.208	0.102	2.92	3.34	1.15	4.93
950	0.27	0.0053	0.0050	0.226	0.105	3.01	4.64	2.22	3.7
1600	0.365	0.0038	0.0037	0.288	0.105	3.00	5.26	2.01	3.58

Table 7.1: Hydraulic conditions and spatial bed elevation statistics

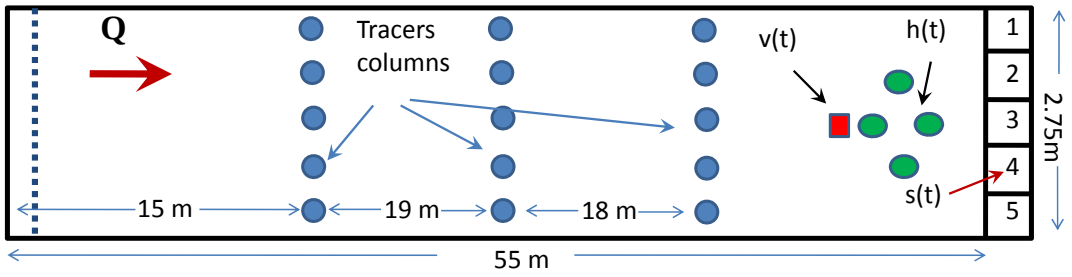

Figure 7.1: Schematic of the experimental setup showing the locations of measurement of bed elevation, velocity fluctuations, sediment flux, and tracer columns. Note that the paramagnetic tracers were introduced 5 min before the flow was shut down.

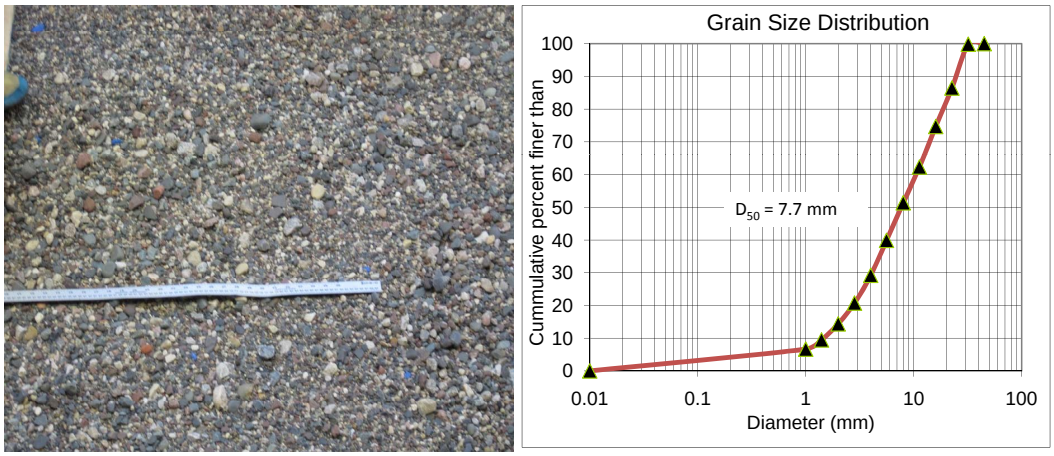

Figure 7.2: (left) A photograph of the water-worked bed showing the grains present on the surface for a discharge of 800 l/s, (right) grain size distribution of the initial bed material.

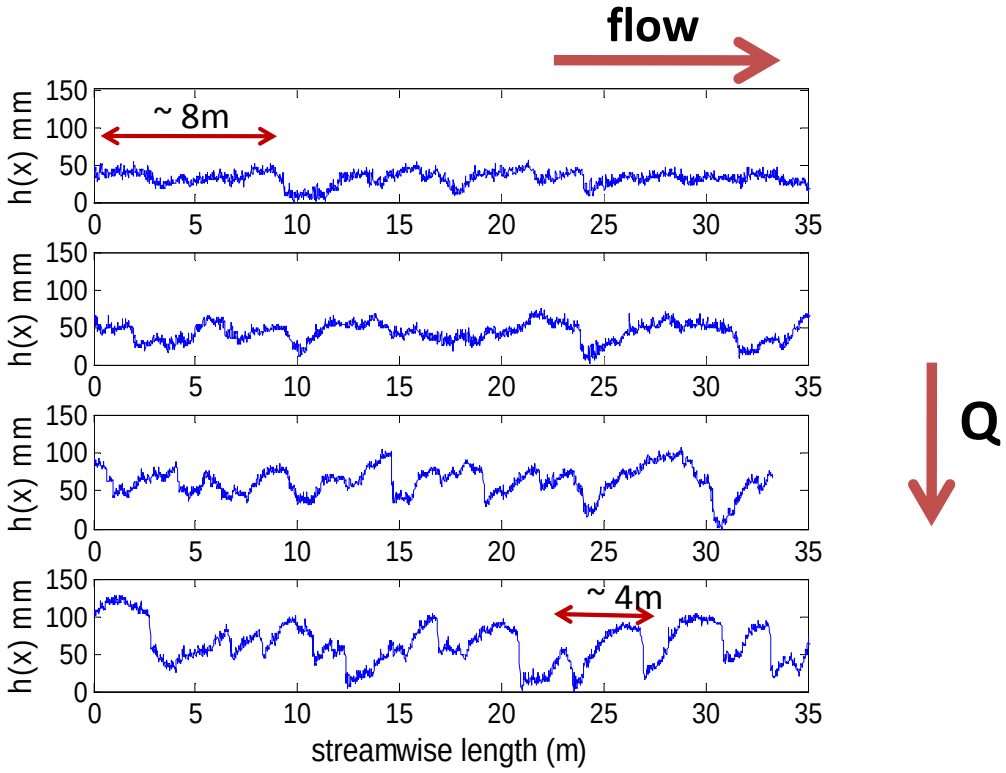

Figure 7.3: Longitudinal transect of bed profile elevations at a resolution of 10 mm for the discharges of 600 l/s, 800 l/s, 950 l/s and 1600 l/s from top to bottom, respectively. Notice that at low discharge of 600 l/s the bedforms are longer (bedload sheets) whereas with increasing discharge the length of bedform l_{bf} decreases while bedform height h_{bf} increases.

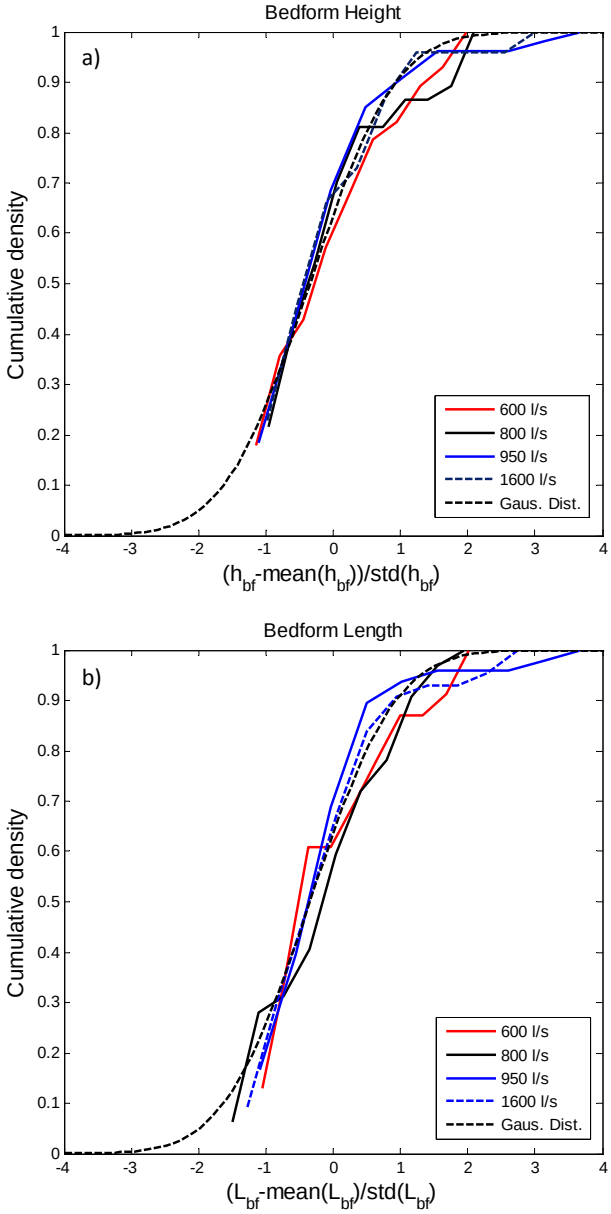

Figure 7.4: Cumulative density function of bedform heights (top) and bedform lengths (bottom) obtained from the spatial transect of the bed elevation (see section 3 for bedform extraction). Note that the distribution of bedform heights and bedform length for each discharge was obtained from the ensemble of bedforms extracted from the transects obtained at distances of 0.5 m across the width of the flume at that particular discharge.

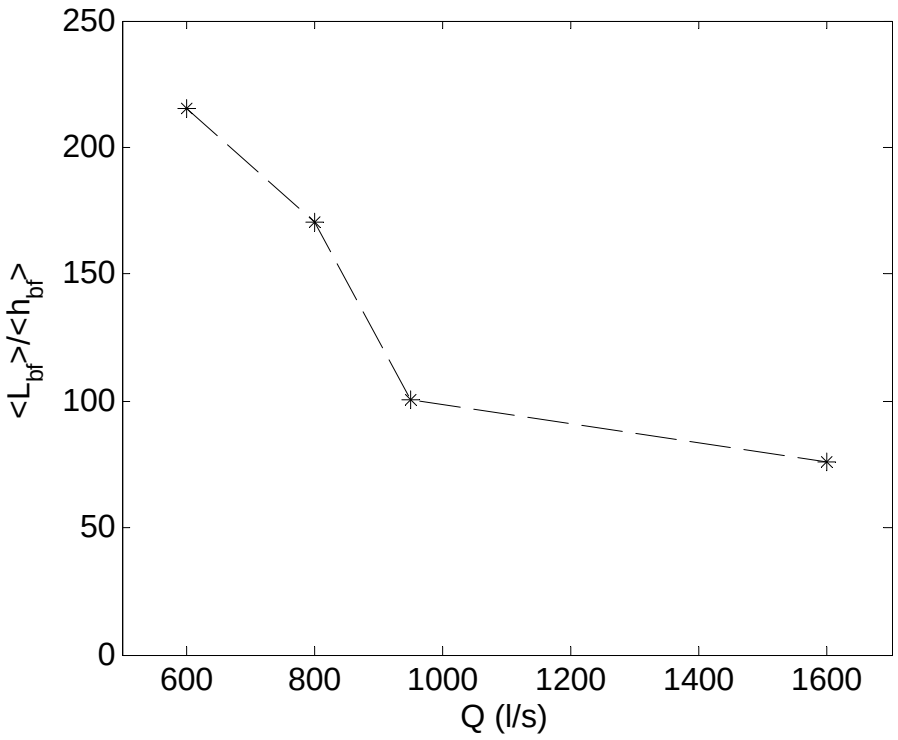

Figure 7.5: Aspect ratio ($\frac{<L_{bf}>}{<h_{bf}>}$) as a function of discharge. Notice that with increasing discharge the aspect ratio decreases.

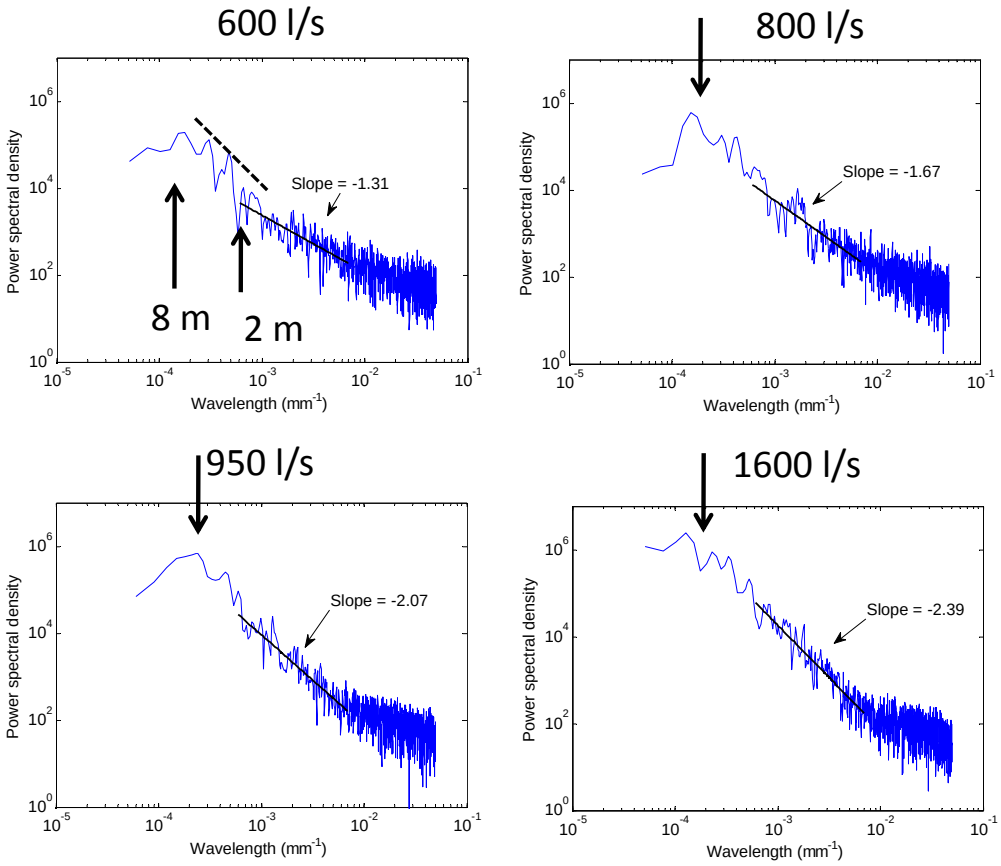

Figure 7.6: Power spectral density of the spatial transect of the bed topography for the discharges of 600 l/s, 800 l/s, 950 l/s and 1600 l/s. Notice the scaling break in the scaling regime of PSD for the low discharge of 600 l/s. This scaling break disappears with increasing discharge.

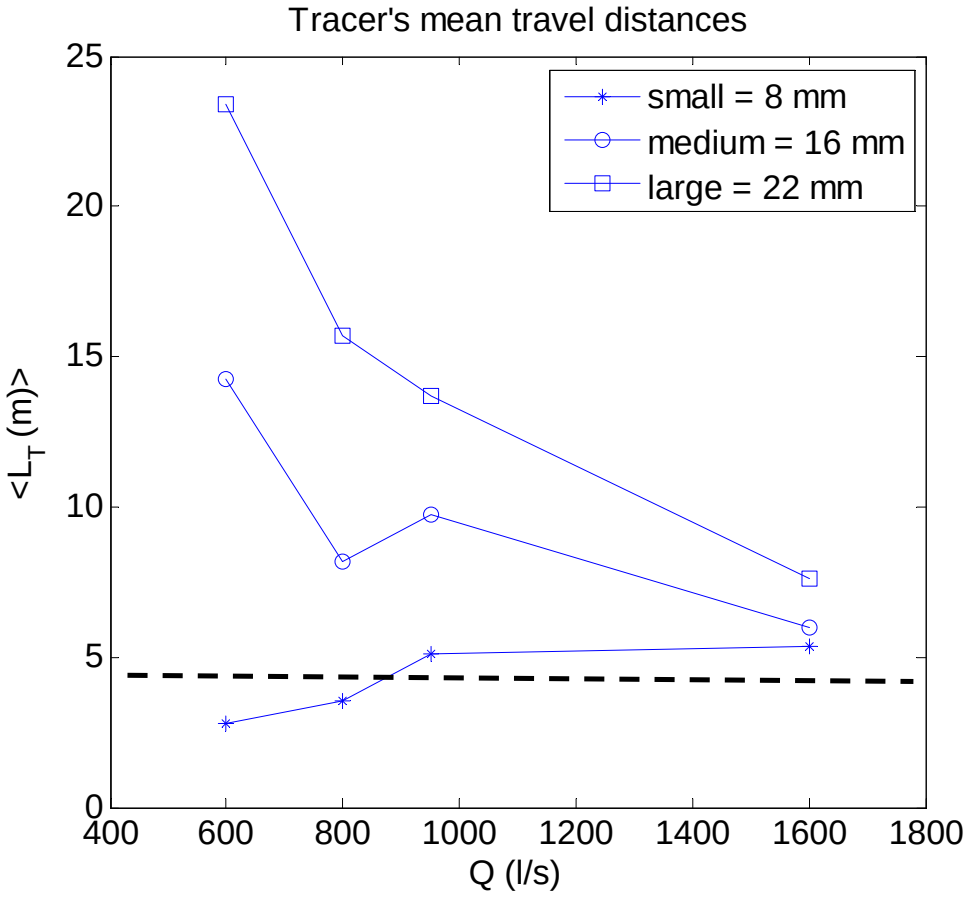

Figure 7.7: Mean travel distances of the large (22 mm), medium (16 mm) and small (8 mm) paramagnetic tracer particles as a function of discharge. Note that with increasing discharge as the bedform increases the mean travel distance decreases.

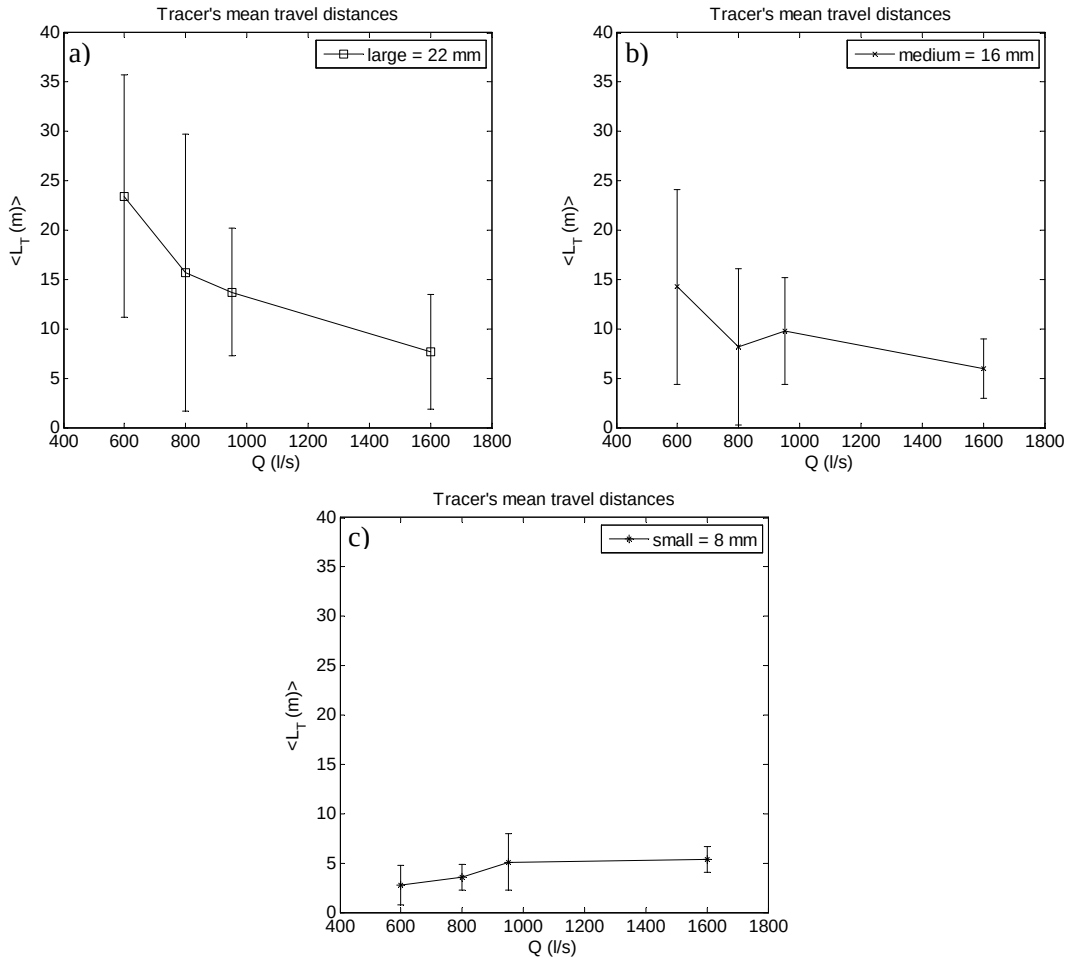

Figure 7.8: Error bars showing the standard deviation of travel distances for the large (a), medium (b) and small (c) paramagnetic tracer particles as a function of discharge. Note that with increasing discharge as the bedform height increases, for the large and the medium particles the standard deviation deviation decrease, whereas for the small particles standard deviation does not change significantly.

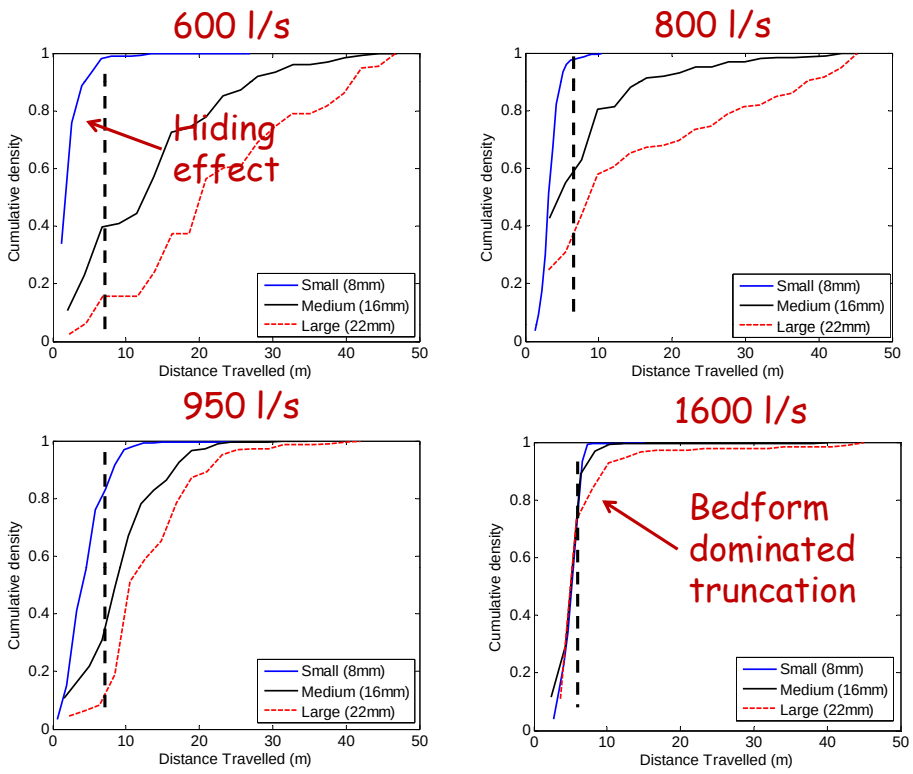

Figure 7.9: Cumulative density functions of tracer travel distances for the discharges of 600 l/s (a), 800 l/s (b), 950 l/s (c), and 1600 l/s (d).

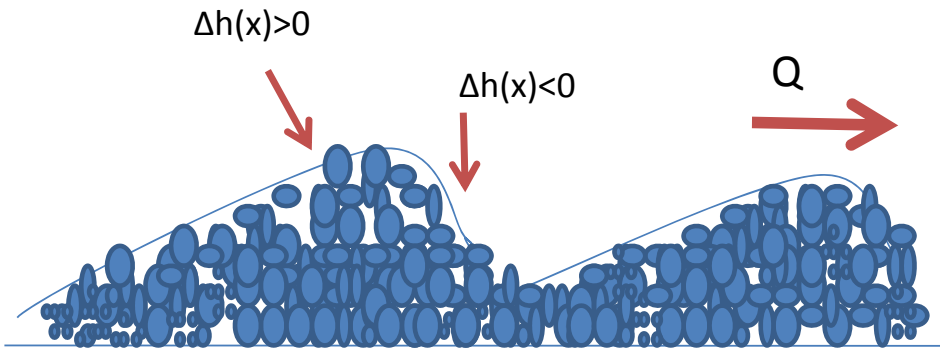

Figure 7.10: Schematic of the bedform showing the stoss and the lee part of the bedforms. Note that the positive increments ($\Delta h(t) = h(t + \Delta(t)) - h(t)$)) corresponds to erosion whereas negative increments corresponds to deposition.

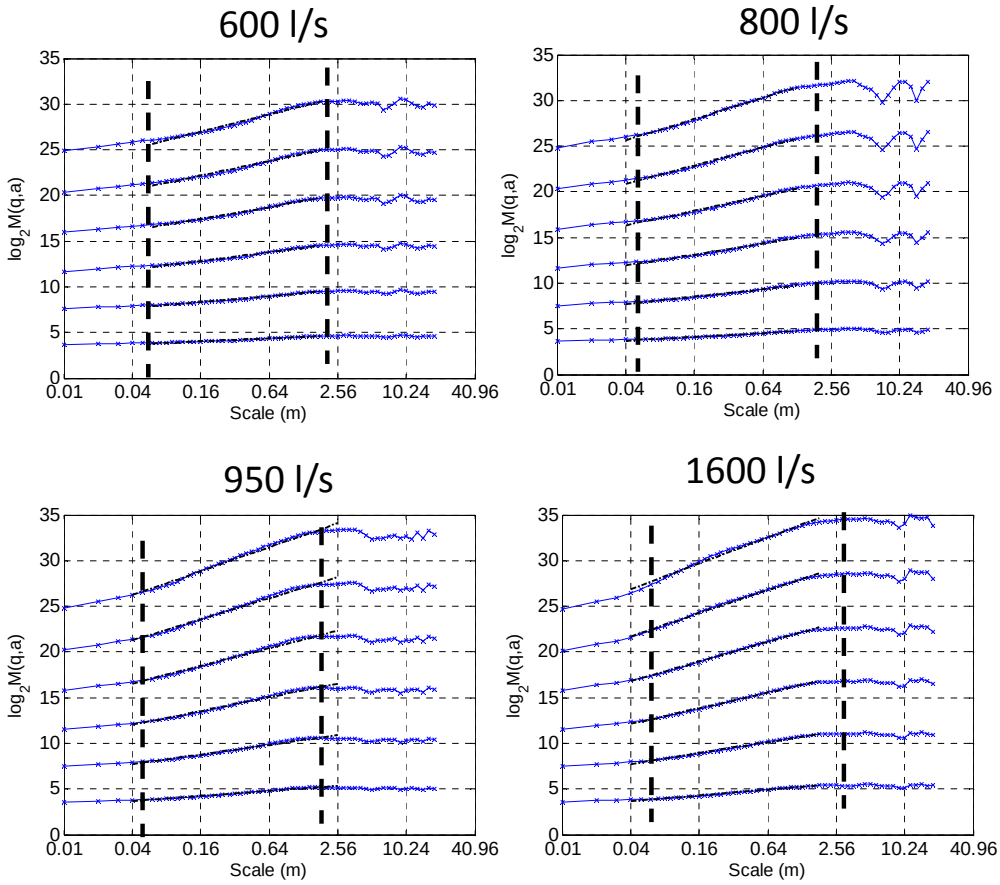

Figure 7.11: Statistical moments of the fluctuations of spatial bed elevation as a function of scale for the discharges of 600 l/s, 800 l/s, 950 l/s and 1600 l/s.

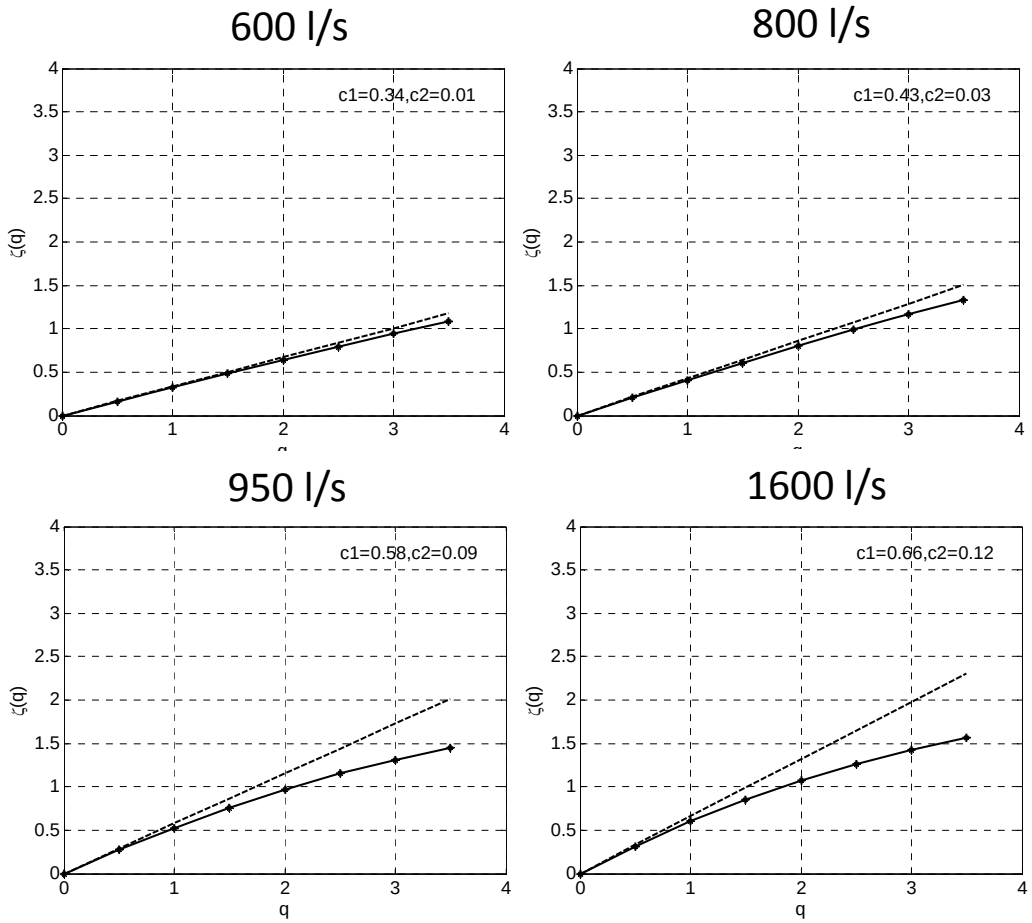

Figure 7.12: The scaling exponents $\tau(q)$ estimated from the log-log linear regressions within the scaling regions shown in Figure 7.11 for discharges of 600 l/s, 800 l/s, 950 l/s and 1600 l/s. Notice the deviation of $\tau(q)$ from the linear line establishing the presence of multifractality and the deviation increases as the discharge increases.

Chapter 8

Concluding Remarks and Future Perspectives

It is a well known fact that the transport of sediment in natural streams is complicated; yet, its understanding is a key requirement in designing hydraulic structures in streams and rivers as well as in predicting stream bed erosion and the transport of sediment and pollutants. At present, most of the data on bed load transport rates are obtained through direct measurements. These measurements, however, are highly variable in space and time and present a limited picture of the sediment transport process in a natural stream. A problem of interest therefore is to develop quantitative relationships between the bedload transport rates to the evolving bed topography and near-bed turbulence. The findings of six papers that comprise this thesis provide a detailed statistical framework to understand and quantify the sediment transport and its interaction with bed topography and near-bed turbulence and also shed light onto the statistical mechanics of sediment transport via relating microscopic properties (for example, grain size, velocity fluctuations etc.) to macroscopic properties (for e.g., bedforms, large scale flow structures) using probabilistic theories for prediction purposes.

The main results of this thesis can be summarized as:

1. Using observations from a controlled laboratory experiment under steady-state conditions we quantified the "roughness" and "intermittency" of bedload sediment transport rates using two parameters: one characterizing the overall roughness of the

series and the other characterizing the spatial inhomogeneity of this roughness, i.e., the clustering of bursts of various strengths. We proposed a theoretical framework that offers the ability to compare not only means but also the whole probability density function, including extreme values or quantiles of the pdfs of sediment transport rates at different temporal scales. This is important for example, when the pdf of sediment transport rates has been estimated from data at one particular sampling interval and an extreme exceedance quantile (say, relevant to an ecological smaller-scale functional disturbance) needs to be estimated. Our methodology can bridge this gap in scales and also provide a framework with in which comparison of sediment rates sampled with different instruments can be made. Our analysis demonstrated that the statistics of sediment transport rates depend strongly on scale (sampling interval) and this dependence varies with the discharge conditions. The documented statistical structure of sediment transport rates can be seen as providing an additional model diagnostic that mechanistic models should be able to reproduce, and as such, it is interesting to ask as to whether any known sediment transport model can reproduce the scaling characteristics reported in this study.

2. We characterized the complex nonlinear multiscale dynamics of bed elevation and the resulting sediment transport series to make inferences about the inherent predictability, or expected upper limit to prediction, by any mechanistic model of sediment transport. We also parameterized this complexity in terms of macroscopic flow and sediment properties (e.g., mean bed shear stress, grain size distribution) to provide useful information for physical model development.

3. We demonstrated how one can estimate time scales of moving bedforms from the spectra of the turbulent velocity fluctuations as it was found that the spectra carries information about the evolving multi-scale nature of bed topography and can thus form a useful tool for non-invasive and economical/robust field monitoring in real rivers. Specifically, we showed that the power spectral density of the near-bed turbulence velocities reveals two distinct scaling ranges: a high frequency range associated with turbulent eddy motions and a low-frequency regime representing the effect of the evolving multiscale bed topography separated by a spectral gap.

4. We proposed a methodology to understand and quantify scale-dependent celerity of migrating bedforms in a sand and gravel bedded channel to quantify scale-dependent

sediment transport. We hope that our results provide objective techniques for comparing the results of morphodynamic models with field or experimental observations, such that inferences can be made beyond average quantities (e.g., mean bedform height, length and celerity), hypotheses can be tested, and guidance for further model development can be provided.

5. Apart from simply quantifying the largest scale present on the bed topography from measured near-bed velocity fluctuations, we showed how the whole pdf of bed elevation fluctuations reflects onto the instantaneous Reynolds stress and suggested instantaneous Reynolds stress as a predictor of bed topography and sediment transport.

6. We showed how multiscale-complex structures in bed topography affect the tracer migration in order to understand and quantify how particle dynamics (microscale) relates to macroscale dynamics i.e., of bedforms, trapping potential, waiting times etc., and how these dynamics can be best accounted for in tracer dispersal and sediment transport models.

The above results were possible only through the extensive controlled laboratory large-scale experiments. We see our study as a first step in the direction of understanding the scale-dependency of sediment transport rates, its interaction with bed topography and near-bed turbulence over the continuum of flow discharge conditions and grain size distributions. More controlled experiments have to be performed and analyzed with different particle sizes (from a single particle size to a broad particle size distribution and for gravel and sand-beds) and a spectrum of discharge rates, to fully characterize the bedload sediment transport fluctuations and how they relate to the bed elevation fluctuations, near bed turbulence and to particle-size dynamics.

Future research: This research shed new light on the coupled dynamics of bed topography, near-bed turbulence and sediment transport and opened up new direction of research. Specifically, some of the future research directions can be outlined out as follows:

1. Understand and quantify how can heavy tail distributions, i.e., thicker than exponential or Gaussian decays, be incorporated in sediment transport models, for example similar to recent methods presented by [197] who proposed a new class of models to predict the movement of tracers in a gravel bed via an extension of the probabilistic Exner equation.

2. Understand and quantify how the evolving bed topography as a function of discharge reflects itself in the stratigraphic record and specifically what of the spatial variability of the time evolving bedform is preserved in stratigraphy.

3. To propose and explore best ways to incorporate velocity fluctuations/ instantaneous shear stress in bedform evolution and sediment transport modeling.

4. An important recent result of this research is the observation of a "spectral gap" in turbulence velocity fluctuations collected above a river bed with evolving bedforms. Efforts are now underway to formally relate the existence of the observed scaling regime in velocity fluctuations due to migrating bed topography to the scaling regime in bed topography via dimensional analysis akin to the one in the theory of turbulence (K41).

5. The often unmeasured small-scale fluctuations in sediment transport are expected to have effect on the stream biological activity and/ or stream vegetation. Now since it is possible to quantify these fluctuations, next step would be to understand and quantify how these fluctuations in sediment transport affects vegetation and nutrients in a streams.

6. A problem of interest to both engineers and scientists is how to translate temporal information into spatial information or vise-versa. This research can be used as a base which can provide direction in understanding the validity of Taylor's hypothesis in river morphodynamic processes such as bedform dynamics, large scale turbulent structures etc., as a function of shear stress and grain size distribution.

References

[1] D. B. Simons, E. V. Richardson, and C. F. Nordin Jr. Bedload equation for ripples and dunes. *U.S. Geol. Surv. Prof. Pap.*, 462(H):1–9, 1965.

[2] K. Bunte and S. R. Abt. Effect of sampling time on measured gravel bed load transport rates in a coarse-bedded stream. *Water Resour. Res.*, 41:W11405, 2005. doi:10.1029/2004WR003880.

[3] C. Torrence and G. Compo. A practical guide to wavelet analysis. *Bull. Am. Meteorol. Soc.*, 79:61–78, 1998.

[4] C. Ancey, T. Böhm, M. Jodeau, and P. Frey. Statistical description of sediment transport experiments. *Phys. Rev. E.*, 74(1):011302, 2006.

[5] A. Singh, K. Fienberg, D. J. Jerolmack, J. Marr, and E. Foufoula-Georgiou. Experimental evidence for statistical scaling and intermittency in sediment transport rates. *J. Geophys. Res.*, 114:F01025, 2009a. doi:10.1029/2007JF000963.

[6] A. Singh, S. Lanzoni, and E. Foufoula-Georgiou. Nonlinearity and complexity in gravel bed dynamics. *Stochastic Environmental Research and Risk Assessment*, 23:967–975, 2009. 10.1007/s00477-008-0269-8.

[7] K. Fienberg, A. Singh, D. Jerolmack, J. Marr, and E. Foufoula-Georgiou. A theoretical framework for interpreting and quantifying the sampling time dependence of gravel bedload transport rates. Minneapolis, April 11-14, 2007.

[8] A. Singh, F. Porté-Agel, and E. Foufoula-Georgiou. On the influence of gravel bed dynamics on velocity power spectra. *Water Resour. Res.*, 46:W04509, 2010a. doi:10.1029/2009WR008190.

[9] F. Iseya and H. Ikeda. Pulsations in bedload transport rates induced by a longitudinal sediment sorting: a flume study using sand and gravel mixtures. *Geografiska Annaler*, 69A:15–27, 1987.

[10] T. G. Drake, R. L. Shreve, W. E. Dietrich, P. J. Whiting, and L. B. Leopold. Bedload transport of fine gravel observed by motion pictures. *J. Fluid Mech.*, 192:193–217, 1988.

[11] V. Nikora, H. Habersack, T. Huber, and I. McEwan. On bed particle diffusion in gravel bed flows under weak bed load transport. *Water Resour. Res.*, 38:1081, 2002. doi:10.1029/2001WR000513.

[12] M.W. Schmeeckle and J. M. Nelson. Direct numerical simulation of bedload transport using a local, dynamic boundary condition. *Sedimentology*, 50(2):279–301, 2003. doi:10.1046/j.1365-3091.2003.00555.

[13] B. M. Sumer, L. H. C. Chua, N. S. Cheng, and J. Fredsøe. Influence of turbulence on bed load sediment transport. *J. Hydraul. Eng.*, 129:585– 596, 2003.

[14] C. Ancey, A.C. Davidson, T. Böhm, M. Jodeau, and P. Frey. Entrainment and motion of coarse particles in a shallow water stream down a steep slope. *J. Fluid Mech.*, 595:83–114, 2008.

[15] R. A. Kuhnle and J. B. Southard. Bed load fluctuations in a gravel bed laboratory channel. *Water Resour. Res.*, 24:247–260, 1988.

[16] B. Gomez, R. L. Naff, and D. W. Hubbel. Temporal variations in bedload transport rates associated with the migration of bedforms. *Earth Surf. Process. Landf.*, 14:135–156, 1989.

[17] J. R. Cudden and T. B. Hoey. The causes of bedload pulses in a gravel channel: The implications of bedload grain-size distributions. *Earth Surf. Proc, Landforms*, 28:1411–1428, 2003.

[18] D. J. Jerolmack and D. Mohrig. A unified model for subaqueous bed form dynamics. *Water Resour. Res.*, 41:W12421, 2005. doi:10.1029/2005WR004329.

[19] S.M. Yarnell, J.F. Mount, and E.W. Larsen. The influence of relative sediment supply on riverine habitat heterogeneity. *Geomorphology*, 80:310–324, 2006.

[20] P. M. Sadler. Sediment accumulation and the completeness of stratigraphic sections. *J. Geology*, 89:569–584, 1981.

[21] P. M. Sadler. The influence of hiatuses on sediment accumulation rates. *GeoResearch Forum*, 5:15–40, 1999.

[22] D. J. Jerolmack and P. M. Sadler. Transience and persistence in the depositional record of continental margins. *J. Geophys. Res.*, 112:F03S13, 2007. doi:10.1029/2006JF000555.

[23] S. Lovejoy and D. Schertzer. Generalized scale invariance and fractal models of rain. *Water Resour. Res.*, 21:1233–1250, 1985.

[24] V. Venugopal, S. G. Roux, E. Foufoula-Georgiou, and A. Arneodo. Scaling behavior of high resolution temporal rainfall: New insights from a wavelet-based cumulant analysis. *Phys. Let. A*, 348:335–345, 2006b.

[25] S. Lovejoy, D. Schertzer, P. Silas, Y. Tessier, and D. Lavallée. The unified scaling model of atmospheric dynamics and systematic analysis in cloud radiances. *Ann. Geophys.*, 11:119–127, 1993.

[26] A. Arneodo, N. Decoster, and S. G. Roux. Intermittency, lognormal statistics, and multifractal cascade process in high-resolution satellite images of cloud structure. *Phys. Rev. Letters*, 83(6):1255–1258, 1999a.

[27] V. Gupta and E. Waymire. *Multiplicative cascades and spatial variability in rainfall, river networks, and floods*, volume 25. Addison-Wesley, Boston, Mass., 1996.

[28] A. Rinaldo, I. Rodriguez-Iturbe, R. Rigon, E. Ijjasz-Vasquez, and R. Bras. Self-organized fractal river networks. *Phys. Rev. Lett.*, 70:822– 825, 1993.

[29] M. Marani, A. Rinaldo, R. Rigon, and I. Rodriguez-Iturbe. Geomorphological width functions and the random cascade. *Geophys. Res. Lett.*, 21:2123–2126, 1994.

[30] B. Lashermes and E. Foufoula-Georgiou. Area and width functions of river networks: New results on multifractal properties. *Water Resour. Res.*, 43:W09405, 2007. doi:10.1029/2006WR005329.

[31] E. Foufoula-Georgiou and V. Sapozhnikov. Anisotropic scaling in braided rivers: An integrated theoretical framework and results from application to an experimental river. *Water Resour. Res.*, 34(4):863–867, 1998.

[32] C. Gangodagamage, E. Barnes, and E. Foufoula-Georgiou. Scaling in river corridor widths depicts organization in valley morphology. *J. Geomorphol.*, 91:198–215, 2007.

[33] G. Parisi and U. Frisch. On the singularity structure of fully developed turbulence. *Turbulence and Predictability in Geophysical Fluid Dynamics, edited by M. Ghil et al.*, pages 84–87, 1985.

[34] U. Frisch. *Turbulence: The Legacy of A. N. Kolmogorov*. Cambridge Univ. Press, New York, 2003.

[35] A. Arneodo, S. Manneville, J. F. Muzy, and S.G. Roux. Revealing a lognormal cascading process in turbulent velocity statistics with wavelet analysis. *Philosophical Transaction: Mathematical, Physical and Engineering Sciences*, 357(1760):415–2438, 1999b.

[36] V. I. Nikora, A. N. Sukhodolov, and P. M. Rowinski. Statistical sand wave dynamics in one-directional water flows. *J. Fluid Mech.*, 351:17–39, 1997.

[37] R. Dinehart. Gravel-bed deposition and erosion by bedform migration observed ultrasonically during storm flow, north fork toutle river, washington. *J. Hydrol.*, 136:51–71, 1992a.

[38] V. Nikora and J. Walsh. Water-worked gravel surfaces: High-order structure functions at the particle scale. *Water Resour. Res.*, 40(W12601), 2004. doi:10.1029/2004WR003346.

[39] J. Aberle and V. Nikora. Statistical properties of armored gravel bed surfaces. *Water Resour. Res.*, 42:W11414, 2006.

[40] J. F. Muzy, E. Bacry, and A. Arneodo. The multifractal formalism revisited with wavelets. *Int. J. Bifurcation Chaos*, 4:245–302, 1994.

[41] P. R. Wilcock, C. H. Orr, and J. D. G. Marr. The need for full-scale experiments in river science. *Eos Trans. AGU*, 89(1), 2008. doi:10.1029/2008EO010003.

[42] E. Meyer-Peter and R. Müller. Formulas for bed-load transport. *Proceedings, 2nd Congress, International Association of Hydraulic Research, Stockholm*, pages 39–64, 1948.

[43] M. Schroeder. *Fractals, Chaos, Power Laws: Minutes from an Infinite Paradise.* W.H. Freeman, New York, 1991.

[44] D. L. Turcotte. *Fractals and Chaos in Geology and Geophysics, 2nd edition.* Cambridge Univ. Press, New York, 1997.

[45] A. Arneodo, E. Bacry, and J. F. Muzy. The thermodynamics of fractals revisited with wavelets. *Physica A*, 213:232–275, 1995.

[46] S. Jaffard. Multifractal formalism for functions. *SIAM J. Math. Anal.*, 28(4):944–998, 1997.

[47] V. Venugopal, S. G. Roux, E. Foufoula-Georgiou, and A. Arneodo. Revisiting multifractality of high-resolution temporal rainfall using a wavelet-based formalism. *Water Resour. Res.*, 42:W06D14, 2006a. doi:10.1029/2005WR004489.

[48] S. Mallat. *A Wavelet Tour in Signal Processing.* Academic, San Diego, Calif., 1998.

[49] P. Kumar and E. Foufoula-Georgiou. Wavelet analysis for geophysical applications. *Rev. Geophys.*, 35(4):385–412, 1997).

[50] A. Arneodo, J. F. Muzy, and S. G. Roux. Experimental analysis of self-similarity and random cascade processes: Application to fully developed turbulence data. *J. De Physique II*, 7:363–370, 1997.

[51] B. Castaing, Y. Gagne, and E. J. Hopfinger. Velocity probability density-functions of high reynolds-number turbulence. *Physica D*, 46:177–200, 1990.

[52] J. Delour, J. Muzy, and A. Arneodo. Intermittency of 1d velocity spatial profiles in turbulence: A magnitude cumulant analysis. *Eur. Phys. J. B.*, 23:243–248, 2001.

[53] P. Frey, C. Ducottet, and J. Jay. Fluctuations of bed load solid discharge and grain size distribution on steep slopes with image analysis. *Experiments in Fluids*, 35:589–597, 2003.

[54] K. Strom, A. N. Papanicolaou, N. Evangelopoulos, and M. Odeh. Microforms in gravel bed rivers: Formation, disintegration, and effects on bedload transport. *J. Hydraulic Engr*, 133:554–567, 2004.

[55] M. W. Schmeeckle, J. M. Nelson, J. Pitlick, and J.P. Bennett. Interparticle collision of natural sediment grains in water. *Water Resour. Res.*, 37 (9):2377–2391, 2001.

[56] A. Papanicolaou, P. Diplas, N. Evangelopoulos, and S. Fotopoulos. Stochastic incipient motion criterion for spheres under various bed packing conditions. *J. Hydraulic Engr.*, 128:369–380, 2002.

[57] A. Kirkbride. *Observations of the influence of bed roughness on turbulence structure in depth limited flows over gravel beds. In: Turbulence: Perspectives on Flow and Sediment Transport.* edited by Clifford N. J., J. R. French and J. Hardisty . W Wiley and Sons, NY, 1993.

[58] J. M. Nelson, R. L. Shreve, R. McLean, and T. G. Drake. Role of near-bed turbulence structure in bed load transport and bed form mechanics. *Water Resour. Res.*, 31:2071–2086, 1995.

[59] R. J. Hardy, S. R. Lane, R. I. Ferguson, and D. R. Parsons. Emergence of coherent flow structures over a gravel surface: A numerical experiment. *Water Resour. Res.*, 43:W03422, 2007. doi:10.1029/2006WR004936.

[60] G. Seminara. Stability and morphodynamics. *Meccanica*, 33:59–99, 1998.

[61] G. Parker. Some random notes on grain sorting. *In: Proc. Grain Sorting Seminar IAHR*, pages 20–76, 1991.

[62] P. R. Wilcock and B. W. McArdell. Surface-based fractional transport rates: mobilization thresholds and partial transport of a sand-gravel sediment. *Water Resour. Res.*, 29:1297–1312, 1993.

[63] P. R. Wilcock and B. W. McArdell. Partial transport of sand/gravel sediment. *Water Resour. Res*, 33:235–245, 1997.

[64] B. Gomez and J. D. Phillips. Deterministic uncertainty in bed load transport. *J. of Hydraulic Engr.*, pages 305–308, 1999.

[65] D. W. Hubbell, H. H. Stevens, J. V Skinner, and J. P. Beverage. Laboratory data on coarse-sediment transport for bedload-sampler calibrations. Technical report, U.S Geological Survey Water-Supply Paper 2299, U.S Geological Survey, Washington DC, 1987.

[66] A. Hamamori. A theoretical investigation on the fluctuation of bedload transport. *Delft Hydraulics Lab. Rep R4. Delft Hydraulics Laboratory. Delft. Netherlands*, 1962.

[67] E. Aurell, G. Boffetta, A. Crisanti, G. Paladin, and A. Vulpiani. Predictability in the large: an extension of the concept of lyapunov exponent. *J. of Phys. A: Math Gen*, 30:1–26, 1997.

[68] E. Aurell, G. Boffetta, A. Crisanti, G. Paladin, and A. Vulpiani. Growth of non-infinitesimal perturbations in turbulence. *Phys. Rev. Lett.*, 77:1262–1265, 1996a.

[69] G. Boffetta, M. Cencini, M. Falconi, and A. Vulpiani. Predictability: a way to characterize complexity. *Physics Reports*, 356:367–474, 2002.

[70] S. Basu, E. Foufoula-Georgiou, and F. Porté-Agel. Predictability of atmospheric boundary-layer flows as a function of scale. *Geophys. Res. Lett.*, 29(21):2038, 2002b. doi:10.1029/2002GL015497.

[71] N. Kleinfelter, M. Moroni, and J. H. Cushman. Application of finite-size lyapunov exponent to particle tracking velocitmetry in fluid mechanics experiments. *Phys. Rev. E*, 72, 2005.

[72] Foufoula-Georgiou E Basu S. Detection of nonlinearity and chaoticity in time series using the transportation distance function. *Phys. Lett. A*, 301:413–423, 2002a.

[73] A. Schreiber, T. Schmitz. Improved surrogate data for nonlinearity tests. *Phys. Rev. Lett.*, 77:635–638, 1996.

[74] J. Theiler, S. Eubank, A. Longtin, B. Galdrikian, and J. D. Farmer. Testing for nonlinearity in time series: the method of surrogate data. *Phys. D*, 58:77–94, 1992.

[75] R. Moeckel and B. Murray. Measuring the distance between time series. *Phys. D*, 102:187–194, 1997.

[76] M. B. Kennel, R. Brown, and H. D. I. Abarbanel. Determining embedding dimension for phase-space reconstruction using a geometrical construction. *Physical Review A*, 45:3403–3411, 1992.

[77] R. Hegger, H. Kantz, and T. Schreiber. Practical implementation of nonlinear time series methods: The tisean package. *Chaos*, 9:413–435, 1999.

[78] E.N. Lorenz. The predictability of a flow which possesses many scales of motion. *Tellus*, 21:289–307, 1969.

[79] E. Aurell, G. Boffetta, A. Crisanti, G. Paladin, and A. Vulpiani. Predictability in systems with many characteristic times: the case of turbulence. *Physical Review E.*, 53:2337– 2349, 1996b.

[80] G. Boffetta, A. Crisanti, F. Paparella, A. Provenzale, and A. Vulpiani. Slow and fast dynamics in coupled systems: a time series analysis view. *Physica D*, 116:301–312, 1998.

[81] G. J. Klaassen. Experiments with graded sediments in a straight flume. Technical report, Delft Hydraulics, The Netherlands, 1990.

[82] A. Blom, J. S. Ribberink, and H. J. de Vriend. Vertical sorting in bed forms: Flume experiments with a natural and a trimodal sediment mixture. *Water Resour. Res.*, 39:1025, 2003. DOI:10.1029/2001WR001088.

[83] H. Kantz and T. Schreiber. *Nonlinear Time Series Analysis*. Cambridge University Press Cambridge UK, 1997.

[84] P. L. Wiberg and J. D. Smith. Velocity distribution and bed roughness in high-gradient streams. *Water Resour. Res.*, 27(5):825838, 1991.

[85] R.L. Dinehart. Evolution of coarse gravel bedforms: field measurements at flood stage. *Water Resour. Res.*, 28(10):2667–2689, 1992b.

[86] A. Robert, A.G. Roy, and B. De Serres. Changes in velocity profiles at roughness transitions in coarse-grained channels. *Sedimentology*, 39:725–735, 1992.

[87] T. Buffin-Bélanger and A. G. Roy. Effects of a pebble cluster on the turbulent structure of a depth-limited flow in a gravel-bed river. *Geomorphology*, 25:249267, 1998. doi:10.1016/S0169-555X(98)00062-2.

[88] R. W. J. Lacey and A. G. Roy. A comparative study of the turbulent flow field with and without a pebble cluster in a gravel bed river. *Water Resour. Res.*, 43:W05502, 2007. doi:10.1029/2006WR005027.

[89] R. J. Hardy, J. L. Best, S. N. Lane, and P. E. Carbonneau. Coherent flow structures in a depth-limited flow over a gravel surface: The role of near-bed turbulence and influence of reynolds number. *J. Geophys. Res.*, 114:F01003, 2009. doi:10.1029/2007JF000970.

[90] A.D. Kirkbride and M.J. McLelland. Visualization of the turbulent flow structures in a gravel bed river. *Earth Surf. Processes and Landforms*, 19:819–825, 1994.

[91] A.D. Kirkbride and R.I. Ferguson. Turbulent flow structure in a gravel-bed river: Markov chain analysis of the fluctuating velocity profile. *Earth Surf. Processes Landforms*, 20:721–733, 1995.

[92] H. Lamarre and A. G. Roy. Reach scale variability of turbulent flow characteristics in a gravel-bed river. *Geomorphology*, 60:95–113, 2005.

[93] R. W. J. Lacey and A. G. Roy. Fine-scale characterization of the turbulent shear layer of an instream pebble cluster. *J. Hydr. Engg.*, 134(7):925–936, 2008.

[94] J. L. Best. *On the interactions between turbulent flow structure, sediment transport and bedform development: some considerations from recent experimental research. In: Turbulence: Perspectives on Flow and Sediment Transport.* edited by Clifford N. J., J. R. French and J. Hardisty . W Wiley and Sons, NY, 1993.

[95] A. Robert, A.G. Roy, and B. De Serres. *Spacetime correlations of velocity measurements at a roughness transition in a gravel-bed river.* Wiley, Chichester, 1993.

[96] M. W. Schmeeckle, J. M. Nelson, and R. L. Shreve. Forces on stationary particles in near-bed turbulent flows. *J. Geophys. Res.*, 112:F02003, 2007. doi:10.1029/2006JF000536.

[97] A.G. Roy, T. Buffin-Belanger, H. Lamarre, and A.D. Kirkbride. Size, shape and dynamics of large-scale turbulent flow structures in a gravel-bed river. *J. Fluid Mech.*, 500:1–27, 2004.

[98] A. B. Shvidchenko and G. Pender. Macroturbulent structure of open-channel flow over gravel beds. *Water Resour. Res.*, 37(3):709719, 2001.

[99] H. Imamoto and T. Ishigaki. The three dimensional structure of turbulent shear flow in an open channel. In *Fifth Congress of the Asian and Pacific Regional Division of the International Association for Hydraulic Research*, Seoul, Korea, 1986a.

[100] H. Imamoto and T. Ishigaki. Visualization of longitudinal eddies in an open channel flow. In *Flow Visualization IV: Proceedings of the Fourth International Symposium on Flow Visualization*, pages 333–337, Hemisphere, Washington, D. C, 1986b.

[101] M. S. Yalin. *River Mechanics.* Elsevier, New York, 1992.

[102] G. Paiement-Paradis, T. Buffin-Bélanger, and A. G. Roy. Scalings for large turbulent flow structures in gravel-bed rivers. *Geophys. Res. Lett.*, 30(14):1773, 2003. doi:10.1029/2003GL017553.

[103] G. A. Marquis and A. G. Roy. Effect of flow depth and velocity on the scales of macroturbulent structures in gravel-bed rivers. *Geophys. Res. Lett.*, 33:L24406, 2006. doi:10.1029/2006GL028420.

[104] R. L. Dinehart. Correlative velocity fluctuations over a gravel river bed. *Water Resour. Res.*, 35(2):569582, 1999.

[105] R. L. Dinehart. Dune migration in a steep, coarse-bedded stream. *Water Resour. Res.*, 25(5):911–923, 1989.

[106] V. Nikora. *Hydrodynamics of gravel-bed rivers: scale issues.* Elsevier, 2008.

[107] V. I. Nikora and D. G. Goring. Flow turbulence over fixed and weakly mobile gravel beds. *J. Hydraul. Eng.*, 126(9):679–690, 2000.

[108] I. Van Der Hoven. Power spectrum of horizontal wind speed in the frequency range from 0.0007 to 900 cycles per hour. *J. Meteor.*, 14:160–194, 1957.

[109] F. Fiedler and H. A. Panofsky. Atmospheric scales and spectral gaps. *Bullet. Amer. Meteor. Soc.*, 51:1114–1119, 1970.

[110] A.S. Smedman-Högström and U. Högström. Spectral gap in surface-layer measurements. *J. Atmos. Sci.*, 32:340–350, 1975.

[111] G.D. Hess and R.H. Clarke. Time spectra and cross-spectra of kinetic energy in the planetary boundary layer. *Quart. J. Roy. Meteor. Soc.*, 99:130–153, 1973.

[112] J. M. Buffington and D. R. Montgomery. A systematic study of eight decades of incipient motion studies, with special reference to gravel-bedded rivers. *Water Resour. Res.*, 33(8):1993–2029, 1997.

[113] M. Parsheh, F. Sotiropoulos, and F. Porté-Agel. Estimation of power spectra of acoustic-doppler velocimetry data contaminated with intermittent spikes. *J. Hydraul. Engg.* In Press.

[114] D. G. Goring and V. I. Nikora. Despiking acoustic doppler velocimeter data. *J. Hydraul. Eng.*, 128(1):117–126, 2002.

[115] R. J. Adrian and C.S. Yao. Power spectra of fluid velocities measured by laser doppler velocimetries. *Exp. Fluids*, 5:117–128, 1987.

[116] P. Stoica and R. L. Moses. *Introduction to spectral analysis*, volume 07458. Upper Saddle River, New Jersey, Prentice Hall, 1997.

[117] A. E. Perry, S. Henbest, and M. S. Chong. A theoretical and experimental study of wall turbulence. *J. Fluid Mech.*, 165:163–199, 1986.

[118] G. G. Katul, C. R. Chu, M. B. Parlange, J. D. Albertson, and T. A. Ortenburger. Low wavenumber spectral characteristics of velocity and temperature in the atmospheric boundary layer. *J. Geophys. Res.*, 100:14243–14255, 1995.

[119] F. Porté-Agel, C. Meneveau, and M. B. Parlange. A scale-dependent dynamic model for large-eddy simulation: application to a neutral atmospheric boundary layer. *J. Fluid Mech.*, 415:216–284, 2000.

[120] B. A. Kader and A. M. Yaglom. Spectra and correlation functions of surface layer atmospheric turbulence in unstable thermal stratification. *In Turbulence and Coherent Structures.*

[121] A. Kolmogorov. Dissipation of energy in the locally isotropic turbulence. *Turbulence: Classic Papers on Statistical Theory, edited by S. K. Friedlander and L. Topper*, pages 151–155, 1961.

[122] I. Nezu and H. Nakagawa. *Turbulence in open-channel flows.* Balkema, Rotterdam, The Netherlands, 1993.

[123] M. F. Lapointe. Burst-like sediment suspension events in a sand bed river. *Earth Surf. Processes Landforms*, 17:253–270, 1992.

[124] E. Foufoula-Georgiou Venugopal, V. F. Porté-Agel and M. Carper. Multiscale interactions between surface shear stress and velocity in turbulent boundary layers. *J. Geophys. Res.*, 108, 2003. doi:10.1029/2002JD003025.

[125] F. A. Vening Meinesz. A remarkable feature of the earths topography. *Proc. K. Ned. Akad. Wet. Ser. B. Palaeontol. Geol Phys. Chem. Anthropol.*, 54:212–228, 1951.

[126] W. I. Newman and D. L. Turcotte. Cascade model for fluvial geomorphology. *Geophys. J. Int.*, 100:433–439, 1990.

[127] J.D. Pelletier. The self-organization and scaling relationships of evolving river networks. *J. Geophys. Res.*, 104:7359–7375, 1999.

[128] P. Passalacqua, F. Porté-Agel, E. Foufoula-Georgiou, and C. Paola. Application of dynamic subgrid-scale concepts from large-eddy simulation to modeling landscape evolution. *Water Resour. Res.*, 42:W06D11, 2006. doi:10.1029/2006WR004879.

[129] V. I. Nikora, D. G. Goring, and B. J. F. Biggs. On gravel-bed roughness characterization. *Water Resour. Res.*, 34(3):517–527, 1998.

[130] A. Marion, S. J. Tait, and I. K. McEwan. Analysis of small-scale gravel bed topography during armoring. *Water Resour. Res.*, 39(12):13–34, 2003. doi:10.1029/2003WR002367.

[131] R.L. Soulsby. Selecting record length and digitization rate for near-bed turbulence measurements. *J. Phys. Oceanogr.*, 10:208–219, 1980.

[132] ASCE Task Force. Flow and transport over dunes. *J. Hydraul. Eng.*, 127:726–728, 2002.

[133] S. F. Leclair. Preservation of cross-strata due to migration of subaqueous dunes: An experimental investigation. *Sedimentology*, 49:1157–1180, 2002.

[134] S. E. Coleman and B. W. Melville. Bed-form development. *J. Hydraul. Eng.*, 120:544–560, 1994.

[135] A. Wilbers. The development and hydraulic roughness of subaqueous dunes. *Neth. Geogr. Stud. , Fac. of Geosci., Utrecht Univ., Utrecht, Netherlands*, 323:224, 2004.

[136] D. R. Parsons, J. L. Best, O. Orfeo, R. J. Hardy, R. Kostaschuk, and S. N. Lane. Morphology and flow fields of three-dimensional dunes, rio parana, argentina: Results from simultaneous multibeam echo sounding and acoustic doppler current profiling. *J. Geophys. Res.*, 110:F04S03, 2005. doi:10.1029/2004JF000231.

[137] M. Venditti, J. G. amd Church and S. J. Bennett. Morphodynamics of small-scale superimposed sand waves over migrating dune bed forms. *Water Resour. Res.*, 41:W10423, 2005. doi:10.1029/2004WR003461.

[138] A. W. E. Wilbers and W. B. M. ten Brinke. The response of subaqueous dunes to floods in sand and gravel bed reaches of the dutch rhine. *Sedimentology*, 50, 2003. doi:10.1046/j.1365-3091.2003.000585.x.

[139] R. J. Schindler and A. Robert. Suspended sediment concentration and the ripple-dune transition. *Hydrol. Processes*, 18:3215–3227, 2004.

[140] J. Best. The fluid dynamics of river dunes: A review and some future research directions. *J. Geophys. Res.*, 110(F04S02), 2005. doi:10.1029/2004JF000218.

[141] F. Fernandez, J. Best, and F. Lopez. Mean flow, turbulence structure, and bed form superimposition across ripple-dune transition. *Water Resour. Res.*, 42:W05406, 2006. doi:10.1029/2005WR004330.

[142] B. McElroy and D. Mohrig. Nature of deformation of sandy bed forms. *J. Geophys. Res.*, 114:F00A04, 2009. doi:10.1029/2008JF001220.

[143] J. R. L. Allen. Current ripples: Their relation to patterns of water and sediment motion. *Elsevier, New York*, page 433, 1968.

[144] J. Barlow. Autocorrelation and cross correlation analysis in electroencephalography. *IRE Trans Med Electron MEG*, pages 179–183, 1959.

[145] T. B. Maddux, J. M. Nelson, and S. R. McLean. Turbulent flow over three-dimensional dunes: 1. free surface and flow response. *J. Geophys. Res.*, 108:6009, 2003. doi:10.1029/2003JF000017.

[146] J. G. Venditti. Turbulent flow and drag over fixed two- and three-dimensional dunes. *J. Geophys. Res.*, 112:F04008, 2007. doi:10.1029/2006JF000650.

[147] S. Lanzoni. Experiments on bar formation in a straight flume: 1. uniform sediment. *Water Resour. Res.*, 36(11):3337–3349, 2000. doi:10.1029/2000WR900160.

[148] S. Lanzoni. Experiments on bar formation in a straight flume: 2. graded sediment. *Water Resour. Res.*, 36(11):3351–3363, 2000. doi:10.1029/2000WR900161.

[149] P. Blondeaux and G. Seminara. A unified bar-bend theory of river meanders. *J. Fluid Mech.*, 157:449–470, 1985.

[150] M. Colombini, G. Seminara, and M. Tubino. Finite-amplitude alternate bars. *J. Fluid Mech.*, 181:213–232, 1987.

[151] B. Federici and G. Seminara. Effect of suspended load on sandbar instability. *Water Resour. Res.*, 42:W07407, 2006. doi:10.1029/2005WR004399.

[152] F. Engelund and J. Fredsøe. Transition from dunes to plane bed in alluvial channels. Technical Report Ser. Pap. 4, Inst. of Hydrodyn. and Hydraul. Eng., Tech. Univ. of Den., Lyngby, 1982.

[153] L. C. Van Rijn. Sediment transport, part iii: Bed forms and alluvial roughness. *J. Hydraul. Engg., ASCE*, 110:1733–1754, 1984.

[154] S. E. Coleman, V. I. Nikora, S. R. McLean, T. M. Clunie, T. Schlicke, and B. W. Melville. Equilibrium hydrodynamics concept for developing dunes. *Phys. Fluids*, 18(105104), 2006. doi:10.1063/1.2358332.

[155] J. F. Kennedy. The mechanism of dunes and antidunes in erodible-bed channels. *J. Fluid Mech.*, 16:521–544, 1963.

[156] J. Fredsøe. On the development of dunes in erodible channels. *J. Fluid Mech.*, 64:1–16, 1974.

[157] Z. G. Ji and C. Mendoza. Weakly nonlinear stability analysis for dune formation. *J. Hydraul. Engg, ASCE*, 123:979–985, 1997.

[158] M. Colombini. Revisiting the linear theory of sand dune formation. *J. Fluid Mech*, 502:1–16, 2004.

[159] Colombini M. and A. Stocchino. Finite-amplitude river dunes. *J. Fluid Mech.*, 611:283–306, 2008. doi:10.1017/s0022112008002814.

[160] J. Nelson, A.R. Burman, Y. Shimizu, S. R. McLean, R. L. Shreve, and M. W. Schmeeckle. Computing flow and sediment transport over bedforms. *Proc. of Int. Conf. on Riv. Cosast. and Est. Morph., RCEM*, pages 861–868, 2005.

[161] S. Tjerry and J. Fredsøe. Calculation of dune morphology. *J. Geophys. Res.*, 110:F04013, 2005.

[162] A. Defina. Numerical experiments on bar growth. *Water Resour. Res.*, 39(4):1092, 2003. doi:10.1029/2002WR001455.

[163] B. Federici and G. Seminara. On the convective nature of bar instability. *J. Fluid Mech.*, 487:125–145, 2003.

[164] S. Onda and T. Hosoda. Numerical simulation on development process of dunes and flow resistance. *Paper presented at River Flow 2004: Second International Conference on Fluvial Hydraulics*, 2004.

[165] S. Giri and Y. Shimizu. Numerical computation of sand dune migration with free surface flow. *Water Resour. Res.*, 42:W10422, 2006.

[166] C. F. Nordin and J. H. Algert. Spectral analysis of sand waves. *J. Hydraul. Div. Am. Soc. Civ. Eng.*, 92(HY5):95–114, 1966.

[167] M. Hino. Equilibrium-range spectra of sand waves formed by flowing water. *J. Fluid Mech.*, 34:565–573, 1968.

[168] S. C. Jain and J.F. Kennedy. The spectral evolution of sedimentary bedforms. *J. Fluid Mech.*, 63:301–314, 1974.

[169] H. Nakagawa and T. Tsujimoto. Spectral analysis of sand bed instability. *J. Hydraul. Eng.*, 110(HY4):467–483, 1984.

[170] J. Aberle, V. Nikora, M. Henning, B. Ettmer, and B. Hentschel. Statistical characterization of bed roughness due to bed forms: A field study in the elbe river at aken, germany. *Water Resour. Res.*, 46:W03521, 2010. doi:10.1029/2008WR007406.

[171] F. M. Exner. Zur dynamik der bewegungsformen auf der erdoberfläche. Technical report, Adakemische Verlagsgeselschaft, Leipzig, Federal Republic of Germany, 1931. In German.

[172] A. J. Raudkivi and H. H. Witte. Development of bed features. *J. Hydraul. Eng.*, 116:1063–1079, 1990.

[173] V. Schwämmle and H. J. Herrmann. Modelling transverse dunes. *Earth Surf. Processes Landforms*, 29(6):769–784, 2004.

[174] M. Crickmore. Effect of flume width on bed-form characteristics. *J. Hydraul. Div. Am. Soc. Civ. Eng.*, 96:473–496, 1970.

[175] P. Julien and G. Klassen. Sand-dune geometry of large rivers during floods. *J. Hydraul. Engg, ASCE*, 121:657–663, 1995.

[176] N. K. K. Gamage and W. Blumen. Comparative analysis of low level cold fronts: Wavelet, fourier, and empirical orthogonal function decompositions. *Mon. Weather Rev.*, 121:2867–2878, 1993.

[177] L. H. Hudgins, C. A. Friehe, and M. E. Mayer. *Fourier and wavelet analysis of atmospheric turbulence.* edited by Y. Meyer, S. Roques, Frontiers, Gif-sur-Yvette, France, 1993.

[178] R. L. Dinehart. Bedform movement recorded by sequential single-beam surveys in tidal rivers. *J. Hydrol.*, 258:25–39, 2002.

[179] M. Wong, G. Parker, G. P. DeVries, T. M. Brown, and S. J. Burges. Experiments on dispersion of tracer stones under lower-regime plane-bed equilibrium bed load transport. *Water Resour. Res.*, 43:W03440, 2007. doi:10.1029/2006WR005172.

[180] Y. Malecot, C. Auriault, H. Kahalerras, Y. Gagne, O. Chanal, B. Chabaud, and B. Castaing. A statistical estimator of turbulence intermittency in physical and numerical experiments. *Eur. Phys. J. B*, 16:549–561, 2000.

[181] S. R. McLean and J. D. Smith. Turbulence measurements in the boundary layer over a sand wave field. *J. Geophys. Res.*, 84(C12):77917808, 1979. doi:10.1029/JC084iC12p07791.

[182] I. B. Aban, M. M. Meerschaert, and A. K. Panorska. Parameter estimation for the truncated pareto distribution. *J. Am. Stat. Assoc.*, 101 (473):270–277, 2006.

[183] A. Clauset, C. R. Shalizi, and M. E. J. Newman. Power law distributions in empirical data. *SIAM Review*, 51(4):661–703, 2009.

[184] M. Wong and G. Parker. Reanalysis and correction of bed-load relation of meyer-peter and mller using their own database. *J. Hydraul. Eng.*, 132:11591168, 2006.

[185] A. Singh, S. Lanzoni, E. Foufoula-Georgiou, and P. R. Wilcock. Multi-scale statistical characterization of migrating bedforms in gravel and sand-bed rivers. *Water Resour. Res.*, 2010b. under review.

[186] D. Schertzer, S. Lovejoy, F. Schmitt, Y. Chiguirinskaya, and D. Marsan. Multifractal cascade dynamics and turbulent intermittency. *Fractals*, 5:427471, 1997.

[187] A. Molini, G. G. Katul, and A. Porporato. Causality across rainfall time scales revealed by continuous wavelet transforms. *J. Geophys. Res.*, 115:D14123, 2010. doi:10.1029/2009JD013016.

[188] Z. Warhaft. Turbulence in nature and in the laboratory. *Proc. Natl. Acad. Sci. USA*, 99(Suppl. 1):2481–2486, 2002.

[189] H. A. Einstein. The bed load transport as probability problem. *Mitteilung der Versuchsanstalt fuer Wasserbau an der Eidgenössischen Technischen Hochschule*, 110, 1937.

[190] H. A. Einstein. The bed-load function for sediment transportation in open channel flows. *Tech. Bull. 1026, Soil Conserv. Serv., U. S. Dep. of Agric., Washington, D.*, page 78, 1950.

[191] A. S. Paintal. A stochastic model of bed load transport. *J. Hydraul. Res.*, 9(4):527554, 1971.

[192] D. J. Furbish, P. K. Haff, W. E. Dietrich, and A. M. Heimsath. Statistical description of slope-dependent soil transport and diffusion like coefficient. *J. Geophys. Res.*, 114:F00A05, 2010. doi:10.1029/2009JF001267.

[193] C. Ancey. Stochastic modeling in sediment dynamics: Exner equation for planar bed incipient bed load transport conditions. *J. Geophys. Res.*, 115:F00A11, 2010. doi:10.1029/2009JF001260.

[194] M. A. Hassan and M. Church. Distance of movement of coarse particles in gravel bed streams. *Water Resour. Res.*, 27:503511, 1991.

[195] M. Church and M. A. Hassan. Size and distance of travel of unconstrained clasts on a streambed. *Water Resour. Res.*, 28:299303, 1992.

[196] V. Ganti, A. Singh, P. Passalacqua, and E. Foufoula-Georgiou. Subordinated brownian motion model for sediment transport. *Phys. Rev. E*, 011111:2867–2878, 2009.

[197] V. Ganti, M. M. Meerschaert, E. Foufoula-Georgiou, E. Viparelli, and G. Parker. Normal and anomalous diffusion of gravel tracer particles in rivers. *J. Geophys. Res.*, 115:F00A12, 2010.

[198] C. Escauriaza and F. Sotiropoulos. Lagrangian model of bed-load transport in turbulent junction flows. *J. Fluid Mech.*, 666:36–76, 2011. DOI: 10.1017/S0022112010004192.

[199] P. Ergenzinger, K. H. Schmidt, and R. Busskamp. The pebble transmitter system (pets): first results of a technique for studying coarse material erosion, transport and deposition. *Zeitschrift für Geomorphologie N.F.*, 33:503–508, 1989.

[200] P. R. Wilcock. Entrainment, displacement and transport of tracer gravels. *Earth Surf. Processes Landforms*, 22:11251138, 1997.

[201] E. F. Chacho, R. L. Burrows, and W. W. Emmett. Detection of coarse sediment movement using radiotransmitters. *In Proceedings XXIII IAHR Congress*, pages 367–373, 1989.

[202] H. M. Habersack. Radio-tracking gravel particles in a large braided river in new zealand: a field test of the stochastic theory of bed load transport proposed by einstein. *J. Hydrol. Proc.*, 15(3):377–391, 2001.

[203] K. M. Hill, L. DellAngelo, and M. M. Meerschaert. Heavy-tailed travel distance in gravel bed transport: An exploratory enquiry. *J. Geophys. Res.*, 115:F00A14, 2010. doi:10.1029/2009JF001276.

[204] M. G. Foley. Gravel lens formation in antidune-regime flow: a quantitative hydrodynamic indicator. *J. Sed. Petr.*, 47:738–746, 1977.